Università degli Studi di Torino
Doctoral School of the University of Torino
PhD Programme in Chemical and Materials Sciences XXXVII Cycle

Tuning nanodiamonds surface and core properties for Reactive Oxygen Species production enhancement and measurement

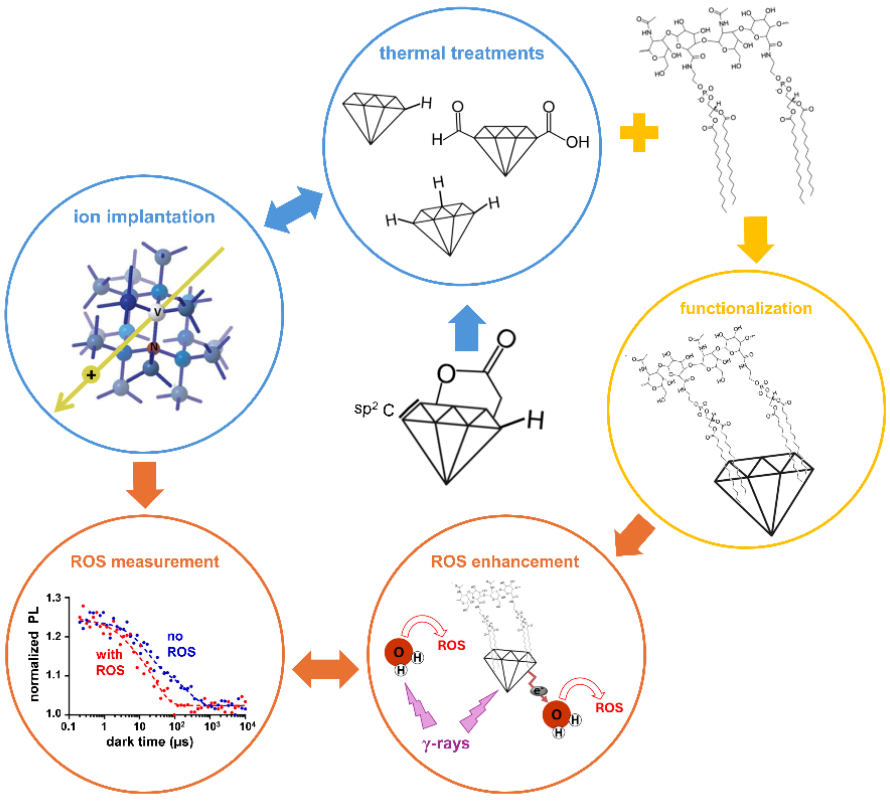

Sofia Sturari

Supervisor:
Prof. Federico Picollo

Università degli Studi di Torino

Doctoral School of the University of Torino

PhD Programme in Chemical and Materials Sciences XXXVII cycle

Tuning nanodiamonds surface and core properties for Reactive Oxygen Species production enhancement and measurement

Candidate: **Sofia Sturari**

Supervisor: Prof. **Federico Picollo**

Jury Members: Prof. **Silvia Giordani**
Dublin City University
School of Chemical Sciences

Prof. **Bohuslav Rezek**
Prague Czech Technical University
Physics Department

Prof. **Ettore Vittone**
Università degli Studi di Torino
Physics Department

Head of the Doctoral School: Prof. Enzo Medico

PhD Programme Coordinator: Prof. Bartolomeo Civalleri

Torino, 2025

"I can live with doubt and uncertainty and not knowing. I think it is much more interesting to live not knowing than to have answers that might be wrong. If we will only allow that, as we progress, we remain unsure, we will leave opportunities for alternatives. We will not become enthusiastic for the fact, the knowledge, the absolute truth of the day, but remain always uncertain…In order to make progress, one must leave the door to the unknown ajar."

-Richard P. Feynmann

"The search for truth is more precious than its possession."

-Albert Einstein

"Non est ad astra mollis e terris via."

-Lucius Annaues Seneca

Table of contents

Preface

Reactive Oxygen Species (ROS), including oxygen free radicals and non-radical oxygen derivatives, are natural byproducts of cellular metabolism. While essential in physiological processes, excessive ROS levels can damage cellular components and contribute to the progression of various diseases. In radiotherapy, ROS production induced by ionizing radiation is used to impair cancer cells, damaging their genetic material. Enhancing this ROS generation within the tumor microenvironment while simultaneously attaining real-time ROS monitoring could significantly improve therapeutic outcomes. This dual functionality can be achieved using nanodiamonds (ND), *i.e.*, diamond nanoparticles. Their surface can indeed be modified to target tumor sites and promote electronic emission under irradiation, resulting in ROS increase at the desired location, whereas photoluminescent Nitrogen-Vacancy (NV) centers in their core can be exploited as sensors for ROS measurement.

The tuning of ND surface terminations can be accomplished through high-temperature thermal treatments in controlled atmosphere. Among the various processes, hydrogenation ones are particularly notable, as they produce hydrogenated ND, which are characterized by a negative electron affinity. This property, besides causing high water-induced surface electrical conductivity, has been found to be responsible for an intense electronic emission from the particles under irradiation. Such phenomenon can be exploited to boost the production of ROS generated in radiotherapy by ionizing radiation, thus enhancing the efficacy of the treatments. The control of NV centers in ND core can instead be achieved through particle modification with ion beams and is of paramount importance in sensing, since these defects can be employed for assessing the concentration of free radicals *via* T_1-relaxometry. The technique measures T_1 relaxation time of negatively charged NV centers (NV^-), as such quantity is shortened when free radicals are present in the environment surrounding ND.

ND hence appear as a promising platform for monitoring radiotherapy treatments while enhancing their effectiveness at the same time. Nevertheless, ND high aggregation tendency in aqueous solutions poses serious challenges for their real application, being cellular environment rich in water. To solve this issue, ND surface can be decorated with hydrosoluble polymers, such as hyaluronic acid (HA). This biodegradable and biocompatible molecule imparts ND better water dispersibility, providing them also with targeting ability, *i.e.*, favoring their internalization in specific tumor cells that overexpress cluster determinant 44 (CD44) HA receptors on their membrane (*e.g.*, breast and lung cancer cells). HA can be attached to ND surface by non-covalent functionalization, exploiting its reaction with phospholipids, such as 1,2-dimyristoyl-*sn*-*glycero*-3-phosphoethanolamine (DMPE),

originating amphiphilic conjugates, which are linkable to the nanoparticles following an extremely straightforward approach.

Tailoring surface and core properties of ND is crucial for designing particles that can effectively amplify ROS production, while allowing for their concurrent measurement. The work of this thesis was carried out with this perspective, focusing on the characterization of ND modified *via* thermal treatments, functionalization with a HA/DMPE conjugate, and ion irradiation, for the development of systems capable of simultaneously enhancing and measuring ionizing radiation-induced ROS production.

The first goal of the experimental activity was attaining a comprehensive knowledge of the effects of thermal treatments in controlled atmosphere on ND properties and establishing an efficient modification protocol to achieve the desired modifications to the ND surface. To this end, the impact of various thermal processes on ND surface terminations was investigated. Such analysis was performed by evaluating the electrical properties of the ND, which were assessed through electrical measurements conducted under controlled humidity conditions. These provided insights into changes in ND surface chemistry and structure, that were then confirmed *via* Diffuse Reflectance Infrared Fourier-Transform (DRIFT) spectroscopy and Raman spectroscopy, and associated with distinct conduction mechanisms, investigating also the effect of particles size. The influence of thermally induced surface terminations was also analyzed in relationship to ND hydrodynamic properties, conducting Dynamic Light Scattering (DLS) and Zeta Potential (ZP) measurements to gain insights into particles behavior in aqueous solutions.

To render ND particles highly dispersible in aqueous environment and simultaneously selective towards CD44-rich tumor cells, modification of thermally treated ND through non-covalent functionalization with HA/DMPE was implemented. Alterations to ND properties induced by derivatization were explored thanks to a comparative characterization of ND before and after surface decoration through various techniques (DRIFT spectroscopy, Raman spectroscopy, Photoluminescence spectroscopy, Scanning Electron Microscopy, DLS analyses, and ZP measurements), allowing to confirm the efficacy of the functionalization approach and its effectiveness in increasing the stability of the particles in water-based solutions. To evaluate the cellular biocompatibility and the targeting action towards CD44-rich cells of the developed particles, the ND were also tested on different cell lines in *in vitro* experiments.

To assess the potential of hydrogenated ND to enhance ionizing radiation-induced ROS production, targeted experiments were undertaken. ND in aqueous solutions were irradiated with γ-rays and the concentration of the generated hydroxyl radicals ($^{\bullet}$OH) in the dispersions was measured *via*

fluorescence spectroscopy, using terephthalic acid as a fluorescent probe molecule. Production of $^{\bullet}OH$ was investigated for hydrogenated ND and their HA-functionalized counterpart, and the results were compared with the aqueous solution alone and control ND, which were not expected to enhance radical generation. Furthermore, to investigate the correlation between the ROS production observed in aqueous solution and the biological effects of the combined action of ND and ionizing radiation, preliminary *in vitro* experiments were performed on a radio-resistant cancer cell line to evaluate cellular viability following ND administration and subsequent γ-photons irradiation.

Finally, the fluorescence properties of NV centers embedded in ND core were investigated to assess the suitability of ion beam-modified particles as tools for measuring ROS production *via* T_1-relaxometry. A photoluminescence spectroscopy characterization of ion beam-irradiated ND was performed to estimate the concentration of NV^- centers formed under different irradiation conditions. The particles with the highest NV^- defects concentration were then selected for preliminary T_1-relaxometry experiments, aimed at measuring T_1 relaxation times both in the absence and in the presence of paramagnetic species.

This work was conducted within the Solid State Physics group at the Physics Department of the University of Torino (UniTo); however, as a result of its significant interdisciplinary nature, it involved collaborations with the Departments of Chemistry (Prof. Lorenzo Mino), Drug Science and Technology (Prof. Silvia Mariangela Arpicco's group), and Oncology (Prof. Chiara Riganti's group) at UniTo, as well as with researchers from the Universitair Medisch Centrum Groningen (Prof. Romana Schirhagl's group).

The thesis is organized as follows.

- Chapter 1 introduces the contextual framework in which the work is inserted, delivering background information about ROS, including the enhancement of their production by radiosensitizers and the various techniques used for their measurement. The chapter also describes the properties of diamond and ND, delving into the use of thermal treatments in tuning ND surface moieties and eventually detailing the applications of ND for increasing and measuring ROS production. The goals of the experimental activity are also presented.
- Chapter 2 outlines the ND samples, as well as the instrumentation employed for their modification and characterization.
- Chapter 3 provides a detailed report of samples processing and the results obtained from the characterization of thermally-modified diamond particles, analyses on HA-functionalized

ND, tests of ND in combination with γ-photons irradiation, and study of ion-beam modified ND for application in T_1-relaxometry.

- Chapter 4 summarizes the key findings of the work, presenting its conclusions and an overview of its future developments.
- The appendix presents the results of additional analyses conducted in relation to the main activity.

1. Introduction

1.1 Reactive Oxygen Species (ROS)

“Reactive Oxygen Species” (ROS) is a broad term encompassing a diverse group of oxidizing chemicals with various properties and biological roles, ranging from cellular signaling to inducing cell damage. The production of ROS through ionizing radiation is the mechanism by which radiotherapy damages cancer cells, ultimately leading to their death. In this context, local enhancement of ROS generation at the tumor site is crucial for improving the efficacy of radiotherapy and can be achieved using radiosensitizing agents. Among these, nanodiamonds are particularly promising due to their exceptional biocompatibility and their ability to enable simultaneous measurement of ROS concentration through T_1-relaxometry. Measuring ROS concentration is indeed a key aspect to understanding their biological consequences, though it often presents challenges with the most widely available techniques.

To deeply examine these concepts, the following sub-sections will describe ROS and their role in radiotherapy, the interaction of ionizing radiation with matter and its effects on cells, the increase of ROS production through radiosensitizers, and the different methodologies for measuring ROS.

1.1.1 ROS definition, biological functions, and role in radiotherapy

Reactive Oxygen Species (ROS) encompass both non-radical oxygen derivatives, such as hydrogen peroxide, and oxygen free radicals, including superoxide and hydroxyl radical [1]. These chemicals contain at least one oxygen atom in their structure and exhibit exceptionally high reactivity, which surpasses that of molecular oxygen. ROS are generated physiologically by cells as a byproduct of normal metabolism occurring in oxidative reaction processes of the mitochondrial respiratory chain [2]. Moreover, ROS are also produced *via* various intra- and extra-cellular processes involved in regulating body homeostasis (*i.e.*, internal stability in response to external changes [3]), such as cell division, differentiation, and death [2,4]. At controlled levels, ROS are essential for normal cell functions, contributing to signaling pathways [4,5] and promoting beneficial effects, including wound healing, repairing processes, and the elimination of pathogens [2]. On the other hand, when ROS are produced in excess or when there is an imbalance between their generation and cells antioxidant defenses, oxidative stress damage occurs [1]. In this respect, ROS disturb a series of events that deregulate cellular behavior, impairing the functionality of critical biomolecules and organelles like DNA, proteins, and lipids [2]. This can result into various diseases such as neurodegeneration, Alzheimer's disease, diabetes, Parkinson's disease, protein misfolding diseases, and ophthalmological diseases [2,6].

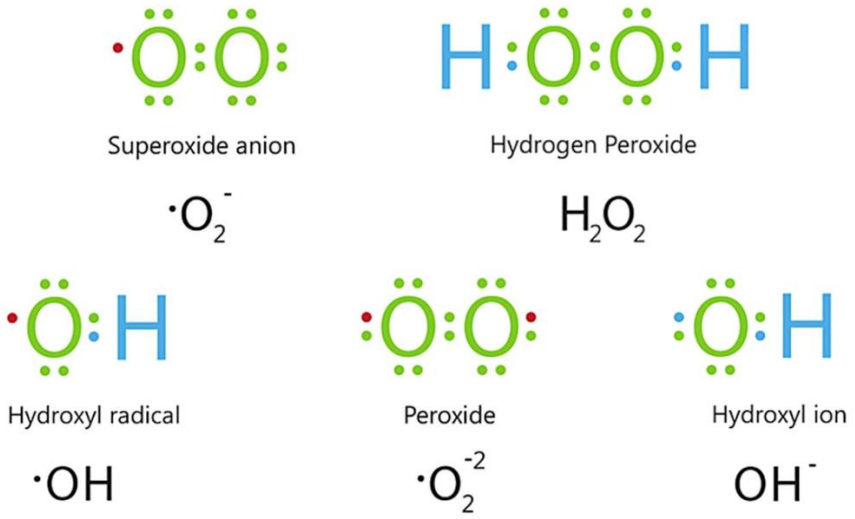

Figure 1-Examples of ROS [7].

Among the various ROS, particular relevance should be given to superoxide anion ($O_2^{\bullet -}$), hydrogen peroxide (H_2O_2), and hydroxyl radical ($^{\bullet}OH$). These are indeed *primary species*, *i.e.*, they are produced directly from molecular oxygen during successive steps of one-electron reductions, as displayed in the reaction below (Eq.1), thus acting as a source of other ROS [1].

$$O_2 \xrightarrow{+e^-} O_2^{\bullet -} \xrightarrow{+e^- (+2H^+)} H_2O_2 \xrightarrow{+e^-} {}^{\bullet}OH \qquad \text{Eq.1}$$

$O_2^{\bullet -}$ is produced enzymatically by the monovalent reduction of oxygen and its levels are controlled by mechanisms of detoxification involving the enzyme superoxide dismutase, which causes the release of less toxic H_2O_2. $O_2^{\bullet -}$ can give rise to peroxynitrite ($ONOO^-$) and $^{\bullet}OH$, reacting respectively with nitric oxide free radical ($^{\bullet}NO$) and H_2O_2 [1,6]. This latter molecule plays a key role in regulating redox signaling at homeostatic physiological levels and is essential for cellular metabolism and survival, both in the extracellular and intracellular environments. When chloride ions are present, H_2O_2 is converted into hypochlorous acid (HClO), which is critical for oxidative damage, including the mechanism through which pathogens are killed by the immune system [1]. The partial reduction of H_2O_2 results in the formation of $^{\bullet}OH$ radical. This is regarded as the most potent oxidant among ROS, having a strong affinity for electronic-rich sites, such as aromatic or sulfur-containing molecules, including proteins and DNA, which damage by altering or impairing their functions. Due to its highly reactive nature and to the fact that it cannot be enzymatically removed, it is not considered as signaling specie, contributing significantly to oxidative stress and tissue damage [1,6].

Other notable ROS which are widely recognized as biomarkers of oxidative stress are hydroperoxyl radical ($HOO^{\bullet}$) and nitric oxide free radical ($^{\bullet}NO$). The former plays a crucial role in lipid

peroxidation by initiating chain reactions that transform polyunsaturated fatty acids into lipid hydroperoxides, which subsequently decompose into secondary products like aldehydes and malondialdehydes [1,6]. On the other hand, $^{\bullet}NO$ serves as a multi-functional regulator and effector of the immune, cardiovascular, and nervous systems when present at optimal levels. However, $^{\bullet}NO$ can also exhibit harmful effects, leading to the formation of highly oxidative species like nitrogen dioxide radical ($^{\bullet}NO_2$), peroxynitrite ($ONOO^-$), nitrosoperoxycarbonate ($ONOOCO_2^-$), and carbonate radical ($CO_3^{\bullet -}$) through reaction with CO_2 [1].

An important pathological condition linked to elevated ROS levels and oxidative stress is cancer [8]. Studies have shown that during the transformation from normal to tumor cells, ROS levels continuously increase [8–10]. This accumulation triggers enhanced antioxidant defense mechanisms, shifting redox homeostasis from a normal state to a new equilibrium characterized by high rates of both ROS generation and scavenging, thereby keeping ROS levels within cancer cells below the toxic threshold [9]. Cancer cells thus depend heavily on their endogenous antioxidant systems, making them particularly susceptible to external factors that induce further ROS generation. This vulnerability is exploited in various anticancer strategies, including molecular targeted drugs, chemotherapeutic agents, and treatments such as sonodynamic and photodynamic therapy [9,11]. In this context, radiotherapy stands out as a widely employed anticancer strategy that induces ROS generation through the use of ionizing radiation [9], encompassing various methodologies that have evolved over the years. Conventional radiotherapy primarily utilizes X-rays and γ-rays [12], while hadrotherapy is based on particles like protons or carbon ions [13], which offer the advantages of dose elimination beyond the target and reduced dose in proximity to the particle end-of-range [14]. As will be detailed in the following sub-sections, the ROS generated by ionizing radiation are the primarily responsible for the biological damage inflicted on cancer cells during radiotherapeutic treatments [15].

1.1.2 Ionizing radiation and ionizing radiation-generated ROS

Ionizing radiation is defined as radiation possessing enough energy to remove one or more electrons from the atoms or molecules it interacts with, resulting in ionization. Given that the typical binding energy of electrons in biological materials is around 10 eV, any radiation must have energy exceeding this threshold to be considered as ionizing [16]. Ionizing radiation encompasses photons (X-rays and γ-rays), as well as neutral particles (like neutrons) and charged particles (such as protons, electrons, and alpha particles). Photons are classified as *indirectly ionizing* because they displace orbital electrons from atoms, which then carry energy away from the primary interaction site. In contrast,

neutral and charged particles are regarded as *directly ionizing*, since they transfer energy through direct collisions with atomic electrons [16].

Most clinical applications rely on the use of photons [17]. When a narrow beam of N_0 monoenergetic photons enters a uniform absorber, the number of photons *N(x)* remaining in the beam at a depth *x*, without any interaction, is described by the following equation (Eq.2):

$$N(x) = N_0\, e^{-\mu x} \qquad \text{Eq.2}$$

where μ represents the linear attenuation coefficient, or macroscopic cross-section, which denotes the probability per unit distance for a photon to interact, having dimensions of inverse length. In media with density ρ, this can also be expressed as the mass attenuation coefficient, μ/ρ [18]. In the 100 keV - 25 MeV energy range, which is the one commonly used in radiotherapy [17], two primary interaction mechanisms between photons and matter should be mentioned, *i.e.*, the photoelectric effect and Compton scattering (Figure 2). The former, dominating for keV energy photons, involves a photon transferring all its energy to a bound electron in a defined electronic shell (K, L, etc.). A portion of the transferred energy is used to overcome the electron binding energy, allowing it to be ejected from the atom, while the remaining energy contributes to the electron kinetic energy (E_k), which is given by:

$$E_k = h\nu - E_b \qquad \text{Eq.3}$$

where $h\nu$ represents photon energy and E_b the electron binding energy. The hole left by the ejected electron can be filled by an electron from an outer shell, resulting in the emission of characteristic X-rays or the release of an Auger electron [18]. On the other hand, Compton scattering, prevailing for photons in the MeV energy range, consists in the partial energy transfer from a photon to a loosely bound outer orbital electron, often referred to as a *free electron*. The incident photon is scattered at an angle θ, while the struck electron recoils with kinetic energy E_k. From conservation of energy and momentum, the equations for the kinetic energy of the electron (E_k) and the energy of the scattered photon ($h\nu'$) are:

$$E_k = h\nu \frac{1 - cos\theta}{\frac{mc^2}{h\nu} + 1 - cos\theta} \qquad \text{Eq.4}$$

$$h\nu' = \frac{h\nu}{1 + \frac{h\nu}{mc^2}(1 - cos\theta)} \qquad \text{Eq.5}$$

being $h\nu$, c and m the initial photon energy, the speed of light in vacuum and the electron mass, respectively. The electron and the photon can then undergo further interactions, causing more ionizations, until their energy is dissipated [18].

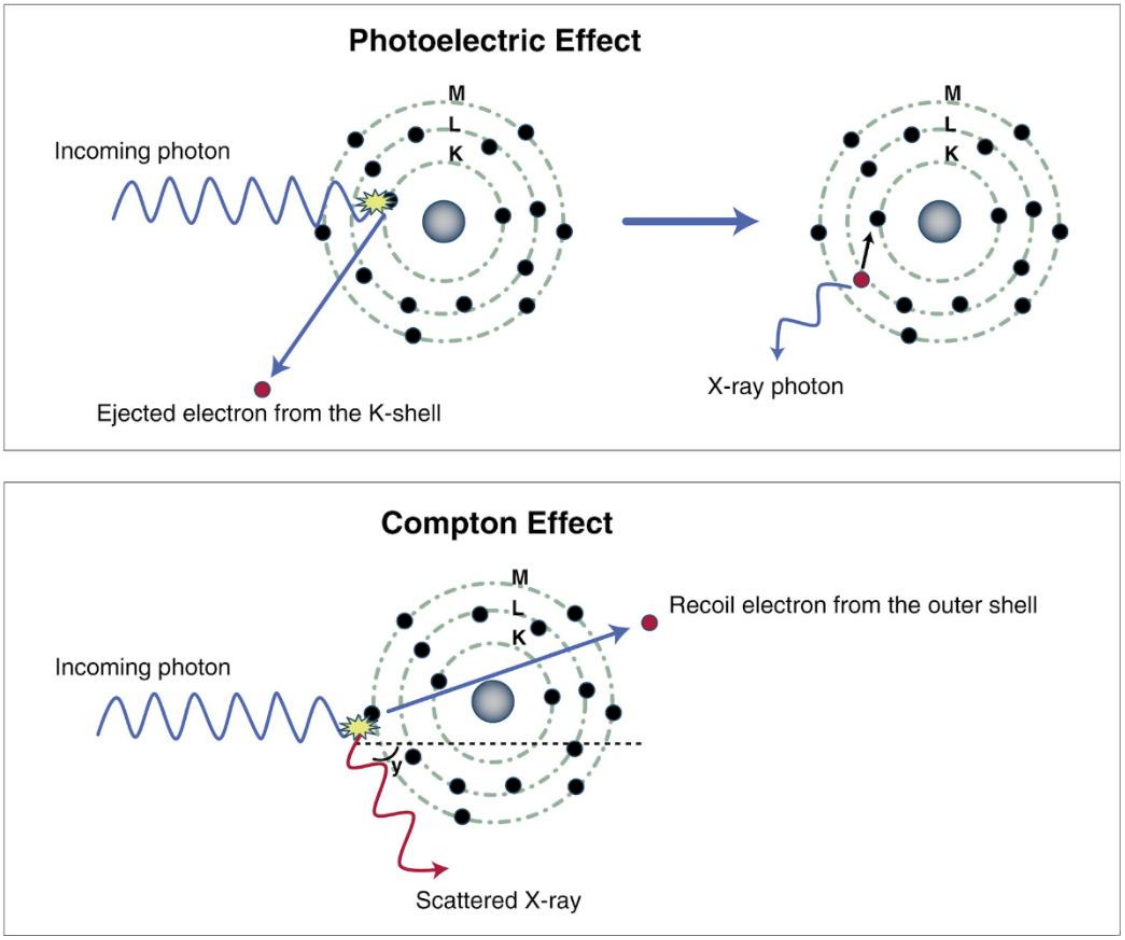

Figure 2-Illustration of photoelectric effect and Compton scattering [19].

Considering both photoelectric effect and Compton scattering, μ can be expressed as:

$$\mu = \tau + \sigma \qquad \text{Eq.6}$$

where τ and σ represents respectively the contribution from the former and the latter phenomenon. τ and σ are both dependent on the atomic number (Z) of the absorber [18,20]:

$$\mu \propto Z^4 \qquad \text{Eq.7}$$

$$\sigma \propto Z \qquad \text{Eq.8}$$

Thus, the likelihood of these interactions increases in materials with a high atomic number [18].

A crucial quantity to consider in connection to radiotherapy is the energy which is imparted by ionizing radiation to a medium. This is typically expressed by the absorbed dose, named also simply dose (D), defined as:

$$D = \frac{\mathrm{d}\epsilon}{\mathrm{d}m} \qquad \text{Eq.9}$$

where $\mathrm{d}\epsilon$ is the average energy transferred to a mass $\mathrm{d}m$ of matter. Such quantity is measured in joules per kilogram (J kg^{-1}), commonly referred to as gray (Gy) [21]. A standard radiation therapy regimen usually involves daily fractions ranging from 1.5 Gy to 3 Gy administered over several weeks [12].

On the other hand, when examining the biological effects of ionizing radiation on cells, it is important to distinguish between *direct* and *indirect* effects. Direct effects involve the ionization of critical cellular components, such as DNA, directly caused by radiation. In contrast, indirect effects result from the interaction of radiation with molecules different from the target ones, such as water, making up 70% - 80% of the cell volume. This gives rise to the production of ROS, which then reach the critical targets by diffusion, leading to harmful effects by inducing oxidative stress [17]. ROS are generated from water in a process called radiolysis, *i.e.*, radiation-induced water decomposition. As displayed in Eq.10, such process starts with the ionization of a water molecule, requiring an energy of 13.6 eV [16], and results in the formation of two highly unstable species, namely a radical cation, $H_2O^{+\bullet}$, and electron. The former is a strong acid and loses proton within 10^{-10} seconds to nearby water molecules, thus producing a hydroxonium ion (H_3O^+) and a hydroxyl radical ($^{\bullet}OH$) according to Eq.11. The electrons released during ionization can travel considerable distances, making recombination unlikely, so that they are captured by other water molecules and become solvated, as shown in Eq.12.

$$H_2O \xrightarrow{\text{ionizing radiation}} H_2O^{+\bullet} + e^- \qquad \text{Eq.10}$$

$$H_2O^{+\bullet} + H_2O \rightarrow H_3O^+ + {}^{\bullet}OH \qquad \text{Eq.11}$$

$$e^- + nH_2O \rightarrow e^-_{aq} \qquad \text{Eq.12}$$

Electronically excited water can also be present, generating through its dissociation (Eq.13) a hydroxyl radical ($^{\bullet}OH$) and a hydrogen radical ($H^{\bullet}$). The formation of hydrogen peroxide ensues from the self-termination of two hydroxyl radicals (Eq.14), while hydrogen is produced in the processes outlined in Eq.15 and Eq.16.

$$H_2O \xrightarrow{\text{ionizing radiation}} {}^{\bullet}OH + H^{\bullet} \quad \text{Eq.13}$$

$$2\,{}^{\bullet}OH \rightarrow H_2O_2 \quad \text{Eq.14}$$

$$2H^{\bullet} \rightarrow H_2 \quad \text{Eq.15}$$

$$2e^-_{aq} + 2\,H^{\bullet} \rightarrow H_2 \quad \text{Eq.16}$$

As detailed in Eq.17 and Eq.18, the reactions of $H^{\bullet}$ and e^-_{aq} with oxygen give respectively rise to into superoxide radical and hydroperoxyl radical ($HO^{\bullet}_2$).

$$e^-_{aq} + O_2 \rightarrow O_2^{\bullet -} \quad \text{Eq.17}$$

$$H^{\bullet} + O_2 \rightarrow HO^{\bullet}_2 \quad \text{Eq.18}$$

The whole set of reactions can be compactly written as illustrated in Eq.19 [22]:

$$H_2O \xrightarrow{\text{ionizing radiation}} {}^{\bullet}OH + e^-_{aq} + H^{\bullet} + H_2O_2 + H_3O^+ + H_2 + O^{\bullet}_2 + HO^{\bullet}_2 \quad \text{Eq.19}$$

Direct and indirect effects are predominant for heavy particles and photons, respectively [15], and both can harm various cellular components, with DNA being the primary target. Radiation can cause single-strand breaks and double-strand breaks, which are disruptions in one or both strands of the double helix. Additionally, other types of damage may occur, including chemical alterations of the nitrogen bases in the DNA backbone and cross-linking, which involves the formation of covalent bonds with proteins or other DNA molecules [17,23].

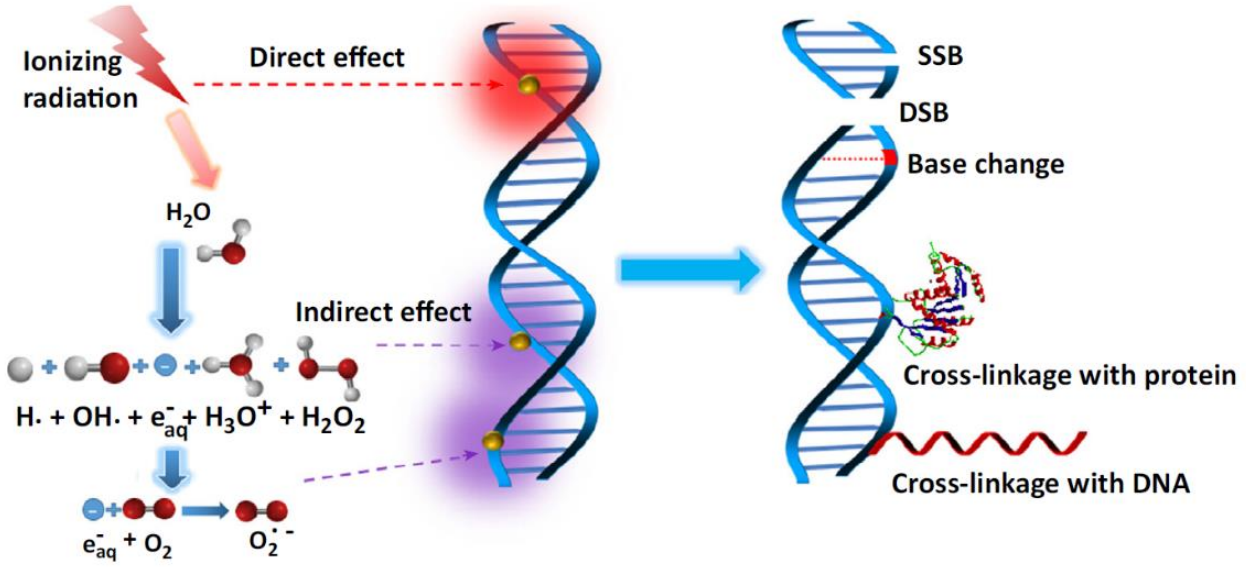

Figure 3-llustration depicting the effect of ionizing radiation on DNA: ionizing radiation can cause direct damage to DNA (direct effect) or can dissociate water molecules, leading to the production of ROS that subsequently damage DNA (indirect effect). Various types of DNA damage may result, including single-strand breaks, double-strand breaks, alterations in nitrogen bases and cross-linking with proteins or other DNA strands [23].

1.1.3 Radiosensitizers: ROS production enhancement by nanoparticles

A higher radiation dose in radiotherapy increases the damage to cancer cells by amplifying both radiation direct effects and ROS production. However, since ionizing radiation affects all tissues indiscriminately, such strategy also leads to increasing damage to healthy organs. This highlights the need for alternative treatments which enhance the effectiveness of radiotherapy without raising radiation doses, thereby minimizing side effects. A promising strategy to achieve this goal rely on the use of radiosensitizers (RS), *i.e.*, molecules or materials that, when combined with radiation, achieve greater tumor killing than would have been expected from radiation alone [24].

Besides small molecules and macromolecules, radiosensitizers include nanomaterials (NM), which are defined as materials having at least one dimension in the size range spanning from 1 nm to 100 nm. NM typically exhibit physicochemical properties that differ significantly from those of bulk materials and are dependent on their size and shape. They are classified into four groups based on the size of x, y, and z dimensions.

- Zero-dimensional NM have all three dimensions with nanoscale size. They encompass nanoparticles (NP) and nanospheres.
- One-dimensional NM are characterized by having two dimensions in the nanoscale range, while the third dimension is not. They include nanorods, nanotubes, and nanowires.
- Two-dimensional NM extend across two dimensions, while the third dimension remains at the nanoscale. Nanofilms, nanolayers, and nano-coatings belong to this group.
- Three-dimensional or bulk NM are not restricted to the nanoscale in any dimension, but they retain nanoscale size in their building blocks. Examples include ordered aggregates of nanoparticles, bundles of nanowires or nanotubes, and multi-nanolayers [25].

In relation to radiosensitizers, particular attention should be given to nanoparticles (NP), due to their preferential accumulation in tumor sites. This results from the Enhanced Permeability and Retention (EPR) effect, a phenomenon allowing NP to penetrate tumor tissue by exploiting the increased gaps between endothelial cells and to be retained because of poor lymphatic drainage [26]. Additionally, NP can be endowed with active targeting action through surface functionalization, which involves decorating their surface with specific molecules binding to overexpressed receptors on cancer cells, thereby further enhancing their delivery to tumor tissues [23]. Once in the tumor site, NP can achieve radio-enhancement through interaction with ionizing radiation which induces the release of a significant quantity of electrons within nanoscale volumes, thereby amplifying both the direct and indirect effects of ionizing radiation (Figure 4) [20,24].

Most current research focuses on high-Z metal NP, such as gadolinium, silver, platinum and especially gold, as these high-Z materials possess strong capabilities for absorbing ionizing radiation and emitting secondary electrons, contributing to localized dose enhancement through photoelectric effect or Compton scattering [20,27,28]. In addition to several *in vitro* investigations, numerous *in vivo* studies have demonstrated the effectiveness of radio-enhancement using metal NP. Pioneering research by Hainfeld et al. showed for instance that the combination of 26 Gy of X-rays with intravenous administration of Au NP at quantities up to 2.7 g per kg of body weight improved the survival of mice with subcutaneous EMT-6 mammary carcinoma compared to those exposed to radiation alone [29]. Another notable example is the study by Zhang et al., which reported an approximately 66% decrease in tumor volume in mice bearing U14 cervical carcinoma when treatment with 5 Gy of X-rays was combined with glutathione-coated gold nanoparticles, rather than using only X-rays [30].

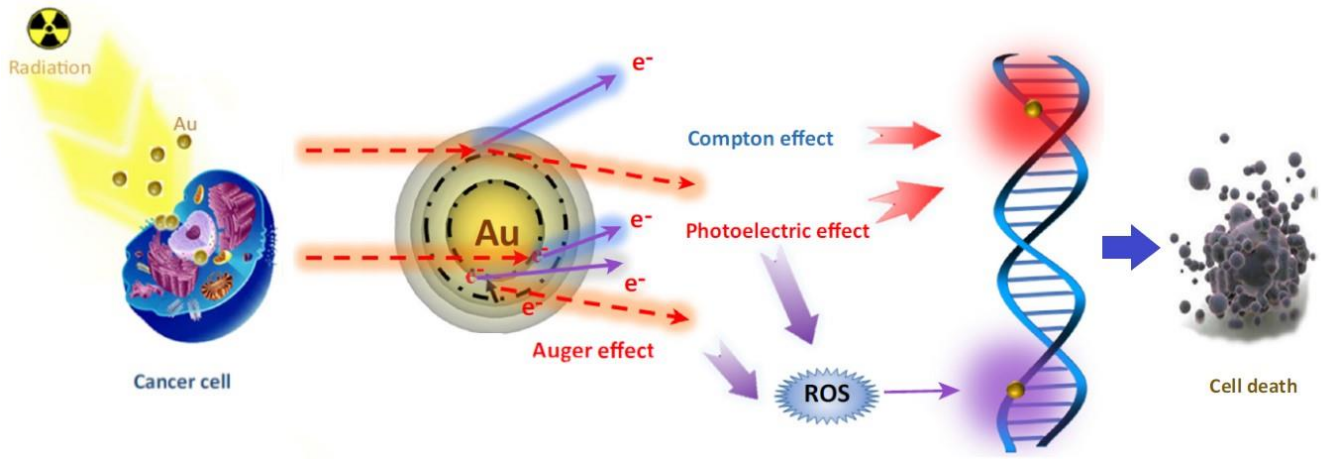

Figure 4-Radiosensitizing mechanism of metallic NP. The NP deposits the radiation dose through photoelectric effect and Compton effect, leading to DNA damage via indirect and indirect processes [23].

However, some inquiries have also uncovered potential hazards related to the use of metal NP. Lee et al. showed for instance that A549 lung epithelial cells underwent morphological changes, including cell shrinkage, few cellular extensions, a restricted spreading pattern, and cell death in a dose-dependent manner when exposed to increasing concentrations of Ag NP for 24 h [31]. Similarly, Labrador-Rached et al. found that citrate-coated Pt NP are toxic to mammalian liver cell line HepG2, compromising basal cellular functionality [32]. Regarding *in vivo* experiments, van der Zande et al. demonstrated that Ag NP that were orally administrated for 21 days in mice (20 mg per kg of body weight) disrupted epithelial cell microvilli and intestinal glands [33], whereas Stefan et al. suggested possible liver toxicity and brain damage caused by Au NP, based on observing an increase of the liver-to-body ratio and a decrease of brain-to-body ratio in rats injected with chitosan-capped Au NP [34].

Due to the concerns related to metal NP utilization, there is a strong imperative to find alternative radio-enhancing platforms that guarantee safety following cellular uptake and nanodiamonds (ND) revealed significant capabilities in this respect. Besides displaying displays superior physical and chemical properties, ND feature chemical inertness and excellent biocompatibility, which are both crucial for their implementation in biological environments [35]. Tailoring of ND surface terminations results in the alteration of their electronic properties and makes possible their application as radiosensitizers [36,37], whereas surface functionalization allows their selective delivery to the tumour tissues [35]. Beside increasing ROS production, the use of ND also enables the measurement of ROS concentration through T_1-relaxometry [38], thus offering the possibility to combine the enhancement of the efficacy of radiotherapy treatments with their tracking. These aspects will be examined in more detail in the following.

1.1.4 ROS measurement techniques

Given the significance of ROS, determining their concentration is crucial for fully understanding their biological effects. In the context of radiotherapy and the enhancement of ROS production by radiosensitizing agents, measuring ROS levels becomes essential not only for monitoring the progress and efficacy of the treatments but also for evaluating the effectiveness of specific radiosensitizers. Although measuring ROS is complex due to their instability, short lifespan (table in Figure 5) and their mutual interactions, an extensive array of techniques is nowadays available [39]. The list below outlines the main methods employed for ROS measurements, providing a brief explanation of their working principle.

- The use of fluorogenic probes is based on non-fluorescent molecules that react with the target ROS to produce fluorescent compounds detectable through fluorescence spectroscopy. Among the most employed ones there are 2',7'-dichlorodihydrofluorescein diacetate and dihydroethidium, both cell permeable and thus suitable also for ROS determination in cells, as well as Amplex Red and terephthalic acid (TPA), typically applied for measurements in aqueous solutions [40].
- Chemiluminescence analyses exploit the emission of photons during the reaction between the species to be detected and an active component, such as bis-N-methylacridinium nitrate, commonly known as "lucigenin", or 5-amino-2,3-dihydroxy-1,4-phthalazinedione, often referred to as "luminol". Both of these compounds can be used for *in vitro* measurements [39,41].
- Spectrophotometric methods operate based on the reaction of ROS with redox substances, measuring the difference in absorbance at various wavelengths between the substrates and

products. Examples include the application of nitroblue tetrazolium to superoxide determination, possible thanks to the production of insoluble purple/blue formazan crystals [42], and the use of 3,3'-diaminobenzidine for H_2O_2 quantification, enabled by the formation of a brown precipitate [39,43].

- Electrochemical techniques measure the current generated by oxidation/reduction reactions involving the species under exam using electrochemical biosensors featuring microelectrodes coated with biomolecules. A common approach, adopted for superoxide recognition, involves electrode coating with protein cytochrome c, that upon reaction with $O^{\bullet 2-}$, undergoes oxidation by the electrode, thus generating a current with intensity proportional to the radicals concentration [44,45].
- Chromatographic methods are prevalently employed for the identification and quantification of hydroxyl radicals. $^{\bullet}OH$ are made to react with reagents such as benzoic acid, salicylic acid, and dimethyl sulfoxide, to generate stable compounds which are then detected *via* liquid chromatography, often coupled with mass spectrometry [39].
- Indirect methods are applied for measurement of ROS in cells and consist in quantifying antioxidant molecules representing the cellular defense capacity against ROS, such as vitamin A or glutathione peroxidase enzyme, or measuring specific compounds that results from ROS-induced damage to proteins, lipids and DNA, including protein carbonyls, malondialdehyde and thymidine glycol [46].
- For the measurement of oxygen free radicals, Electron Spin Resonance (ESR), also known as Electron Paramagnetic Resonance, is often used. This technique detects the resonance absorption of microwave radiation by unpaired electrons, promoting transitions between different spin states, in the presence of a static magnetic field [47]. Given that most kinds of oxygen radicals are short-lived, ESR frequently relies on the used spin traps that stabilize radicals either by incorporating them into their structures or by being oxidized to form more stable radicals with half-lives of several hours. Examples of the first group are the nitrone compound 5,5-dimethyl-1-pyrroline N-oxide and its structural analogues, whereas cyclic hydroxylamines, like 1-hydroxy-3-carboxy-pyrrolidine, belong to the second type of traps [39].

Any of the above techniques could be employed to determine ROS levels, but the choice of specific methods is clearly dictated by experimental requirements, which necessitate a careful evaluation of the pros and cons of each approach [39]. For instance, fluorogenic probe molecules offer the benefit of being extremely easy to use, allowing for product quantification through a straightforward calibration procedure. However, they often suffer from photobleaching and typically need to be used

in high concentrations. Chemiluminescence-based methods, despite the advantage of not requiring an excitation source and be applicable in different environments, involve several steps-reaction and unstable probe radical intermediates. Although benefiting from simple protocols and low cost, spectrophotometric techniques have a low sensitivity and high detection limits. The use of electrochemical biosensors, while offering the capability of performing also *in vivo* ROS detection, presents drawbacks related to the immobilization of the biomolecules onto the microelectrodes surface, that is critical for the long-term stability of the devices. Chromatographic techniques, rapid and sensitive, still present shortcomings due to their reliance on complex reaction processes and products, as well as demanding sample preparation procedures needed. On the one hand, indirect methods measure ROS concentrations while providing biological feedback on their action. On the other hand, they necessitate a precise understanding of cellular mechanisms and of the molecules involved in the cellular response to oxidative stress. Finally, ESR is quantitative accurate and allows collection of precise information, enabling to distinguish among the different kinds of radicals, but difficult spectra interpretation and technique costliness are an issue [39,48].

In addition to the possibilities listed previously, ROS determination can be accomplished through a further technique, *i.e.*, nanodiamonds-based T_1-relaxometry. Developed quite recently, T_1-relaxometry is a method for ROS radicals measurement which makes use of Nitrogen-Vacancy (NV) centers, specific crystal lattice defects in diamond, changing their fluorescent properties based on their magnetic environment. Being sensitive to the electron spin of free radicals, generating spin-noise, NV centers allow conversion of magnetic signals into optical ones, thus dramatically increasing redout sensitivity [38]. T_1-relaxometry, although limited to radicals detection, is particularly promising due to its wide applicability [49–52], the absence of photobleaching of NV centers, and the possibility to measure in real-time the total amount of free radicals generated while simultaneously localizing their production [38]. Further details about nanodiamonds-based T_1-relaxometry will be discussed in sub-section 1.3.5.

Molecule		Half-Life (at 37 °C)
Free radicals	$O_2^{\bullet -}$	10^{-6} s
	$OH^{\bullet}$	10^{-9} s
	$ROO^{\bullet}$	7 s
	$RO^{\bullet}$	10^{-6} s
Nonradicals	$^1O_2$	10^{-6} s
	H_2O_2	chemically stable

Figure 5-Approximate half-lives at 37 °C of some ROS [43].

1.2 Diamond

As nanodiamonds are diamond crystals with nanometric dimensions, they share many of the properties of diamond itself, including its inertness and biocompatibility. Similarly to the bulk material, ND exhibit peculiar electronic properties when their surface is modified with specific terminations and can host Nitrogen-Vacancy color centers, with the former aspect being linked to their use in enhancing ROS production for radiosensitization, while the latter allowing for the implementation of T_1-relaxometry. The following sub-sections will therefore provide a general outline of diamond features, including a detailed examination of the effect of surface terminations on electronic emission and electrical conductivity, as well as a discussion of the characteristics of Nitrogen-Vacancy color centers.

1.2.1 Structure, properties, synthesis, and classification of diamond

With its name derived from the Greek αδαμας (*adamas*), meaning "unbreakable", diamond is a material consisting of atoms of carbon, element belonging to the fourth column of the periodic table with a ground-state electron configuration $1s^2\ 2s^2\ 2p^2$. Carbon exhibits a remarkable range of allotropes, including naturally occurring materials (such as amorphous carbon, graphite, and diamond), as well as synthetic ones (like carbon nanotubes, graphene, and fullerenes). Its allotropic forms differ significantly in their atomic bonding, based on the different atomic hybrid configurations adopted by carbon atoms, resulting in distinct material structure and properties. In diamond, each carbon is characterized by sp^3 hybridization of atomic orbitals, allowing the formation of strong σ bonds with four adjacent atoms, giving rise to a tetrahedral structure with angles of 109°28'. In contrast, graphite features sp^2 hybridization of carbon atoms. These arrange themselves into six-membered hexagonal rings, forming layers, each referred to as graphene, which loosely stack on top of one another thanks to weak Van der Waals bonds [53].

Given the positive standard Gibbs free energy change for the conversion of graphite to diamond ($\Delta G° = 2.9$ kJ mol^{-1} at 298.15 K and 1.013×10^5 Pa) [54], diamond is thermodynamically unstable with respect to graphite, making the reaction $C_{graphite} \rightarrow C_{diamond}$ favored in the reverse direction. However, as illustrated in the carbon phase diagram, diamond exists as a metastable phase at ambient temperature and atmospheric pressure, remaining kinetically stable due to the extremely slow conversion to graphite under ordinary conditions [53].

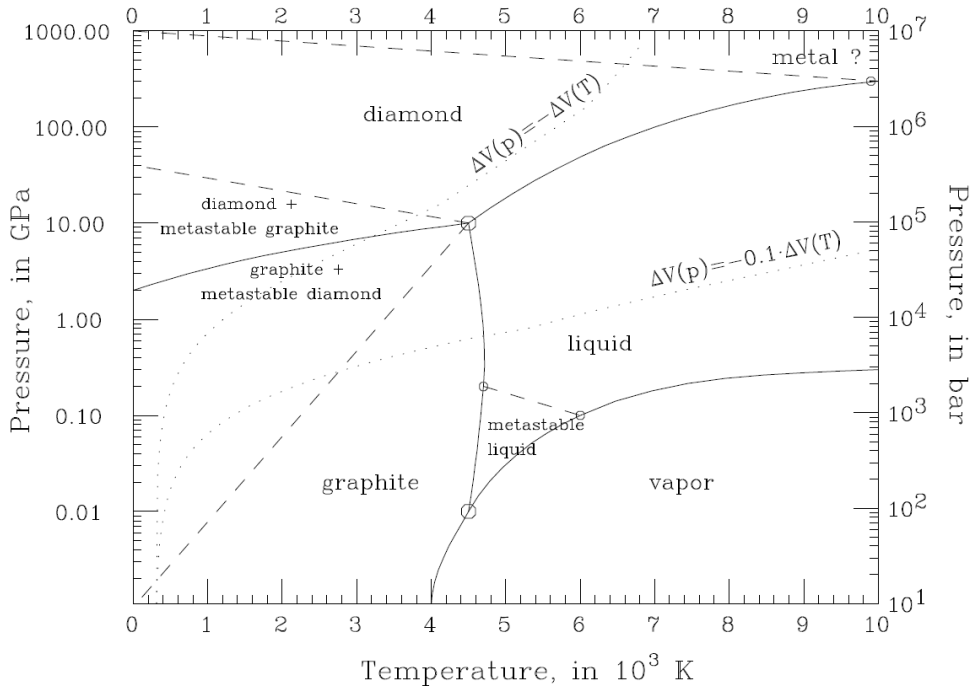

Figure 6-Phase diagram of carbon [55].

The highly isotropic crystal structure of diamond is based on a face-centered cubic (FCC) lattice with a diatomic basis where atoms occupy the positions (0, 0, 0) and (¼, ¼, ¼) in the cubic cell, belonging to $Fd\bar{3}m$ space group cell, and lattice constant of 0.357 nm. Such arrangement gives diamond an atomic density of 1.77×10^{23} atoms cm^{-3}, that is the highest of any known material and results in an exceptionally high gravimetric density of 3.52 g cm^{-3}.

Covalent bonds between carbon atoms in diamond have a short bond length of 0.154 nm and a high bond energy of 711 kJ mol^{-1} (equivalent to 7.37 eV per atom), which form the basis of the material exceptional mechanical and chemical properties [53]. The former include extreme hardness, rated 10 on the Mohs scale [56], the greatest among natural materials, and remarkable stiffness, with a Young's modulus of 1220 GPa [53]. The latter encompass instead high chemical inertness and biocompatibility, which render diamond particularly suitable for applications involving biological systems [57]. Additionally, diamond display excellent thermal properties, featuring both an extremely low linear thermal expansion coefficient (0.8×10^{-6} K^{-1}) and an exceptionally high thermal conductivity of 2200 W m^{-1} K^{-1}, that results from its reduced phonon density at ordinary temperatures, minimizing the likelihood of lattice vibrations interacting [53]. On the other hand, from the viewpoint of optical properties, diamond possess a large refractive index, with an average value of 2.42 across the visible spectrum, determining its brilliant sparkle and widespread use in jewelry, and, in absence of impurities, it exhibits transparency over a wide range of wavelengths, spanning from ultraviolet to far-infrared. Moreover, with its wide indirect band gap of 5.49 eV, diamond can

host a significant number of defects that alter its optical properties, particularly the so-called *color centers*. Over 500 different types of these centers are known, mainly created through ion irradiation processes [58]. Finally, diamond also stands out for its electrical properties, being one of the best electrical insulating materials when dopants and specific surface terminations are not present. Its resistivity is equal to 10^{16} Ω cm [53].

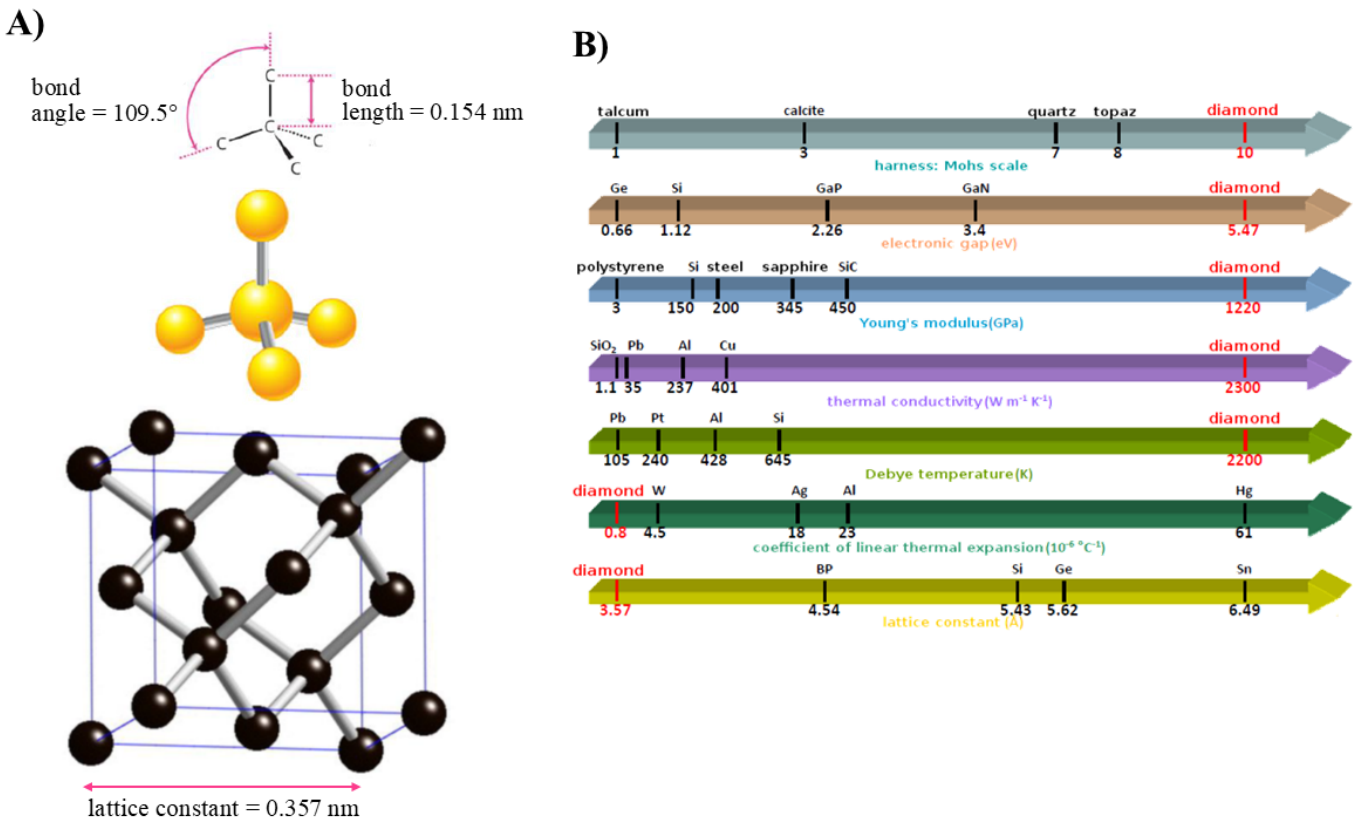

Figure 7-A) Diamond structure [59]. B) Properties of diamond compared with other materials.

The outstanding properties of diamond, which are compared with those of other materials in Figure 7B, make it highly attractive for a wide range of applications. These, spanning from its use as an abrasive or heat sink to its utilization in quantum computing or biosensors, prompted the development of various methods to artificially synthesize it [53]. Natural diamond indeed, due to its rarity, high cost, and variable characteristics, is impractical for commercial and scientific uses. A popular approach for diamond synthesis is High Pressure High Temperature (HPHT) technique, in which graphite is heated to average temperatures ranging from 2000 K to 3000 K, under pressures of approximately 10 GPa. Such method effectively replicates natural diamonds formation process, as under such extreme conditions diamond becomes thermodynamically favored with respect to graphite [60]. Another widespread synthetic process is Low Pressure Low Temperature technique, commonly known as Chemical Vapor Deposition (CVD), that instead synthesize diamond employing

reduced temperature of about 900 °C and 10 Pa pressure, starting from a mixture of hydrogen with a gaseous carbon-containing precursor, *e.g.*, methane or ethylene, and a substate material. The gases are introduced into an evacuated chamber where they undergo partial dissociation, through the use of microwaves, sparks, or a heating filament, generating methyl radicals ($CH_3^{\bullet}$) that deposit onto the substate, allowing diamond growth thanks to the removal of surface hydrogen atoms and the addition of further $CH_3^{\bullet}$ radicals. CVD synthesis is particularly advantageous because it enables precise control over the introduction of impurities through the addition of other gases, such as nitrogen and boron, to the reaction mixture [60].

Although diamond can contain several types of impurities, nitrogen and boron atoms are the most common, as these elements are carbon neighbors in the periodic table. On the basis of their concentration and material visible absorption spectrum, diamond can be divided into four types. Specifically:

- Type Ia contains up to 1000 ppm of nitrogen, present in aggregated form, and shows strong optical absorption below 300 nm, giving it a colorless appearance. Accounting for the 98% of natural diamonds, it is generally employed in jewelry or in applications requiring high hardness.
- Type Ib is characterized by nitrogen concentrations of up to 500 ppm, as structurally isolated atoms. This group, which typically includes HPHT synthetic diamonds, has an absorption window at longer wavelengths, *i.e.*, around 400 nm, resulting into a yellowish color.
- Type IIa features a nitrogen concentration lower than 10 ppm and is optically transparent, exhibiting a transmittance that ranges from 225 nm to 2000 nm. Such category encompasses most of the diamonds produced by CVD technique, while including only the 2% of natural diamonds.
- Type IIb has less nitrogen than Type IIa, with boron impurities becoming crucial, leading to p-type semiconductor characteristics [53].

1.2.2 Diamond surface: oxygen and hydrogen terminations

The most important surfaces in diamond are the (1 1 1) and (1 0 0) surfaces (Figures 8A and 8B), both of which are characterized by dangling bonds [61]. Specifically, the (1 1 1) surface features one dangling bond per surface atom, while the (1 0 0) surface shows two of them per surface atom. These unsaturated bonds can promote surface reconstruction, leading to the formation of π-bonded chains in the case of the (1 1 1) surface and carbon dimers for the (1 0 0) surface [62]. Alternatively, dangling bonds can be saturated by heteroatoms, among which hydrogen and oxygen are the most common ones. The presence of hydrogen on the diamond surface is often the result of synthesis conditions

(*e.g.*, CVD process) [61], whereas oxygen terminations are typically obtained upon acid purification treatments or exposure to oxygen plasma [63]. As shown in Figures 8C and 8D, hydrogen, saturating just one dangling bond per carbon atom, stabilizes the reconstructed (1 0 0) surface, while oxygen, as a divalent atom, saturates two dangling bonds at the same time and, according to the proposed models, can bind to (1 0 0) surface adopting the ketone configuration (top-site model with one oxygen double bonded to each surface carbon atom) or through a bridge bonding structure (bridge-site model where oxygen atoms connect adjacent surface carbon atoms) [62].

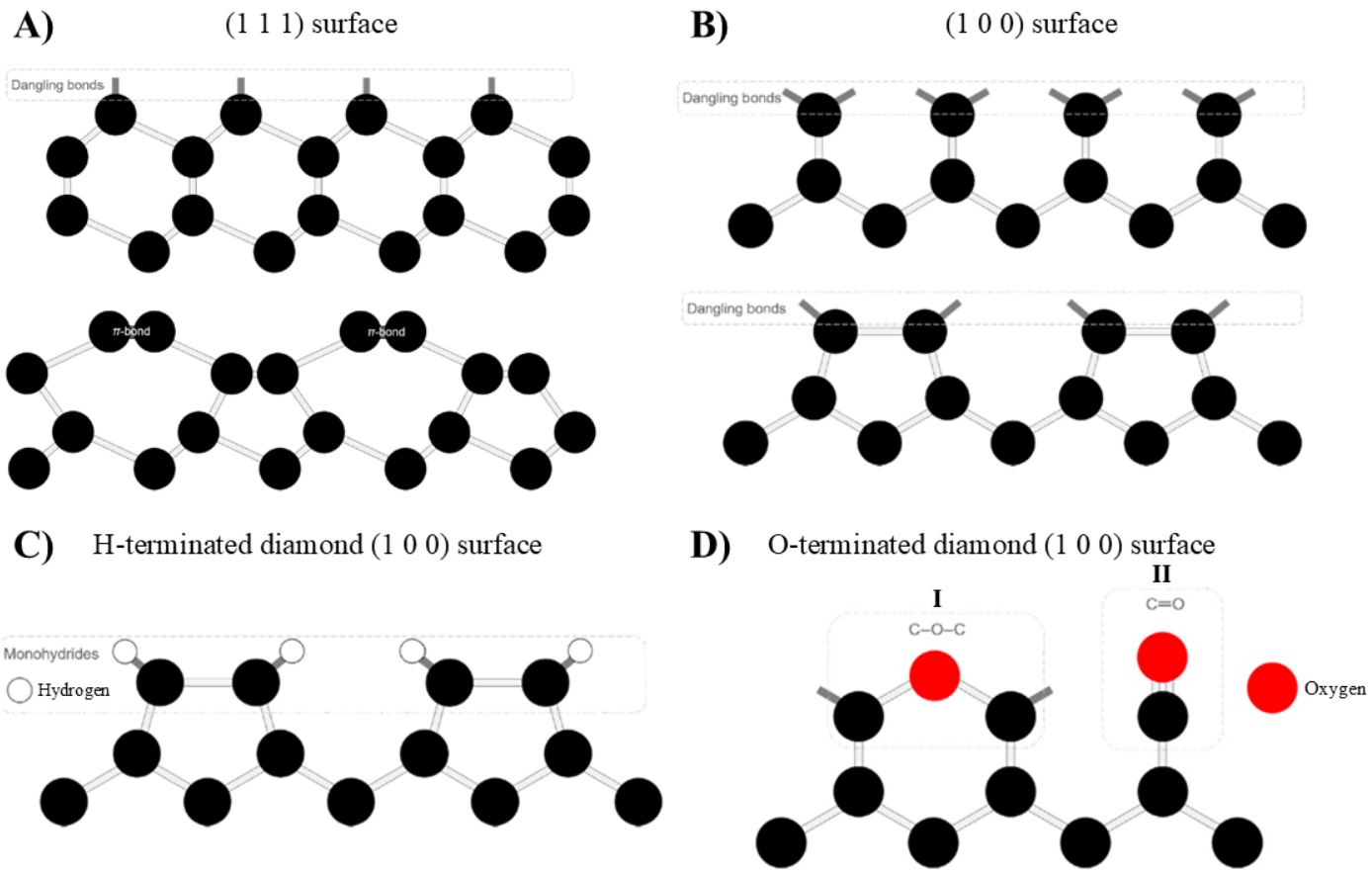

Figure 8-Side-view schematic models of different types of surfaces in diamond [62]. A) (1 1 1) surface. B) (1 0 0) surface. The ideal surface structure and the reconstructed surface are displayed for both cases in the upper and bottom part of the figures respectively. C) (1 0 0) diamond surface with hydrogen terminations. D) (1 0 0) diamond surface with oxygen terminations, displaying the various oxygen bonding configurations (I: bridge bonding, I: ketone bonding).

Diamond surface structure deserves special attention, as it plays a crucial role in determining the properties of the material. Specifically, hydrogen terminations attract particular interest, providing diamond with negative electron affinity. Defined as the energy difference between the vacuum level (E_{vac}) and the conduction band minimum (E_c), electron affinity is indeed equal to -1.3 eV in hydrogenated diamond [64]. Such value can be explained following a simple electrostatic model, considering that heteropolar bonds between carbon and surface-terminating atoms carry a dipole

moment with sign and magnitude depending on the difference in electronegativity between the bonded atoms. Let p represent the component of the dipole moment of a bond terminating the surface that is oriented perpendicular to it and consider this positive with positive partial charge pulled towards the vacuum side and negative partial charge pulled towards diamond side. A layer of these dipoles with areal density n generates an electrostatic potential step perpendicular to the surface across a distance in the order of the surface bonds length, which originates a proportional change in electron affinity ($\Delta\chi$) given by the following expression (Eq.20), where e and ε_0 are respectively the elementary charge and the vacuum permeability [61].

$$\Delta\chi = -e\Delta V = \frac{-epn}{\varepsilon_0} \qquad \text{Eq.20}$$

C-H bond is polarized with a positive partial charge δ+ on the hydrogen atom, given that the electronegativity of hydrogen ($X_H = 2.20$ on Pauling's scale) is lower than that of carbon ($X_C = 2.50$) [65], and hence the dipole moment component of the C-H bonds perpendicular to the surface is positive (for the (1 0 0) surface, p = 0.08 eÅ), thus χ is decreased till becoming negative [61]. Conversely, due to the large electronegativity of oxygen (X_O = 3.44), in the case of oxygen terminations p is negative, thus yielding positive electron affinity with a value of +1.7 eV.

As a result of the negative electron affinity (NEA), hydrogen-terminated diamond displays an intense electron emission of conduction band electrons into vacuum under irradiation. This fingerprint feature can be for instance observed in scanning electron micrographs or photoelectron yield spectra [66].

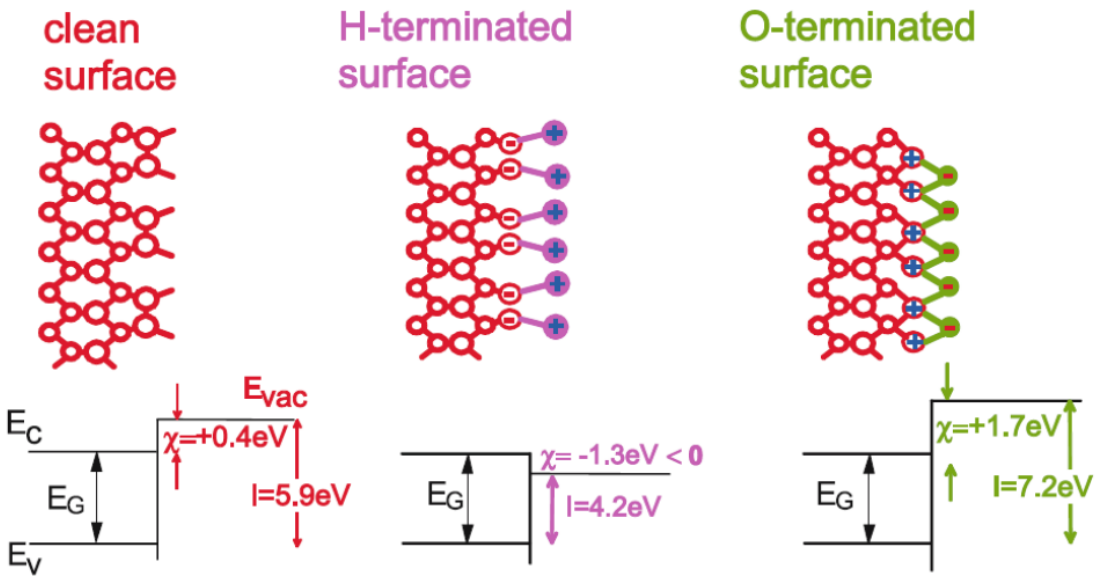

Figure 9- Illustration of the changes in electron affinity and ionization energy of diamond surfaces due to hydrogen and oxygen terminations, along with band diagrams for both clean and fully H/O-terminated diamond surfaces [61].

Additionally, hydrogen surface terminations impact on diamond ionization energy, defined as the difference between E_{vac} and the top of the valence band (E_v), lowering it to 4.2 eV. This implies that electrons can be transferred from E_v to physisorbed surface adsorbates, particularly water, if their electron affinity surpasses/comes close to this value. The electron exchange results in the formation of a sub-surface hole accumulation layer, leading to considerably high surface electrical conductivity [61]. First reported by Maier et al. in 2000, the phenomenon has been interpreted in the framework of an electrochemical surface transfer doping model, schematically shown in Figure 10A [67]. This assumes that the thin water layer formed over diamond surface upon atmosphere exposure acts as an electron acceptor system, thus leaving holes as mobile charge carriers. Electron transfer, producing the reduction of hydroxonium ion to H_2 and H_2O (Eq.21), is driven by the difference between the chemical potential of diamond (*i.e.*, the Fermi level, E_F) and that of electrons in the liquid phase, continuing as long as μ_e lies below E_F.

$$2\ H_3O^+ + 2\ e^- \leftrightarrow 2\ H_2O_2 + H_2 \qquad \text{Eq.21}$$

The space charge due to the compensating holes in the diamond indeed drives surface band bending, raising μ_e until equilibrium is reached, when μ_e and E_F are equal at the interface. According to Nernst's equation, the equilibrium value of μ_e relative to the vacuum level, considered as the common reference for the solid and the adsorbed water layer aqueous, can be expressed as:

$$\mu_e = \mu_0 - \frac{kT}{2}\ ln\left(\frac{([H_3O^+]/[H_3O^+]_{SHE})^2}{[H_2]/[H_2]_{SHE}}\right) \qquad \text{Eq.22}$$

where $[H_3O^+]$, $[H_2]$, $[H_3O^+]_{SHE}$ and $[H_2]_{SHE}$ are respectively the hydroxonium ions and hydrogen concentrations in the system and under standard hydrogen electrode (SHE) conditions and $\mu_0 = 4.44$ eV represents the SHE chemical potential for electrons. As $[H_2]$ can be replaced by H_2 partial pressure (p_{H_2}) and $[H_3O^+]$ by the pH value of the aqueous layer, the previous equation at room temperature can be rewritten as:

$$\mu_e = 4.44\ eV - \frac{0.058\ eV}{2}\ \left(2\ \text{pH} + log\ \left(\frac{p_{H_2}}{bar}\right)\right) \qquad \text{Eq.23}$$

At the interface, since the concentration of dissolved hydrogen is in the ppm range, hydrogen partial pressure can be taken as $p_{H_2} \approx 10^{-3}$ mbar, whereas water pH value is around 6 because of the air content of CO_2 in standard atmospheric conditions. Therefore, the chemical potential μ_e of an aqueous wetting layer can be calculated as $\mu_e = \mu_0 + 0.18$ eV $= -4.26$ eV and, considering $\chi = -1.3$ eV, the pinning position of E_F is approximately 50 meV below Ev at the water/diamond interface (inset of

Figure 10B). The surface holes on the diamond are neutralized by anions (HCO_3^-) that remain unbalanced after the reduction of H_3O^+ ions [67].

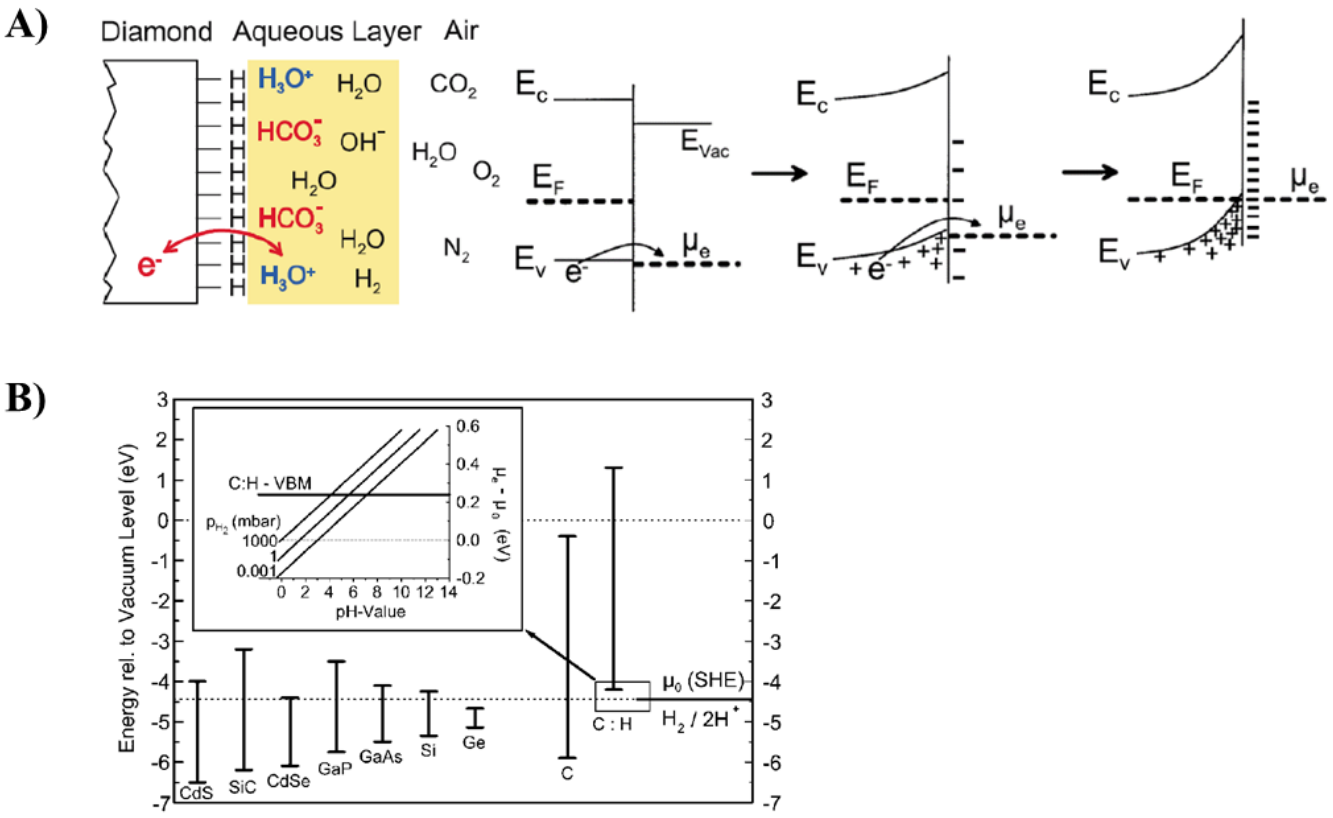

Figure 10-A) Scheme of the surface doping originating from the interaction of hydrogen terminations with water, giving rise surface conductivity. The transfer of electrons from diamond to hydroxonium ion in the adsorbed water layer leaves holes and uncompensated anions on the surface behind. This space-charge separation results in holes confinement to the surface by an upward band bending potential [61,67]. B) Band edges energies with respect to the vacuum level of various semiconductors, hydrogen-free diamond and hydrogenated diamond. The inset displays the modification of the chemical potential μ_e relative to μ_0 as a function of hydrogen partial pressure and pH value [67].

Maier et al. showed that the high surface conductance of hydrogenated diamond films, with values between 10^{-6} Ω^{-1} - 10^{-4} Ω^{-1}, was lost upon samples oxidation, as this dropped to below 10^{-10} Ω^{-1}. Moreover, they reported that the conductance of hydrogenated samples annealed in ultra-high vacuum decreased till below 10^{-10} Ω^{-1}, rising again after air exposure to air, because of the removal of water and its subsequent re-adsorption. They hence demonstrated that hydrogenated surface is a requirement for observing high surface electrical conductivity in diamond, but that such condition alone is not sufficient, as the presence of atmospheric adsorbates is also essential [67].

Another notable characteristic of the hydrogenated diamond surface is its hydrophobic nature, in contrast to the oxidized surface, which exhibits significant hydrophilicity. This was for example demonstrated by Ostrovskaya et al., who examined the water wettability of CVD diamond films

through contact angle measurements, finding a water contact angle of 93° for hydrogenated samples and 32° for oxidized ones. The increased hydrophobicity resulting from hydrogen terminations was attributed to weaker surface interactions with water molecules, produced by the smaller dipole moment of the C-H heteropolar bond with respect to that of the C-O bond [68]. These results were corroborated by Seshan et al. [66] and Kaibara et al. [69]. The latter group also conducted adhesion force measurements using Atomic Force Microscopy with gold-coated hydrophobic tips and hydrophilic tips constituted by silicon with native oxide. With the former tips, a stronger adhesion force was recorded on the hydrogenated surface, while the hydrophilic tip measured greater adhesion on the O-terminated surface [69].

1.2.3 Nitrogen-Vacancy center in diamond

Diamond can host various types of lattice point defects, such as vacancies and interstitial or substitutional atoms. These introduce into the energy gap additional electronic levels, which can be close to the valence and/or conduction bands, thus giving rise to semiconductor behavior, or deep, resulting in localized electronic states, among which transitions of electrons upon photoexcitation occur [53]. When electrons return to the ground state by emitting a photon at longer wavelength with respect to that of the excitation, the photoluminescence phenomenon known as fluorescence takes place. If emission concerns light in the visible spectral range, the defects are known as *color centers* [70]. Naturally present in diamond or introduced on-purpose by exploiting ion beams [71], color centers encompass a wide variety of defects, typically in the form of vacancies (V) adjacent to an impurity, including thin-vacancy (SnV) [72], magnesium-vacancy (MgV) [73] and silicon-vacancy (SiV) centers [74], and captured interest for applications in fluorescence imaging, as well as in quantum computing and sensing [75].

Among color centers, Nitrogen-Vacancy (NV) center is undoubtedly the most remarkable one. This defect, having C_{3v} symmetry, is composed by a substitutional nitrogen atom positioned next to a vacant site (Figure 11A) and can occur in two identified charge states, neutral (NV^0) and negative (NV^-). The former is a system comprising 5 electrons, where two come from the nitrogen atom and three from the dangling bonds of carbon, and has a spin S = ½ of the ground state, while the NV^- center has six electrons, with the extra electron being trapped by the vacancy, and exhibit a ground-state spin S = 1 [76]. Fluorescence spectrum of NV^0 and NV^- centers (Figure 11B), observable upon 532 nm wavelength (green) laser excitation, is characterized by a narrow feature known as the *zero-phonon line* (ZPL), which arises from purely electronic transitions, and a broad band named *phonon sideband*, originating by the coupling of electronic transitions with lattice vibrations (phonons). The ZPL appears at 575 nm (2.156 eV) for the NV^0 center and at 638 nm (1.945 eV) for

the NV^- center, whereas the phonon sideband is visible in the 600 nm - 750 nm and 650 nm - 750 nm spectral range in the former and in the latter case respectively [77].

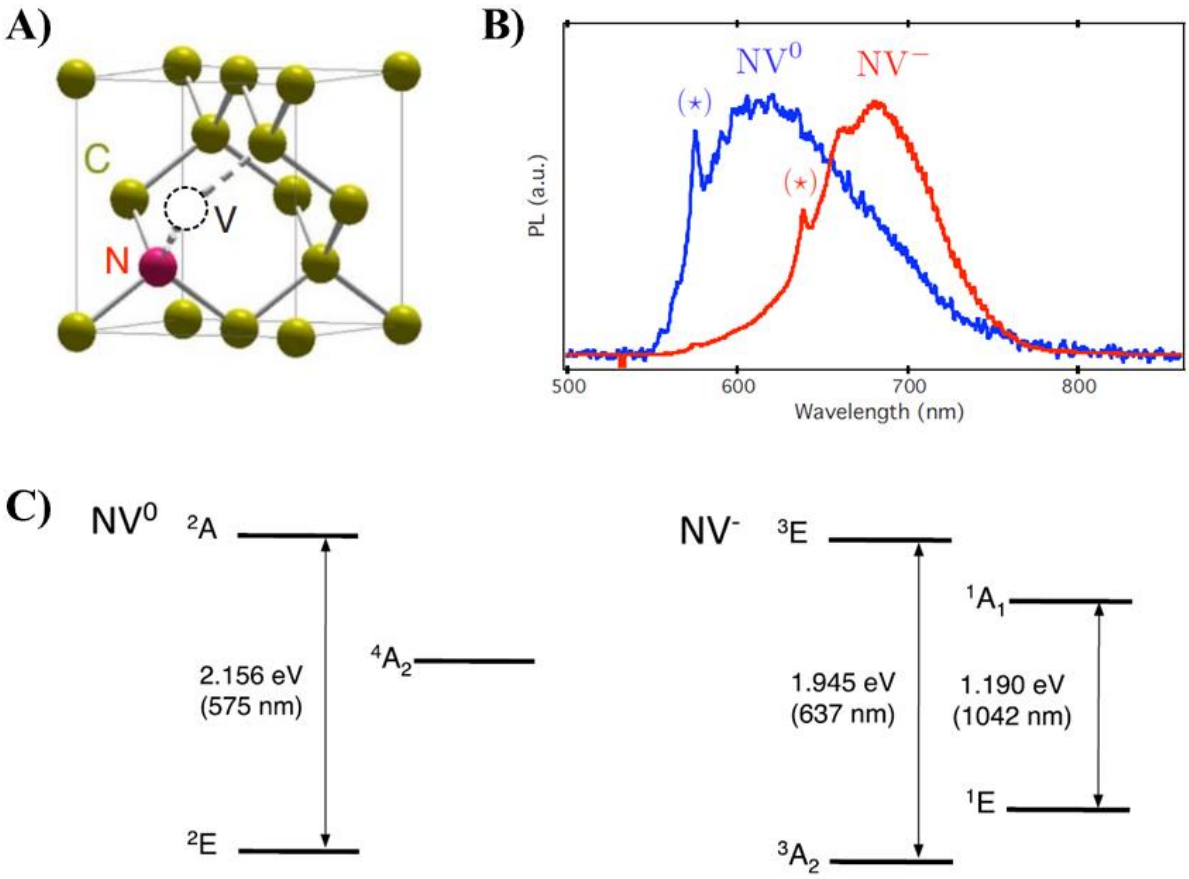

Figure 11-A) Structure of the NV center in the diamond lattice [78]. B) Photoluminescence spectra of NV^- and NV^0 centers under 532 nm of laser excitation (the symbol (*) indicates the zero-phonon lines) [78]. C) NV centers electronic structure [79].

The formation of the two types of NV centers is influenced by nitrogen concentration and surface terminations, as these impact on the position of the Fermi level. With respect to diamond valence band, the ground state of the NV^0 center is at a higher energy by 1.2 eV, that of the NV^- center is at 2 eV, and, when the nitrogen concentration is low, the Fermi level lies at 2.75 eV. As seen in sub-section 1.2.2, hydrogen terminations lead to the formation of a sub-surface hole accumulation layer with upward band bending. This phenomenon makes the Fermi level be positioned below the ground state energy level of NV^- centers, thereby favoring NV^0 states. On the other hand, increasing the concentration of nitrogen, the Fermi level rises toward the conduction band, as the impurity acts as electron donor, resulting in a higher population of the level associated with NV^- centers. The effect of oxygen terminations is opposite to that of hydrogen, causing downward band bending, thus creating a condition that enhances the likelihood of NV^- states. The influence of surface terminations is calculated to extend up to about 20 nm in depth [77,80].

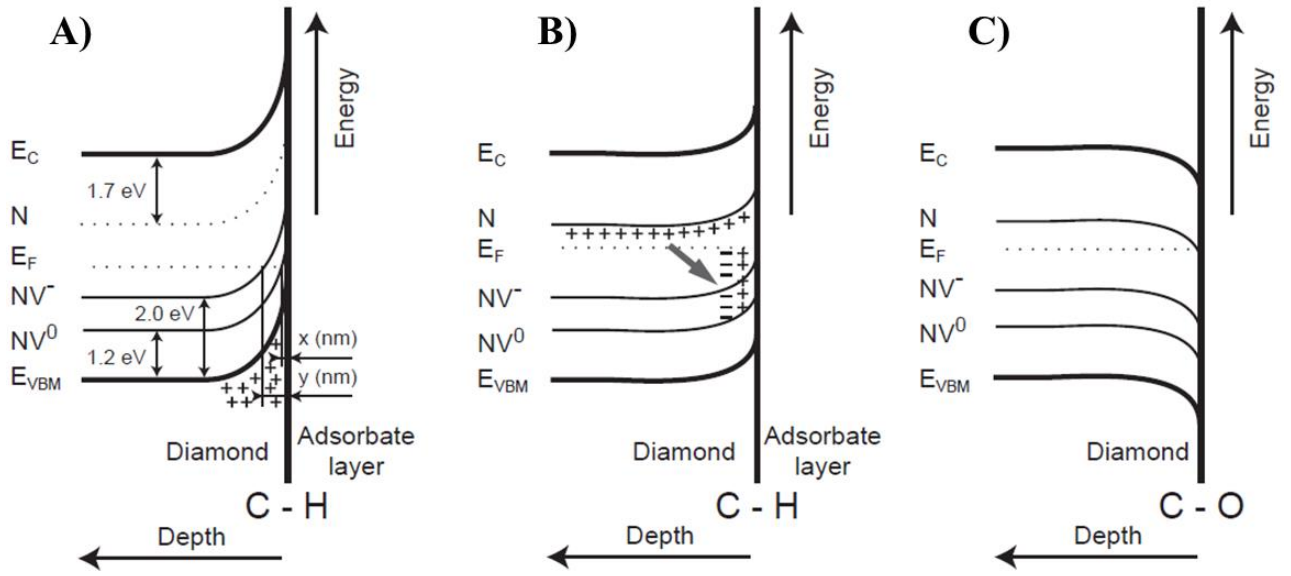

Figure 12-Band structure of diamond containing NV centers in different cases [80]: A) hydrogen terminations and low nitrogen concentration (*x* and *y* represent the depth); B) hydrogen termination and high nitrogen concentration; C) oxygen terminations.

Between the two kinds of NV centers, NV^- center is generally considered more interesting from the applicative point of view, due to its peculiar electronic structure (reported in detail in Figure 13). This consists of a ground state $^3A_2$ and an excited state ^3E, which are spin triplets, and two metastable states ^1A and ^1E, that are instead spin singlets. Both $^3A_2$ and ^3E feature two $m_s = \pm 1$ sublevels, which are degenerate in the absence of a magnetic field and more energetic than the $m_s = 0$ one, with zero-field splitting (ZFS) values of 2.87 GHz and 1.42 GHz in the ground and excited states respectively. Due to the small ZFS, the population of the different magnetic sub-levels is almost the same at room temperature, thus electrons in the ground state are in a mix of $m_s = 0$ and $m_s = \pm 1$ states. As illustrated in Figure 13, a laser pulse with energy greater than 1.945 eV (*e.g.*, a green laser) can promote electronic transitions from $^3A_2$ to excited states well above ^3E. From there, electrons quickly relax down to the ^3E *via* non-radiative transitions, typically without changing their spin state, and then they return to $^3A_2$. Depending on the value of m_s, this process can occur through different pathways. Generally, electrons with $m_s = 0$ transit directly from ^3E to $^3A_2$, thus giving rise to photoluminescence emission. Conversely, if $m_s = \pm 1$, electrons often (with about 45% probability) undergo intersystem crossing with spin change to $m_s = 0$, decaying non-radiatively from ^3E to the ^1A state, then from ^1A to ^1E emitting a photon in the infrared spectral region (at 1043 nm wavelength), and finally from ^1E to $^3A_2$ again in a non-radiative manner [77,81,82].

An implication of the set of phenomena described above is that electrons with $m_s = \pm 1$ give rise to a dimmer photoluminescence compared to those with $m_s = 0$. Additionally, this sets the possibility to realize spin polarization through optical pumping, namely induce the conversion from the “darker”

$m_s = \pm 1$ states to the "brighter" $m_s = 0$ by keeping on the excitation laser for a sufficient long time. If the laser is switched off, electrons are allowed to decay to the thermal equilibrium situation [83]. The return to a mixture of $m_s = 0$ and $m_s = \pm 1$ states is marked by a decrease of photoluminescence over time occurring with a characteristic time that is the spin-lattice relaxation lifetime T_1 (or longitudinal relaxation lifetime) [38,84]. T_1 in diamond is in the order few milliseconds at room temperature [85], but it can be shortened in presence of spin noise in the environment surrounding the NV^- center. As it will be outlined in sub-section 1.3.5, this property constitutes the foundation of nanodiamonds-based T_1-relaxometry technique, enabling oxygen free radicals measurement [38].

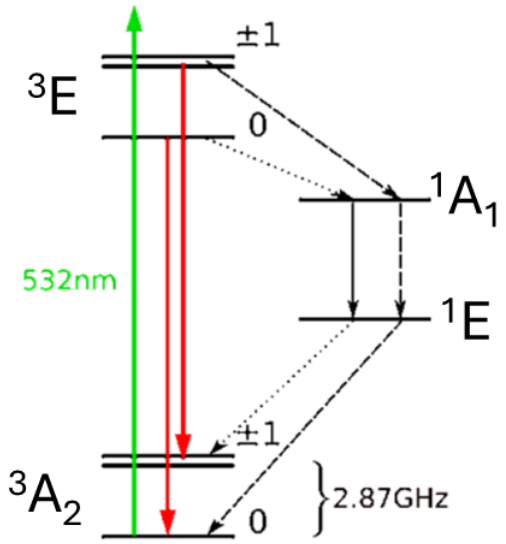

Figure 13-Fine structure of the NV^- center [86].

1.3 Nanodiamonds (ND)

The upcoming sub-sections will illustrate key aspects of ND, focusing on their structure, production techniques, properties and surface modification methods, highlighting their impact on ND features. Finally, the application of ND in radiosensitization and ND-based sensing of oxygen free radicals will be addressed.

1.3.1 ND structure, synthesis and properties

ND are diamond nanocrystals with size typically covering the 5 nm - 300 nm range. Characterized by a peculiar core-shell structure (Figure 14), they are composed by a diamond core, a middle layer made up of distorted sp^3 phases and amorphous carbon, and an outer shell constituted by sp^3 and sp^2 carbon atoms whose dangling bonds are terminated by various functionalities [35].

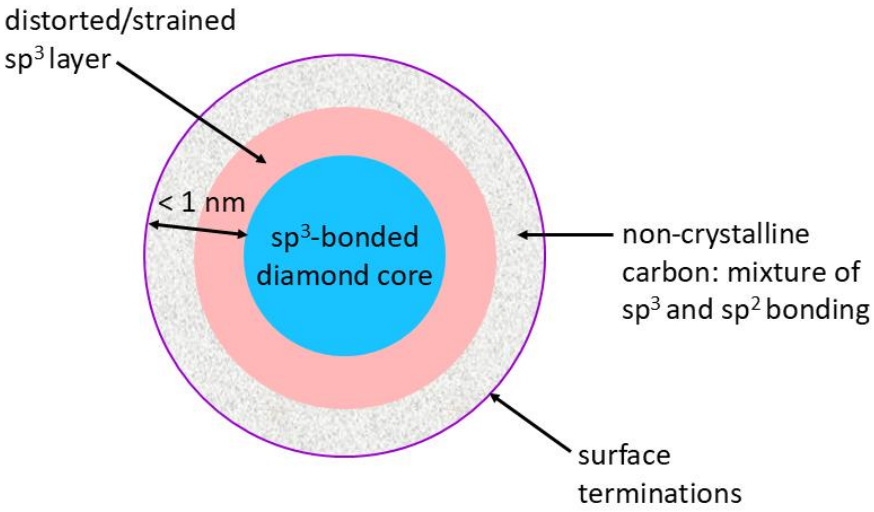

Figure 14-ND structure [87].

The dimensions and specific features of ND strongly depend on the method employed for their synthesis. Currently, a broad set of procedures for synthesizing ND is available [88]. Bottom-up approaches encompass production from molecular precursors, like adamantanes [89,90] and CVD synthesis [91], whereas examples of top-down strategies are high-energy ion irradiation of graphite [92], laser ablation [93], and bulk diamond patterning joined to directional reactive ion etching [94]. However, the most widely used synthetic techniques, belonging respectively to the former and the latter group, are detonation synthesis [95,96] and milling of High Pressure High Temperature (HPHT) microdiamond powders [97].

Detonation ND (DND) are obtained from the controlled explosion of carbon-containing compounds, such as a mixture of 2,4,6-trinitrotoluene (TNT) and 1,3,5-trinitroperhydro-1,3,5-triazine (hexogen), taking place in a closed chamber. This process results in the formation of liquid carbon nanodroplets, which are rapidly converted into diamond nanoparticles through fast cooling with water or ice. DND commonly exhibit a round or oval shape and have size up to 10 nm, while featuring a considerable amount of graphitic carbon on their surface and containing several impurities and defects. On the other hand, fabrication of ND from crushing occurs through bulk diamonds fragmentation *via* mechanical ball milling, bead-assisted sonic disintegration, or utilization of a hydraulic press. These ND have generally a dimension spanning from 20 nm - 30 nm to several hundreds of nm and are sharp faced. In comparison to those produced from detonation, they bear a lower quantity of sp^2 carbon and impurities [88,98].

Due to their unique physical and chemical properties inherited from diamond, ND are studied in several research areas, including tribology [99–101], composites [102–104], energy technologies [105–107], catalysis [108–111], and photonics [112–114]. Moreover, ND are also highly

valued in biomedicine [88,115]. A key feature of ND for applications in this field is their high surface-to-volume ratio, which makes their properties highly sensitive to surface modifications [116,117].

One way to alter the surface of ND is through the tuning of their surface terminations *via* post-synthetic procedures such as wet chemistry processes [35,118,119], exposure to microwave plasma [120,121], ball milling [122], or high-temperature thermal treatments in controlled atmosphere [117,123,124] (detailed in sub-section 1.3.2). As will be discussed later, tailoring the surface terminations of ND is crucial for obtaining particles that can effectively enhance the production of radiation-generated ROS, allowing their use in radiosensitization.

ND surface can also be modified through surface functionalization, which involves the attachment of molecules *via* covalent or non-covalent bonds with surface terminations. Functionalization is often employed to give ND active targeting capabilities by linking moieties acting as ligands that bind to overexpressed receptors on cancer cells [125]. This enhances EPR effect and can be exploited for the selective delivery of drugs (*i.e.*, drug delivery) or for imaging purposes. Indeed, ND can be used for the visualization of tumor cells, owing to their intrinsic photoluminescence properties derived from lattice defects, particularly NV centers [126–128]. Being characterized by intense and stable fluorescence emission, they set ND apart from organic fluorophores, which are generally prone to photobleaching and quenching, and render them ideal fluorescent cellular biomarkers [129–131].

In addition to vascular endothelial growth factor [132], folic acid [133], transferrin [134], antibodies [135,136], and mannose [137], one of the most relevant targeting agents that can decorate the surface of ND is hyaluronic acid (HA). This naturally occurring polysaccharide is known for its high biocompatibility and biodegradability, and it is recognized by CD44 receptors [138,139], which are overexpressed on the surface of several tumor cells, including those of the liver, prostate, and breast [140,141]. HA can also improve the colloidal stability of nanoparticles due to its high hydrophilicity, preventing their aggregation in aqueous media and enabling their effective applicability in the water-rich cellular environment [142,143]. Although research on HA-functionalized ND is still limited, their favorable properties have already been demonstrated in some studies. For instance, Yun et al. and Han et al. showed biocompatibility, safety, and selectivity of ND covalently derivatized with HA, highlighting their potential in photodynamic and photothermal cancer therapy [144], and in liver-targeted imaging [145], respectively. On the other hand, Cui et al. investigated HA-decorated ND as theranostic platforms for the treatment of triple-negative breast cancer, displaying that the developed nano-systems exhibited uniform dimensions, excellent hydrodynamic properties, high biocompatibility, and predominant localization in tumor cells. They

also revealed that HA can be non-covalently attached to ND, linking it to the particles *via* charge complexation with a protamine sulfate layer [146,147]. Chernysheva et al. similarly demonstrated that the adsorption of miramistin on ND enhances HA adsorption, thus further opening the pathway to simple non-covalent derivatization approaches for the development of HA-functionalized ND [148].

Another noteworthy feature of ND in the biomedical sector is the possibility of using them as sensors [149,150], particularly thanks to the spin-dependent fluorescence properties of the NV^- centers [151–153]. Specifically, these can be exploited for sensing oxygen free radicals in the surroundings of ND through T_1-relaxometry [38]. Based on detecting the changes in T_1 time induced by paramagnetic species, this technique allows local measurements of radicals in real-time and has been successfully employed to measure free radical generation in various environments, such as human dendritic cells [154], cancer cells [49], umbilical vein endothelial cells [155], and sperm cells [50].

1.3.2 Thermal treatments on ND and surface terminations

The surface of post-synthesis ND is characterized by the presence of miscellaneous functional groups, with the main ones being oxygen-containing species such as carboxyls, carbonyls, acid anhydrides, ethers, and alcohol functions. Achieving uniformity in surface chemistry is essential to obtain particles with well-defined characteristics. Properties such as ND interaction with water, which is an essential feature to consider when dealing with biological systems, as well as NV centers photoluminescence emission, or particle electronic properties are indeed greatly affected by surface terminations. Additionally, making ND surface moieties homogeneous can serve as an intermediate step to prepare ND for functionalization, increasing the number of binding sites for the attachment of the desired molecules [117,156].

Various thermal treatments in controlled atmosphere can be used to modify the surface of ND, thus accomplishing the described goals.

- Annealing treatments: they are conducted in inert environment, such as under nitrogen/argon flow or in vacuum at temperatures around 800 °C [157]. Often the first stage for further processing, these procedures graphitize ND surface amorphous carbon components, without undermining the diamond core of the particles, concurrently standardizing the surface by eliminating the originally present functional groups [123,124]. This typically results in a hydrophobic surface, which can drive ND aggregation in aqueous media [123,158]. Moreover, annealing processes also have the effect of mobilizing vacancies, allowing them to pair with

nitrogen atoms throughout the lattice and form new NV centers [71,159,160]. Annealing can also be performed at high temperatures when exceeding 800 °C. However, high-temperature annealing treatments can lead to extensive surface graphitization [157] or microstructural transformation, inducing ND conversion to carbon nano-onions [161–163].

- Oxidation treatments: they are carried out in oxidizing atmosphere of air or oxygen at temperatures ranging from 400 °C to 550 °C [158,164]. They purify ND from graphitic layers, causing the selective removal of sp^2 carbon [164,165], thereby reducing the shielding and quenching effects produced by such phases on the photoluminescence of NV centers in the particle core [166]. Concurrently, oxidation treatments promote the formation of oxygen-containing functionalities, that render ND hydrophilic and consequently prone to disperse in water-based solutions [123,158,167]. When the oxidation processes are more aggressive, *i.e.*, when conducted at higher temperatures or/and for longer durations, generally oxygenated moieties tend to form in greater number [124,168]. The purified surface obtained upon ND oxidation can be the starting point for additional treatments, such as hydrogenation processes [117].

- Hydrogenation treatments: they are performed by heating ND in reducing atmosphere of hydrogen gas at temperatures greater than 600 °C [169]. They create surface hydrogen terminations and etch non-diamond carbon, while simultaneously eliminating surface oxygen-containing functionalities, thereby increasing surface hydrophobicity [124,170–172]. The presence of hydrogen terminations also modifies ND band structure, giving the particles properties analogous to those of the hydrogenated bulk diamond. These include high surface electrical conductivity (sub-section 1.3.3) and the capability of an intense electronic emission under irradiation, the latter enabling their application as radiosensitizers (sub-section 1.3.4).

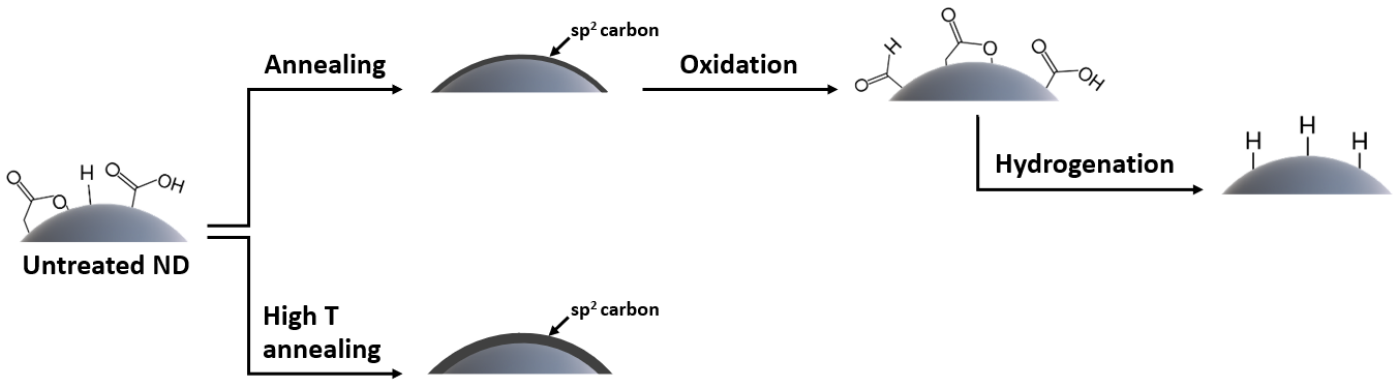

Figure 15-Examples of thermal treatments scheme for modifying ND surface.

1.3.3 Effect of surface terminations on ND electrical properties

The surface modifications induced by thermal treatments have a significant influence on the electrical properties of ND [123,169,173–179]. Understanding the connection of such properties with surface characteristics is crucial for determining whether the surface chemistry of ND can be identified through their electrical characterization, as different surface terminations seem to be linked to distinct electrical conduction mechanisms. Moreover, this relationship can provide valuable insights into the behavior of ND in a wide range of applicative contexts.

The link between ND surface structure and electrical properties represents a complex issue which has been investigated from different perspectives in literature. Some research evidenced the increase in electrical conductivity induced by the formation of surface graphite. Kuznetsov et al., for instance, investigated the resistivity of vacuum-annealed detonation ND by conducting four-point probe measurements, finding that ND became highly conductive when subjected to annealing at temperatures larger than 1100 K, as surface graphitization occurred upon this process [173]. Similar findings emerged from impedance spectroscopy measurements by Jackman's group [174,175]. They examined detonation ND, both in form of aggregates and individual particles, heated at different temperatures, reporting a loss of dielectric character when exceeding a specific threshold, *i.e.*, 350 °C and 400 °C for individual and aggregated ND respectively, suggesting the onset of a partial graphitization dynamics [174,175]. Čermák et al. also studied the link between ND electrical properties and graphitic phases formation. Employing atomic force microscopy (AFM), they measured local electrical conductivity of HPHT ND after thermal or plasma treatments, connecting its enhancement to a higher concentration of sp^2 bonds with respect to the as-received ND [176].

On the other hand, other works focused on electrical conductivity of ND following their hydrogenation. As discussed in sub-section 1.2.2, it is well established that surface hydrogenation of bulk diamond makes material electron affinity negative and thus determines a substantial p-type surface electrical conductivity, due to the formation of sub-surface holes resulting from the transfer of electrons to surface adsorbed water [67]. In recent years, a mechanism analogous to the one occurring in diamond was proposed for hydrogen-terminated diamond nanoparticles, linking it to enhanced electrical conductivity. This was first suggested by Kondo et al., who observed that upon thermal hydrogenation in the 600 °C - 900 °C temperature range the resistivity of detonation ND reduced from 10^7 Ω cm to 10^5 Ω cm, attributing the phenomenon to the transfer doping model [169]. The effectiveness of hydrogenation was confirmed *via* Fourier transform infrared and X-ray photoelectron spectroscopies, whereas a possible role of sp^2 phases was ruled out based on the reduction of the sp^2/sp^3 carbon ratio at increasing temperature of the hydrogenation process [169].

These results were validated by an impedance spectroscopy characterization by Welch et al., who studied hydrogen-terminated ND both in air and in vacuum [177]. They revealed that the low impedance response was three orders-of-magnitude lower for hydrogenated ND compared to untreated ND in air environment, while registering an extremely high impedance when the hydrogenated samples were tested in vacuum. Such findings supported the interpretation of hydrogenation process inducing surface transfer doping in the nanoparticles, as the effect should not be seen in vacuum conditions, because of the removal of adsorbates from the surface [177]. The relatively high conductivity of hydrogenated ND was also demonstrated by the previously mentioned AFM analyses by Čermák et al. [176]. Given the effectiveness of the employed hydrogenation treatment in establishing hydrogen terminations on ND and the absence of amorphous or graphitic carbon, they suggested that the increased conductivity of their particles should be originated exclusively by surface transfer doping mechanism [176].

In addition to graphite and hydrogen terminations, also the presence of water adsorbed on the surface has been shown to affect the electrical properties of ND. Surface adsorbed water indeed generates hydroxonium ions (H_3O^+), thus allowing electrical conduction to take place *via* charge transport due to Grotthuss mechanism, *i.e.*, proton hopping [123,178]. This involves a chain process where covalent and hydrogen bonds are sequentially broken and reformed, enabling the transfer of a proton from an H_3O^+ ion to a neighboring water molecule, which in turn forms a new H_3O^+ ion, thus initiating another proton hop to the next water molecule, according to the reaction below (Eq.24) :

$$H_2O^+ + H_3O^+ \rightarrow H_3O^+ + H_2O \qquad \text{Eq.24}$$

The impact of surface-adsorbed water on ND conductivity was demonstrated by Piña-Salazar et al. [178]. They observed significant differences in the electrical conductivity of untreated detonation nanodiamonds when exposed to humid air compared to after thermal process in vacuum, highlighting that in the former case ND conductivity rose as the amount of adsorbed water increased, whereas in the latter situation it dropped by two orders of magnitude, as a result of the elimination of the adsorbed water molecules [178]. Another evidence was provided by Denisov et al. [179]. They measured the conductivity of chlorinated and untreated detonation-synthesis ND pellets at varying water vapor relative pressure (p/p_s), revealing that in the $0\% < p/p_s < 98\%$ range this increased by five to six orders of magnitude, owing to water adsorption. Denisov et al. strongly emphasized the influence of oxygen-containing surface functional groups on the amount of adsorbed water and on electrical conduction, stressing the fact that a higher concentration of oxygenated moieties was connected to increased water adsorption capacity and, consequently, higher electrical conductivity [179]. Oxygenated groups, being highly hydrophilic due

to their ability to easily form hydrogen bonds with water, indeed promote water adsorption on the surface of ND, thereby enhancing the effect of the Grotthuss mechanism on particles electrical conductivity. This was further highlighted in the context of a study carried out in the Solid State Physics group of the University of Torino, examining the effects of reducing and oxidizing thermal processes on ND interaction with water [123]. In such work, differently sized milled and detonation ND were characterized by combining current-voltage characteristics measurements and various spectroscopic techniques. The results demonstrated that both untreated ND and the ones subjected to thermal oxidation processes in air were generally more conductive than those heated in inert atmosphere, consistently with the higher hydrophilicity of the formers, due to more numerous oxygen-containing terminations on the surface [123].

The above-listed body of studies prompt further investigations into the effect of surface treatment on the electrical properties of ND. Despite the findings examined, there is the lack of works where the electrical properties of ND are systematically correlated with different surface terminations in a comprehensive manner, considering the existence of multiple factors that influence electrical conductivity. Part of the doctoral work was therefore devoted to filling this gap.

1.3.4 ND as radiosensitizers

Like their bulk counterpart, ND with surface hydrogen terminations are characterized not only by high electrical conductivity, but also by an intense electronic emission under irradiation. This property has been ascribed once more to negative electron affinity and it has been shown to enhance the production of ROS induced by ionizing radiation, thus becoming relevant in the framework of radiosensitizers [36,37,172,180].

Experimental evidence includes investigations by Arnault's group. In one of their works, they reported increased cell death in both Caki-1 kidney human cancer cell line and ZR-75-1 human mammary carcinoma cells following co-exposure to hydrogenated ND and 4 Gy of γ-photons at 662 keV and correlated the observed effects with higher intra-cellular ROS levels measured at 1 hour and 24 hours post-irradiation [36]. Similarly, in other studies they demonstrated an increase in $^{\bullet}OH$ generation when hydrogenated ND were present during the irradiation of aqueous solutions with both X-rays at 17.5 keV [37] and γ-rays at 1.3 MeV [180] at different doses. Focusing on the measurement of $^{\bullet}OH$ concentration by using coumarin as fluorescent probe, they registered 40% and 50% higher radical production in the presence of hydrogenated ND compared to radiation alone, in the former and latter case respectively [37,180]. Moreover, the potential of hydrogenated ND in intensifying radiation effects on cancer cells was underlined in a recent work conducted by the Solid State Physics group of the University of Torino, demonstrating that the combination of these particles with 5 Gy of

γ-photons at 1.3 MeV energy led to a greater reduction in the survival of DAOY human medulloblastoma cells relative to the sole radiation [172].

Despite these promising findings, further investigations into the applicability of hydrogenated ND as radiosensitizers are required. In particular, the problem of their pronounced aggregation in aqueous solutions should be addressed, as it poses a serious obstacle to their use in cells and their possible future applications *in vivo* [172].

1.3.5 ND-based T_1-relaxometry

Nanodiamonds-based T_1-relaxometry, also called *diamond magnetometry*, is a technique for sensing magnetic fields, based on measuring how magnetic noise modifies the longitudinal spin relaxation time (T_1) of the NV^- center electron spin in ND [38]. Relaxometry was first demonstrated in 2013 when it was proved that T_1 is reduced in presence of paramagnetic ions [84], and since then, it has been used in various sensing applications, with one of the most widespread being the detection of ROS radicals and the measurement of their concentration [49–51,154,155,181–184].

T_1 relaxation time in relaxometry is measured by monitoring the fluorescence of NV^- centers using a setup like the one illustrated in Figure 16. The core of the system is a laser which serves as optical excitation source, emitting green light at 532 nm and pulsed by an acousto-optic modulator (AOM). This device operates based on the acousto-optic effect, where acoustic waves, generated by a piezoelectric transducer, propagate through a crystal, causing periodic variations in its refractive index and thus creating a diffraction grating that diffracts the incoming laser beam. By modulating the amplitude of the acoustic waves, the amount of light diffracted into the first order can be controlled, allowing laser pulses to be generated by switching the electric signal on and off. The pulsed laser light is directed *via* a dichroic mirror and focused onto the sample through an objective lens. The sample, containing ND particles, is positioned on a piezoelectric stage for precise alignment. The light emerging from the specimen is collected through the objective, directed by the dichroic mirror to a filter, isolating the red fluorescence emitted by NV^- centers, and then passes through a pinhole before detection by a Single Photon Avalanche Diode (SPAD) [182,185].

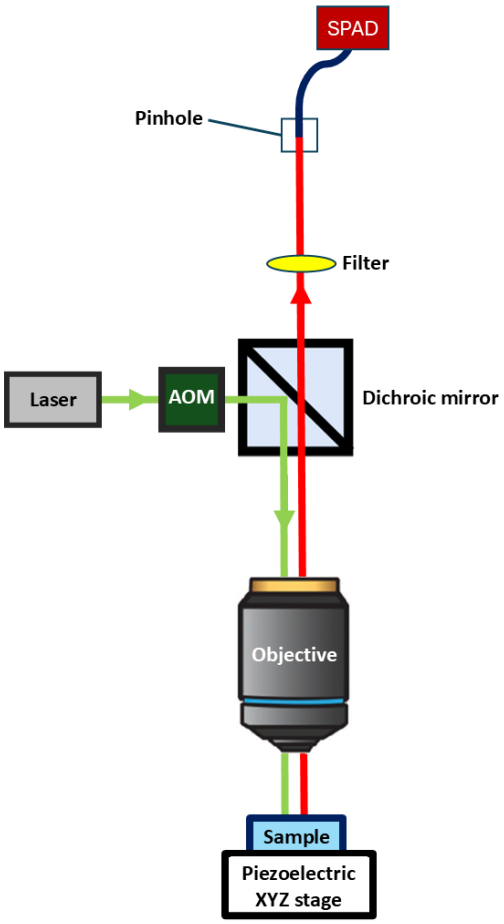

Figure 16- Schematic of an experimental setup for T_1-relaxometry. Laser light (532 nm emission wavelength) is pulsed by an AOM and directed through a dichroic mirror into an objective lens, which focuses the excitation light onto the sample containing ND, placed on a piezoelectric stage. The light emerging from the sample is collected through the objective and directed through the dichroic mirror. The red fluorescence signal from the NV^- centers in ND is isolated by a filter, and, after passing through a pinhole, reaches a SPAD detector.

As seen in sub-section 1.2.2, owing to spin-dependent intersystem-crossing towards intermediate singlet states, optical pumping of NV^- centers leads to an efficient electron spin polarization into the $m_s = 0$ sublevel, characterized by stronger photoluminescence with respect to the $m_s = \pm 1$ states. This enables the measurement of T_1 relaxation time through the scheme shown in Figure 17A, consisting in a sequence of $(n + 1)$ laser pulses, each lasting T_L ($T_L \approx 5$ µs). The pulses are separated by n time intervals, each referred to as dark time (τ), whose duration is exponentially increased (typically from 0.2 µs to 2000 µs) [185]. The first laser pulse initializes the electron spins into the $m_s = 0$ sublevel, thus maximizing photoluminescence. The pulses delivered after the first dark time instead serve a dual purpose. The first part of each pulse, indicated as rw in Figure 17A, is used to probe the centers

spin state, while the second part repumps the centers back into the $m_s = 0$ state. Indeed, during the dark time intervals the NV^- centers are kept in dark and electron spins can relax toward a mixture of $m_s = 0$ and $m_s = \pm 1$ states, leading to a decrease in photoluminescence. The fluorescence signal is measured by the SPAD after each dark time for a time interval corresponding to rw. If more time is left for spin relaxation, photoluminescence will be weaker and hence the experimental output is a series of photoluminescence points showing a decreasing trend with increasing τ values, like the blue points displayed in the graph of Figure 17B. In presence of paramagnetic species in the surrounding of a NV^- defect, electron spin relaxation is faster and the resulting photoluminescence data points will be characterized by a steeper decrease [52,84], as the red points shown in the graph of Figure 17B.

Considering the relaxation of a single NV^- center, the photoluminescence signal can be written as a function of τ as:

$$I(\tau) \approx A_0 n_0(\tau) + A_1[n_{+1}(\tau) + n_{-1}(\tau)] \quad \text{Eq.25}$$

where A_0 and $A_1 < A_0$ represent the photoluminescence rates associated with the spin states $m_s = 0$ and $m_s = \pm 1$, respectively. $n_{0,\pm 1}(\tau)$ are instead the spin populations before applying the readout optical pulse, which are evaluated within the simplified four-level model shown in Figure 17C, including the ground-states spin sublevels $m_s = 0, \pm 1$ and the lowest-lying singlet state, thereafter referred to as the metastable state. T_1 is defined as the decay time of the population n_0, hence:

$$T_1 = (3\, k_{01})^{-1} \quad \text{Eq.26}$$

with k_{01} being the two-way transition rate between $m_s = 0$ and $m_s = \pm 1$. At short time scale, the spin populations are also affected by relaxation from the metastable state, with a population $n_m(\tau)$ which decays towards the ground state spin sublevels according to the following equation:

$$n_m(\tau) = n_m(0)\, e^{-\frac{\tau}{T_m}} \quad \text{Eq.27}$$

where $n_m(0)$ is the initial population of the metastable state, whereas T_m is the metastable state decay time. T_m can be expressed through the decay rates from the metastable state to the $m_s = 0$ and $m_s = \pm 1$ states, *i.e.*, k_{m0} and k_{m1}:

$$T_m = (k_{m0} + 2\, k_{m1})^{-1} \quad \text{Eq.28}$$

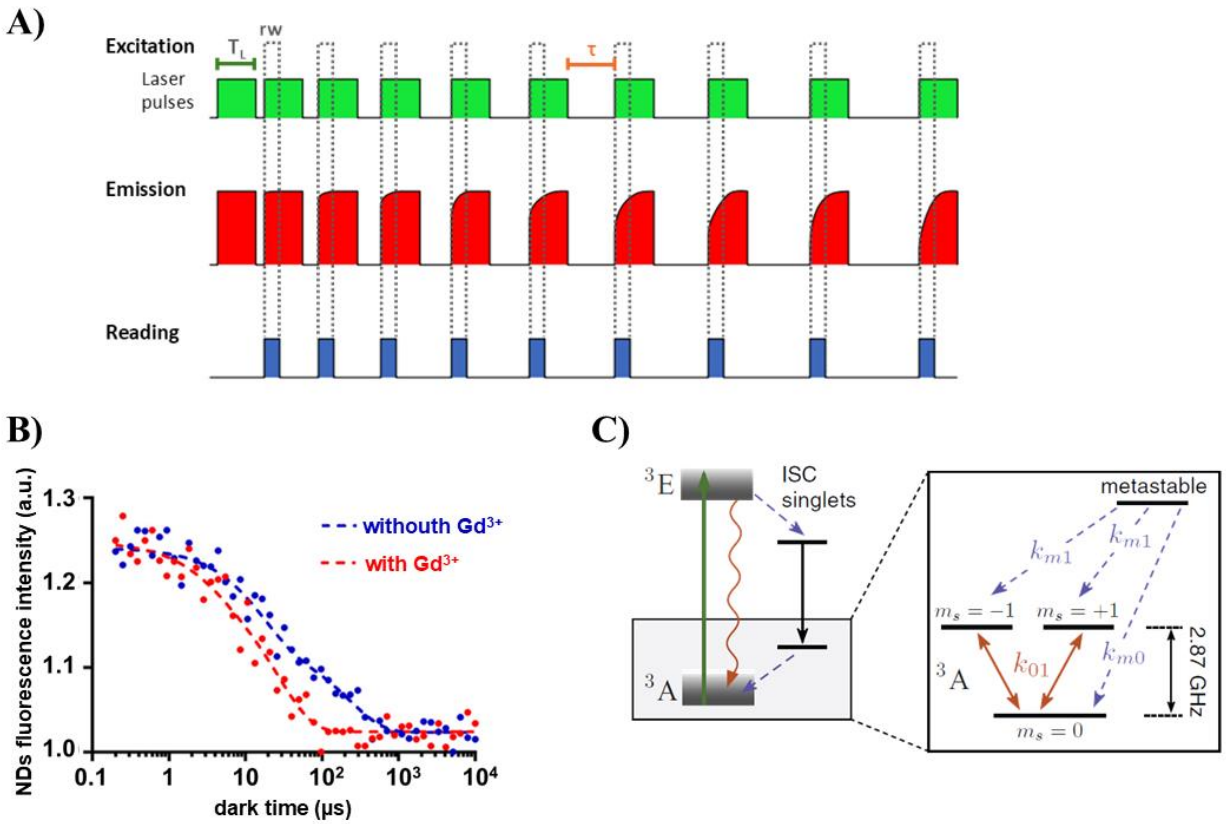

Figure 17-A) Laser pulses sequence for T_1-relaxometry measurements (adapted from [52] and [38]). The green rectangles indicate when the laser is on. The pulses, lasting T_L, are separated by a dark time τ, which is systematically increased. The red rectangles depict the red fluorescence signal emitted by NV^- centers in response to the excitation provided by the laser pulses. The blue rectangles show the time windows (*rw*) in which photoluminescence is measured. B) Example of curves obtained in T_1-relaxometry measurements (adapted from [181]). The red curve is characterized by a steeper decrease compared to the blue one, as it has been recorded in presence of paramagnetic species (Gd^{3+} ions in this case), shortening T_1 time. C) Simplified energy-level structure of the NV^- center, used as reference to calculate the expression of the photoluminescence signal $I(\tau)$ [84].

Using classical rate equations within this four-level model, the PL signal $I(\tau)$ can be written as:

$$I(\tau) \approx I(\infty)\,[1 - C_m e^{-\frac{\tau}{T_m}} + C_1\, e^{-\frac{\tau}{T_1}}] \qquad \text{Eq.29}$$

where the constants $I(\infty)$, C_1 and C_m are given by the expressions reported in Eq.30, Eq.31 and Eq.32 [84].

$$I(\infty) = \frac{A_0 + 2\,A_1}{3} \qquad \text{Eq.30}$$

$$C_1 \approx \frac{A_0 - A_1}{A_0 + 2\,A_1}\,[3\,n_0(0) - 1 + n_m(0)] \qquad \text{Eq.31}$$

$$C_m \approx n_m(0) \quad \text{Eq.32}$$

T_1 can be thus extracted from Eq.29 by fitting experimental data. Relaxometry, however, is typically performed using ensembles of NV^- centers, as this facilitates the detection of the ND, making them easier to spot even in presence of background fluorescence from the sample. Additionally, measuring multiple NV centers reduces variability between individual particles [52]. It has been found that the photoluminescence data concerning ensemble relaxation can be meaningfully fitted by different exponential models, with the simplest one being the single exponential model [185]:

$$I(\tau) \approx c_0 + c_1 e^{-\frac{t}{T_1}} \quad \text{Eq.33}$$

It is important to note that, to serve as suitable probes for relaxometry measurements, ND must have a high density of NV centers within their core. Since native NV defects generally do not produce a photoluminescence signal intense enough for practical applications, their concentration is typically increased artificially. In nitrogen-rich particles, such as type Ib ND, this can be accomplished by introducing additional vacancies into the lattice through irradiation with electrons [186], neutrons [187], or ions [71]. With regard to ion beam-based methods, a widespread approach involves irradiating ND with H^+ ions at energies in the MeV range [168,188]. These create new vacancies by colliding with the nuclei of carbon atoms, displacing them from their lattice positions. Vacancies are formed randomly in the ion-irradiated volume and so ND undergo annealing following H^+ irradiation to allow the coupling of the newly created defects with nitrogen impurities, which is a thermodynamically favored process [71,160]. On the other hand, for particles with low nitrogen content, NV center creation can be achieved through direct irradiation with nitrogen ions, that simultaneously introduces both heteroatoms and vacancies [71].

1.4 Objectives of the experimental work

The research activity regarded the optimization of ND properties for the applications mentioned in this introductory chapter, *i.e.*, enhancing ionizing radiation-induced ROS production and measuring ROS concentration through T_1-relaxometry.

The first part of the work focused on preliminary processing of ND and analysis of the physicochemical properties of thermally modified ND, aimed at acquiring a comprehensive understanding of the effects of thermal treatments on particle surface. As highlighted in the previous sections, different thermal processes impart specific characteristics to the ND. Besides being essential for any applicative context, achieving a detailed knowledge of these properties was crucial for the subsequent steps of the work, as it also allowed for the selection of an appropriate thermal treatment

scheme to effectively obtain the desired modifications to the ND surface. Processed ND were characterized by means of an innovative approach based on samples electrical characterization in different and carefully controlled humidity conditions, where the information on particles surface chemistry and structure was inferred from the analysis of their electrical behavior and then confirmed through Diffuse Reflectance Infrared Fourier-Transform (DRIFT) spectroscopy and Raman spectroscopy. The experimental setup for electrical measurements in controlled humidity conditions was developed and tested by the candidate, whereas the results of such kind of analysis were published in [124]. Additionally, to delve into ND particles hydrodynamic behavior in relation to the modification of their surface, Dynamic Light Scattering (DLS) and Zeta Potential (ZP) analyses in aqueous medium were performed.

After gaining in-depth insights into the surface properties of ND and developing a thermal processing protocol for their treatment, this scheme was applied to modify ND which were subsequently functionalized with hyaluronic acid (HA) *via* a non-covalent approach, using a conjugate of HA with 1,2-dimyristoyl-*sn-glycero*-3-phosphoethanolamine phospolipid. This activity was conducted in collaboration with the research group led by Prof. Silvia Mariangela Arpicco at the Department of Drug Science and Technology of the University of Torino and that led by Prof. Chiara Riganti at the Oncology Department of the same university, and resulted in the findings published in [189]. The work targeted at designing ND particles with high dispersibility in aqueous solutions and selectivity towards specific cancer cells. Such properties were sought to enhance ND performance in clinical applications, allowing their use in water-rich environments and increasing their internalization in tumor cells characterized by the overexpression of CD44 HA receptors. To validate the functionalization strategy and investigate changes in surface chemistry, structure, photoluminescence properties, particle size and morphology, and hydrodynamic behavior, induced by derivatization with HA, a comparative characterization of ND before and after functionalization was performed, utilizing a broad set of different techniques, including DRIFT spectroscopy, Raman spectroscopy, photoluminescence spectroscopy, Scanning Electron Microscopy, DLS, and ZP measurements. The developed ND were eventually tested on three different human adenocarcinoma cell models to assess their biocompatibility and uptake mediated by CD44 receptors.

To evaluate the potential in increasing the concentration of ionizing radiation-induced ROS, HA-functionalized particles and their non-functionalized counterparts were employed in experiments of induced radiolysis aimed at estimating ROS production in aqueous solutions under γ-ray irradiation, with a focus on hydroxyl radicals. The generation of $^{\bullet}OH$ was investigated by irradiating aqueous suspensions of ND containing terephthalic acid as a fluorogenic probe with a radiotherapy

linear accelerator (LINAC). The suspensions were analyzed through spectrofluorimetric measurements to detect any differences in •OH radical generation due to the different types of ND under investigation. Additionally, to correlate the observed ROS production in aqueous solutions with the effects of the combination of ND and ionizing radiation on cells, preliminary experiments were conducted to evaluate cellular viability after ND administration followed by γ-photon irradiation. These were performed in collaboration with Prof. Chiara Riganti's research group and concerned a radio-resistant cancer cell line.

Finally, with the aim of developing ND as tools to measure ROS production through T_1-relaxometry, the candidate carried out a photoluminescence spectroscopy characterization of proton-irradiated ND, estimating the concentration of NV^- centers formed under different irradiation conditions. The conditions maximizing the production of NV^- defects and the photoluminescence were selected to modify particles that were tested in preliminary T_1-relaxometry experiments, conducted at the Biomedical Engineering Department of the Universitair Medisch Centrum Groningen under the guidance of Prof. Romana Schirhagl's research group, to measure T_1 relaxation time both in the absence and in the presence of paramagnetic species.

2. Experimental setups

2.1 ND samples

The research activity has been conducted on diamond particles produced from the milling of type-Ib HPHT single crystals (nominal nitrogen concentration between 10 ppm and 100 ppm).

The majority of the experimental work focused on the following batches of ND:

- Micron+ ND with a median diameter of 240 nm, obtained from ElementSix™ and designated as "large ND"/^{l}ND throughout the text;
- MSY ND with a median diameter of 55 nm, provided by Pureon and referred to as "small ND"/^{s}ND in the following.

Some characterizations were also conducted on two supplementary batches:

- MSY ND with a median diameter of 125 nm, sourced from Pureon and labelled as "medium ND"/^{m}ND;
- ElementSix™ Micron+ microdiamonds with a median diameter of 6 µm, purchased from ElementSix™ and indicated as "µD".

The various samples are shown in Figure 18: ^{l}ND and µD appear as light grey powders, whereas ^{m}ND and ^{s}ND take the form of dark grey powders. Prior to investigations all samples underwent various thermal treatments using the system described in the following section.

Figure 18-Diamond particles employed in experimental activity.

2.2 Thermal treatments system

Thermal treatments on ND were carried out using a ThermoConcept ROT 60/300/12 tube furnace (Figure 19A). The furnace can reach temperatures up to 1200 °C with a power output of 3 kW and its control system enables the precise adjustment of processes duration and temperature, as well as the programming of various thermal ramps, while maintaining a controlled atmosphere (inert gases, air, oxygen, …), thus allowing to perform the desired treatment protocol.

Samples were placed into the furnace tube after being loaded into inert alumina crucibles. They underwent different processing steps, which are detailed in the scheme shown at the beginning of Chapter 3. Annealing processes were conducted at 800 °C for 2 h under a flow of nitrogen, which was provided by a gas tank. High-temperature annealing treatments were instead performed by heating ND for 2 h at temperatures ≥ 900 °C in low vacuum (approximately 0.2 mbar), that was created by connecting a mechanical vacuum pump to the furnace tube. Air oxidation procedures were carried out following annealing treatments at temperatures between 400 °C and 500 °C in oxidizing atmosphere, attained by leaving the furnace tube open during the treatment, thus exposing the samples to oxygen from the air. Finally, hydrogenation processes were performed under hydrogen flow at temperatures between 800 °C and 900 °C, either after an annealing or an oxidation step. Hydrogen was produced through water electrolysis employing a Parker Domnick Hunter 60H Hydrogen Generator (Figure 19B), which delivers gas with a purity greater than 99.999% and a pressure up to 7 bar.

A Key Instruments flowmeter was used to regulate the gas flow during annealing and hydrogenation treatments, with flow rates set to approximately 0.2 l min^{-1} and 0.1 l min^{-1}, respectively.

Figure 19-A) ThermoConcept ROT 60/300/12 tube furnace. B) Parker Domnick Hunter 60H Hydrogen Generator.

2.3 Ion accelerator at Legnaro National Laboratories

Ion beam-based modification of ND was performed to create new NV centers within the particles. To this aim, ND were irradiated with 2 MeV energy protons using the AN2000 accelerator (Figure 20) at the Legnaro National Laboratories (LNL) of the *Istituto Nazionale di Fisica Nucleare* (INFN). This facility is employed by around 30 international research groups annually, operating for a total of 2500 hours. The main experiments include ion beam lithography for microfabrication, elemental analysis *via* nuclear techniques, ion channeling, Elastic Recoil Detection Analysis (ERDA) and Proton-Induced X-ray Emission (PIXE) on various materials such as semiconductors, ceramics, and environmental samples.

The AN2000 is capable of accelerating both protons and monovalent helium ions (He^+) and consists of a Van de Graaff-type electrostatic accelerator with a single loading stage and a maximum terminal voltage of 2 MV. The treatment chamber is provided with a precision sample holder allowing micrometric adjustments in all three spatial directions, as well as rotation steps of 1°, enabling sample inclination relative to the beam direction. The beam spot size can be varied from a few hundred micrometers to approximately 5 mm.

Sample preparation for ion irradiation involved dispersing the ND in isopropanol and depositing them on a silicon wafer in a layer with uniform thickness of approximately 30 µm.

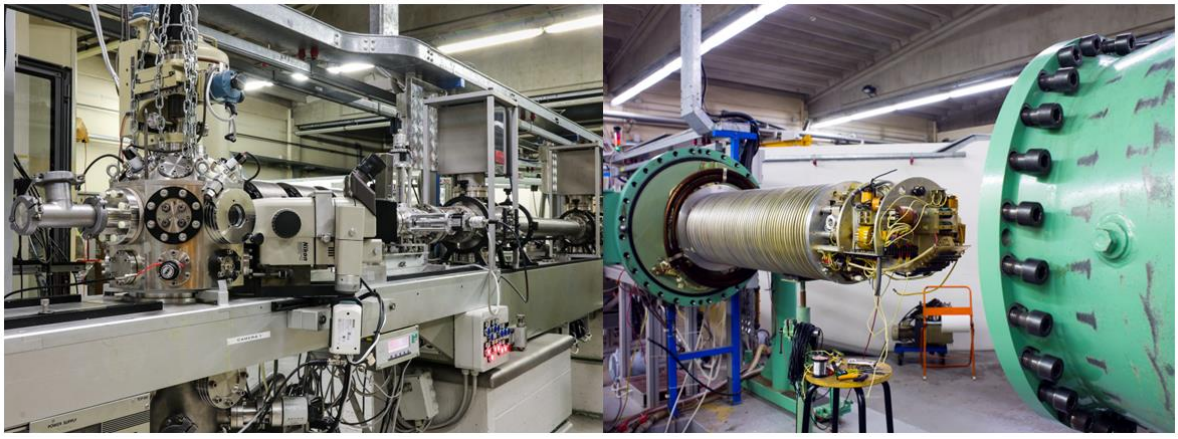

Figure 20-AN2000 accelerator at Legnaro INFN laboratories.

2.4 Setup for electrical measurements in controlled humidity conditions

To investigate the effects of thermal treatments on ND electrical properties with surface terminations and their interaction with environmental water vapor, electrical measurements on ND were performed. ND electrical characterization was conducted under controlled-atmosphere conditions with varying relative humidity levels by employing a setup devised by the candidate, after placing

the samples in a cylindrical cell (Figure 21A). This was 3D-printed with a stereolithography Form 3B 3D-printer using Formlabs Durable Resin and had a depth d = (2.85 ± 0.05) mm and an inner diameter D = (7.50 ± 0.05) mm. The cell was sealed with aluminum electrodes, whose contact with ND was ensured by two springs, applying constant and uniform pressure.

The ND-filled cell was positioned within a probe station composed by a vacuum chamber connected to a mechanical vacuum pump and to the electrical characterization apparatus (Figure 21B). The cell was evacuated to approximately 0.4 mbar for 15 min to remove any pre-existing adsorbed water on the ND before measuring its impedance. This quantity is referred to as "ND impedance" or |Z| throughout the text and it was used to evaluate the electrical properties of the different samples. Impedance measurements were carried out using a Hioki IM3536 LCR meter (Figure 21D), operating in the 4 Hz - 8 MHz frequency range and capable of measuring impedances up to 9.99999 GΩ. The measuring voltage and frequency were respectively set to 1 V and 15 Hz.

After the above-described vacuum procedure, water vapor was introduced into the chamber *via* a valve connected to a water tank. The water pressure reached inside the chamber was measured using a piezo-resistive Thyracont VD81 vacuum gauge (Figure 21E) and this pressure was converted into a relative humidity value using the August-Roche-Magnus equation:

$$p_s = 6.1094\, e^{\frac{17.625\,T}{T+243.04}} \qquad \text{Eq.34}$$

where p_s is the water saturation vapor pressure in mbar and T is the temperature in °C [190]. The chamber relative humidity was held constant for 10 minutes to allow the ND to adsorb environmental water until saturation, after which the impedance was re-measured. Subsequently, the water vapor pressure was reduced and maintained at a constant level for another 10 minutes. This procedure was repeated for each sample to collect impedance values at progressively lower relative humidity levels, ranging from about 90% to 25%, in addition to the impedance value recorded after the initial 15-minute vacuum exposure.

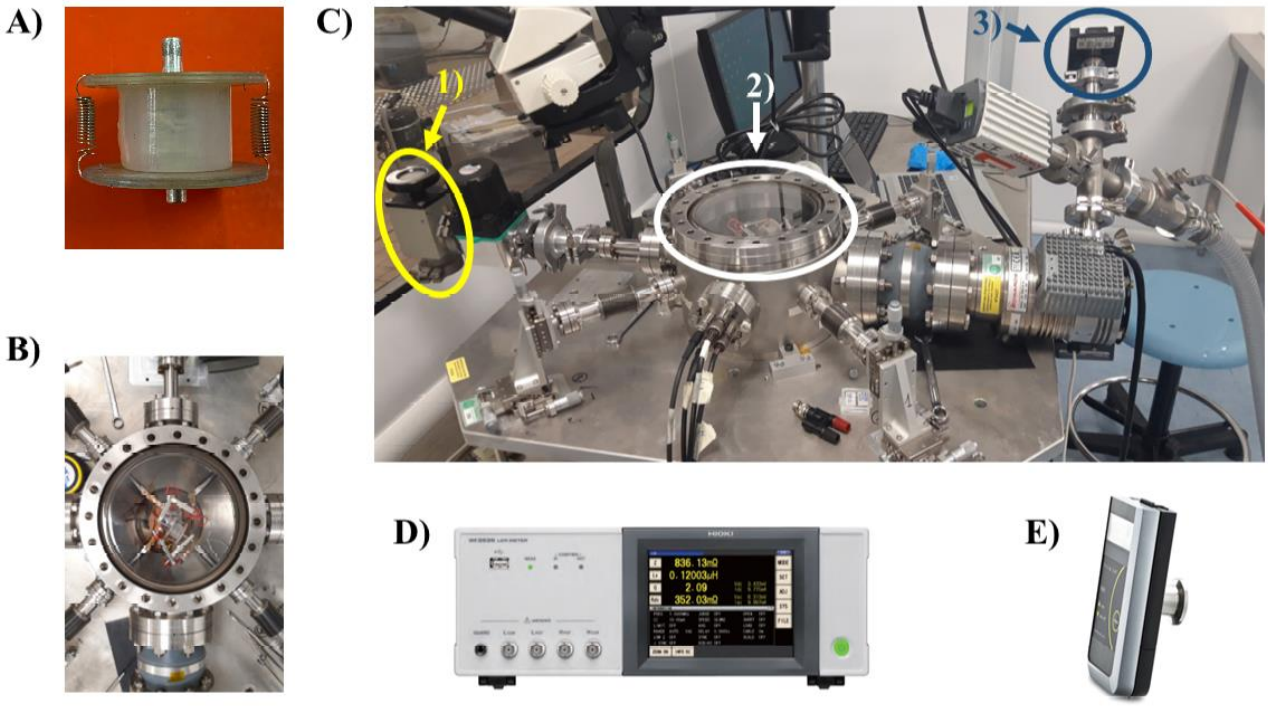

Figure 21-Setup for ND electrical characterization in controlled humidity conditions. A) Cell employed as sample holder for ND powders. B) ND-filled cell inside the probe station. C) Comprehensive view of the characterization setup, showing the probe station vacuum chamber (2) connected to the water tank (1) and the gauge used to read water vapor pressure (3). D) Hioki IM3536 LCR meter. E) Thyracont VD81 vacuum gauge.

2.5 Diffuse Reflectance Infrared Fourier-Transform spectroscopy

Fourier-transform infrared spectroscopy (FTIR) is a simple and non-destructive tool, providing valuable insights into materials surface chemistry by allowing the identification of surface functional groups and investigation of other surface-related properties, such as surface hydrophilicity. When dealing with materials that scatter light, such as powders, FTIR is commonly performed in diffuse reflectance mode, being known as Diffuse Reflectance Infrared Fourier Transform (DRIFT) spectroscopy. In the scattering process, infrared light passes through the solid particles and can be absorbed if vibrational transitions occur. The scattered light then carries information about these transitions, which is analyzed to obtain the sample spectrum. The incident light on the sample may result in a single reflection from the surface (specular reflectance) or be multiply reflected, thus giving rise to diffusely scattered light over a wide area (Figure 22A). In DRIFT measurements, collection optics are designed to reject the specularly reflected radiation and capture as much of the diffuse reflected light as possible [191].

To investigate the surface chemistry of ND samples, their DRIFT spectra were collected using a Bruker Vector 22 FTIR spectrometer (schematized in Figure 22B) equipped with a nitrogen-cooled mercury-cadmium-telluride detector. Each spectrum was recorded in dry air ambient conditions (*i.e.*,

relative humidity ~ 10%), by averaging 64 acquisitions at 2 cm^{-1} spectral resolution. The collected reflectance values were successively converted to pseudo-absorbance values, following the equation:

$$A = -\log R \qquad \text{Eq.35}$$

where R represents the measured reflectance and A is the corresponding pseudo-absorbance.

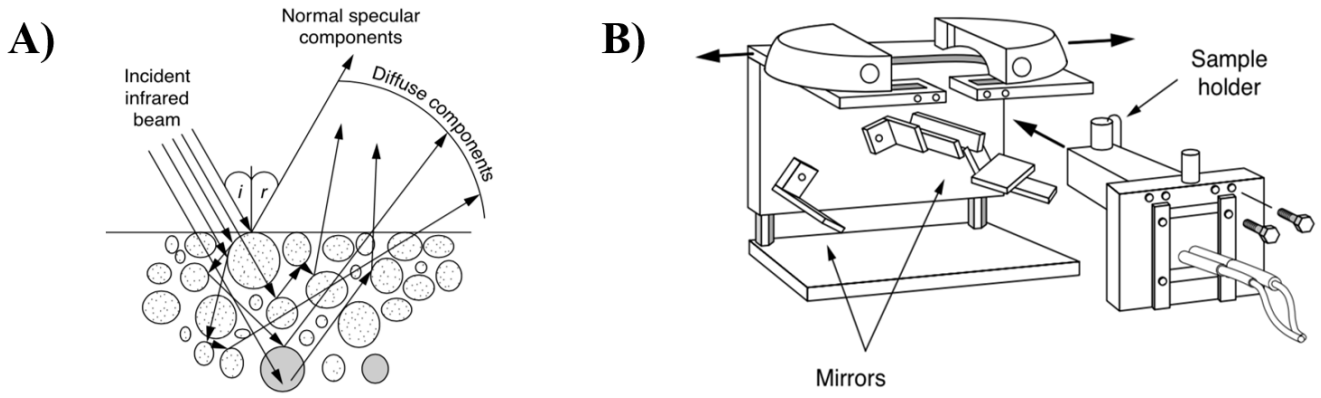

Figure 22-A) Radiation diffused by a sample in form of powders. B) Scheme of the Bruker Vector 22 FTIR spectrometer internal construction.

2.6 Raman and Photoluminescence spectroscopies

Raman spectroscopy is a technique complementary to infrared spectroscopy, serving as an effective tool for analyzing the unique chemical fingerprints of molecules and solids. It is based on the Raman effect, first observed by C.V. Raman in 1928, which involves the inelastic scattering of light by matter, arising in crystals from the interaction between incident photons and optical phonons [192]. The laser light used as a probe beam in Raman spectroscopy can also induce photoluminescence phenomena, leading to the fluorescence emission of NV centers in the ND core. This allows for the simultaneous collection of Raman and photoluminescence spectra in a single measurement.

Raman and photoluminescence spectroscopy of the ND, conducted to investigate samples structural characteristics and their fluorescence properties deriving from NV centers, were performed using the Horiba Jobin Yvon HR800 Raman micro-spectrometer at the Scansetti Interdepartmental Centre of the University of Turin. The spectrometer is equipped with a 600 lines/mm diffraction grating, providing a Raman shift resolution of 3 cm^{-1}, and a CCD detector with Peltier cooling system (-70 °C). The instrument, which is controlled *via* computer through *LabSpec* software, also includes an Olympus BX41 optical microscope with a set of objectives (10×, 20×, 50×, and 100×), coupled to a color video camera, allowing sample observation and precise laser focusing on the desired point and focal plane. The optical excitation source is a 532 nm Nd-YAG solid-state laser, whose power intensity can reach values up to 25 mW and can be regulated by filters inserted along the optical path.

As with the preparation performed prior to ion irradiation, ND were dispersed in isopropanol and deposited on a silicon wafer for the acquisition of Raman and photoluminescence spectra.

Figure 23-Raman spectrometer at the Scansetti Interdepartmental Centre (University of Turin).

2.7 Scanning Electron Microscopy

Scanning Electron Microscopy (SEM) employs a finely focused beam of electrons as a probe to image a sample with nanometer-scale resolution. The electron beam is generated through thermionic emission, focused by a series of electromagnetic lenses, and then scanned in a raster scan pattern across different areas of the specimen. Images are produced by the signals resulting from interactions between the probe electrons and the atoms of the material under investigation, which are shown in Figure 24A. The most commonly analyzed output is the one originated by secondary electrons, arising from surface or near-surface areas of the sample due to the inelastic scattering of the primary electron beam. These electrons carry information on surface topography, thus providing valuable insights on fine surface details and morphological characteristics of the sample examined [193].

SEM was employed to investigate ND size distribution and their morphology. Observations were conducted with the FEI - Inspect F^{TM} (Figure 24B) available at Nanofacility Piemonte (INRiM). The instrument, equipped with a Field Emission Gun (FEG) 35 source, was operated in secondary electrons detection mode under high-vacuum conditions (approximately 10^{-6} mbar pressure). The acceleration voltage was set to 5 kV, thus providing a spatial resolution of about 10 nm.

To set up samples for imaging, diluted dispersions of ND in isopropanol were prepared (ND concentration lower than 1 mg ml^{-1}) and then subjected to sonication for 30 minutes using an Elmasonic S15H ultrasonic device (35 W ultrasonic power). After sonication, droplets of the ND suspensions were deposited onto silicon substrates and allowed to air-dry. The ND were intentionally

left uncoated with metal to prevent any potential morphological changes, though this approach might have introduced some charging effects.

ImageJ software was employed for size distribution analysis. The dimensions of the nanocrystals were assessed from the collected micrographs by manually outlining the contours of the ND projected areas, focusing on well-separated particles. Assuming a spherical shape for the ND, the measured data were converted to diameter values and particle size histograms were constructed using an appropriate binning method.

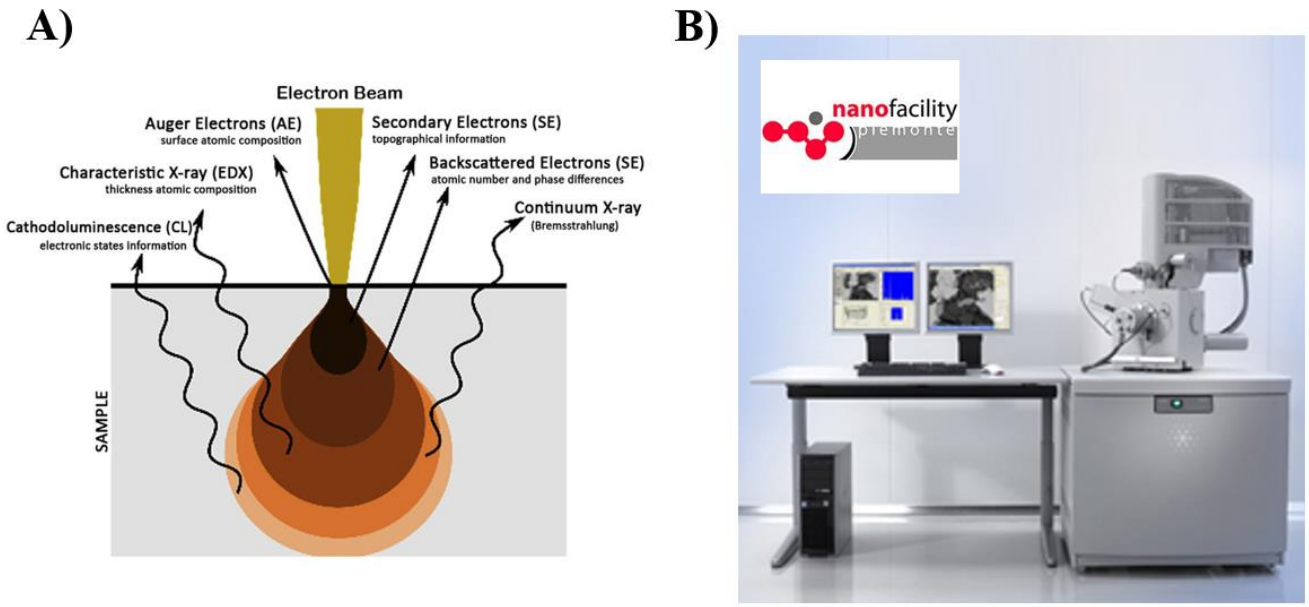

Figure 24-A) Signals generated by the interaction of electrons with a material. The ones most commonly detected in electron microscopy are secondary electrons and backscattered electrons. B) Inspect F^{TM} SEM at Nanofacility Piemonte (INRiM).

2.8 Dynamic Light Scattering and Zeta Potential measurements

Dynamic Light Scattering (DLS), also known as photon correlation spectroscopy or quasi-elastic light scattering, is a hydrodynamic technique used to determine the diameter of particles suspended in liquids by measuring their translational diffusion coefficient [194]. Since such physical quantity is strongly influenced by the nature of particle surface, as well as by the concentration and type of ions in the suspending medium, the measured size value is similarly affected [195]. This makes DLS a valuable tool for investigating changes in particles dimensions in relation to these factors. In addition to particle diameter, DLS measurements provide information on the distribution of particle size, estimated through the polydispersity index (PDI). A higher PDI value indicates less uniform particle dimensions within the sample and *vice versa* [196].

On the other hand, Zeta Potential (ZP) analysis is a hydrodynamic technique for the evaluation of electrical potential at the slipping plane of nanoparticles suspended in liquids, which is defined as *zeta potential*. ZP is commonly determined by measuring the electrophoretic mobility of particles dispersed in media with moderate electrolyte concentration and it is influenced by composition and the pH of the suspending medium. ZP offers insights into particles surface charge and their stability in colloidal suspension, giving information on their tendency to aggregate. Particles endowed with large negative or positive ZP values, *i.e.*, ZP < -30 mV or ZP > +30 mV, are considered highly stable in suspension, repelling each other and thus preventing their aggregation. Conversely, particles featuring ZP low in absolute are prone to aggregate, coagulate, or flocculate, as a result of van der Waals inter-particle attraction [197].

DLS and ZP analyses were carried out to investigate ND behavior in water-based solutions, in terms of their size distribution, surface charge and eventual aggregation in aqueous media. DLS measurements were performed by employing a Zetasizer Nano ZS (Figure 25A), controlled *via* a computer thanks to the Zetasizer software and equipped with a 4 mW power 633 nm He-Ne laser. The instrument is capable of measuring particle sizes in the 0.3 nm - 10 μm range, with particle concentrations spanning from 0.1 ppm to 40% w/v. Analyses were conducted at a scattering angle of 173°, pouring ND dispersions into disposable DTS0012 cuvettes (Figure 25B).

The Zetasizer Nano ZS was used also to perform ZP measurements, loading ND suspensions into the folded capillary cell DTS1070 (Figure 25C and Figure 25D), characterized by two gold-plated copper electrodes at the ends. The application of an electric field (E) to the cell electrodes makes charged particles acquire a net average velocity (v). By measuring v and calculating the ratio between v and E, particles electrophoretic mobility (U_E) is obtained, allowing ZP value to be derived using Henry's equation. v was measured by the Zetasizer Nano ZS with a technique combining laser Doppler anemometry and phase analysis light scattering. The method registers the phase difference between the laser beam incident on the moving particles and the light they scatter. This is related to the frequency shift between the scattered signal and the reference one, which is proportional to v and, consequently, to U_E and ZP [198,199].

Both DLS and ZP assessment were carried out at 25 °C after samples ultrasonic stirring.

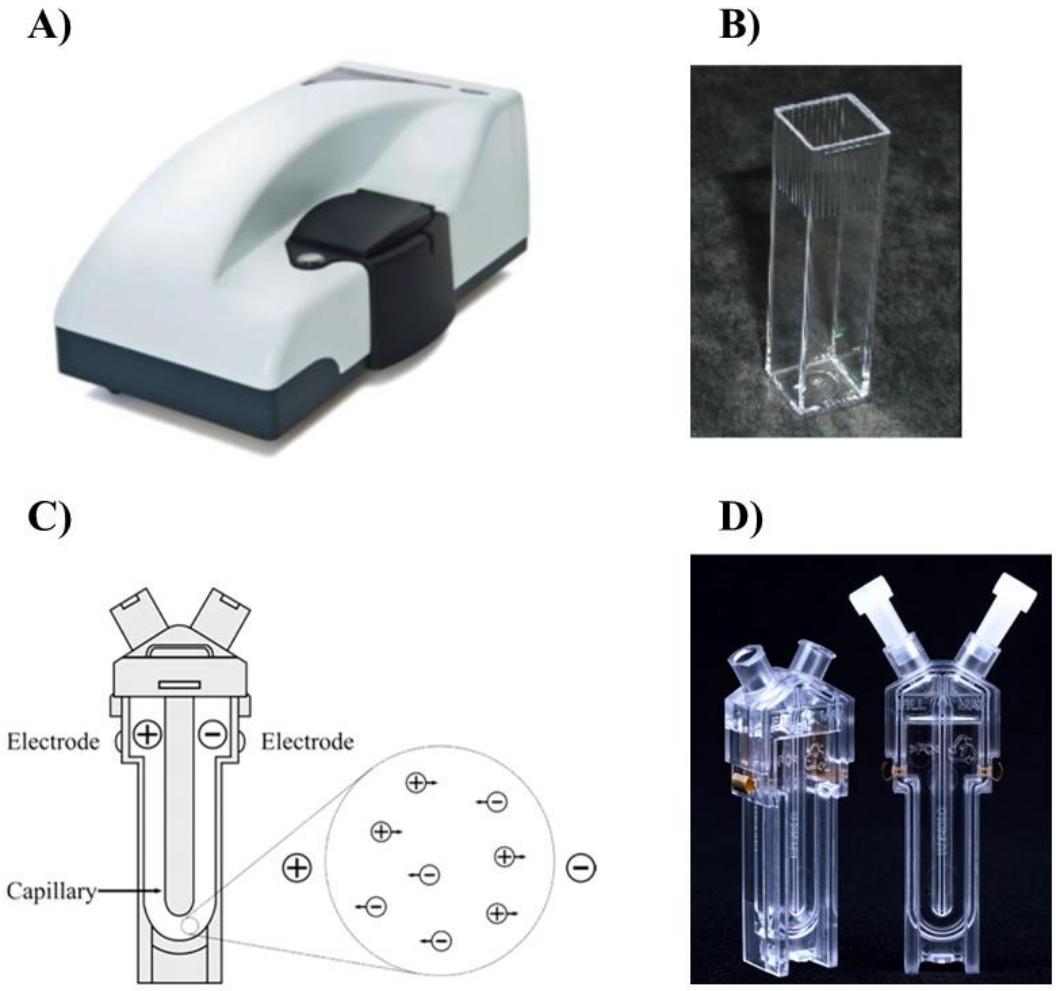

Figure 25-A) Zetasizer Nano ZS. B) DTS0012 cuvette employed in DLS measurements. C) Scheme of the folded capillary cell used in zeta potential analyses. D) DTS1070 cell for zeta potential determination.

2.9 Measurement of hydroxyl radical production from aqueous dispersions of ND upon irradiation with γ-photons

With the aim of assessing ND potential as radiosensitizers, the concentration of hydroxyl radicals (•OH) formed upon γ-photons irradiation of ND aqueous suspensions was measured *via* fluorescence spectroscopy.

Samples were prepared by diluting concentrated aqueous dispersions of ND with Gomori Phosphate-Buffered Saline (PBS) solution containing terephthalic acid (TPA) at a concentration of 0.05 mM. TPA was employed as a probe for radicals detection, due to its ability to react with these species to form a single hydroxylated product, *i.e.*, 2-hydroxyterephthalic acid (HTPA) [200,201], according to the reaction displayed in Figure 26. Unlike TPA, HTPA is a fluorescent molecule, exhibiting a bright and stable emission at approximately 430 nm when excited by light at 315 nm wavelength. HTPA can hence be revealed through fluorescence spectroscopy, thus allowing indirect

quantification of the •OH. The choice of TPA was dictated by the fact that this probe does not features shortcomings in sensitivity or selectivity, as it does not require long irradiation times and/or high concentrations, which may impact the behavior and composition of the sample. Additionally, such compound is relatively easy to handle, posing minimal risk to the operator [201–203].

After preparation, ND suspensions were ultrasonically stirred for at least 30 minutes and then poured into 1.5 ml vials for irradiation with γ-photons.

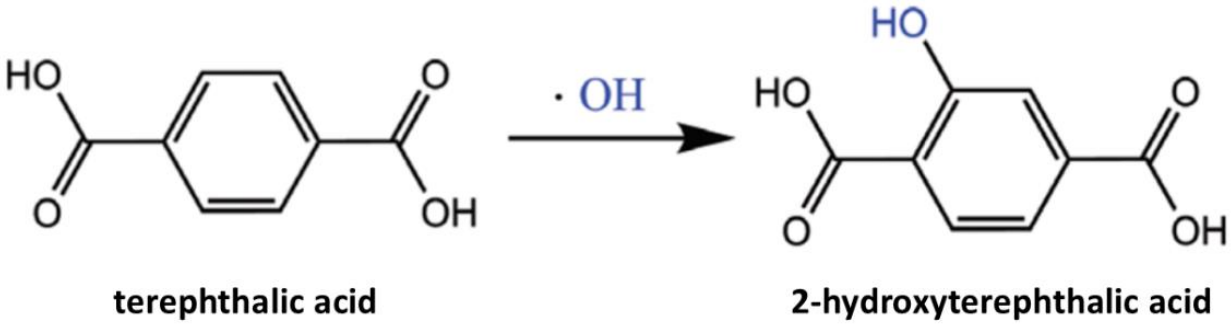

Figure 26-Hydroxylation reaction of terephthalic acid (non-fluorescent), resulting in the fluorescent molecule 2-hydroxyterephthalic acid.

The irradiation was carried out using an Elekta SL18 Precise radiotherapy LINAC (Figure 27), employing photons which were generated by the impact of electrons accelerated by a 15 MV potential on a tungsten target. The samples were placed at the machine isocenter point, located at about 1 m from the accelerator target, and exposed to a radiation dose of 4.1 Gy, delivered at a rate of 4 Gy/min, with the beam field size set to 20 × 20 cm².

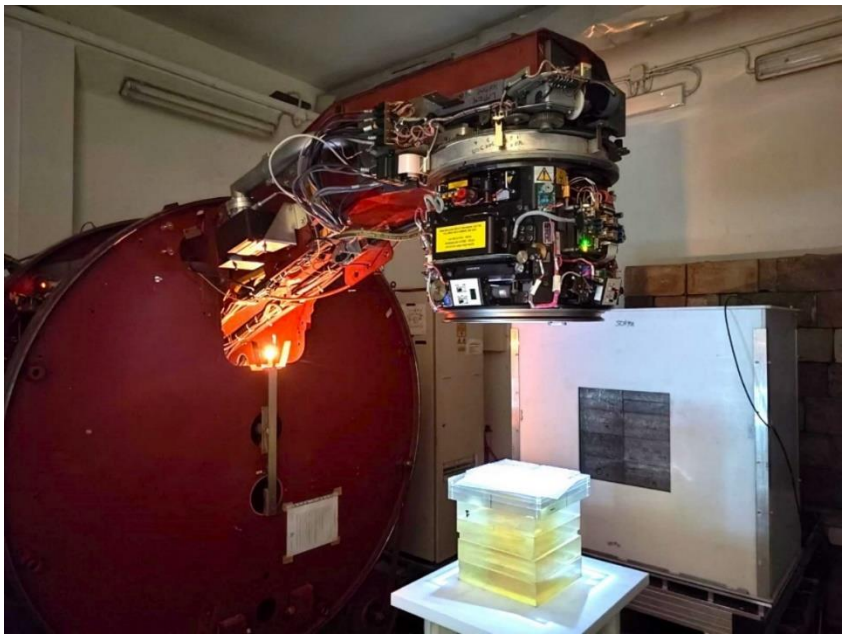

Figure 27- Elekta SL18 Precise radiotherapy LINAC.

To perform fluorescence spectroscopy measurements for evaluating ˙OH radical concentration in the different ND suspensions, the irradiated samples were moved into all sides-polished UV and visible light transparent quartz cuvettes. These were inserted into a fluorometer assembled by the researchers of Solid State Physics group (Figure 28). The instrument employs a Thorlabs UV-visible LED 315W as light source, featuring a spectral output centered at 315 nm, a forward current of 30 mA and a power output of 0.600 mW. The LED, powered by an electronic board delivering a power supply current of 15 mA, is enclosed into a Thorlabs CVH100 cuvette holder, shielding the sample cuvettes from external light and reducing environmental light noise. The light emitted from the samples is collected orthogonally to the optical path of the incident radiation using an optical fiber with a numerical aperture of 0.50 and a core diameter of 200 µm. Fluorescence spectra were acquired by an Ocean Optics QEPro Spectrometer, equipped with a thermoelectrically cooled Hamamatsu S70311006 detector, cooling to 15 °C - 20 °C below ambient temperature, and controlled by the OceanView software, setting integration time to 30 s.

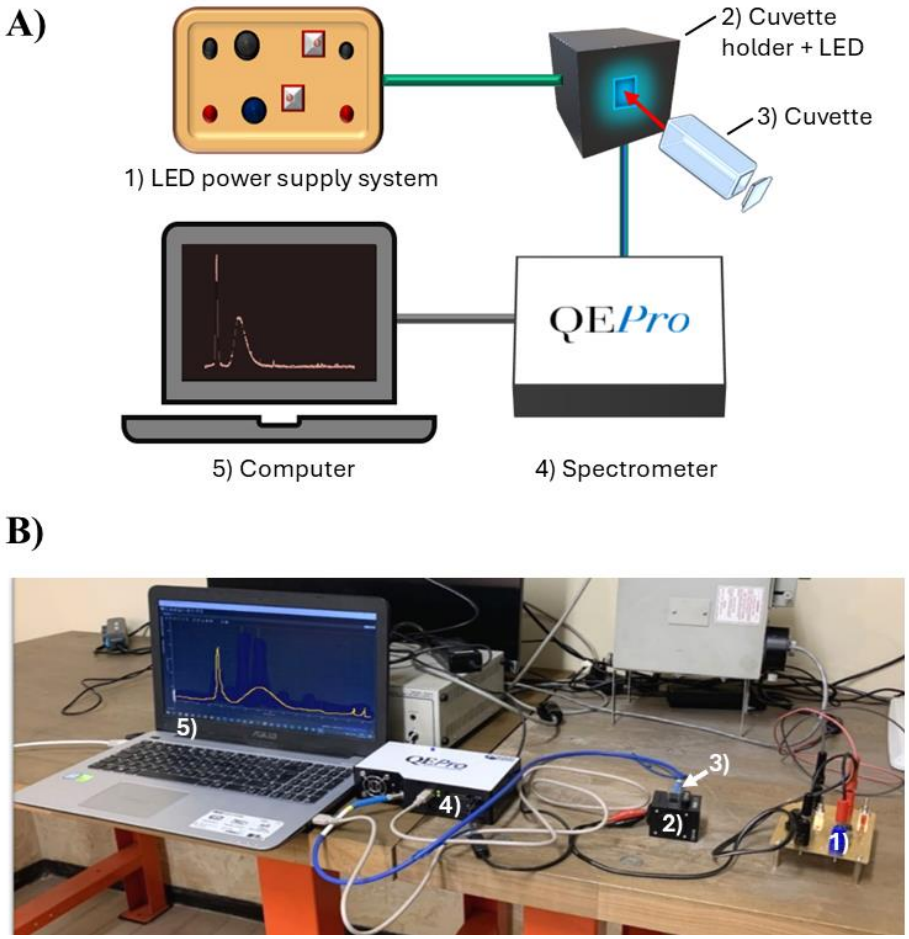

Figure 28-A) Scheme of the fluorometer used to measure the fluorescence of the TPA-containing ND dispersions upon irradiation with γ-photons for evaluating ˙OH radical production. B) Fluorometer setup. An electronic board (1) powers the 315 nm led excitation source, enclosed into the cuvette holder (2), where the cuvette containing ND dispersions (3) is placed. The spectrometer (4), connected to a computer (5), allow to collect fluorescence spectra.

To obtain information about •OH radical production, the recorded fluorescence spectra were analyzed by evaluating the area underneath HTPA emission peak, integrating each spectrum in the 360 nm - 560 nm interval. Area values were then converted to concentrations exploiting a proper calibration curve, correlating HTPA concentration to the measured fluorescence intensity, as illustrated in sub-section 3.3.1.

2.10 System for T_1-relaxometry measurements

T_1-relaxometry characterization was carried out on ion beam-modified ND to measure their T_1 time and investigate their ability to detect paramagnetic species.

Measurements were conducted at the Universitair Medisch Centrum Groningen using a custom-built confocal setup that has been assembled by the researchers of the Biomedical Engineering Department from the research group led by Prof. Romana Schirhagl.

The setup is divided into two distinct sections, where the first one is dedicated to the creation of the laser pulsing sequence necessary for the measurements, while the second one is devoted to laser focusing on the sample and collection of the NV centers photoluminescence signal. These are respectively illustrated in Figure 29 and Figure 30.

The first part of the system is composed by a Ventus 532 laser, emitting green light at 532 nm, and a Gooch & Housego 3350-199 acousto-optic modulator (AOM), employed to pulse the laser light in a double-pass configuration. In this arrangement the laser light passes through the AOM twice, thus preventing alterations of the beam direction. Indeed, when a laser beam is sent through an AOM, the first-order diffraction emerges at a small angle θ, which varies depending on the power and driving frequency applied to the AOM. By passing through the AOM a second time, any beam deflection is compensated, eliminating the need for frequent realignment of the entire setup [204]. Such configuration is implemented by directing the laser light though a half-wave plate, polarizing it linearly in one direction, and then through a polarizing beam splitter, which transmits it to a quarter-wave plate, that changes the light polarization to circular. The circularly polarized beam enters the AOM and is reflected back by a mirror. The beam then passes through the AOM and the quarter-wave plate again, where its polarization is modified back to linear, but with its direction rotated by 90° compared to the initial one. This change in polarization allows the beam exiting the AOM to be reflected by the polarizing beam splitter, thus separating it from the incoming light. The reflected beam is then directed through an optical fiber, which guides it to the second part of the setup.

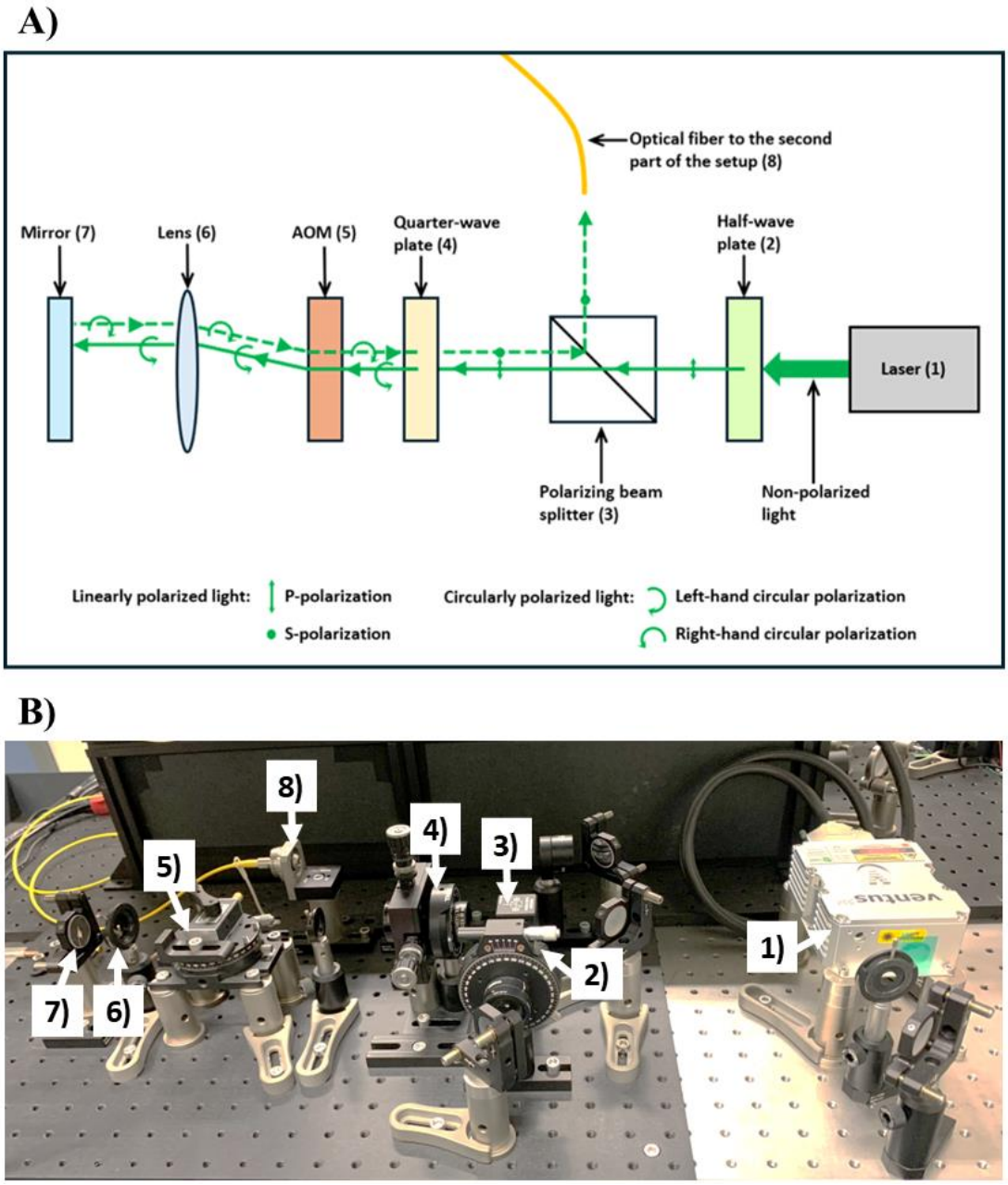

Figure 29- Section of the T_1-relaxometry measurement setup at the Universitair Medisch Centrum Groningen dedicated to creating the laser pulsing sequence. A) Schematic showing the various components of the laser pulsing system. B) Laser pulsing system. The laser (1) emits light that passes through a half-wave plate (2), polarizing it linearly. The linearly polarized beam then enters a polarizing beam splitter (3), which directs it to a quarter-wave plate (4), converting the polarization to circular. The circularly polarized beam passes through the AOM (5), then through a lens (6), and is reflected back by a mirror (7), thus passing once more through the AOM and the quarter-wave plate. This returns the polarization to linear, but rotated by 90° with respect to the initial direction, allowing it to be reflected by the polarizing beam splitter and directed into an optical fiber (8).

The system second unit consists of a confocal microscope in an inverted configuration, with an Olympus UPlanSApo100× oil objective (characterized by a numerical aperture of 1.40 and a working distance of 0.12 mm), responsible for laser focusing and NV fluorescence signal collection, which is

positioned beneath the sample, placed on a holed piezoelectric stage. This specific design is particularly suitable for performing relaxometry *in vitro*, as it allows measurements to be conducted while keeping the samples inside Petri dishes or culture plates. The laser light emerging from the setup first module is directed through a dichroic mirror, dividing the excitation light from the output red fluorescence signal, then to a scanning mirror, which allows addressing different parts of the sample, and eventually through the objective, thus reaching the sample. After excitation of the NV centers in the ND, red fluorescence is emitted and photoluminescence light is directed back the same path until the dichroic mirror that sends it to the detection path, contained within a dark box to reduce counts from reflected light. There, a manually adjustable filter wheel, equipped with different high-pass filters (600 nm, 650 nm and 700 nm), allows selection of the desired wavelengths. After passing a pinhole, the fluorescence signal is detected by a Single-Photon-Avalanche-Diode (SPAD).

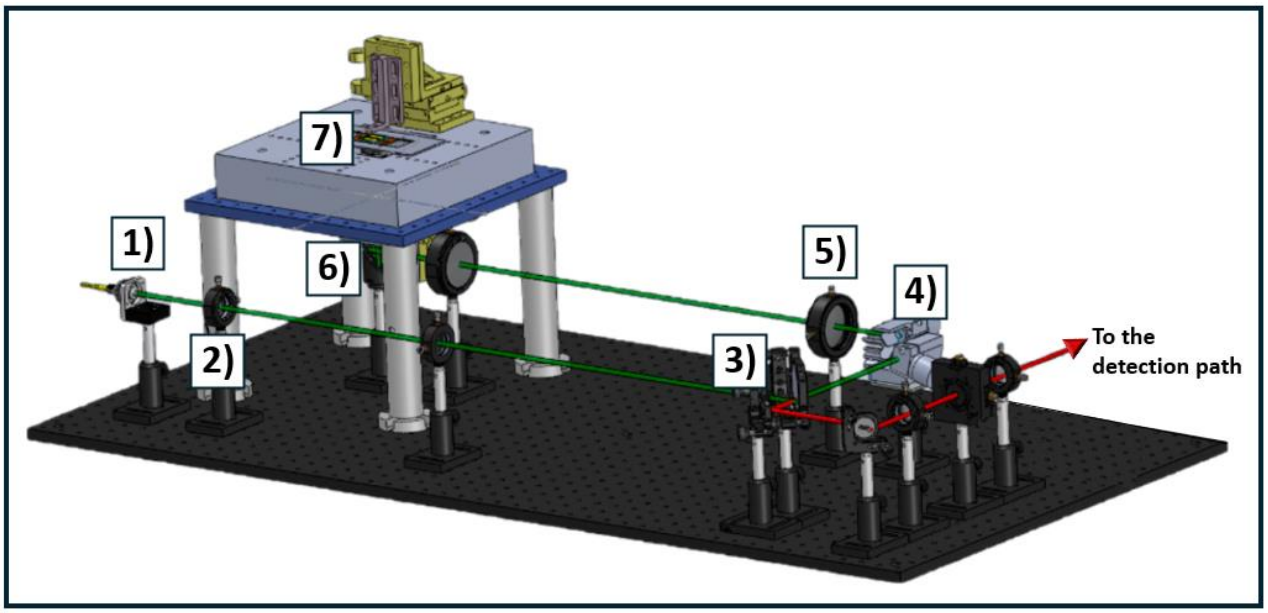

Figure 30- Schematics showing the section of the T_1-relaxometry measurement setup at the Universitair Medisch Centrum Groningen dedicated to laser focusing on the sample and collection of the NV center photoluminescence signal (adapted from [182]): 1) fiber port, 2) lenses for beam size adjustment, 3) dichroic mirror directing only NV fluorescence to the detector, 4) scanning mirror for positioning the laser at different locations on the sample, 5) additional lens, 6) objective enabling focus scanning, 7) piezoelectric stage for precise sample positioning.

The setup also includes a bright-field microscope, which is used to collect images simultaneously, and is controlled via computer using a customized LabVIEW program, developed by Prof. Romana Schirhagl's research group.

Measurements were conducted by setting the laser power to 50 µW and exploiting a pulse train of 51 laser pulses, each lasting 5 µs, interspersed with 50 dark times, which were exponentially varied from 0.2 µs to 2 ms. To obtain sufficient signal-to-noise ratio, the pulsing sequence, taking around 12 ms,

was repeated 10^4 times for each measurement, resulting in a total measurement duration of approximately 2 minutes. The photoluminescent signal from the NV centers was detected above 600 nm and was quantified in a detection window of 1 μs.

Relaxation curves were acquired for particles with fluorescence counts between 5×10^5 and 6×10^6. Counts outside this range were excluded, as they likely indicate dirt particles on the surface, aggregates, background noise, or exceptionally large or small particles [52]. For each type of sample, measurements were conducted on at least 30 different particles to ensure robust statistical analysis. A tracking algorithm within the LabVIEW control program was used to monitor the movement of each ND, ensuring it remained in focus, and the collected curves were fitted with a single exponential model. Only T_1 time values within the 10 μs to 1 ms range, regarded to have physical meaning [52], were considered.

3. Results

As mentioned in section 2.1, diamond particles with different median diameter, *i.e.*, 55 nm ("^{s}ND"), 125 nm ("^{m}ND"), 240 nm ("^{l}ND") and 6 µm ("µD") were investigated. The particles involved in each part of the experimental work are introduced at the beginning of each of the following sections. ^{l}ND, ^{s}ND, and ^{m}ND are referred to simply as "ND" within the sub-sections, unless specifying the particle size is important. On the other hand, the 6 µm median diameter diamond particles are always indicated as "µD" within the text.

All the results presented refer to samples subjected to various thermal treatments, which were conducted using the system described in section 2.2 and are summarized in the diagram shown in Figure 31. The names of the different processes are displayed within the white-filled rectangles, together with details regarding the type of atmosphere, duration, and temperature. In cases where multiple procedures were undetaken at different times and temperatures, a range is indicated, with more detailed information provided in the figures of appendix A. The blue arrows illustrate the sequence of treatments, while the rectangles with solid blue fill report the detailed samples nomenclature, providing a complete summary of all processing steps applied to a given batch of particles. This naming system is employed in sub-section 3.1.1, where it was crucial to highlight both type and order of the performed procedures, and in sub-section 3.1.2, being closely connected to the previous one. The labels indicated by the black arrows are instead used to differentiate the samples from sub-section 3.1.3 onwards, as the treatment scheme remained consistent, following the set of processes written in blue. For simplicity, ^{l}ND, ^{s}ND, and ^{m}ND and µD are all indicated as "ND" in the scheme.

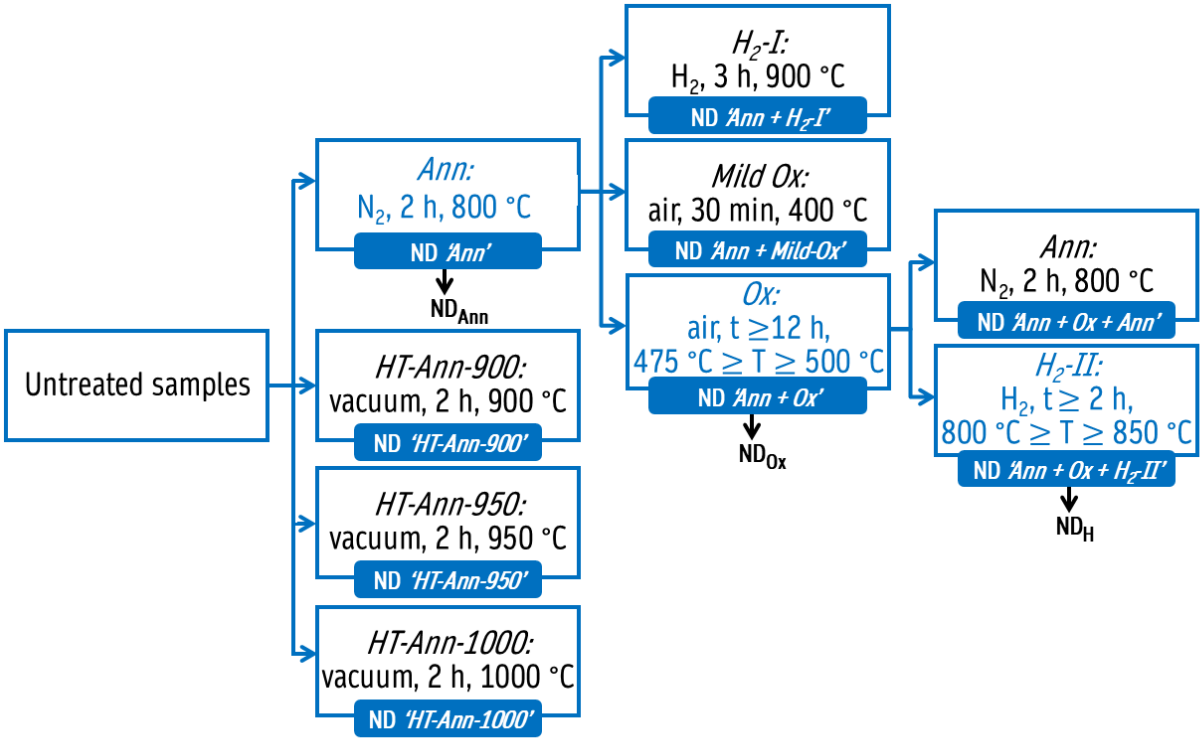

Figure 31-Thermal treatments carried out on the samples examined in this thesis (further details are available in appendix A), including annealing ('*Ann*'), high-temperature annealing ('*HT-Ann*'), oxidation ('*Mild-Ox*' and '*Ox*'), and hydrogenation ('H_2-*I*' and 'H_2-*II*') processes. The names of the treatments are reported inside the white-filled rectangles, whereas their sequence is indicated by the blue arrows. The complete nomenclature of the samples, summarizing all the processing steps conducted on a given batch of particles, is shown inside the blue rectangles. This is used to label the samples in sub-sections 3.1.1 and 3.1.2. From sub-section 3.1.3 onwards, samples are named with the labels indicated by the black arrows, as the treatment scheme remained the same, consisting of the set of processes written in blue. For simplicity, in the scheme ^{l}ND, ^{s}ND, and ^{m}ND and µD are all indicated as "ND".

Annealing treatments in N_2 atmosphere at 800 °C were conducted with the aim of standardizing particle surface, through the elimination of surface functional groups, and graphitizing surface amorphous carbon components, while avoiding to damage the diamond core. The processes were performed on both pristine or previously treated particles, and they are indicated as '*Ann*'. On the other hand, annealing processes in vacuum at temperatures higher than 800 °C were meant for inducing graphitization, disregarding any possible degradation of the diamond phase. They were carried out at 900 °C, 950 °C, and 1000 °C, and they are respectively labelled '*HT-Ann-900*', '*HT-Ann-950*', and '*HT-Ann-1000*'. Following the '*Ann*' step, air oxidation treatments were implemented with the purpose of removing selectively sp^2 carbon, thus purifying particles from graphitic layers, concurrently fostering the formation of surface oxygenated moieties. Two types of oxidation procedures were carried out: these are called '*Mild Ox*' and '*Ox*' respectively, based on the processing parameters. The former was conducted in mild conditions, *i.e.*, at 400 °C for 30 min,

whereas the '*Ox*' treatments were executed at higher temperatures for longer durations and were also exploited as intermediate steps for subsequent processing. Eventually, hydrogenation treatments under hydrogen flow were carried out to create C-H bonds on the surface. They are designated as '*H_2-I*' and '*H_2-II*,' depending on whether they followed '*Ann*' or '*Ox*' process respectively.

3.1 Properties of diamond particles upon different thermal treatments

The influence of thermal treatments on the surface properties of diamond particles was evaluated starting from assessing their impact on particles electrical behavior. As detailed in the introduction (in sub-section 1.3.3), thermal treatments lead to surface modifications that relevantly affect electrical properties. Clarifying how these correlate with surface characteristics is essential to understand if surface chemistry and structure can be inferred from electrical measurements, as various surface terminations appear to be associated with distinct electrical behavior. Despite the extensive literature on the topic, the effect of different surface modifications and diamond particles size on this aspect has never been systematically correlated and examined. The work presented in sub-sections 3.1.1 and 3.1.2 was carried out with the goal of achieving this purpose. The relationship between electrical properties and different thermal treatments in controlled atmosphere was examined by linking sample electrical behavior with surface chemical and structural changes and with a specific conduction mechanism. To this aim, samples electrical characterization in different and controlled relative humidity conditions was performed, employing the system and the methodology described in section 2.4, joined with spectroscopic analyses, including Diffuse Reflectance Infrared Fourier Tansform (DRIFT) and Raman spectroscopies. This type of characterization was conducted on ^{l}ND (240 nm median diameter), which were subjected to all the thermal treatments illustrated in the scheme of Figure 31. The results, presented in sub-section 3.1.1, allowed in-depth comprehension of the relationship of the electrical conductivity with surface moieties, leading also to define a protocol for ND annealing, oxidation, and hydrogenation treatments. Further investigations conducted to investigate the connection between particle size and electrical properties focused on ^{s}ND (55 nm median diameter) and µD (6 µm median diameter) and are reported in sub-section 3.1.2, where they are commented in relation to the findings on ^{l}ND.

To study samples hydrodynamic behavior in aqueous solution, thus gaining insights into particles aggregation tendency and surface charge, Dynamic Light Scattering (DLS) and Zeta Potential (ZP) analyses were also performed. These measurements were undertaken on the ^{l}ND, specifically on the samples labelled with the compact names "ND_{Ann}", "ND_{Ox}", and "ND_{H}", and their outcomes are illustrated in sub-section 3.1.3.

3.1.1 Electrical properties, surface chemistry and structure

The results of electrical characterization at varying relative humidity (hereafter "RH") of the ND subjected to all the thermal treatments shown in scheme of Figure 31 are presented in Figure 32A, Figure 33A and Figure 34A, and summarized in the table of Figure 35.

Figure 32A displays the outcomes of impedance measurements conducted at varying RH from the samples labelled as ND '*Ann*', ND '*Ann + Ox*', ND '*Ann + Mild Ox*' and ND '*Ann + Ox + Ann*'. Preliminary Raman spectroscopy confirmed the absence of graphitic carbon in these samples following thermal treatments, thus allowing the exclusion of sp^2 phases as a factor influencing their electrical properties. The corresponding Raman spectra are reported in Figure 57 of appendix B. The impedance of the ND, exceeding the upper limit of the instrumental range when measured after the samples were kept in vacuum, decreases with rising values of RH. This observation underlines a relevant impact of adsorbed water on ND electrical properties and seems to indicate that these are primarily governed by proton hopping taking place in water. Experimental data are indeed in accordance with findings on non-graphitized ND reporting a conductivity increase with increasing amount of water adsorbed on particles surface, ensuing from a progressively more pronounced influence of the Grotthuss mechanism [123,178].

For the ND '*Ann*', |Z| reduces from (6700 ± 1500) MΩ at the lowest RH value to (620 ± 140) MΩ at the highest RH level. For the ND '*Ann + Ox*', the dependence of impedance on hydration conditions appears even more marked, as the variation in |Z| spans over two orders of magnitude, passing from (760 ± 170) MΩ to (3.2 ± 0.7) MΩ in the RH interval under exam. Notably, the impedance values collected for the ND '*Ann + Ox*' are much lower with respect those measured for the ND '*Ann*', with a difference of about one order of magnitude at the lowest RH value, increasing up to two orders of magnitude when RH is maximum. The impedance of the ND '*Ann + Mild Ox*' also varies over two orders of magnitude, *i.e.*, from (9000 ± 2000) MΩ to (27 ± 6) MΩ, over the explored RH range. Nevertheless, for the ND '*Ann + Mild Ox*' impedance values are consistently one order of magnitude higher than those of the ND '*Ann + Ox*' samples and approach the values measured for ND '*Ann*' when RH is decreased below 60%. On the other hand, the ND '*Ann + Ox + Ann*' show impedance values similar to those of the ND '*Ann*', displaying also an analogous one-order-of-magnitude |Z| change across the RH interval under investigation.

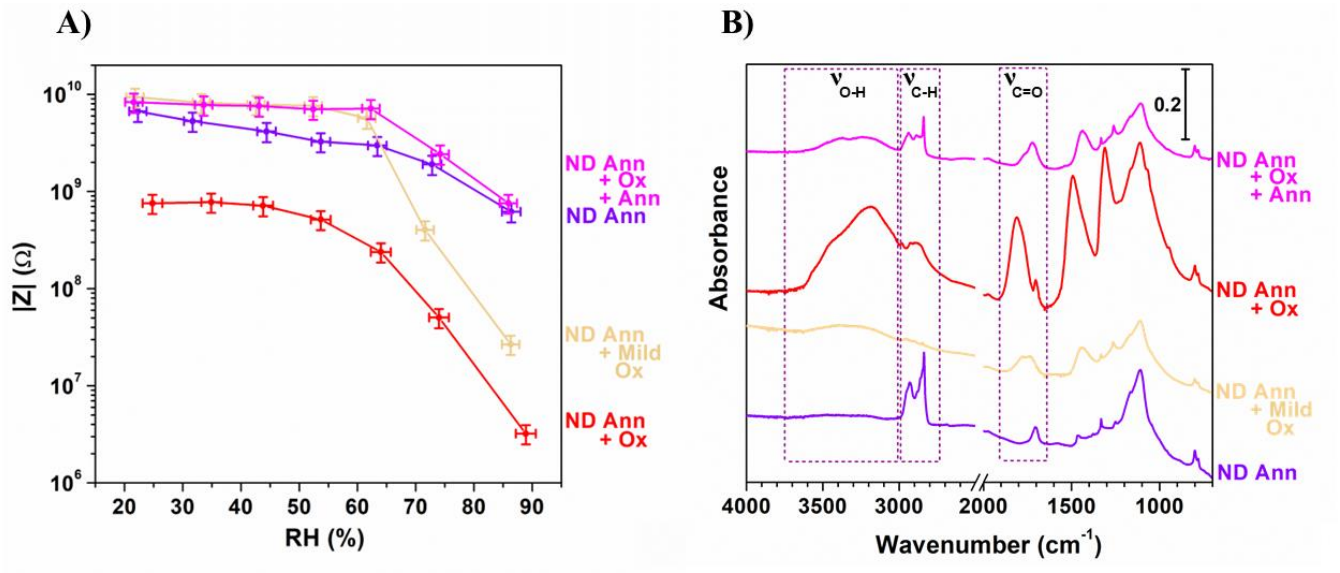

Figure 32-Electrical and spectroscopic characterization of the ND samples ([l]ND; 240 nm median diameter) labelled as ND '*Ann*', ND '*Ann + Ox*', ND '*Ann + Mild Ox*' and ND '*Ann + Ox + Ann*'. A) Electrical impedance of the samples at different relative humidity (RH) conditions. B) Samples DRIFT spectra. The regions of O-H stretching (ν_{O-H}), C-H stretching (ν_{C-H}) and C=O stretching ($\nu_{C=O}$) are marked with dashed contours rectangles.

The electrical behaviour of the various samples seems to suggest a difference in their surface chemistry, promoting or limiting water adsorption and thus determining the observed variations of electrical properties with changing RH. Based on the findings reported in [179] and [123], and considering that the presence of surface oxygen-containing moieties favours the adsorption of water, it could be assumed that such a difference is due to a different amount of oxygenated groups on ND surface.

This hypothesis is corroborated by the analysis of samples DRIFT spectra, which are reported in Figure 32B. The DRIFT spectrum of the ND '*Ann*' is characterized by relevant features in the spectral range between 2990 cm^{-1} and 2800 cm^{-1} (indicated as "ν_{C-H}"), which is attributable to C-H bonds asymmetric and symmetric stretching. The almost complete absence of signals in the 3650 cm^{-1} - 3000 cm^{-1} interval (labelled as "ν_{O-H}") is linked to the lack of O-H stretching modes of both surface adsorbed water and surface moieties [205]. Moreover, only a minor band at 1705 cm^{-1} is visible in the spectral range associated to C=O stretching (referred to as "$\nu_{C=O}$"). The '*Ann*' step thus results in the predominance of C-H moieties, with oxygen-containing groups being nearly entirely absent. Consequently, the ND '*Ann*' exhibit minimal affinity towards water, whose presence is indeed undetectable. Meaningful spectral alterations can be observed in the spectrum of the ND '*Ann + Ox*', which exhibits a broad feature in the ν_{O-H} spectral range and extremely faint bands in the ν_{C-H} one. Additionally, in the $\nu_{C=O}$ spectral region a broad and complex band at 1800 cm^{-1} can be observed. This is ascribable to the C=O stretching vibration in various surface groups, such as

carboxylic acids, esters, lactones, and acid anhydrides [206–208]. The same surface oxygen-containing functionalities also cause the appearance of new spectral features in the 1500-1300 cm^{-1} spectral range, typical of ketones and epoxides vibrations [206,207]. From the previously commented spectral bands it can be inferred that the '*Ox*' step promotes the formation of oxygenated groups, thus increasing surface hydrophilicity. The spectrum of the ND '*Ann* + *Mild Ox*' shows similarities to that of the ND '*Ann* + *Ox*', with key features including the suppression of C-H bands and the appearance of both $\nu_{C=O}$ and ν_{O-H} stretching bands. These features highlight that even the milder oxidation process introduces oxygen-containing functionalities and enhances the water affinity of the ND surface. However, the comparison between the spectrum of the ND '*Ann* + *Mild Ox*' and that of the ND '*Ann* + *Ox*' allows to notice that the intensity of the O-H stretching and $\nu_{C=O}$ bands, as well as the features at lower wavenumbers, is greatly reduced in the former. This indicates considerable changes between different oxidation conditions, revealing that the '*Mild Ox*' process induces only limited formation of oxygenated groups and imparts reduced hydrophilicity to the surface, resulting in a lower amount of adsorbed water on the ND '*Ann* + *Mild Ox*'. The spectrum of the ND '*Ann* + *Ox* + *Ann*' is instead characterized by the disappearance of the $\nu_{C=O}$ band, along with a concurrent decrease in the O-H band intensity, a slight intensification of the bands between 2990 and 2800 cm^{-1}, and the partial suppression of the signals at lower wavenumbers. These modifications indicate that the '*Ann* + *Ox* + *Ann*' treatment removes oxygen-containing groups and produces C-H moieties, thereby providing again the ND surface with a pronounced hydrophobic character.

The stronger dependence on relative humidity and smaller |Z| values observed for the ND '*Ann* + *Ox*' can thus be attributed to the presence of surface oxygenated functional groups, like carboxylic acids, hydroxyls, and esters, originated by the '*Ox*' step [123,164,179,205,206]. These groups promote water adsorption by increasing surface hydrophilicity, thus enhancing Grotthuss mechanism and consequently improving electrical conduction. In contrast, the weaker conductivity and impedance dependence from RH observed for ND '*Ann*' and ND '*Ann* + *Ox* + *Ann*' can be linked to the hydrophobic nature of the surface, which causes limited water adsorption, thus reducing the impact of Grotthuss mechanism on electrical conductivity. This hydrophobicity is due to the '*Ann*' step, eradicating oxygenated groups rather than prompting their formation. Finally, the higher impedance values measured for ND '*Ann* + *Mild Ox*' compared to ND '*Ann* + *Ox*' are associated with a smaller amount of oxygen-containing surface groups, determining water adsorption to a lower extent and thus a more limited contribution of the Grotthuss mechanism. The lower surface density of oxygenated species is caused by the chosen oxidation conditions, which are considerably less aggressive for the

ND '*Ann* + *Mild Ox*' in comparison to the ND '*Ann* + *Ox*', resulting less effective in establishing oxygen-containing groups.

In contrast to the samples discussed so far, the ND subjected to hydrogenation processes, *i.e.*, the ND '*Ann* + H_2-*I*' and ND '*Ann* + *Ox* + H_2-*II*', exhibit an impedance trend showing minimal dependence on RH. This is evident from Figure 33A, which presents the results of electrical measurements for the hydrogenated samples, besides those for the ND '*Ann*' and ND '*Ann* + *Ox*', included for comparison. Similarly to the ND yielding the data of Figure 32, also the ND '*Ann* + H_2-*I*' and ND '*Ann* + *Ox* + H_2-*II*' are insufficiently conductive following vacuum exposure to be tested by the measuring apparatus. The impact of surface graphite on the electrical behavior can be ruled out once more, as no graphite G-band is detectable in hydrogenated ND Raman spectra, as displayed in Figure 57 of appendix B.

The impedance of the ND '*Ann* + H_2-*I*' reaches (2700 ± 600) MΩ when RH is about 25%, decreasing to (1000 ± 200) MΩ at RH value around 90%, while the same quantity for the ND '*Ann* + *Ox* + H_2-*II*' drops from (200 ± 40) MΩ at the lowest RH level to (59 ± 13) MΩ at the highest. For the hydrogenated samples, the impedance variation is thus limited to a three-fold factor over the examined RH range. The one-order-of-magnitude difference in impedance between the ND '*Ann* + H_2-*I*' and the ND '*Ann* + *Ox* + H_2-*II*' highlights that the former sample is more insulating than the latter. The comparison of the ND '*Ann* + H_2-*I*' and ND '*Ann* + *Ox* + H_2-*II*' with the ND '*Ann*' and ND '*Ann* + *Ox*' underscores that the ND '*Ann* + H_2-*I*' are more conductive than the ND '*Ann*' below 60% RH and that the conductivity of the ND '*Ann* + *Ox* + H_2-*II*' is likewise enhanced with respect to the ND '*Ann* + *Ox*'. At RH levels of about 25% and 35%, impedance values are lower by two folds for the ND '*Ann* + H_2-*I*' compared to the ND '*Ann*' and by an order of magnitude for the ND '*Ann* + *Ox* + H_2-*II*' with respect to the ND '*Ann* + *Ox*'.

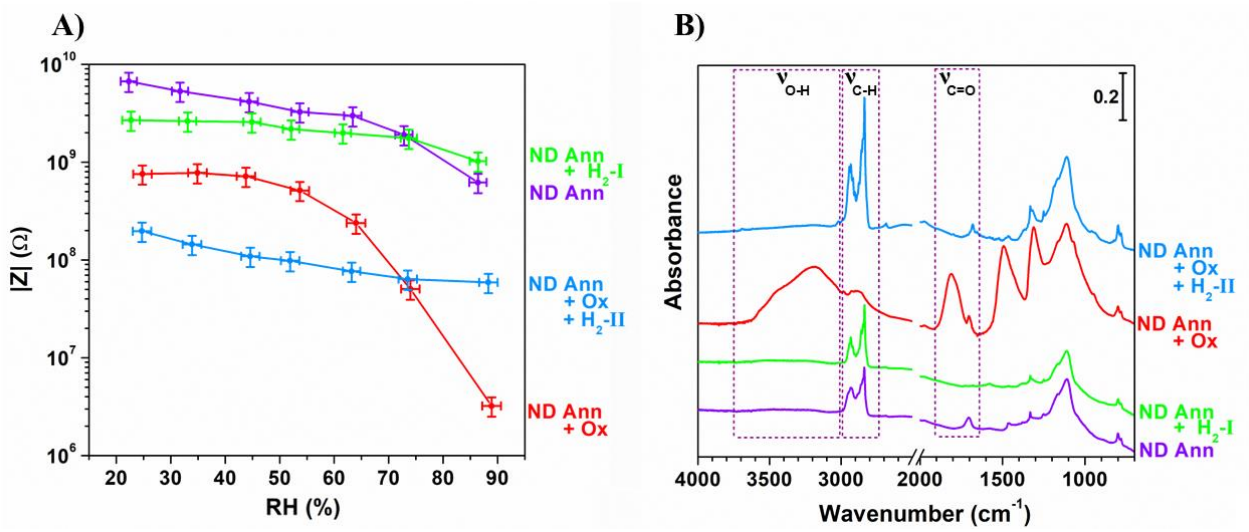

Figure 33- Electrical and spectroscopic characterization of the ND samples ([l]ND; 240 nm median diameter) labelled as ND '*Ann* + H_2-*I*' and ND '*Ann* + *Ox* + H_2-*II*'. The data concerning the ND '*Ann*' and ND '*Ann* + *Ox*' have been also reported for sake of comparison. A) Electrical impedance of the samples at different relative humidity (RH) conditions. B) Samples DRIFT spectra. The regions of O-H stretching (ν_{O-H}), C-H stretching (ν_{C-H}) and C=O stretching ($\nu_{C=O}$) are marked with dashed contours rectangles.

The high impedance values measured upon treating hydrogenated samples in vacuum and the weak dependence of impedance on RH seem to indicate a surface chemistry linked to a distinct conduction mechanism in these samples with respect to one governing the electrical properties of the previously analyzed ND. Assuming the effectiveness of the hydrogenation treatments, the surface of ND '*Ann*+ H_2-*I*' and ND '*Ann*+ *Ox* + H_2-*II*' should exhibit a hydrophobic character [171], arising from the removal of oxygenated moieties [209]. As a result, it could be inferred that hydrogenated ND adsorb water to a restricted extent, and therefore proton hopping has not an influence on their electrical conduction. The electrical behavior of ND '*Ann*+ H_2-*I*' and ND '*Ann*+ *Ox* + H_2-*II*' could be explained with the introduction of hydrogen terminations on the surface, assuming that electrical conduction is due to surface transfer doping mechanism [169] induced by a very limited amount of water adsorbed on the surface, sufficient to trigger the formation of sub-surface holes by electron transfer. On one hand, the larger conductivity of ND *'Ann* + *Ox* + H_2-*I'* with respect to ND *'Ann* + H_2-*I'* could be attributed to an improved efficiency of the hydrogenation process when conducted after the *'Ox'* treatment. On the other hand, the influence of hole conduction in hydrogenated samples could become noticeable only when reducing RH, as the relatively strong impact of Grotthuss mechanism on the impedance values of ND *'Ann'* and ND *'Ann* + *Ox'* makes these samples more conductive than hydrogenated ND at high RH levels.

Such interpretation is reinforced by the analysis of the ND *'Ann* + H_2-*I'* and ND *'Ann*+ *Ox* + H_2-*II'* DRIFT spectra, displayed in Figure 33B , where also the spectra of the ND *'Ann'* and ND *'Ann* + *Ox'*

are reported for sake of comparison. The DRIFT spectrum of the ND '*Ann* + *Ox* + *H₂-II*' shows a marked enhancement of the signals associated with C-H stretching compared to the spectrum of the ND '*Ann* + *Ox*'. Additionally, the partial suppression of the spectral features below 1500 cm^{-1} can be noted. A similar, though less pronounced, increase in C-H stretching bands is evident in the spectrum of the ND '*Ann* + *H₂-I*' relative to that of the ND '*Ann*'. The efficacy of the hydrogenation treatment can thus be validated by these experimental evidences, which show the effective formation of hydrogen terminations, thus supporting the potential impact of transfer-doping mechanism on electrical conductivity. The intensity of the C-H stretching bands is notably higher for ND '*Ann* + *Ox* + *H₂-II*' than for ND '*Ann* + *H₂-I*', demonstrating that the preceding '*Ox*' step increases the efficiency of the hydrogenation process. The reduced hydrophilicity of the hydrogenated ND is indicated by the absence of significant features in the 3650 cm^{-1} - 3000 cm^{-1} spectral range and the concurrent drastic reduction in the $\nu_{C=O}$ band intensity. '*H₂-I*' step hence maintains the hydrophobicity of ND '*Ann*', whereas the '*H₂-II*' process renders the ND '*Ann* + *Ox*' hydrophobic by eliminating oxygen-containing surface moieties.

The electrical properties of the ND '*HT-Ann*' display a totally different behavior from those of the samples shown in Figure 32A and Figure 33A, as they are completely unaffected by water. The electrical characterization results for ND '*HT-Ann*' are presented in Figure 34A, accompanied by the ones for the ND '*Ann*' for comparison. The data show that ND '*HT-Ann*' have constant impedance values independently of RH conditions. Notably, the same impedance values are observed even after the ND are kept in a vacuum environment, as illustrated in Figure 58A of appendix B. Additionally, it can be noted that the impedance of the ND '*HT-Ann*' depends on the treatment temperature. Specifically, the impedance of the ND '*HT-Ann-1000*', that is in the kΩ range, is lower than that of the ND '*HT-Ann-950*', being in the 10 MΩ range. In turn, this value is smaller than the impedance recorded for the ND '*HT-Ann-900*', which is similar to that of the ND '*Ann*', varying in the GΩ range.

The results of electrical characterization for the ND '*HT-Ann*' can be interpreted by inferring the effects of the '*HT-Ann*' treatments on particles surface structure. Even in a chemically inert atmosphere, structural modifications can occur in the ND at temperatures exceeding 900 °C [157]. Such changes can lead to the formation of surface graphite in the ND '*HT-Ann*', unlike what happens for the ND '*Ann*'. The monotonous decrease in impedance can thus be explained with surface graphitization becoming more pronounced with increasing temperatures, whereas the absence of a correlation between impedance and RH can be attributed to the lack of oxygen-containing groups on the surface. This is expected from annealing treatments and is indeed confirmed by the DRIFT spectra

of the ND '*HT-Ann*' (shown in Figure 58B of appendix B), revealing the absence of oxygenated moieties and any other identifiable surface functionality.

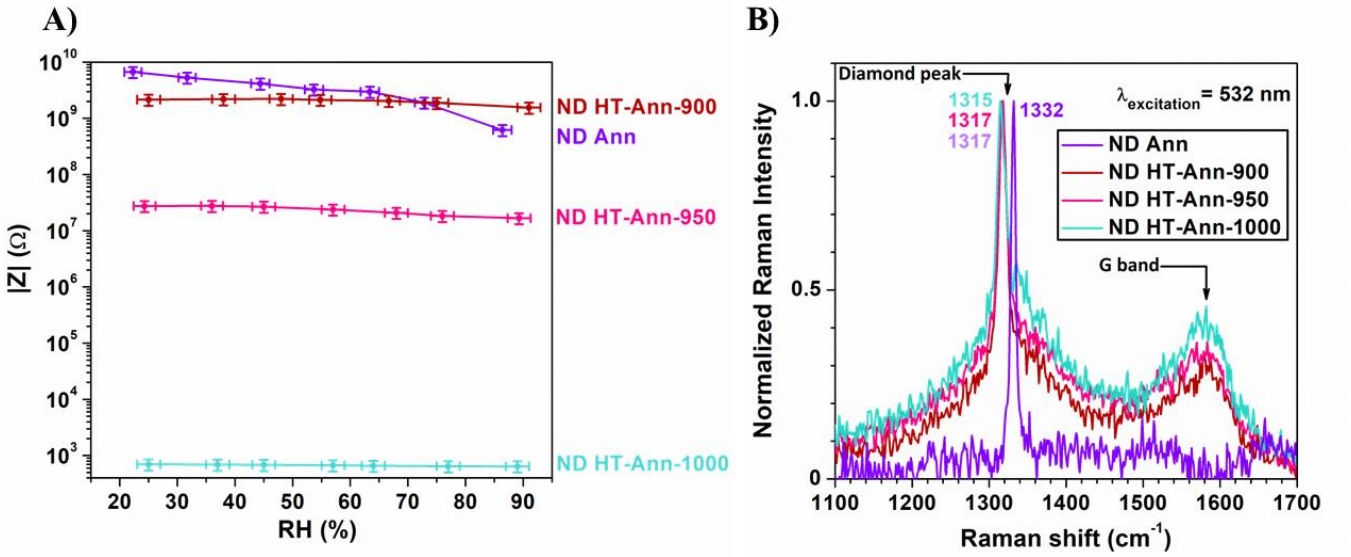

Figure 34- Electrical and spectroscopic characterization of the ND samples ([l]ND; 240 nm median diameter) labelled as ND '*HT-Ann-900*', ND '*HT-Ann-950*' and ND '*HT-Ann-1000*'. The data concerning the ND '*Ann*' have been also shown for comparison purposes. A) Electrical impedance of the samples at different relative humidity (RH) conditions. B) Samples Raman spectra. Diamond peak and graphite G-band are highlighted by black arrows. The value of diamond peak position is also reported.

Further insights on ND '*HT-Ann*' samples can be gained from the analysis of their Raman spectra, reported in Figure 34B, alongside the spectrum of the ND '*Ann*' for comparison purposes. The spectra are normalized to the intensity of the first-order Raman peak of diamond. In addition to the first-order diamond peak, the spectra of the ND '*HT-Ann*' feature the G-band at 1580 cm^{-1}, that is unequivocally ascribable to sp^2 carbon hybridization [58], confirming that the '*HT-Ann*' treatments lead to the formation of graphite on ND surface [157]. From the presence of the first-order diamond peak, also observed in the ND '*Ann*' spectrum, it can be however evidenced that the diamond phase in the nanoparticles core is not entirely lost following the '*HT-Ann*' process. The peak appears at 1317 cm^{-1} for the ND '*HT-Ann-900*' and ND '*HT-Ann-900*', while it is observed at 1315 cm^{-1} for the ND '*HT-Ann-1000*'. Compared to the peak position at 1332 cm^{-1} in both the ND '*Ann*' and bulk diamond [58], these values are downshifted. This downshift is ascribable to the heating of the surface graphitic layer caused by laser irradiation [119]. The normalization of the Raman spectra shown in Figure 34B reveals that the ratio between the diamond and graphitic phases decreases with increasing the '*HT-Ann*' treatments temperature. This observation reflects an increasingly pronounced graphitization process, consistently with the conclusions drawn from the electrical characterization results discussed earlier.

ND sample	$\|Z\|_{25}$ (MΩ)	$\|Z\|_{90}$ (MΩ)	Ratio between $\|Z\|_{25}$ and $\|Z\|_{90}$
Ann (800 °C)	6700 ± 1500	620 ± 140	11
Ann + Ox	760 ± 170	3.2 ± 0.7	238
Ann + Mild Ox	9000 ± 2000	27 ± 6	333
Ann + Ox + Ann	8300 ± 1900	760 ± 170	11
Ann + H_2-I	2700 ± 600	1000 ± 200	3
Ann + Ox + H_2-II	200 ± 40	59 ± 13	3
HT-Ann-900	2200 ± 500	1600 ± 300	1
HT-Ann-950	28 ± 6	17 ± 4	2
HT-Ann-1000	0.00070 ± 0.00016	0.00064 ± 0.00014	1

Figure 35-Impedance values measured from ND ([l]ND; 240 nm median diameter) at relative humidity ~ 25% (indicated as $|Z|_{25}$) and relative humidity ~ 90% (indicated as $|Z|_{90}$). The ratio between $|Z|_{25}$ and $|Z|_{90}$ is also reported.

In conclusion, the analysis of the electrical behavior of ND subjected to various thermal treatments revealed different particles surface chemistry and structure that drive distinct conduction mechanisms, often influenced by hydration conditions. The marked dependence of electrical properties on RH level, as well as the improved conductivity, especially at high RH conditions, observed in ND subjected to oxidation treatments, was proved to be connected to the presence of oxygen-containing functional groups introduced by such processes, significantly enhancing particles hydrophilicity and thus water adsorption. In contrast, the weak impedance dependence on RH exhibited by the ND treated with hydrogenation processes, suggesting surface transfer doping mechanism as electrical conduction pathway, was demonstrated to be linked to the formation of hydrogen terminations. Finally, the conduction behavior shown by the samples annealed at high temperature, independent of the impact of environmental water, was associated to sp^2 C formed by graphitization processes, becoming more relevant at higher temperatures.

These findings elucidate the complex interplay between surface terminations, structural features, and the electrical properties of ND, providing a detailed understanding of the mechanisms underpinning electrical conduction, along with the effects of different thermal treatments on ND surface features. They also guided the selection of an optimal treatment protocol for further experimental activities. Specifically, annealing at 800 °C emerged as an effective method for standardizing the ND surface while avoiding structural alterations caused by higher temperatures. On the other hand, the '*Ann + Ox*' sequence was proved to be more effective than the '*Ann + Mild Ox*' scheme in achieving surface oxidation. Finally, the '*Ann + Ox + H_2-II*' treatment was found to optimize hydrogenation efficiency, producing a higher density of hydrogen terminations compared to the '*Ann + H_2-I*' process. Based on these considerations, '*Ann*', '*Ann + Ox*' and '*Ann + Ox + H_2-II*' were designated

as standard treatments for samples processing and thus applied to modify the ND employed in the subsequent experimental activities.

3.1.2 Impact of particle size on electrical properties

A characterization analogous to the analysis presented in the previous sub-section concerning ^{l}ND (240 nm median diameter) was carried out on ^{s}ND and µD (with median diameters of 55 nm and 6 µm respectively) in order to assess if the behaviour of electrical properties in relationship to surface chemistry and structure is maintained with changing particles size and investigate whether the trend of electrical conductivity can be correlated with particle dimension. ^{s}ND and µD were processed according to the '*Ann* + *Ox*' and '*Ann* + *Ox* + H_2-*II*' treatments, as these emerged as the most effective ones for surface oxidation and hydrogenation respectively. The formation of oxygenated groups and hydrogen terminations on the surface of ^{s}ND and µDs through these processes was indeed confirmed *via* DRIFT spectroscopy, whose results are shown in Figure 59 of appendix C.

The impedance values measured for ^{s}ND and µD are displayed in Figure 36 and summarized in the table of Figure 37, accompanied by those collected from ^{l}ND, reported for sake of comparison. In complete analogy with the observations on ^{l}ND, the impedance of ^{s}ND and µD was too high to be measured by the setup in a vacuum, thus demonstrating that also in this case the presence of adsorbed water on the surface is a crucial requirement for electrical conduction.

The graph of Figure 36A displays the results of electrical measurements carried out on the ^{s}ND '*Ann* + *Ox*' and the µD '*Ann* + *Ox*'. Similarly to ^{l}ND '*Ann* + *Ox*', both the samples exhibit impedance values that strongly depend on RH and decrease with increasing RH level, thus suggesting that electrical conduction occur *via* the Grotthuss mechanism also in these particles. The |Z| value for ^{s}ND decreases from (64 ± 14) MΩ to (0.035 ± 0.008) MΩ from the lower to the upper boundary of the investigated RH interval, while for µD it drops from (10000 ± 2000) MΩ to (42 ± 9) MΩ under the same conditions. In both cases, the impedance increases by approximately three orders of magnitude transitioning from high to low humidity conditions. It is worth noting that the impedance values lower with decreasing particles median diameter. This trend can be easily linked with particle size, as it is ascribable to the larger surface-to-volume ratio of smaller diamond particles, which promotes greater water adsorption and, consequently, enhances conductivity through the action of Grotthuss mechanism.

The outcomes of the electrical characterization of the ^{s}ND '*Ann* + *Ox* + H_2-*II*' and µD '*Ann* + *Ox* + H_2-*II*' are shown in Figure 36B. The considerably weak impedance variation as a function of RH exhibited by the ^{l}ND is observed also for ^{s}ND and µD and can once again be attributed

to surface transfer-doping conduction. As RH increases, the |Z| value decreases from (5600 ± 1300) MΩ to (3800 ± 900) MΩ for ^{s}ND and from (200 ± 40) MΩ to (59 ± 13) MΩ for µD. In this case, the impedance change is hence limited to approximately a factor of 1 and 20, respectively. It is noteworthy that the increase in impedance as a function of particle size follows the somewhat unexpected non-monotonic trend ^{l}ND → µD → ^{s}ND, thus suggesting a more complex connection between electrical properties and particle size in these samples. This can be rationalized by assuming that electrical conduction is influenced by two distinct factors related to the surface doping mechanism, namely the formation and the movement of sub-surface holes. On one side, smaller diamond particles are expected to favor holes production due to their higher surface-to-volume ratio, which enhances water adsorption, thus promoting transfer doping by increasing electron transfer from the diamond phase to the water adsorbed on the surface. On the other side, it is important to account for the fact that the holes travel through the diamond material, as they are generated below the particles surface. Consequently, their movement should be favored within individual diamond particles (intraparticle) rather than between different particles (interparticle), and hence more efficient in larger particles as a result of the longer geometrical path available for charge carriers transport. A balance between these competing mechanisms can thus take place in ^{l}ND, resulting in their higher conductivity compared to ^{s}ND and µD.

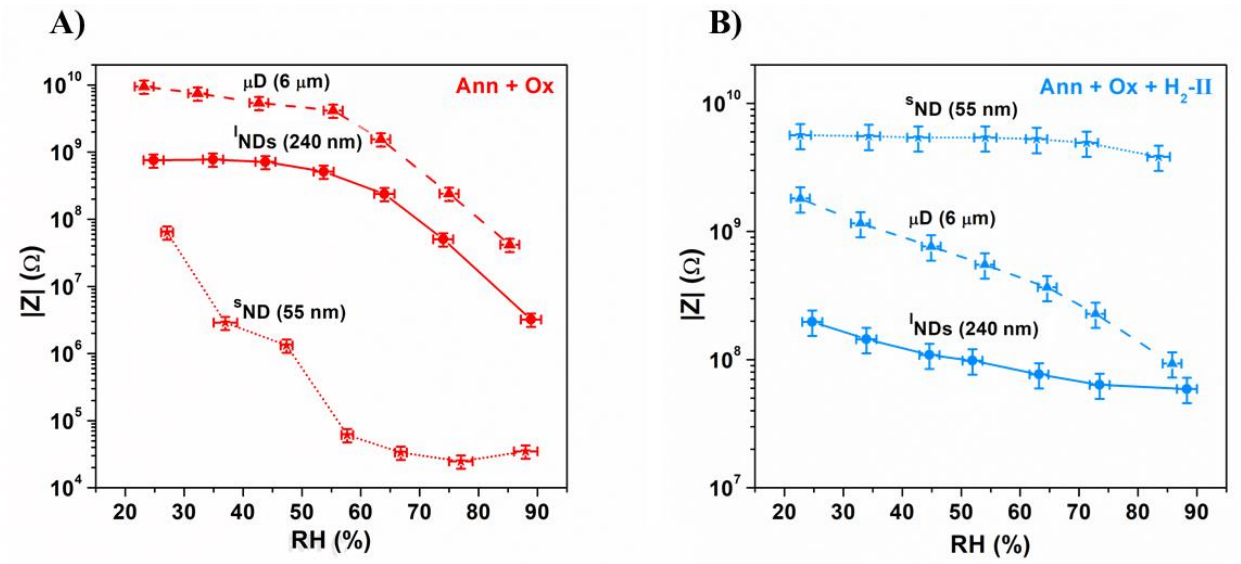

Figure 36-Electrical characterization of ^{s}ND (55 nm median diameter) and µD (6 µm median diameter) at different relative humidity (RH) conditions. The data from the ^{l}ND (240 nm median diameter) have been also shown for comparison purposes. A) Samples subjected to '*Ann + Ox.*' treatment. B) Samples subjected to '*Ann + Ox + H_2-II*' treatment.

Sample	$\|Z\|_{25}$ (MΩ)	$\|Z\|_{90}$ (MΩ)	Ratio between $\|Z\|_{25}$ and $\|Z\|_{90}$
^{s}ND *'Ann + Ox'*	64 ± 14	0.035 ± 0.008	1829
^{l}ND *'Ann + Ox'*	760 ± 170	3.2 ± 0.7	238
µD *'Ann + Ox'*	10000 ± 2000	42 ± 9	238
^{s}ND *'Ann + Ox + H_2-II'*	5600 ± 1300	3800 ± 900	1
^{l}ND *'Ann + Ox + H_2-II'*	200 ± 40	59 ± 13	3
µD *'Ann + Ox + H_2-II'*	1800 ± 400	90 ± 20	20

Figure 37-Impedance values measured for the ^{s}ND (55 nm median diameter) and µD (6 µm median diameter) at relative humidity ~ 25% (indicated as $|Z|_{25}$) and relative humidity ~ 90% (indicated as $|Z|_{90}$). The ratio between $|Z|_{25}$ and $|Z|_{90}$ is also displayed. The data from ^{l}ND (240 nm median diameter) are shown for comparison purposes.

3.1.3 Hydrodynamic behavior in aqueous solution

The colloidal stability and aggregation tendency in aqueous solution of the ND subjected to '*Ann*', '*Ann + Ox*' and '*Ann + Ox + H_2-II*' processes (the treatments written in blue in the scheme of Figure 31), *i.e.*, ND_{Ann}, ND_{Ox} and ND_H, were evaluated by means of DLS and ZP analyses. These were conducted by dispersing ND in a 0.5 mM NaCl water solution at a particle concentration of 50 µg ml^{-1}, employing bath sonication for 15 minutes.

The results of hydrodynamic measurements collected immediately after sonication are shown in Figure 38. Figure 38A displays the size distributions by number of the different samples, accompanied by a table in the inset showing particles polydispersity index (PDI). For the ND_{Ox}, the size distribution shows that hydrodynamic size values are similar to the dimension of the ND in their dry state. This, combined with their small PDI, *i.e.*, (0.100 ± 0.015), indicates effective particle dispersion. Such behaviour can be attributed to the remarkable hydrophilicity of ND_{Ox} surface, arising from the presence of oxygen-containing functionalities [123,172], as evidenced by the DRIFT spectroscopy results illustrated in sub-section 3.1.1. Surface hydrophilic nature renders the ND inclined to disperse easily, preventing them from agglomeration. On the other hand, the hydrodynamic size values of the ND_{Ann} and ND_H exceed the dimension of the primary particles and their PDI are much higher compared to that of ND_{Ox}, being respectively (0.50 ± 0.04) and (0.58 ± 0.07). Such observations reveal the occurrence of particles aggregation phenomena and poor dispersibility. These can be explained by the low affinity of ND_{Ann} and ND_H for water, associated with C-H species and the absence of oxygenated groups on the surface [123,172], as observable in their DRIFT spectra (sub-section 3.1.1), making the ND prone to agglomerate. Aggregation tendency appears to be more pronounced for ND_H than for ND_{Ann}, likely due to the higher abundance of surface C-H moieties in the former compared to the latter.

Figure 38B presents a plot of ND ZP as a function of the peak value of the DLS size distributions by number. The graph clearly evidences that a high absolute value of ZP is correlated with better particles dispersibility. A larger |ZP| is indeed associated with greater surface charge, which causes repulsion between particles, thus avoiding their aggregation and ensuring suspension stability [197]. It can be noted that all the ND samples feature a negative ZP, but the ND_{Ox} exhibit higher ZP absolute value, *i.e.*, (32.6 ± 0.5) mV, with respect to the ND_{Ann} and ND_{H} , that respectively display |ZP| values of (19.67 ± 0.15) mV and (20.3 ± 0.2) mV. The high |ZP| measured for the ND_{Ox} can once more be linked to surface oxygenated groups, imparting a strong negative charge to the surface, leading to effective particle suspensibility [123,210]. In contrast, the values measured for the ND_{Ann} and ND_{H} are below the threshold of hydrodynamic stability, *i.e.*, |ZP| = 30 mV [197], underscoring their instability in suspension. Such instability is also visually evident in the dispersions, which change from a turbid to an almost transparent appearance within a few minutes after sonication because of particle aggregation. Notably, the pronounced tendency of ND_{Ann} and ND_{H} to agglomerate poses significant challenges in performing new hydrodynamic measurements, resulting in heterogeneous data over time, probably due to the formation of increasingly larger aggregates. This aspect of the hydrodynamic behavior of ND_{Ann} and ND_{H} will be more deeply examined in the following, by systematically monitoring ND suspensions over a period of up to one month, as illustrated in sub-section 3.2.2.

To sum up, the hydrodynamic characterization of the ND samples highlighted that ND_{Ann} and ND_{H} are inclined to aggregate in aqueous environment, unlike ND_{Ox}, whose oxygenated surface moieties promote their stability in suspension. These observations evidenced the necessity of increasing the dispersibility of ND_{Ann} and, particularly, ND_{H} to ensure their applicability in aqueous environment for subsequent experimental work.

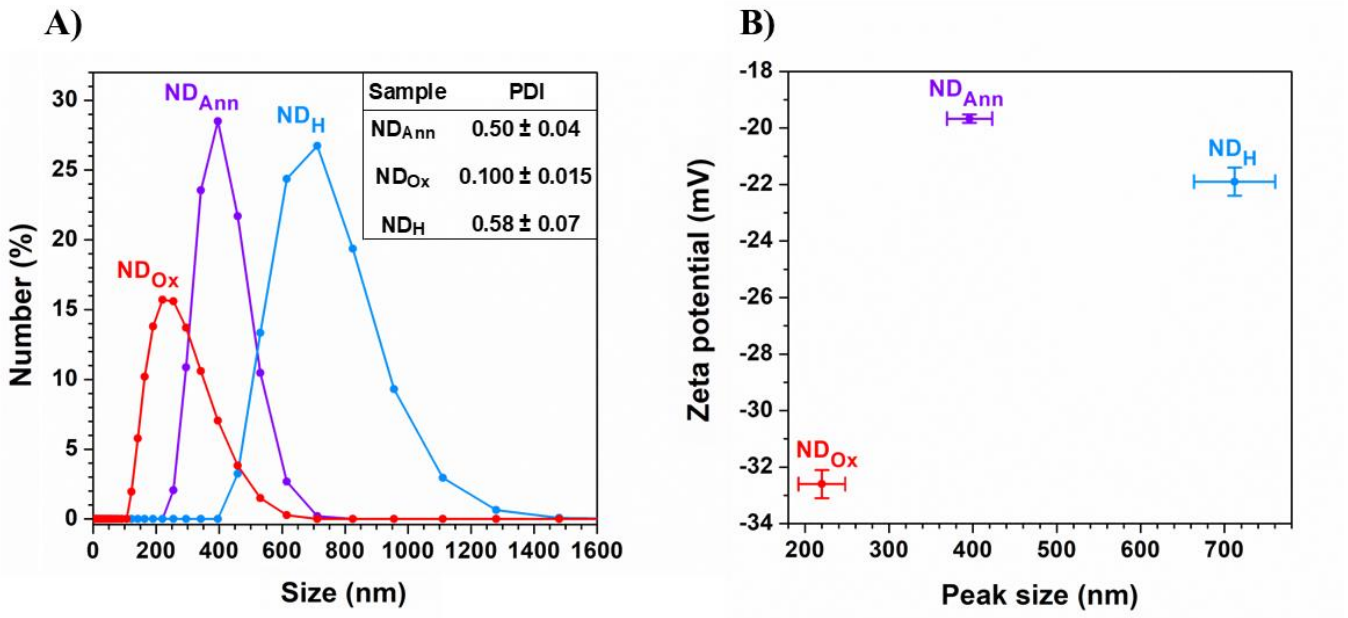

Figure 38-Results of DLS and ZP analyses from ND_{Ann}, ND_{Ox} and ND_H (^{l}ND; 240 nm median diameter in the dry state). Measurements were performed in a 0.5 mM NaCl aqueous solution with a particle concentration of 50 µg ml^{-1} upon bath sonication for 15 min. A) DLS size distribution by number and values of samples polydispersity index (PDI). B) ZP as function of the peak size of the DLS distributions by number.

3.2 Development of hyaluronic acid (HA)-functionalized ND

This section presents the results regarding the characterization and the cellular testing of ^{s}ND (55 nm median diameter) functionalized with hyaluronic acid (HA), which were conducted in close collaboration with the research groups led by Prof. Silvia Mariangela Arpicco at the Drug Science and Technology Department of the University of Torino and that lead by Prof. Chiara Riganti at the Oncology Department of the same university. HA was attached to the surface of ND featuring different surface chemistry, *i.e.*, ND_{Ann}, ND_{Ox} and ND_H, whose functionalized equivalents were respectively labelled as "HA-ND_{Ann}", "HA-ND_{Ox}" and "HA-ND_H", by employing a non-covalent approach based on the use of a conjugate of HA and 1,2-dimyristoyl-sn-glycero-3-phosphoethanolamine (DMPE) phospholipid. Surface decoration with HA was carried out with dual purpose. On one hand, it aimed to prevent ND aggregation in aqueous environment, improving their stability in suspension. Indeed, as examined in the sub-section 3.1.3, agglomeration problems can affect ND particles, particularly if the surface is hydrophobic. On the other hand, functionalization intended to confer ND active targeting capabilities, particularly towards cancer cells overexpressing the HA cluster determinant 44 (CD44) receptor. The specificity imparted to ND by HA was sought both because it enables visualization of CD44-overexpressing cancer cells through the intrinsic photoluminescent properties of ND due to the NV centres and also because it can be exploited for targeted radiosensitization of these cells.

Sub-section 3.2.1 briefly describes the synthesis of the HA/DMPE conjugate and the procedure used for ND functionalization. Sub-section 3.2.2 instead illustrates the data from DRIFT spectroscopy, Raman spectroscopy, photoluminescence spectroscopy, Scanning Electron Microscopy (SEM), DLS measurements and ZP analyses in aqueous media, carried out on the ND samples both before and after derivatization. Such comprehensive characterization, aimed at assessing particles surface chemistry, structure, optical properties, size and morphology, as well as hydrodynamic behavior, was conducted to gain insight into the effectiveness of the adopted functionalization approach and assess possible alteration to the ND original properties due to HA attachment. Finally, sub-section 3.2.3 displays the results obtained from tests of the ND on different human adenocarcinoma cell lines. These include viability assays to evaluate particle biocompatibility, as well as uptake measurements and confocal microscopy images to assess cellular internalization *via* CD44 receptors and investigate intracellular particle localization.

3.2.1 ND functionalization with a HA-phospholipid conjugate

The ND were functionalized with HA *via* a non-covalent functionalization method by employing a 200 kDa conjugate of hyaluronic acid and DMPE phospholipid, indicated in the following as "HA/DMPE". This novel and simple derivatization strategy was developed by Prof. Arpicco's group, who also carried out the synthesis of the HA/DMPE. In brief, they synthesized the conjugate by linking the phospholipid to HA *via* amidic bonds in the presence of a soluble carbodiimide derivative, thus obtaining a product where the phospholipid amino group is randomly linked to the carboxylic residues of HA. For the functionalization, ND were dispersed in MilliQ® water at a concentration of 0.5 mg ml^{-1} and bath sonicated for 90 min, keeping the temperature below 25 °C. Afterwards, the amount of HA/DMPE to give a 1:5 HA/DMPE:ND weight ratio was added to the ND suspensions, that were bath sonicated once more for 90 min at a temperature below 25 °C. Eventually, the suspensions were centrifuged at 11000 rpm for 5 min to remove the possible excess of HA/DMPE and a carbazole assay was performed, confirming that all the HA/DMPE was bound to the ND surface.

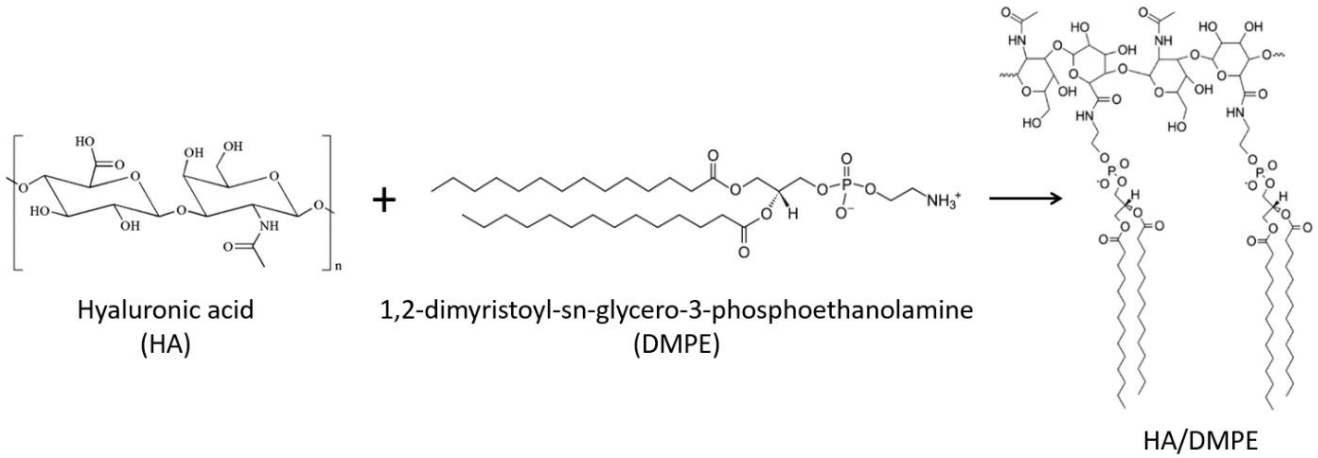

Figure 39-Structure of the HA/DMPE conjugate employed for ND (^{s}ND; 55 nm median diameter) functionalization, synthesized by the researchers of the group led by Prof. Silvia Mariangela Arpicco at the Drug Science and Technology Department of the University of Torino.

3.2.2 Characterization of HA-functionalized ND

The ND were first characterized through DRIFT spectroscopy to evaluate their surface chemistry, assessing both the effectiveness of the thermal processes in modifying particles surface and the success of the non-covalent functionalization with the HA-based conjugate. Samples DRIFT spectra are reported in Figure 40A. It can be noted that the spectra of the non-functionalized particles display several analogies with those examined in sub-section 3.1.1. The DRIFT spectrum of ND_{Ann} shows indeed distinctive features in the 3000 cm^{-1} - 2800 cm^{-1} spectral range, corresponding to the asymmetric and symmetric stretching of C-H bonds (ν_{C-H}) [123,124,205], no signals between 3700 cm^{-1} and 3000 cm^{-1} associated with O-H stretching (ν_{O-H}) in surface adsorbed water and oxygen-containing groups [211], and only a weak band at 1705 cm^{-1} in the C=O stretching region ($\nu_{C=O}$) [206]. These observations confirm the effectiveness of the annealing process in introducing C-H moieties on the particle surface, along with the hydrophobic behavior of the ND_{Ann}. On the other hand, the spectrum of ND_{Ox} exhibits a broad ν_{O-H} band, accompanied by a prominent and complex signal at 1800 cm^{-1}, which is ascribed to C=O stretching in various surface functionalities (such as carboxylic acids, acid anhydrides, esters, and lactones) [206,207], and several bands in the spectral range between 1500 cm^{-1} and 1300 cm^{-1}, corresponding to vibrations of epoxides and ketones [206,207], together with a shoulder at 1630 cm^{-1}, attributed to the water bending mode [123,205]. Similarly to the ND_{Ann}, both the signal at 1705 cm^{-1} and C-H stretching vibrations can be detected for ND_{Ox}, but their intensities are respectively higher and lower than in the previous case. Such observations underscore the success of the oxidation treatment in the formation of oxygen-containing surface moieties, imparting high hydrophilicity to the ND_{Ox}. Finally, the DRIFT spectrum of ND_{H} closely resembles that of ND_{Ann}, revealing the absence of the ν_{O-H} band and that of the main signals

associated with oxygenated functionalities, namely the band at 1800 cm^{-1} and the features between 1500 cm^{-1} and 1300 cm^{-1}. However, C-H stretching bands intensity is enhanced in ND_H compared to ND_{Ann}. These spectral features collectively demonstrate the efficacy of the hydrogenation treatment in establishing C-H bonds on the ND_H surface, thereby imparting the expected hydrophobic nature to the particles.

Before examination of HA-ND_{Ann}, HA-ND_{Ox} and HA-ND_H, HA alone was analyzed with the goal of determining distinctive markers to confirm its presence on the surface of the functionalized samples. The spectrum of HA exhibits a broad band centred at 3390 cm^{-1}, along with a faint shoulder around 3100 cm^{-1} and signals in the 3000 cm^{-1} - 2800 cm^{-1} spectral region. Such bands are respectively associated to hydrogen-bonded OH groups, N-H vibrations and C-H stretching [212]. The multiple complex bands emerging in the spectral range between 1750 cm^{-1} and 1500 cm^{-1} are instead attributed to amide I and II and to the vibrations of various carbonyl and carboxyl groups, whereas the broad signal spanning from 1200 cm^{-1} to 1000 cm^{-1} gathers C-O stretching vibrations in alcohols and antisymmetric C-O-C stretching in glycosidic groups [213].

The comparison between the DRIFT spectra of the derivatized ND and those of their non-hyaluronated equivalents highlights relevant changes in the shape of the characteristic bands of the latter after functionalization. By comparing the spectra of HA-ND_{Ann} with ND_{Ann}, a modification in the C-H stretching signals can be observed, with a similar alteration detectable in the spectrum of HA-ND_H when compared to ND_H. On the other hand, when observing the spectrum of HA-ND_{Ox} with respect to the one of ND_{Ox}, changes can be noticed in the O-H and C=O stretching bands. Moreover, the presence of additional bands becomes evident in the spectra of the functionalized ND when viewed alongside those of the ND prior to derivatization. These additional features correspond to the distinctive bands identified for HA and are consistent across the spectra of HA-ND_{Ann}, HA-ND_{Ox} and HA-ND_H. Remarkably, in the spectra of HA-ND_{Ann} and HA-ND_H it is possible to see the presence of ν_{O-H} signal, that is absent in the spectra of both ND_{Ann} and ND_H. Additionally, the intensity of the bands related to C-H stretching is enhanced in the spectrum of HA-ND_{Ox} compared to that of ND_{Ox}. The observed alterations in the DRIFT spectra following ND surface decoration with HA suggest successful modification of the particles. This conclusion is further supported by the analysis of DRIFT spectra collected at reduced HA/DMPE:ND ratios (1:10 and 1:15), shown in Figure 60 of appendix D. These reveal a decrease in the intensity of the bands associated with HA in the ND samples functionalized with lower amounts of the conjugate, thus confirming the correlation between the previously commented DRIFT features and the anchoring of HA to the ND surface.

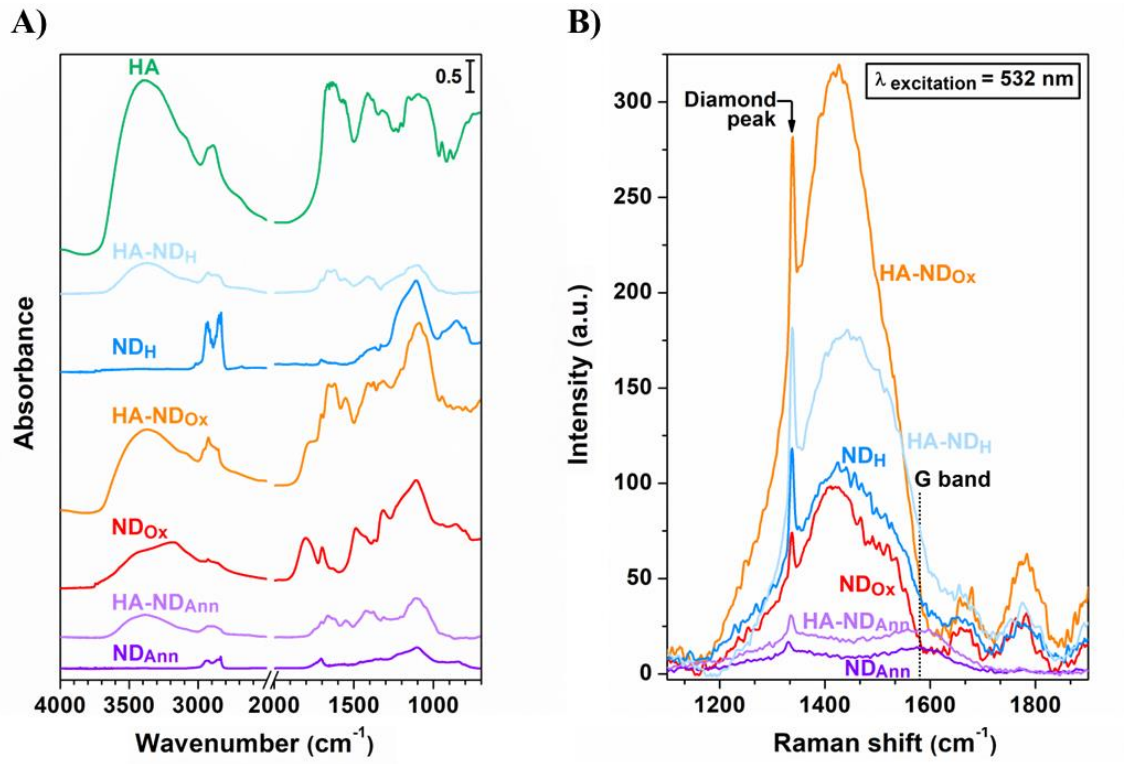

Figure 40-DRIFT and Raman spectra of ND_{Ann}, ND_{Ox} and ND_H samples (^{s}ND; 55 nm median diameter), along with those of their functionalized counterparts, HA-ND_{Ann}, HA-ND_{Ox} and HA-ND_H. A) DRIFT spectra. Also the spectrum of HA alone is reported. B) Raman spectra (obtained after baseline subtraction).

To analyze the structure of the ND samples, detecting any potential structural alterations induced to the particles by the functionalization, Raman spectroscopy was carried out. The corresponding results are shown in Figure 40B. ND Raman spectra all feature the first-order Raman peak of diamond, whereas the G-band appears only in the spectra of ND_{Ann} and HA-ND_{Ann} as a weak signal at 1580 cm^{-1} [58]. These observations suggest the formation of some graphite upon the annealing treatment, followed by its removal through subsequent oxidation and hydrogenation treatments [164], coherently with the findings reported in [168] for this kind of ND. The Raman spectra of ND_{Ox} and HA-ND_{Ox}, as well as those of ND_H and HA-ND_H, show a signal at 1405 cm^{-1}, accompanied by a broad shoulder and additional features above 1600 cm^{-1}. These signals are not due to Raman scattering, being instead related to the photoluminescence of NV centres [58], as will be further discussed in the following (in connection with Figure 42). In more detail, the feature at 1405 cm^{-1}, corresponding to a wavelength value of 575 nm, is attributed to the zero-phonon line of NV^0 centers, whereas the other peaks are associated with phonon replicas arising from the interaction between phonon states and electronic transitions [58]. Notably, the spectral features characterizing ND_{Ann}, ND_{Ox} and ND_H are conserved in the Raman spectra of their functionalized counterparts, namely HA-ND_{Ann}, HA-ND_{Ox} and HA-ND_H. This indicates that the attachment to the surface of HA does not

cause alterations to the structure of the ND, preserving both diamond and graphite content of the original particles.

With the aim of investigating the median size of the ND in their dry state and evaluating particle morphology, SEM analysis was performed. Samples size distributions derived from SEM micrographs are displayed in Figure 41A, Figure 41B and Figure 41C for the non-functionalized ND and in Figure 41D, Figure 41E and Figure 41F for the hyaluronated ones. The median size diameters (D_{med}) of the ND_{Ann}, ND_{Ox}, and ND_{H} align consistently with each other, being respectively 53 nm, 55 nm and 53 nm, with corresponding standard deviations (σ) of 10 nm, 10 nm and 9 nm. These values also mirror the dimensions indicated by the producer (D_{med} = 50 nm ± 10 nm), thus revealing that thermal treatments do not relevantly impact on particle size. For the functionalized ND, the median size diameters are 54 nm for HA-ND_{Ann}, 55 nm for HA-ND_{Ox}, and 52 nm for HA-ND_{H}, with corresponding standard deviations of 10 nm, 10 nm, and 8 nm, respectively, which closely match those of their non-hyaluronated counterparts. Additionally, as shown in Figure 41, which also includes details from SEM images of the ND, the functionalized particles exhibit the same irregular and jagged geometry observed in the non-functionalized ND. The results from both particles size distribution and shape analysis hence indicate that the derivatization does not discernibly affect the geometry nor the size of the ND in their dry state.

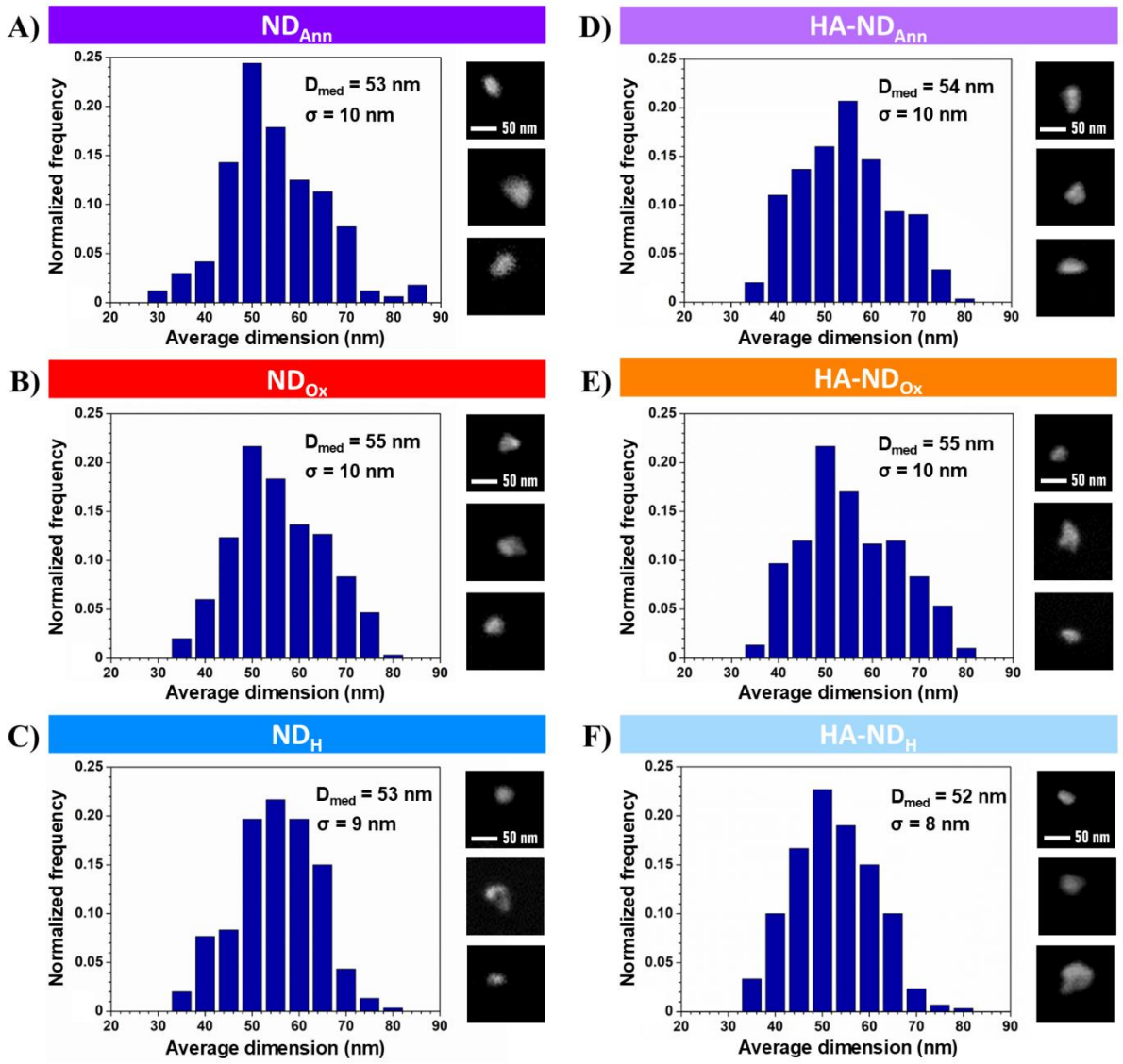

Figure 41- Size distributions of the ND obtained from SEM images. Particle size histograms were constructed based on 3-4 micrographs, considering 300 ND, except for ND_{Ann}, where the distribution was obtained from 168 particles. Details from SEM micrographs displaying ND particles are also presented. A) ND_{Ann}, B) ND_{Ox}, C) ND_{H}, D) HA-ND_{Ann}, E) HA–ND_{Ox}, and F) HA–ND_{H}.

Subsequently, ND samples were investigated through photoluminescence (PL) spectroscopy to assess their PL properties, being these crucial for particles visualization in cells. PL spectrum was collected not only for the ND, but also for the sole conjugate to evaluate its potential contributions in reducing particles intrinsic fluorescence *via* any quenching effect. The recorded PL spectra are reported in Figure 42, where the wavelength interval enclosed by the black-contoured rectangle corresponds to the region displayed in Figure 40B in Raman shift values. In addition to signals arising from PL effects, such spectral range is indeed also characterized by features due to Raman scattering, as discussed above. The PL spectra of all the ND exhibit a broad band ranging from 600 nm to 780 nm, which is attributed to the overlap of the phonon sidebands of NV^0 and NV^- centers, spanning the

600 nm - 750 nm and 650 nm - 750 nm wavelength ranges, respectively [77]. In the spectra of ND_{Ox}, HA-ND_{Ox}, ND_H, and HA-ND_H, signals corresponding to the zero-phonon lines of both NV center types are also observable. Specifically, the feature appearing at 638 nm is linked to NV^- centers, while the one at 575 nm, falling within the contoured region and corresponding to 1405 cm^{-1} on the Raman shift scale, is attributed to NV^0 centers [77], as already previously discussed. A thorough analysis of the PL spectra of the non-functionalized ND reveals that the fluorescence of ND_H is higher than that of ND_{Ox}, with the latter in turn exhibiting enhanced fluorescence compared to ND_{Ann}. This pattern can likely be attributed to the removal of graphitic phases *via* oxidation and combined oxidation + hydrogenation treatments, as suggested by Raman spectroscopy data. Graphitic phases are indeed known to have a quenching effect on the NV centers PL, so their reduction should result in an enhancement of particles fluorescence [166]. Interestingly, for the HA-ND_{Ann}, HA-ND_{Ox}, and HA-ND_H the PL remains comparable to, or in some cases exceeds, that of their unmodified counterparts. The impact of the HA-based conjugate on the optical properties can be hence considered negligible, as demonstrated by its PL spectrum, showing no new detectable PL bands or peaks. The crucial conclusion that can be thus drawn from samples PL spectra is that the fluorescence properties of the ND are preserved upon functionalization, thereby maintaining the particles potential for cellular visualization.

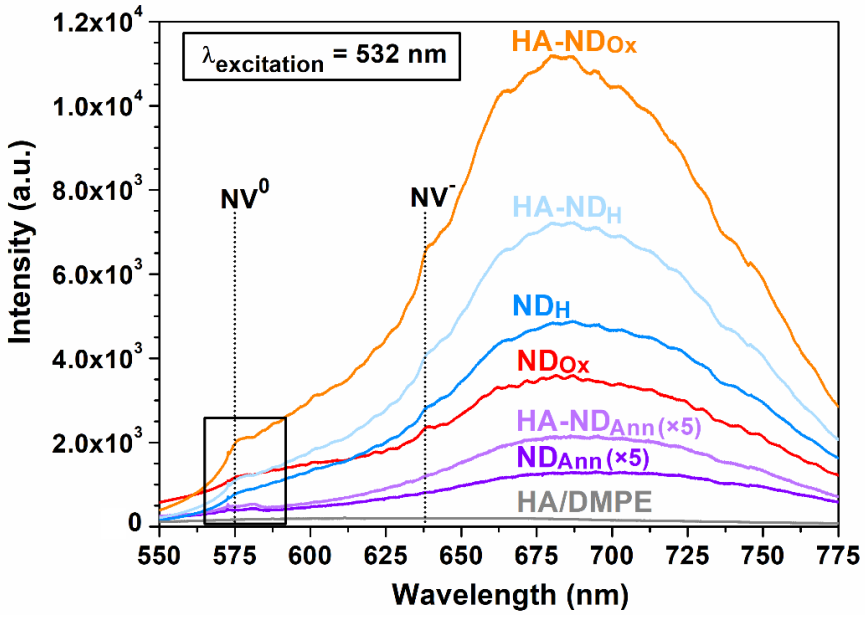

Figure 42-Photoluminescence spectra of ND_{Ann}, ND_{Ox}, ND_H (^{s}ND; 55 nm median diameter) and their functionalized equivalents HA-ND_{Ann}, HA-ND_{Ox} and HA-ND_H, along with that of the HA/DMPE conjugate. For ND_{Ann} and HA-ND_{Ann} the PL spectra are multiplied by a factor of five for better visualization. The black rectangle highlights the region shown in Figure 40B.

Eventually, to assess the stability and the behavior of the particles in an aqueous medium, DLS and ZP measurements were performed on ND dispersed at a particle concentration of 50 µg ml^{-1}. These analyses were conducted immediately after a 3 h-sonication process. The obtained results are shown in Figure 43, reporting a plot of the ZP value for each sample against the median hydrodynamic diameter obtained from DLS size distribution by number, along with a table showing samples polydispersity index (PDI) values. Focusing on non-functionalized ND, it can be noted that in ND_{Ann} and ND_{Ox} aggregation phenomena seems to be practically absent directly after prolonged sonication. This can be inferred by their median hydrodynamic diameters, both measuring (59 ± 4) nm, closely matching the particles dry-state size derived *via* SEM microscopy, as well as by their small PDI values, *i.e.*, (0.18 ± 0.02) for ND_{Ann} and (0.122 ± 0.012) for ND_{Ox}. In contrast, ND_H appear to show a slight tendency to clustering, as indicated by their greater median diameter of (80 ± 12) nm and their PDI of (0.21 ± 0.02). Nevertheless, it should be noted that in this case the hydrodynamic size exceeds the corresponding dry median diameter only by a factor of about 1.5, thus indicating that aggregation is limited to only a few ND. Overall, these results hence suggest that, unlike the 15-minute sonication used for preparing the dispersions examined in sub-section 3.1.3, the 3 h-sonication effectively disperses non-functionalized ND, minimizing aggregation even for the particles which are more prone to agglomerate, *i.e.*, ND_{Ann} and ND_H.

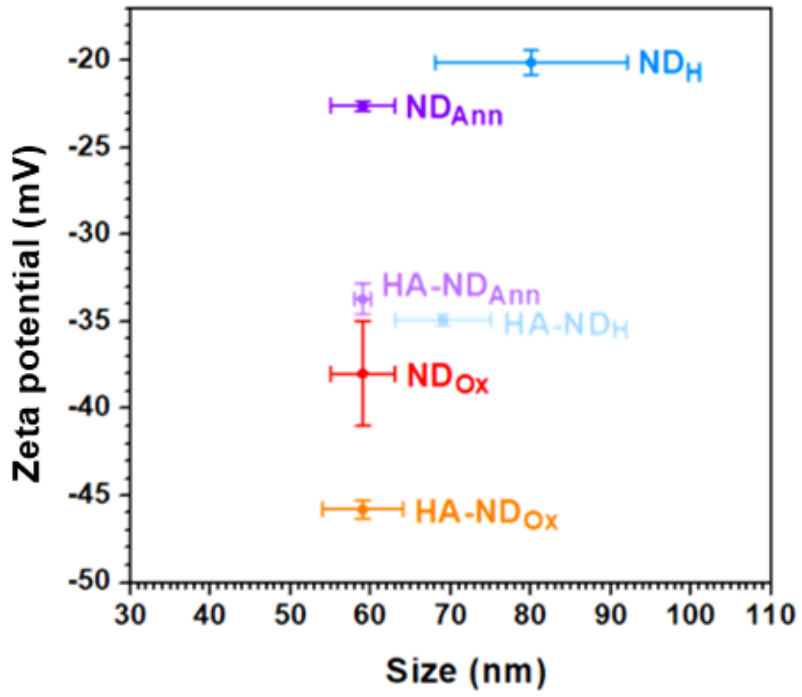

Sample	PDI
ND_{Ann}	0.18 ± 0.02
ND_{ox}	0.122 ± 0.012
ND_H	0.21 ± 0.02
HA-ND_{Ann}	0.166 ± 0.017
HA-ND_{ox}	0.153 ± 0.015
HA-ND_H	0.119 ± 0.012

Figure 43-Hydrodynamic characterization results for ND_{Ann}, ND_{Ox}, ND_H, HA-ND_{Ann}, HA-ND_{Ox}, and HA-ND_H (^{s}ND, 55 nm median diameter in their dry state), illustrated as ZP values plotted against the median hydrodynamic diameters derived from DLS measurements, along with a table reporting samples PDI values. The analyses were conducted in water solution at a particle concentration of 50 µg ml^{-1} after 3 hours of sonication of ND suspensions.

In alignment with the data presented in sub-section 3.1.3, the ZP values of ND_{Ann}, ND_{Ox}, and ND_{H} are all negative. ND_{Ox} again display the most negative ZP, with value of (-38 ± 3) mV, reflecting the strong negative surface charge imparted by surface oxygenated moieties, and suggesting good particles stability in suspension [123,210]. On the other hand, ND_{Ann} and ND_{H} exhibit ZP values of (-22.6 ± 0.3) mV and (-20.1 ± 0.7) mV respectively, both falling outside the range of hydrodynamic stability [197], thus pointing to poor long-term suspensibility of the particles. Indeed, similarly to what observed in sub-section 3.1.3, ND_{Ann} and ND_{H} start agglomerating shortly after sonication. This aggregation led once more to experimental challenges in performing further hydrodynamic measurements. Due to high clustering, which probably causes particles precipitation, thus lowering the effective concentration of ND in suspension, DLS and ZP data collected more than a few minutes after sonication lack reproducibility or are completely inconsistent. The severe aggregation tendency displayed by ND_{Ann} and ND_{H} was increasingly pronounced within a few hours after sonication and became markedly evident when monitoring the appearance of the suspensions at room temperature over a period of several days. Figure 44A and Figure 44B show the pictures of the ND_{Ann} suspension shortly after the treatment with ultrasounds and after a week, respectively. In the former case the particles appear as well dispersed, whereas in the latter case they have completely precipitated, as noticeable by the transparency of the solution. An analogous behaviour was observed for the ND_{H}, precipitating completely over a similarly long period. In contrast, consistently with their more negative ZP, ND_{Ox} remained in a dispersed state over more days, showing a relevant visible precipitation only after one month, as observable from Figure 44C and Figure 44D.

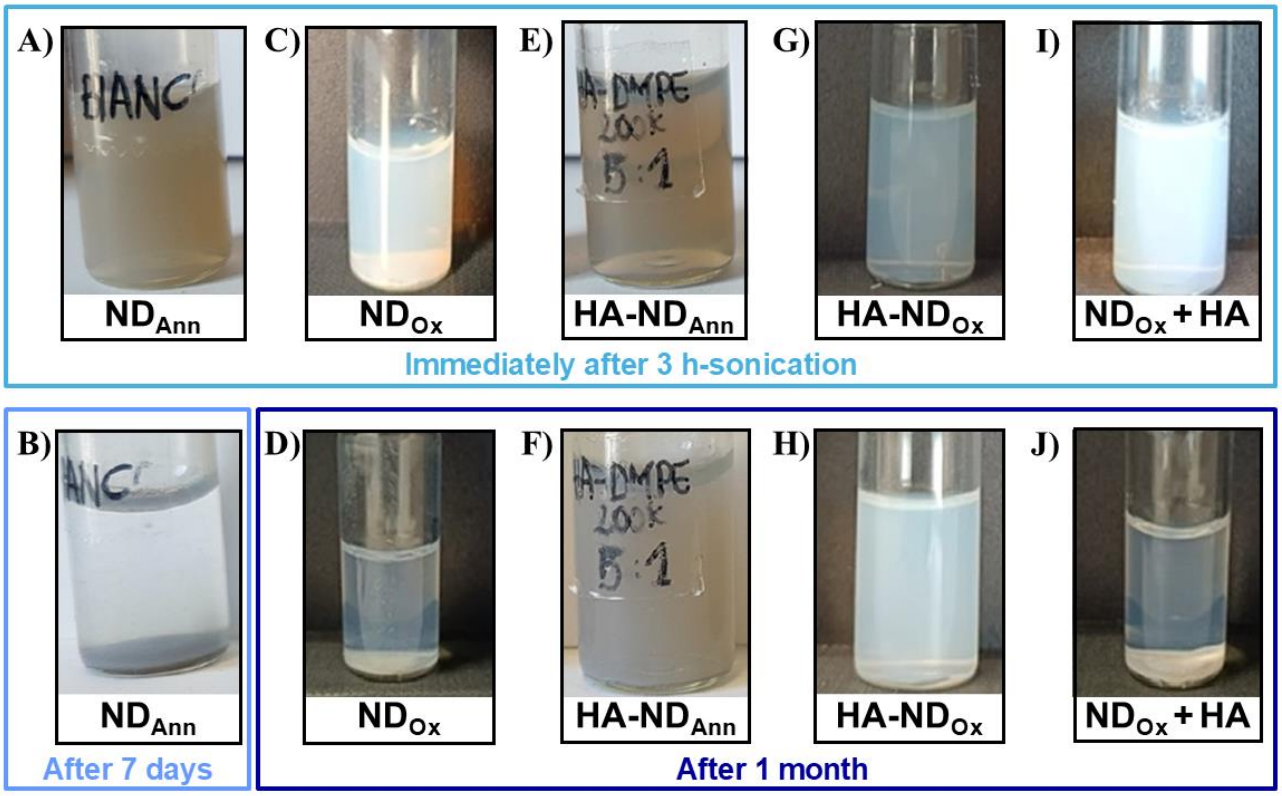

Figure 44- Representative photographs of ND (^{s}ND, 55 nm median diameter in their dry state) dispersions immediately after the 3 h sonication treatment and after a period of several days. A) ND_{Ann} after sonication; B) ND_{Ann} after 7 days; C) ND_{Ox} after sonication; D) ND_{Ox} after one month; E) HA-ND_{Ann} after sonication; F) HA-ND_{Ann} after one month; G) HA-ND_{Ox} after sonication; H) HA-ND_{Ox} after one month; I) ND_{Ox} with unconjugated 200 kDa HA after sonication; J) ND_{Ox} with unconjugated 200 kDa HA after one month.

Upon modification with HA/DMPE, ND hydrodynamic median diameter remains essentially unchanged: as observable from Figure 43, the values collected for HA-ND_{Ann}, HA-ND_{Ox} and HA-ND_{H} are indeed close to those of their non-functionalized counterparts, being respectively (59 ± 1) nm (59 ± 5) nm and (69 ± 6) nm. Also PDI values do not generally modify to a relevant extent, being (0.166 ± 0.02) for HA-ND_{Ann} and (0.153 ± 0.015) for ND_{Ox}, with a reduction with respect to their non-functionalized counterpart observable only for HA-ND_{Ann}, having PDI of (0.119 ± 0.012). On the other hand, all the functionalized ND feature relevant changes in ZP values. While ZP remains negative, it considerably increases in absolute value, with |ZP| for HA-ND_{Ann}, HA-ND_{Ox} and HA-ND_{H} respectively equal to (33.7 ± 0.3) mV, (45.8 ± 0.5) mV and (34.9 ± 0.3) mV. Such alterations in ZP can be explained based on the effect of the carboxylic groups present in HA structure, increasing the negative charge on the surface of the ND. This experimental evidence further supports the conclusion of a successful modification of the particles with the HA/DMPE conjugate. A noteworthy consideration is that the ZP values of the hyaluronated ND all lie in the hydrodynamic stability range, suggesting enhanced stability of the particles in suspension. This was verified through visual inspection of the suspensions over a one-month period. The appearance of the HA-ND_{Ann}

dispersion immediately after sonication and that of the same suspension after one month are respectively shown in Figure 44E and Figure 44F, whereas analogous pictures for HA-ND_{Ox} are displayed in Figure 44G and Figure 44H. It can be noted that the hyaluronated ND maintain a high dispersion degree and long-term stability in aqueous media thanks to the functionalization with HA (a similar behavior to that of HA-ND_{Ann} and HA-ND_{Ox} was observed for HA-ND_H). Importantly, hydrodynamic stability can be attributed to the HA being attached to the ND surface. In fact, the same behavior is not observed when the ND particles are dispersed with unconjugated HA. This is clearly visible in Figure 44I and Figure 44J, showing, as an example, ND_{Ox} in the presence of unconjugated 200 kDa HA immediately after sonication and after one month. Unlike HA-ND_{Ox}, where a high degree of dispersion is preserved, the presence of unconjugated HA results in particle aggregation, thus confirming that the key factor responsible for the excellent dispersibility and stability of the ND preparations is the functionalization with the HA/DMPE conjugate. In conclusion, ND hydrodynamic analysis demonstrates that the derivatization of ND with HA enhances particles stability in suspension and allows the ND to maintain a high dispersion degree for a long time, preventing particles clustering and precipitation, especially in the case of ND_{Ann} and ND_H.

Taken together, the data from ND characterization prove the successful anchoring of HA to the particle surface and show that the functionalization preserves the structural characteristics, size, and morphology of the ND. Furthermore, the results indicate that derivatization maintains the fluorescence properties of NV color centers, while imparting enhanced hydrodynamic stability to the ND in aqueous solution. On the strength of these encouraging findings, the ND were then tested on different cancer cell lines, as it will be illustrated in the following sub-section.

3.2.3 Test of HA-functionalized ND on cells

In collaboration with Prof. Chiara Riganti's research group of the Oncology Department of the University of Torino, the developed ND were tested on three different models of human adenocarcinoma cells, performing cell viability assays and uptake measurements, aimed respectively at evaluating particles cytotoxicity and internalization mediated by CD44 HA-receptors. Both analyses were conducted at different ND concentrations and at varying times after particle incubation into cells. Confocal microscopy was also carried out to investigate particles intracellular distribution and assess the suitability of the ND for labelling CD44-rich cells.

Cells representative of pancreatic, breast, and lung cancers were selected for the experiments, as these rank among the most prevalent and aggressive cancer types. For each kind of cancer, two distinct cell lines were considered: one with low levels of the CD44 receptor ($CD44^{low}$) and the other one with high CD44 expression ($CD44^{high}$), allowing for a more thorough comparison of the effects of the bare

and HA-functionalized ND. Specifically, the chosen cells were Capan-1 ($CD44^{low}$) and PANC-1 ($CD44^{high}$) human pancreatic adenocarcinoma cells, human breast cancer cells MCF-7 ($CD44^{low}$) and MDA-MB-231 ($CD44^{high}$), and human non-small lung cancer cells Calu-3 ($CD44^{low}$) and A549 ($CD44^{high}$). The cells were maintained in their respective media (DMEM for Capan-1, PANC-1, and MCF-7, RPMI 16140 for MDA-MB-231 and Calu-3, and HAM's F12 for A549) containing 1% v/v penicillin-streptomycin and 10% Fetal Bovine Serum. Prior to the analyses with ND, evaluation of the amount of surface CD44 receptor was carried out by flow cytometry as described in [214], using a Guava Millipore flow cytometer equipped with EasyCite software.

To conduct cell viability tests, 1×10^4 cells were seeded into a 96-well white plate and incubated for 24 h, 48 h and 72 h either with fresh medium or medium containing ND at 0.5 μg ml^{-1}, 5 μg ml^{-1}, 10 μg ml^{-1}, or 20 μg ml^{-1}. Cell viability was measured by assessing the cellular levels of Adenosine TriPhosphate (ATP), which represents a marker for metabolically active cells, as its concentration declines very rapidly under conditions of cell death or stress [215]. ATP concentration was evaluated through the ATPlite assay system, based on the emission of photons at 560 nm wavelength due to the chemiluminescent reaction of ATP with added luciferase enzyme and D-luciferin, which was monitored by using a Synergy HT microplate reader. The viability was expressed as a percentage, by normalizing the luminescence recorded for the ND-treated cells to that of the cells without the ND, which was considered as 100%.

Figure 45 presents the results of cell viability assays performed on lung cancer cells Calu-3 ($CD44^{low}$) and A549 ($CD44^{high}$) upon ND administration. The graph reveals that all the viability values remain consistently high, with reductions not exceeding 30% even at the highest particle concentration (20 μg ml^{-1}) and at the longest incubation time (72 h), demonstrating that the ND in all their formulations are safe for the cells under exam. Similarly, concentration- and time-dependent experiments demonstrate good biocompatibility of the various ND types across the other two pairs of cell lines as well, as viability reductions again remain below 30% for all the ND concentrations and the time points tested, as shown in Figure 61 of appendix D. Notably, the not significant differences in cytotoxicity observed across cancer cell lines of different origins and tumor sub-type indicate that the high biocompatibility of ND is neither tumor- nor cell line-dependent.

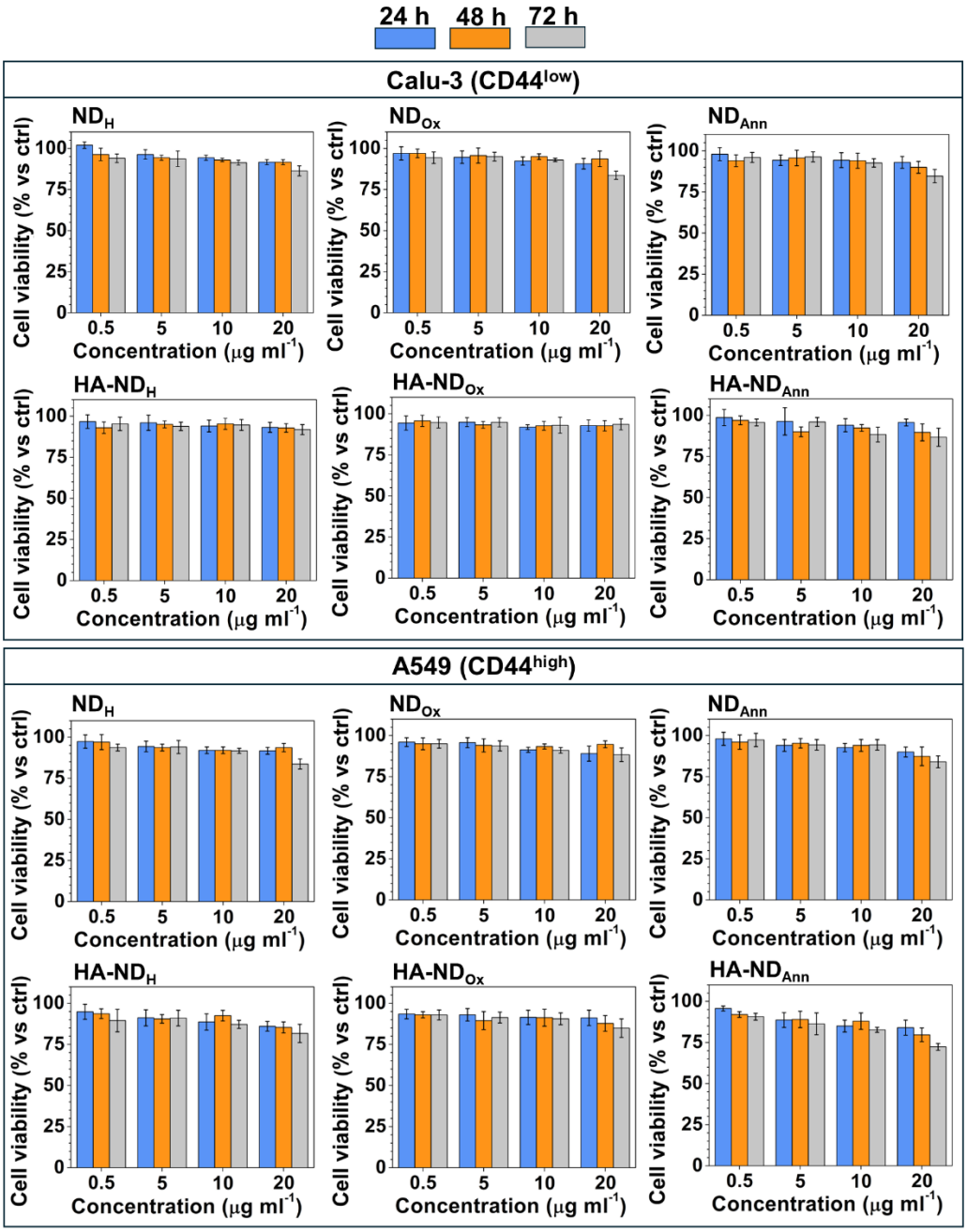

Figure 45-Viability values at 24 h, 48 h and 72 h measured for human non-small lung cancer cell lines Calu-3 ($CD44^{low}$) and A549 ($CD44^{high}$) incubated with ND_{Ann}, ND_H, ND_{Ox}, HA-ND_{Ann}, HA-ND_H and HA-ND_{Ox} (^{s}ND; 55 nm median diameter) at 0.5 μg ml^{-1}, 5 μg ml^{-1}, 10 μg ml^{-1}, and 20 μg ml^{-1}. The results were obtained *via* chemiluminescence-based assay performed in triplicate (n = 3 independent experiments).

After evaluating cell viability, ND cellular uptake was investigated. To this aim, 1 × 10^5 cells were seeded into a 96-well black plate and incubated with ND at the same concentrations tested in viability assays, *i.e.*, 0.5 μg ml^{-1}, 5 μg ml^{-1}, 10 μg ml^{-1}, and 20 μg ml^{-1}, for time periods of 1 h, 3 h, 6 h, or 24 h. To specifically examine the role of CD44 receptors in the uptake process after 24 h, the cells treated with the hyaluronated ND were investigated under three different conditions: incubated with

ND alone, co-incubated with a saturating amount of blocking anti-CD44 antibody ab157107 (diluted 1:100), and co-incubated with excess HA (at concentration equal to 100 μM). The last two conditions were meant to block CD44-mediated internalization *via* CD44 receptors inhibition or saturation respectively, thus enabling the detection of possible changes in the uptake of the functionalized ND. After incubation, the cells were washed twice with Phosphate-Buffered Saline (PBS) and then rinsed with 300 μl of PBS. To assess particle uptake, intracellular fluorescence was measured, detecting the intrinsic fluorescence of the ND by employing a Synergy HT microplate reader, analogously to viability tests.

The outcomes of uptake measurement for the lung cancer cells Calu-3 ($CD44^{low}$) and A549 ($CD44^{high}$) are shown in Figure 46 as representative examples, while the corresponding data for the pancreas cancer cell lines Capan-1 ($CD44^{low}$) and PANC-1 ($CD44^{high}$), as well as those for the breast cancer cell lines MCF-7 ($CD44^{low}$) and MDA-MB-231 ($CD44^{high}$), are presented in Figure 62 of appendix D. The graphs show that the cellular uptake for all ND types depends on both particle concentration and incubation time, increasing as these two parameters rise. The analysis of the results obtained from the non-functionalized ND highlights no significant differences in uptake between $CD44^{low}$ and $CD44^{high}$ cells, suggesting that these particles undergo non-specific internalization across the different cell types. Notably, in Calu-3 ($CD44^{low}$), PANC-1 ($CD44^{high}$), and MDA-MB-231 ($CD44^{high}$) cells, ND_{Ox} are less efficiently taken up with respect to ND_{Ann} and ND_{H} (Figure 46 and Figure 62 in appendix D). Such experimental evidence can be explained by considering the strong negative charge of the ND_{Ox} surface, originating from surface oxygenated groups, which are deprotonated at physiological pH. This charge could reduce the efficiency of particle diffusion, due to electrostatic repulsion with glycolipids and glycoproteins present on the cell surface [216,217]. Focusing on the hyaluronated particles, it can be noted that in $CD44^{low}$ cells their uptake is comparable but slightly enhanced with respect to that of their non-functionalized counterparts. On one hand, this could be attributed to the general facilitation of cellular uptake conferred by ND surface coatings, as observed in studies involving coating with zwitterionic moieties [218]. On the other hand, such observation seems to imply a role of HA in enhancing ND internalization through interaction with CD44 receptors, triggering receptor-mediated endocytosis pathways. This hypothesis is supported by the significant reduction, up to 50%, in the uptake of HA-decorated ND at 24 h when CD44-blocking antibody or excess HA are present. However, the differences in uptake between HA-decorated ND and bare particles are more noticeable in $CD44^{high}$ cells, where, interestingly, the reduction in uptake upon treatment with CD44-blocking antibody or excess HA reaches approximately 80%. These findings suggest that CD44-mediated endocytosis is not the predominant uptake mechanism in $CD44^{low}$ cells, whereas it plays a key role in $CD44^{high}$ cells, resulting in relevantly enhanced internalization of the

functionalized ND compared to the non-functionalized ones. Taken collectively, the results hence demonstrate that an increased particles uptake occurs upon functionalization when cells rich in CD44 receptor are the target, thus proving that the HA-coating successfully imparts targeting action to the ND.

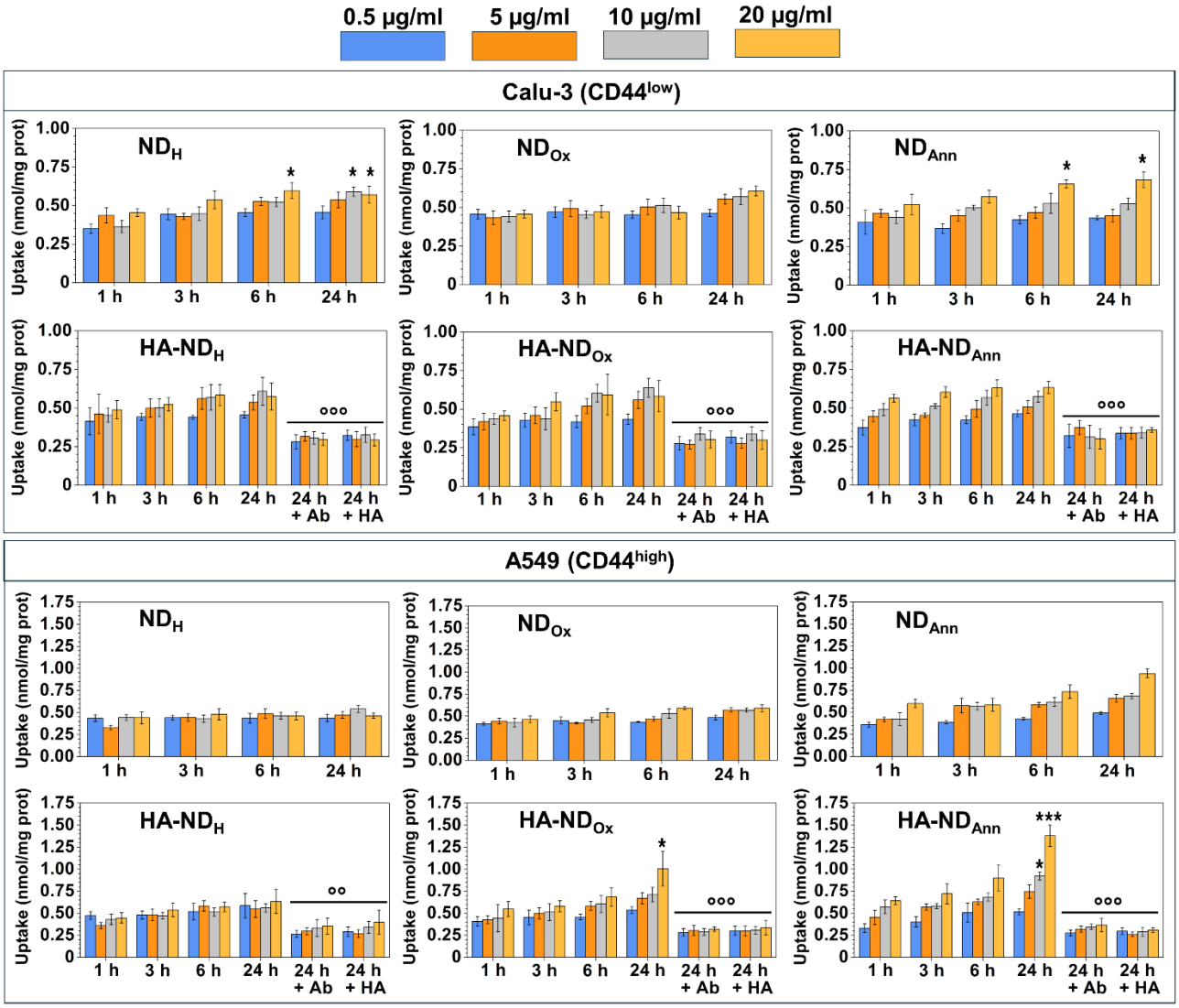

Figure 46-Uptake of ND_{Ann}, ND_H, ND_{Ox}, HA-ND_{Ann}, HA-ND_H and HA-ND_{Ox} (^{s}ND; 55 nm median diameter) at 0.5 µg ml^{-1}, 5 µg ml^{-1}, 10 µg ml^{-1}, and 20 µg ml^{-1}, after 1 h, 3 h, 6 h, and 24 h in human non-small lung cancer cell lines Calu-3 ($CD44^{low}$) and A549 ($CD44^{high}$). The results were obtained by a fluorimetry-based assay performed in triplicate (n = 3 independent experiments). When indicated, an anti-CD44 neutralizing antibody (labelled as Ab and diluted 1:100) or 100 µM hyaluronic acid (HA) were co-incubated. Significance levels are indicated with asterisks (*) or circles (○). The asterisks refer to comparisons between cells treated with ND and control sample (ND-free cells): *$p < 0.05$; ***$p < 0.001$. The circles refer instead to comparisons between the cells treated with Ab/HA and the cells without Ab/HA: ○○$p < 0.01$; ○○○$p < 0.001$.

Eventually, to assess the possibility of visualizing the ND inside the cells, thus evaluating their potential in labelling CD44-rich cells, the intracellular distribution of ND_{Ox} and HA-ND_{Ox} in

A549 ($CD44^{high}$) lung cancer cells was analyzed by means of confocal microscopy. For images acquisition, A549 cells were grown on 22 mm cover glasses and then incubated with ND_{Ox} or HA-ND_{Ox} at concentration of 100 μg ml^{-1}. After the incubation, the cells were treated for 10 min with a PBS solution containing 0.5 μg ml^{-1} 5-carboxy-fluorescein diacetate N-succinimidyl ester (CFSE) fluorescent cell staining dye, enabling cells long-term visualization. The cells were then washed once in PBS and fixed at room temperature (RT) with 4% paraformaldehyde for 15 minutes. Thereafter, treatment with 0.1% Triton-X-100 detergent in PBS for 10 min was performed, followed by 3 washes in PBS. Nucleus staining was then performed with 4′,6-diamidino-2-phenylindole (DAPI) fluorescent DNA dye at 0.5 μg ml^{-1} in PBS for 10 min at RT. Eventually, cells mounting was carried out keeping the cells in Fluoromount™ Aqueous Mounting Medium, designed for the preservation of samples fluorescence, avoiding photobleaching phenomena. Images were acquired using a Leica SP8 confocal system with HyVolution 2 with a 60× objective and zoom 2×, and analyzed by employing Adobe Photoshop CS.

Figure 47 shows the images of the cells after 6 h or 24 h of incubation with ND, demonstrating a time-dependent accumulation for both functionalized and non-functionalized particles. Notably, the hyaluronated ND reached the highest level of intracellular accumulation after 6 h, whereas the bare ones attained a comparable accumulation already after 3 h (image not reported). This observation supports the previous considerations about the mechanisms involved in cellular uptake of the particles, corroborating the idea that internalization of non-functionalized ND occurs *via* non-specific endocytosis, while functionalized ND are prevalently internalized *via* receptor-mediated endocytosis, as the former process exhibits faster kinetics compared to the latter [219]. At 24 h the amount of both types of particles inside the cells is similar, thus likely indicating a saturation in the uptake mechanisms. Interestingly, it can be noticed that the ND are mainly localized in the perinuclear regions.

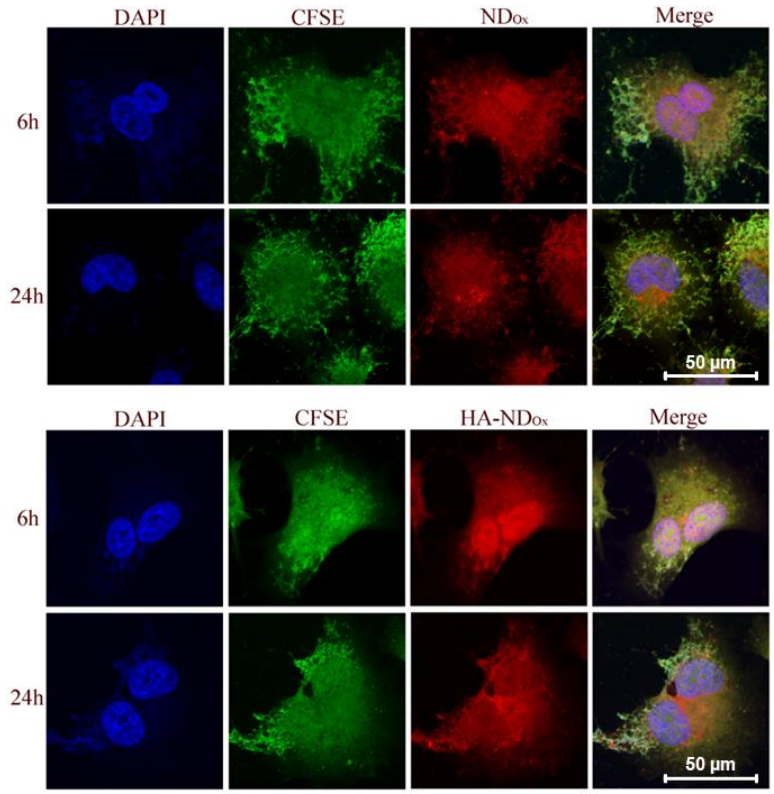

Figure 47-Representative microscopy images of A549 ($CD44^{high}$) lung cancer cells incubated with 100 µg ml^{-1} ND_{Ox} and HA-ND_{Ox} (^{s}ND; 55 nm median diameter) for 6h and 24 h. DAPI (4′,6-diamidino-2-phenylindole) and CFSE (5-carboxy-fluorescein diacetate N succinimidyl ester) dyes were employed to visualize the cell nuclei and the whole cells, respectively.

In summary, cellular testing of ND demonstrate their biocompatibility, enhanced uptake in CD44-rich cells upon functionalization with HA/DMPE, and predominant localization in proximity to the cell nuclei following internalization. These findings underscore the potential of HA-functionalized ND for targeted applications in CD44-overexpressing cells, including their use in cell visualization and the specific delivery of ND to these cells for radiosensitization purposes.

3.3 ND interaction with γ-photons: ROS generation and biological effects

This section presents the results of measurements aimed at assessing the potential of ND to boost ionizing radiation-induced ROS production, thus enhancing the susceptibility of tumour cells to radiation. As detailed in the introduction (in sub-section 1.3.4), an increase in cellular death due to the enhancement of ROS generation is expected when ionizing radiation is delivered in presence of hydrogenated ND. To investigate this phenomenon, the effect of ND on the generation of •OH radicals induced in aqueous solution by γ-photon irradiation was evaluated. Terephthalic acid (TPA) fluorogenic probe was employed to detect •OH species, based on its hydroxylation reaction that yields the fluorescent 2-hydroxyterephthalic acid (HTPA), allowing for the indirect determination of •OH

concentration *via* fluorescence spectroscopy. Moreover, to assess the biological effects of hydrogenated ND in combination with ionizing radiation, preliminary viability tests were conducted on radio-resistant cancer cells following co-treatment with ND and γ-photons. The above-described analyses were carried out on a sub-set of the samples presented in the previous section (^{s}ND with 55 nm median diameter). Specifically, the HA-decorated ND labelled as "HA-ND_{Ann}" and "HA-ND_{H}" were selected, featuring enhanced hydrodynamic stability in aqueous environment and specificity for CD44-rich cells, as well as their non-functionalized counterparts, *i.e.*, ND_{Ann} and ND_{H}.

The measurements of hydroxyl radical production from γ-photons-irradiated ND are illustrated in subsection 3.3.1, along with the results of preliminary experiments conducted to define a protocol to carry out the analyses. The outcomes of viability assays on cells co-exposed to ND and γ-photons are instead reported in sub-section 3.3.2.

3.3.1 Hydroxyl radical production from irradiated ND

Prior to analyzing hydroxyl radical production from HA-decorated and non-functionalized ND upon γ-rays exposure, some preliminary steps were undertaken to select the most suitable irradiation conditions and define a protocol for •OH radical detection in solution.

First, the fluorescence response of the TPA fluorogenic probe was characterized by evaluating the intensity of the fluorescence signal of the HTPA formed from TPA following irradiation at different doses of γ-photons. To this aim, TPA was dissolved in Phosphate-Buffered Saline (PBS) at a concentration equal to 0.05 mM and the obtained solution was irradiated with γ-photons at doses of 1 Gy, 2 Gy, 3 Gy, 4 Gy and 5 Gy. These dose values were chosen as they cover the typical dose range administered during individual sessions of radiotherapy (1.5 Gy - 3 Gy) [12] and include also those employed in previous studies to assess the radiosensitizing effects of ND [36,37,172,180]. Figure 48 shows the fluorescence intensity of the HTPA generated from the TPA solution as a function of the delivered γ-photons dose. Fluorescence intensity was determined by integrating the area under the fluorescence peak of HTPA within the 360 nm - 560 nm wavelength range, thus it is referred to as "mean intensity area" (A_{mean}) in the graph. The experiments were conducted in triplicate, with each data point representing the average of 3 fluorescence spectra, and error bars indicating the maximum semi-dispersion. The plot displays that A_{mean} increases linearly with the dose, thus revealing that the data can be fitted with the equation $A_{mean} = \alpha + \beta D$, where D represents the dose of γ-photons, whereas α and β are respectively the values of the line intercept and slope. From the fit, the value of α was determined to be $(5.1 \pm 0.5) \times 10^3$, while those of β was found to be $(11.55 \pm 0.14) \times 10^3$ Gy^{-1}.

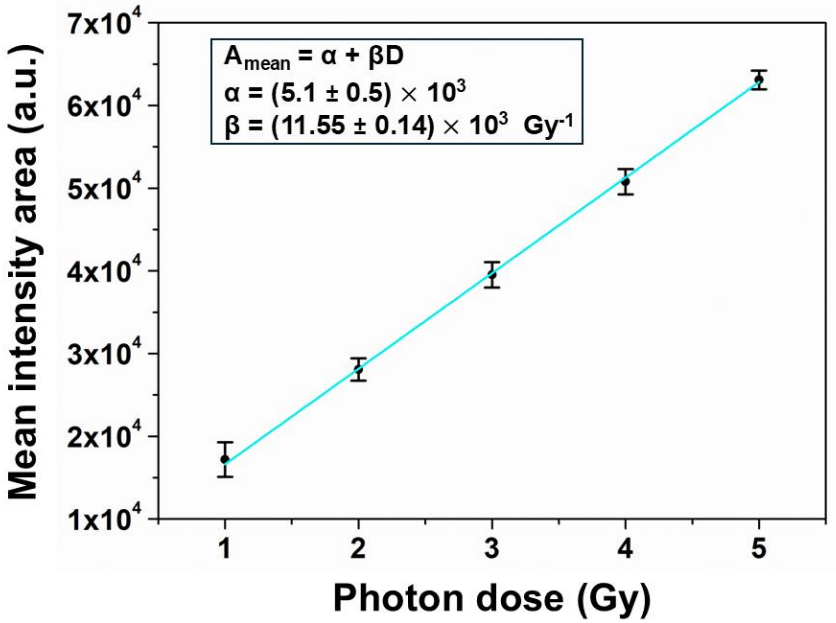

Figure 48-Mean intensity area of the fluorescence peak of HTPA formed from TPA dissolved in PBS (TPA concentration equal to 0.05 mM) as a function of the delivered γ-photon dose. Each data point was obtained by averaging 3 fluorescence spectra, with error bars indicating the maximum semi-dispersion. The plot reveals a linear increase in A_{mean} with the dose (D), fitted by the equation $A_{mean} = \alpha + \beta D$.

Subsequently, the values of A_{mean} were correlated with the corresponding concentration values of •OH radicals. Since the concentration of •OH is proportional to that of the generated HTPA, it can be assumed that each •OH radical results in the formation of one HTPA molecule. Therefore, the concentration of hydroxyl radicals can be estimated as equivalent to the HTPA concentration. This approximation neglects •OH-•OH recombination, potential reactions of •OH with other ROS species and conversion efficiency of the fluorescent probe, allowing for the establishment of a calibration curve between fluorescence intensity and •OH concentration by evaluating A_{mean} in solutions with known HTPA concentrations. Such a calibration was carried out by preparing PBS solutions of HTPA with concentrations ranging from 0.05 µM to 0.6 µM and collecting fluorescence spectra for each of them. The resulting data are shown in Figure 49, displaying A_{mean} as a function of HTPA concentration. Similarly to what reported in Figure 48, each data point results from the average of 3 spectra, as the experiments were once more conducted in triplicate, with error bars representing the maximum semi-dispersion. The graph shows that fluorescence intensity values grow linearly as HTPA concentration increases. The concentration of •OH can thus be derived from the linear fit of the data, yielding the equation $A_{mean} = \rho + \sigma c$, where c represents the HTPA concentration which can be taken equal to that of •OH radicals, while the line intercept and slope have respectively values of $\rho = (2 \pm 2) \times 10^3$ and $\sigma = (260 \pm 5)\ 10^3$ µM^{-1}.

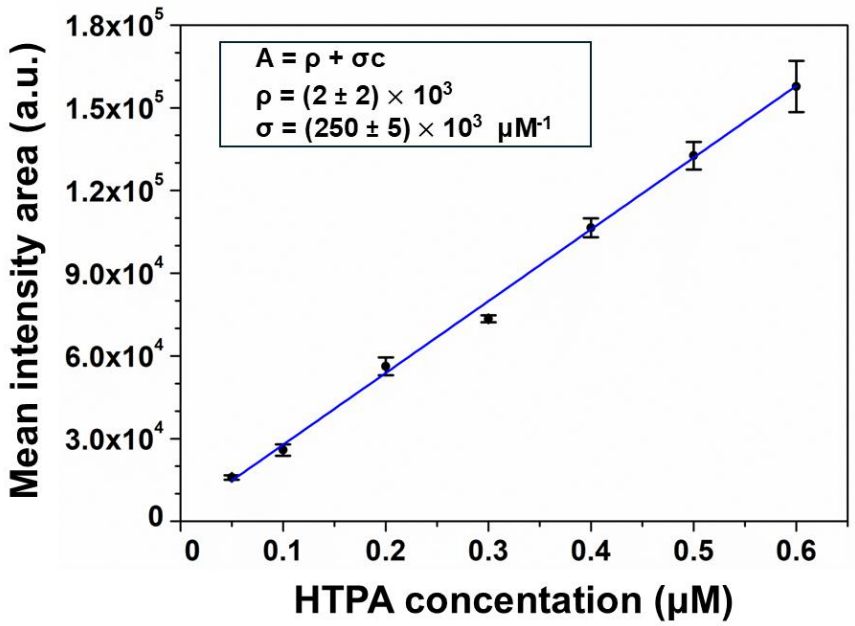

Figure 49-Calibration curve correlating the intensity of HTPA fluorescence signal (A_{mean}) with HTPA concentration in PBS solution. Each data point was obtained by averaging 3 fluorescence spectra, with error bars indicating the maximum semi-dispersion. The dataset follows a linear trend, as highlighted by the linear fit, according to the equation $A_{mean} = \rho + \sigma c$, where c is HTPA concentration.

For the subsequent experiments, a standard γ-photon dose of 4.1 Gy was chosen, as this value closely aligns with that used in a previous study investigating the radiosensitizing effect of ND [36] and has also been considered in other similar works [37,172,180], while ensuring a good signal-to-noise ratio for the recorded fluorescence.

The effects of HA-ND_{Ann}, HA-ND_H, ND_{Ann} and ND_H on •OH production following γ-photons exposure were studied by irradiating the particles dispersed at 10 μg ml^{-1} concentration in the TPA-containing PBS solution. Prior to these investigations, the concentration of •OH generated by γ-irradiation was measured in the TPA solution upon addition of hyaluronic acid (HA) alone at two different concentrations, *i.e.*, 2 μg ml^{-1} and 100 μg ml^{-1}. These measurements were conducted to assess whether HA interferes with •OH detection, thereby ensuring the reliability of the tests involving HA-functionalized ND. It is indeed well-established that HA undergoes degradation by ROS, especially by •OH, inducing chain cleavage through breakage of glycosidic bonds [220,221]. This reaction has been indicated as the basis of HA scavenging properties towards ROS [222], which have been demonstrated in several studies, including [223], [224], and [225]. Given these considerations, it was essential to evaluate any potential influence of HA presence on the analyses as a validation step. The HA concentration of 2 μg ml^{-1} was chosen as it theoretically corresponds to the amount of HA in solution that is non-covalently bound to the surface of the functionalized ND. This was estimated based on the preparation protocol, where HA-decorated ND are obtained by mixing the

HA/DMPE conjugate with the bare ND in a 1:5 weight ratio, considering that particle concentration in the TPA solution is 10 μg ml^{-1}. On the other hand, the HA concentration of 100 μg ml^{-1} was selected as a 50-fold higher value than the amount of HA associated with the hyaluronated ND to represent an extreme-case scenario. Figure 50 shows •OH radical concentrations measured in the HA-free solution and in the solutions with HA at the two specified concentrations. The data are presented as box plots, obtained from 5 independent measurements for each condition. It can be noted that in the solutions containing 2 μg ml^{-1} and 100 μg ml^{-1} HA, •OH concentration values are approximately 5% and 50% lower, respectively, compared to that measured for the solution without HA. Statistical analysis confirmed that the decrease in •OH concentration observed for HA at 2 μg ml^{-1} is not significant, whereas the opposite holds true for HA at 100 μg ml^{-1}. These results confirm the radical scavenging action of HA, while suggesting that such an effect is relevant only at high HA concentration, as no significant suppression of •OH occurs at the concentration of HA mimicking that present in the system due to the functionalized ND. Under the adopted experimental conditions, interference from HA on •OH determination was therefore excluded.

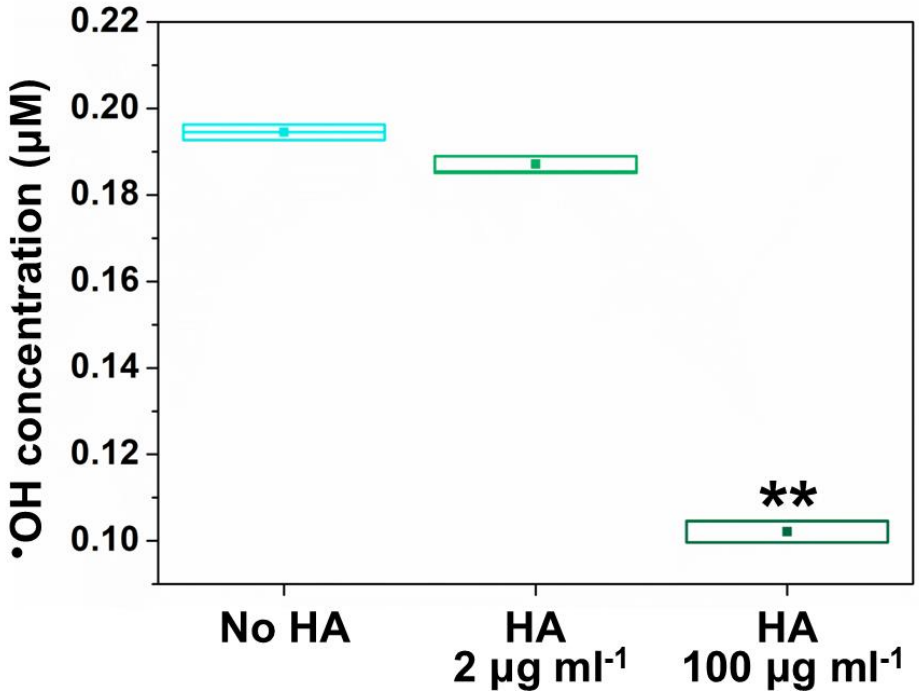

Figure 50-Concentration of •OH radicals generated by γ-photon irradiation (4.1 Gy) in TPA solutions without HA, with HA at 2 μg ml^{-1}, and with HA at 100 μg ml^{-1}. Box plots represent five independent measurements, with mean and median values shown respectively as squares and horizontal lines within each box. The box size indicates the standard error on the mean. Statistical analysis was performed using ANOVA with Tukey's multiple comparison test. The asterisks (*) denote statistical significance compared to the solution without HA (**$p < 0.01$).

The graph in Figure 51 displays box plots showing the hydroxyl radical concentrations measured with HA-ND$_{Ann}$, HA-ND$_H$, and ND$_H$, normalized to the •OH concentration detected with ND$_{Ann}$, which

represents the control condition for this experiment.The data are illustrated as box plots drawn from 5 independent measurements for each kind of ND. For HA-ND_{Ann}, no significant rise in the amount of •OH radicals can be noted. Such a result was not unexpected, as the non-functionalized counterpart of HA-ND_{Ann}, *i.e.*, ND_{Ann}, do not exhibit •OH production-enhancement capabilities, while HA does not exert any effect increasing the concentration of •OH. In contrast, in the presence of HA-ND_H and ND_H, a moderate, but significant, increase in the generation of •OH is observed. This increment attains approximately 15% for HA-ND_H and 10% for ND_H, with a significant difference between the HA-decorated and the non-functionalized particles. The increase in •OH concentration registered for HA-ND_H and ND_H could be explained based on the intense emission of electrons under irradiation that is expected from hydrogenated ND, resulting from negative electron affinity due to hydrogen terminations. Previous studies indeed suggest that hydrogen-terminated ND are capable of amplifying the generation of ROS through electron release, thus complementing the ROS species created by ionizing radiation [36,37,180]. Specifically, this phenomenon has been indicated as the basis of the radiosensitizing effect of hydrogenated ND [36]. It is interesting to notice that experimental data are directly supported by prior findings, as they closely align with the results reported in [37] and [180], which demonstrate a hydroxyl radical overproduction of about 10% compared to water in the presence of hydrogen-terminated ND at 10 μg ml^{-1}. On the other hand, the significant difference in radical production between HA-ND_H and ND_H, evidencing a higher •OH concentration with the former particles, could find a rationale by considering the improved hydrodynamic properties of HA-ND_H. As illustrated in sub-section 3.3.2, hyaluronated ND exhibit a better stability in aqueous media with respect to bare ND, being less prone to aggregation. Consequently, it could be assumed that HA-ND_H expose a larger surface area to the aqueous phase. This probably results in a more efficient transfer of emitted electrons to water molecules initiating secondary radiolysis, thus leading to a more marked ROS enhancement compared to ND_H, where instead clustering phenomena could hinder the interaction between emitted electrons and water, reducing the efficiency of ROS enhancement.

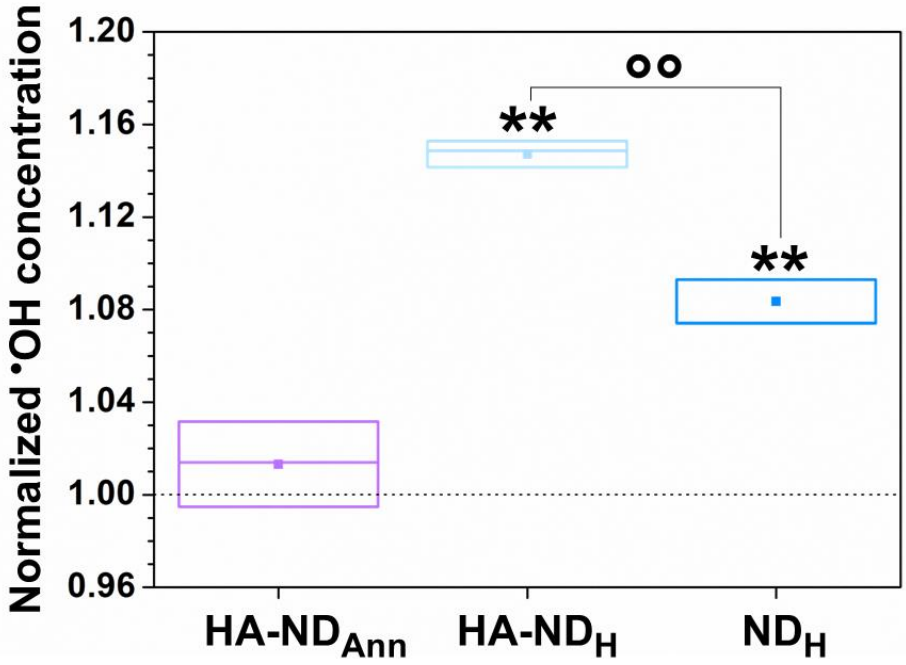

Figure 51- Concentration of •OH radicals measured upon γ-photon irradiation (at 4.1 Gy dose) in TPA solutions with HA-ND$_{Ann}$, HA-ND$_{H}$, and ND$_{H}$, normalized to the •OH concentration detected with ND$_{Ann}$ (^{s}ND; 55 nm median diameter). Box plots were obtained from 5 independent measurements, with mean and median values shown respectively as squares and horizontal lines within each box. The box size indicates the standard error on the mean. Statistical analysis was performed using ANOVA test with Tukey's multiple comparison test. The asterisks (*) indicate statistical significance compared to the reference value of 1.00 (**$p < 0.01$), marked by the dashed line, which represents no enhancement in •OH production. The circles (○) instead denote significant differences between different samples (○○$p < 0.01$).

Based on these promising outcomes, preliminary investigations were conducted to correlate the observed differences in radical production with biological effects, testing co-treatment with γ-rays and ND on the viability of radio-resistant cancer cells, as illustrated in the following sub-section.

3.3.2 Biological effect of ND in combination with γ-irradiation

With the aim of investigating the effect of ND in combination with γ-photon irradiation on a cell model, in collaboration with Prof. Chiara Riganti's research group of the Oncology Department of the University of Torino, preliminary viability assays were conducted on a radio-resistant cancer cell line upon incubation with ND and subsequent γ-ray exposure.

Such tests were performed on SU8686 cell line, representative of human pancreatic adenocarcinoma. These cells were selected as a model for a tumor that is not only difficult to remove surgically, but also inherently radioresistant. The cells were cultured in RPMI 16140 medium supplemented with 1% v/v penicillin-streptomycin and 10% fetal bovine serum. To perform viability assays, 3×10^3 cells were seeded into a 96-well white plate and incubated overnight either with fresh medium or medium containing ND$_{Ann}$, HA-ND$_{Ann}$, ND$_{H}$, or HA-ND$_{H}$, at the same concentration considered in •OH radical

measurements, *i.e.*, 10 μg ml^{-1}. The cells were exposed to γ-photons at a dose of 3 Gy, and their viability was assessed 48 h post-irradiation by determining the concentration of mitochondrial dehydrogenase enzymes, serving as markers for metabolically active cells, *via* spectrophotometric measurements. These were carried out by adding to the cells WST-1 tetrazolium salt, which is reduced by the mitochondrial dehydrogenases to form a yellow formazan product with an absorption maximum at 440 nm. The absorbance at this wavelength, proportional to the concentration of the marker enzymes, was measured using a Synergy HT microplate reader. To account for background interference, absorbance values at 660 nm were subtracted from those at 440 nm. Viability results were expressed as a percentage, calculated by normalizing the absorbance difference at the various conditions to the value obtained for the non-irradiated cells without ND, *i.e.*, the control sample, which was considered as 100%.

The results of viability measurements for both non-irradiated and irradiated cells are presented in Figure 52. Figure 52A shows the viability values for the non-irradiated cells, both alone and with the different types of ND, indicating no significant reduction in viability following cell incubation with the particles. This demonstrates the lack of cytotoxicity of the ND also on this cell line, allowing to exclude the possibility that any post-irradiation reduction in viability could be attributed to the presence of ND. Figure 52B illustrates the viability results obtained for the cells exposed to γ-rays. Compared to the control condition, the viability of irradiated ND-free cells decreases by only approximately 20%, confirming the radio-resistance of this cell line. In the presence of the ND in all their formulations, viability reductions are more pronounced, suggesting an effect of the combination between the particles and ionizing radiation on cell functioning. Notably, the viability of γ-photons-exposed cells treated with HA-ND_H is reduced by approximately 40% relative to the control case and it is significantly lower than that of the irradiated cells alone. This viability decrease could be associated with an increased production of ROS due to HA-ND_H, as suggested by the $^{\bullet}OH$ radicals measurements examined in the previous sub-section. However, also the viability values of irradiated cells incubated with ND_{Ann} and HA-ND_{Ann} are significantly reduced compared to those of irradiated ND-free cells, while this is not the case for ND_H. The latter observation could be linked to the less efficient ROS enhancement by ND_H, which probably causes the formation of these species in a concentration that is not sufficient to produce any biological action. On the other hand, the reductions registered in the presence of ND_{Ann} and HA-ND_{Ann} are more complex to explain, not being connected with the results of the experiments presented in sub-section 3.3.1. It could be assumed that the combined action of radiation and ND_{Ann} or HA-ND_{Ann} induces a cell-damaging mechanism independent of ROS generation. However, this hypothesis would require systematic investigation from a biological perspective to be validated. Furthermore, additional tests should be conducted to

confirm the observed trends in the viability of irradiated cells incubated with different types of ND. These points pave the way for future research, which should focus on further viability assays on the same cell line, viability assessments on other cell types, and detailed biological investigations to fully elucidate the processes responsible for potential decreases in viability.

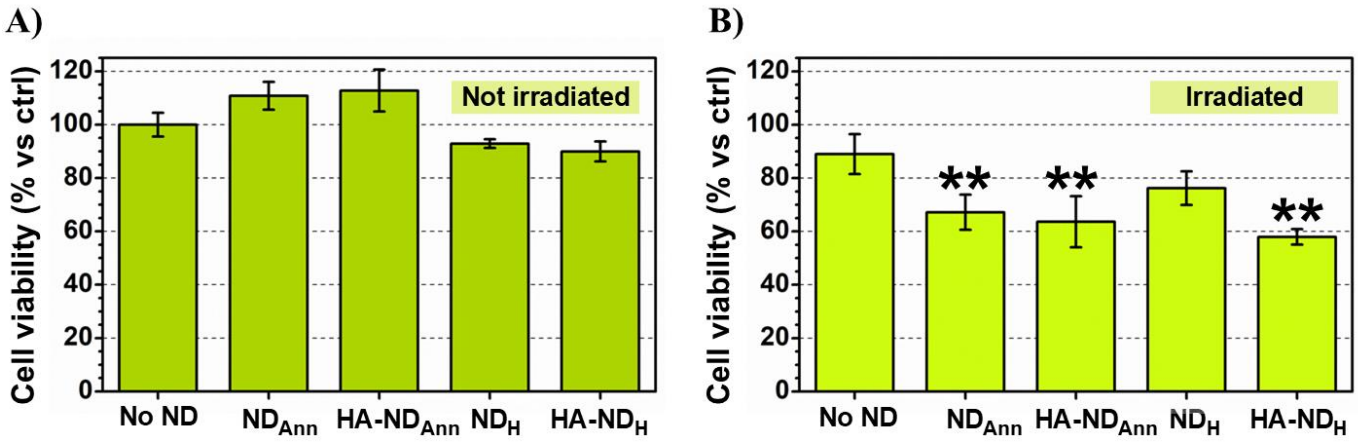

Figure 52-Viability values for human pancreatic cancer cells SU8686, either alone or incubated with ND_{Ann}, HA-ND_{Ann}, ND_H or HA-ND_H (^{s}ND; 55 nm median diameter) at 10 μg ml^{-1}. The results were obtained through spectrophotometric-based assay performed in triplicate. A) Viability values for non-irradiated cells. B) Viability values for cells exposed to γ-rays (3 Gy). Statistical analysis was performed using ANOVA test with Tukey's multiple comparison test. The asterisks (*) indicate statistical significance compared to the viability measured for the irradiated cells without the ND (**$p < 0.01$).

3.4 Ion beam-modification of ND for application in T_1-relaxometry

After tuning ND surface properties to enhance ROS production, the experimental activities focused on optimizing ND core-related features, specifically targeting the creation and the control of NV centers, with the aim of making ND suitable for free radical measurements *via* T_1-relaxometry.

As highlighted in sub-section 1.3.5, successful detection of free radicals with ND requires increasing the concentration of NV defects, particularly NV^-, through artificial methods. A common approach for type-Ib ND involves irradiation with MeV energy proton beams to introduce new vacancies in the lattice, followed by thermal annealing to couple these vacancies with native nitrogen impurities. In this context, irradiation parameters are crucial for promoting NV formation in specific charge states. Notably, ion fluence must be carefully selected to favor the creation of NV^- centers over NV^0 while ensuring a good PL signal. To determine the optimal proton fluence to guarantee both these conditions, the study detailed in sub-section 3.4.1 was conducted. Utilizing the AN2000 facility at LNL (described in section 2.3), ^{l}ND (240 nm median diameter) were irradiated with a 2 MeV H^+ beam at different ion fluences. After undergoing post-irradiation annealing, these ND were

characterized via photoluminescence spectroscopy to evaluate their optical properties and quantify the produced NV^-/NV^0 ratio as a function of the proton fluence.

The results reported in sub-section 3.4.2 regard instead preliminary T_1-relaxometry characterization of ^{m}ND (125 nm median diameter), modified using the irradiation conditions identified as optimal in sub-section 3.4.1. T_1-relaxometry measurements were performed at the Universitair Medisch Centrum Groningen in collaboration with prof. Romana Schihagl's research group, employing the setup detailed in section 2.10.

3.4.1 Characterization of ion-beam modified ND

As described in section 2.3, sample preparation for ion beam modification consisted of dispersing ND (details of their thermal processing in appendix A) in isopropyl alcohol, followed by their deposition onto a silicon wafer (~ 1.5 cm × 1.5 cm), resulting in a layer with a thickness of about 30 µm upon drying. With the purpose of creating new vacancies in the ND, the sample was irradiated with a 2 MeV H^+ ion microbeam (10 µm × 10 µm) using the AN2000 accelerator at LNL, exposing different areas to varying ion fluences in the range from 1.0×10^{13} cm^{-2} to 1.2×10^{18} cm^{-2}. The fluence delivered to each region was estimated from the integrated charge, collected by a Faraday cup positioned inside the irradiation chamber, diving this value by that of the proton charge and the beam area. After proton irradiation, the sample underwent an annealing process (details provided in appendix A) aimed at inducing the migration of the created vacancies, thus allowing their coupling with nitrogen atoms and, consequently, the formation of new NV centers.

The sample was analyzed via photoluminescence (PL) spectroscopy, collecting PL spectra from each irradiated area. To study the PL signal at different fluences, the intensity of the PL ascribable to NV centers was evaluated by calculating the integral of the collected spectra between 565 nm and 780 nm. Figure 53A shows the plot of the integrated PL intensity against the ion fluence delivered to the ND. Each blue point in the graph corresponds to the average of the integrals of three different spectra acquired from each region, with error bars representing the maximum semi-dispersion, while the dashed red line displays the integrated PL from unirradiated ND, reported for comparison. Due to uncertainties in the estimation of the irradiated area and the integrated charge, a 20% spatial variation of the fluence values should be also considered. It can be noted that the PL of the ion beam-modified ND remains similar to that of the non-irradiated particles up to a fluence of 3.0×10^{14} cm^{-2}. Beyond this value, the PL intensity undergoes a remarkable enhancement, increasing with rising fluence and finally reaching a maximum at a fluence of 3.0×10^{16} cm^{-2}, where it becomes approximately 9-fold-higher than that of the unirradiated ND. Starting from 2.7×10^{17} cm^{-2}, PL starts to decrease, eventually dropping below that of the non-irradiated ND at the highest fluences explored

(*i.e.*, 9.0 × 10^{17} cm^{-2} and 1.2 × 10^{18} cm^{-2}). The initial increase in PL can be attributed to the introduction of a higher number of vacancies with increasing fluence, leading to the formation of more numerous NV centers, up to the point of nitrogen impurity saturation. At first analysis, such a saturation point seems to be the fluence at which the maximum PL intensity is achieved, *i.e.*, 3.0 × 10^{16} cm^{-2}. Notably, this value is compatible with that reported in [168] upon ND irradiation with the same kind of ions (*i.e.*, 2 MeV energy protons). In that work such a fluence value was associated with an induced vacancies density (ρ_{vac}) in the order of 10^{19} cm^{-3}. Considering the atomic density of diamond (ρ_{diam} =1.77 × 10^{23} cm^{-3}) and a nominal concentration of nitrogen impurities typical of HPHT diamond, *i.e.*, about 100 ppm, the volume density of nitrogen impurities can be taken equal to $\rho_N \approx 1.77 \times 10^{19}$ cm^{-3}. Consequently, the above-mentioned density of ion-induced vacancies can be estimated as comparable to ρ_N, thus supporting the previous conclusion. Nonetheless, according to the results reported in [168], the saturation of N impurities with vacancies takes place from an irradiation fluence of ≈10^{17} cm^{-2}, which is slightly larger than the fluence maximizing PL intensity. This discrepancy can be rationalized by considering that PL is limited by the actual density of defects, due to PL quenching phenomena between the NV emitters and surrounding defects [168]. These can cause PL decrease before reaching N impurities saturation, finally producing the PL drop for the highest fluence values.

To correlate the observed PL intensity trend with the formation of NV centers in different charge states, further analysis was conducted to estimate the NV^-/NV^0 ratio at each value of ion fluence. This assessment was carried out by calculating the contributions of the two kinds of centers to the experimental PL signal (PL^{exp}). Labelling $PL^{exp}_{NV^0}$ and $PL^{exp}_{NV^-}$ the PL signals ascribable to NV^0 and NV^- defects respectively, PL^{exp} can be expressed as:

$$PL^{exp} = PL^{exp}_{NV^0} + PL^{exp}_{NV^-} \quad \text{Eq.36}$$

where $PL^{exp}_{NV^0}$ and $PL^{exp}_{NV^-}$ can be rewritten according to the following equations.

$$PL^{exp}_{NV^0} = a\, PL^{exp} \quad \text{Eq.37}$$

$$PL^{exp}_{NV^-} = b\, PL^{exp} \quad \text{Eq.38}$$

PL^{exp} hence becomes:

$$PL^{exp} = a\, PL^{exp} + b\, PL^{exp} \quad \text{Eq.39}$$

where the coefficients a and b are the relative contributions of the NV^0 and NV^- charge states with respect to the total PL, so that $a + b = 1$. Therefore, NV^-/NV^0 PL ratio can be obtained by evaluating the value of $\frac{b}{a}$. To extract NV^-/NV^0 PL ratio from each spectrum, different linear combinations of individual NV^0 and NV^- spectra were compared. Normalized spectra of mere NV^0 and NV^- ($S_{NV^0}(\lambda)$ and $S_{NV^-}(\lambda)$ respectively) were extrapolated from [226] and used to calculate the total NV emission spectra $S_{NV}(\lambda)$:

$$S_{NV}(\lambda) = a\, S_{NV^0}(\lambda) + b\, S_{NV^-}(\lambda) \qquad \text{Eq.40}$$

Following the normalization of each experimental spectrum, the combination of a and b best describing the experimental data was identified by finding the values minimizing the following expression:

$$\sum_{\lambda} \left(S_{exp}^{norm}(\lambda) - S_{NV}(\lambda)\right)^2 \qquad \text{Eq.41}$$

where $S_{exp}^{norm}(\lambda)$ represents the normalized experimental spectrum.

Figure 53B shows the NV^-/NV^0 PL ratio, extracted from PL spectra analysis, as a function of ion fluence. The plot shows that the amount of NV^- centers relative to that of NV^0 generally increases at lower fluences, then the trend undergoes a flattening for fluences between 3.0×10^{15} cm^{-2} and 1.0×10^{16} cm^{-2}, and finally a decrease, starting from 3.0×10^{16} cm^{-2}. The drop of the NV^-/NV^0 ratio by increasing ion fluence can be explained based on previous works, attributing it to the reduction in the amount of isolated nitrogen atoms acting as electron donors, resulting in the rise of the relative number of NV^0 centers. On the other hand, the increase in the NV^-/NV^0 ratio at smaller fluence values is more difficult to interpret, as it lacks an explanation in prior studies, although such a trend has been reported both in [227] and [168]. Nevertheless, the crucial finding emerging from Figure 53B is that the maximum NV^-/NV^0 is produced for fluences in the 3.0×10^{15} cm^{-2} - 1.0×10^{16} cm^{-2} range. As evident from Figure 53A, the maximum PL in this interval is reached at a fluence value of 1.0×10^{16} cm^{-2}. This hence appears as the most suitable one for obtaining ND to be employed in T_1-relaxometry, combining high PL signal and maximization of the relative amount of NV^- defects.

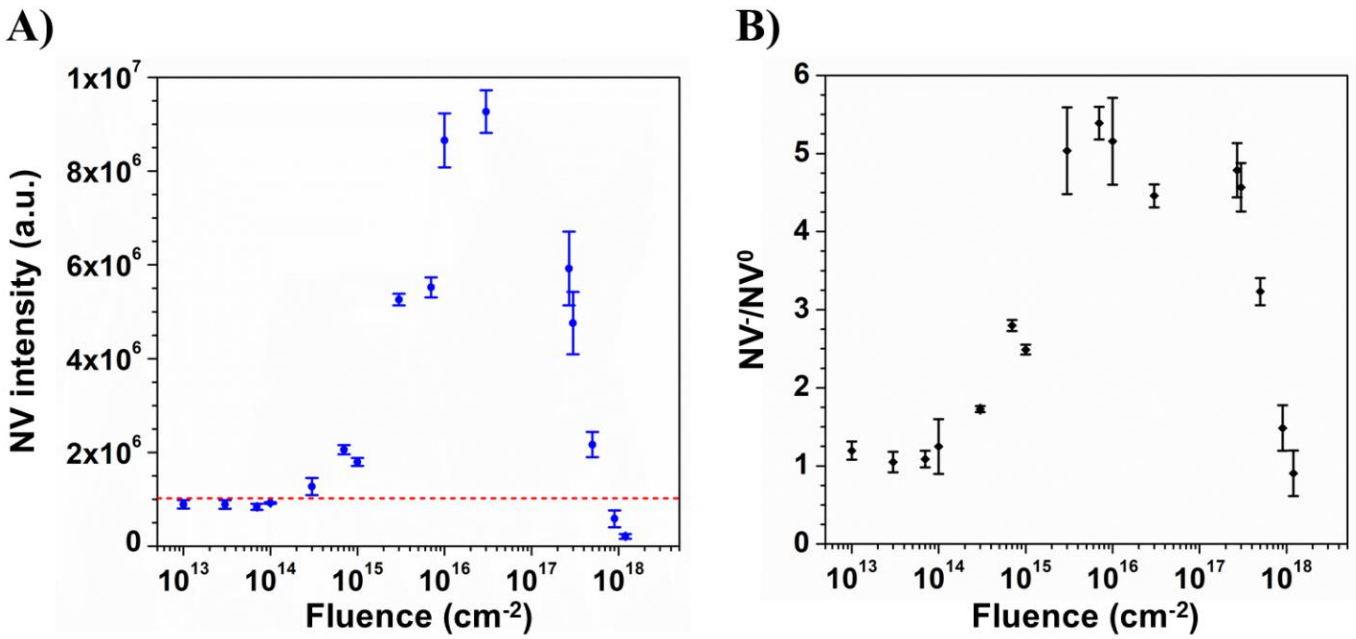

Figure 53-PL characterization of ND ([l]ND; 240 nm median diameter) irradiated with 2 MeV energy protons at different ion fluences. A) Integrated NV PL intensity as a function of the delivered ion fluence. The red dashed line represents the PL intensity of non-irradiated ND. B) Calculated NV^-/NV^0 ratio as a function of the ion fluence.

3.4.2 Application of ion-beam modified ND in T_1-relaxometry

In collaboration with Prof. Schirhagl's research group at the Biomedical Engineering Department of the Universitair Medisch Centrum Groningen, preliminary T_1-relaxometry characterization was conducted on ND irradiated with protons at a fluence of 1.0×10^{16} cm^{-2}, identified as the condition that maximizes the NV^-/NV^0 ratio while ensuring a high PL signal, to evaluate their suitability as probes for free radical detection.

To prepare the ion-irradiated ND (details of their thermal processing in appendix A) for relaxometry measurements, the particles were dispersed at 10 µg ml^{-1} in Milli-Q water and then deposited onto the surface of glass-bottom quartered Petri dishes (100 µl of dispersion per compartment). Prior to deposition, the dish surfaces were activated by oxygen plasma treatment, conducted in a plasma oven for 15 minutes with gas pressure adjusted to 0.2 mbar. This treatment aimed to introduce hydrophilic functional groups onto the glass surfaces, enhancing the attraction with the ND to secure firm deposition, thus minimizing particles movement [183]. Relaxation curves were first collected on the particles alone to determine their baseline relaxation time. Subsequently, a 100 nM solution of gadolinium chloride ($GdCl_3$) was added to the Petri dishes (50 µl per compartment) to mimic the presence of free radicals with paramagnetic Gd^{3+} ions and curves acquisition was repeated.

Figure 54A provides an example of T_1-relaxometry measurements conducted on the ion-irradiated ND in the absence and presence of Gd^{3+} ions. The plot displays NV photoluminescence (PL) intensity

as a function of dark time, normalized to the mean PL value of the last 10 data points, used as a reference to account for the fully relaxed state of the system. Both datasets show a decreasing trend with increasing dark time; however, this decrease appears to be more pronounced in the presence of Gd^{3+}, suggesting a faster PL decay and, consequently, a shorter T_1 relaxation time under these conditions. Such a behavior is confirmed by data fitting to a single exponential model, which reveals a shorter T_1 value when the ND are exposed to Gd^{3+}. These observations align with previous studies showing that paramagnetic species accelerate electron relaxation to the ground state in NV^- centers [52,84,185]. Figure 54B shows box plots illustrating the T_1 values obtained from the fitted curves for both the ND alone and the ND with Gd^{3+}, with each point corresponding to an individual T_1 measurement. Upon adding Gd^{3+} ions, T_1 relaxation time undergoes a significant reduction of approximately 30%. This result seems to indicate that ion-irradiated ND effectively hold potential for use in T_1-relaxometry as probes for paramagnetic species. Nevertheless, a relevant dispersion can be noted among the individual data points. This variability in relaxation times could stem from the inherent size distribution of the ND. Indeed, as demonstrated by Tetienne et al. [84], particle size strongly affects T_1, with smaller ND exhibiting shorter T_1 values, due to the interaction of the NV^- electron spin with paramagnetic centers on the ND surface. Achieving a high degree of uniformity in particle size is therefore crucial to ensure consistent T_1 measurements. Moreover, to assess the sensitivity of ion-irradiated ND to different paramagnetic ion concentrations, additional tests should be conducted to investigate the decrease in T_1 at varying Gd^{3+} concentrations. Based on these considerations, future work will focus on techniques for sorting particles by size and evaluating the impact of Gd^{3+} concentration variation on T_1, with the goal of allowing reliable free radical detection and quantification using the developed ND in T_1-relaxometry.

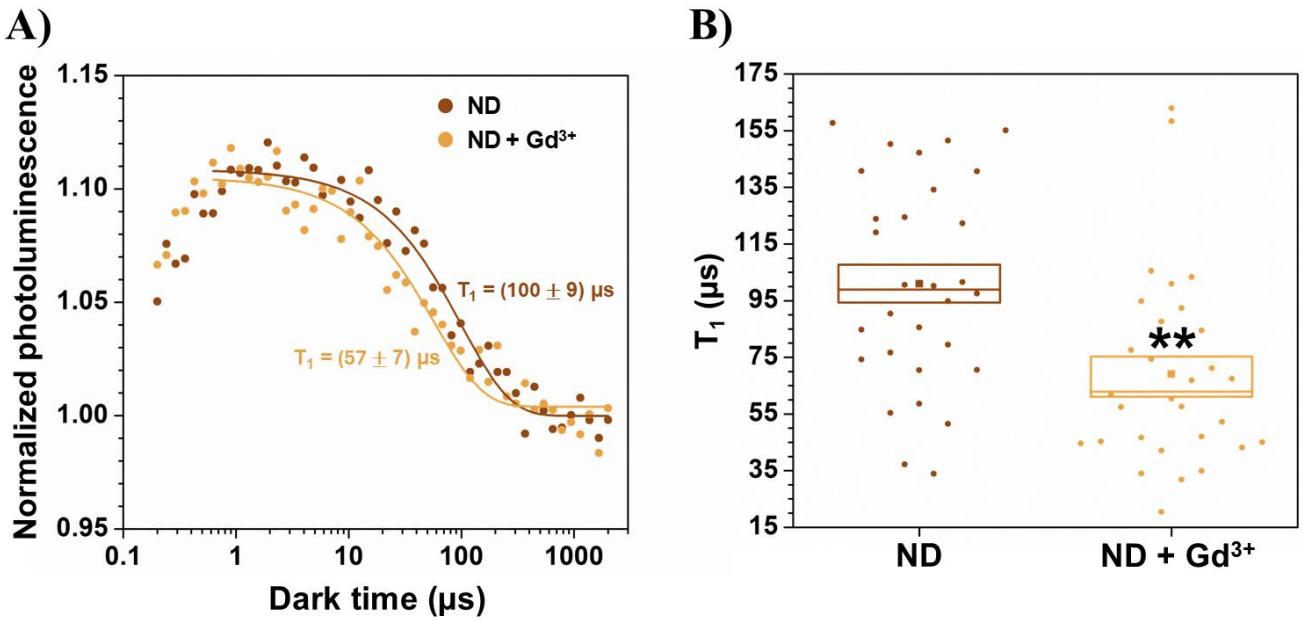

Figure 54-T_1-relaxometry characterization of ion-irradiated ND (^{m}ND; 125 nm median diameter). A) Example of T_1-relaxometry measurement conducted on the ND in the absence and in the presence of paramagnetic Gd^{3+} ions. PL is reported as normalized to the mean of the last 10 data points, taken as reference for fully-relaxed NV^-. To extract T_1 time values data were fitted to a single exponential model. B) Box plots displaying T_1 relaxation time obtained from T_1 curves fitting for ND in the absence and in the presence of paramagnetic Gd^{3+} ions. Each measurement, corresponding to a curve, is represented as a point, whereas mean and median values are shown respectively as squares and horizontal lines within each box. The box size indicates the standard error on the mean. Statistical analysis was performed by employing paired samples t-test. The asterisks (*) denote statistical significance compared to the T_1 value in the absence of Gd^{3+} ions (**$p < 0.01$).

4. Conclusions and future developments

The work illustrated in this thesis aimed to optimize the properties of both the surface and the core of nanodiamonds (ND) for their application in enhancing the production of ionizing radiation-generated Reactive Oxygen Species (ROS) and determining their concentration through T_1-relaxometry.

The first objective of the experimental activities was to develop a thorough understanding of the effects of thermal treatments in controlled atmospheres on ND surface properties and to establish an effective protocol for achieving specific surface modifications. To this end, ND subjected to various thermal processes were characterized in terms of their electrical properties through electrical measurements conducted in controlled humidity conditions. These provided indirect information into changes in particles surface chemistry and structure, which were subsequently validated through Diffuse Reflectance Infrared Fourier-Transform (DRIFT) spectroscopy and Raman spectroscopy and were linked to distinct conduction mechanisms, with additional analyses focusing on the influence of particle size. Furthermore, to assess the impact of thermally induced surface terminations on the hydrodynamic properties of ND in aqueous solutions, Dynamic Light Scattering (DLS) and Zeta Potential (ZP) measurements were conducted.

The study of the electrical properties of ND processed with different thermal treatments evidenced distinct surface modifications linked to specific conduction mechanisms. Oxidized ND were found to exhibit enhanced conductivity compared to those subjected to annealing at 800 °C, particularly at high humidity levels, along with a pronounced dependence of conductivity on humidity. On the other hand, hydrogenated ND were characterized by high conductivity at low humidity levels and weak conductivity dependence with varying humidity, while the ND annealed above 900 °C showed a conductivity that was systematically larger than the one registered in the other samples, independently of humidity conditions. Based on DRIFT spectroscopy results, the electrical behavior of oxidized ND was attributed to oxygenated moieties introduced onto the particle surface by oxidation, which increase the hydrophilicity of the particles, promoting water adsorption and thus enhancing electrical conduction *via* the Grotthuss mechanism. In contrast, electrical conduction in hydrogenated ND was linked to hydrogen terminations driving water-induced surface transfer doping mechanism. In the framework of Raman spectroscopy analysis, the electrical properties of the ND annealed above 900 °C were instead associated with graphitization of particles surface. Besides highlighting the relationship between surface terminations, structural features, and the electrical properties of ND, the analysis just discussed allowed to identify optimal procedures for ND surface modification. Annealing at 800 °C was shown to effectively standardize the ND surface without causing structural damage, while harsh oxidation treatments proved to outperform mild ones in the formation of

oxygenated moieties. Additionally, hydrogenation processes were found to be more efficient when performed after oxidation rather than after annealing. These treatments were thus applied for processing ND in the following steps of the experimental work.

The electrical characterization of diamond particles of different sizes evidenced that the oxidized samples exhibit a clear relationship between electrical properties and particle dimension, with conductivity directly correlated to the surface area, depending on the amount of adsorbed water. Conversely, in the hydrogenated samples the connection between electrical properties and particle size was found to be to be more complex, suggesting that two competing mechanisms, *i.e.*, formation and transport of holes, influence electrical conduction in different ways, making it difficult to establish a direct correlation between electrical conductivity and particle dimension.

DLS and ZP analyses performed on ND aqueous suspensions after 15-min sonication treatment revealed that oxidized ND exhibit high dispersibility and stability in water-based media. Conversely, annealed ND and hydrogenated ND showed a marked tendency to aggregate and precipitate. These findings evidenced the need to improve the hydrodynamic behavior of ND for subsequent experiments involving their employment in aqueous solution.

In the following phase of the experimental activity, annealed ND, oxidized ND, and hydrogenated ND were modified through surface functionalization with hyaluronic acid (HA), aiming both at increasing their dispersibility in aqueous environment and impart selectivity towards cells overexpressing HA receptors (CD44) for use of the particles in clinical application. Functionalization was implemented though a non-covalent approach using a conjugate of HA with the phospholipid 1,2-dimyristoyl-*sn*-*glycero*-3-phosphoethanolamine (DMPE). Alterations to ND properties induced by derivatization were explored thanks to a comparative analysis of the particles both before and after surface decoration. Specifically, particles surface chemistry, structure, size, optical properties, and hydrodynamic behavior were investigated by employing DRIFT spectroscopy, Raman spectroscopy, Scanning Electron Microscopy, photoluminescence spectroscopy, and DLS and ZP measurements. After characterization, the ND were also tested on three different models of human adenocarcinoma cells, assessing their biocompatibility, uptake and cellular distribution.

DRIFT spectroscopy results revealed relevant changes in the ND spectral features upon derivatization, which were attributed to the presence of HA anchored on the surface, thus allowing to validate the adopted derivatization method. On the other hand, Raman spectroscopy and Scanning Electron Microscopy evidenced that neither the structure nor the particles size in dry state were modified by the HA/DMPE conjugate, while photoluminescence spectroscopy proved that surface decoration preserved the fluorescence properties of Nitrogen-Vacancy (NV) color centers.

Hydrodynamic analyses conducted after 90 minutes of sonication revealed that, although non-functionalized particles are effectively dispersed through prolonged ultrasonic treatment, they are not stable in suspension over time, especially in the case of annealed ND and hydrogenated ND, aggregating quickly. Notably, functionalized ND were found to keep stability in suspension up to one-month period, thanks to HA attached to the surface.

Viability assays across pancreatic, breast, and lung cancer cell lines indicated the biocompatibility of both non-functionalized and HA-decorated ND with no relevant differences observed among cell lines of different origins and tumor sub-types. Uptake measurements revealed a time- and concentration-dependent internalization of ND into cells, with enhanced accumulation of hyaluronated particles compared to non-functionalized ones in CD44-rich cells. These results demonstrated the targeting capabilities of HA-decorated ND, suggesting their internalization *via* CD44-mediated endocytosis, in opposition to non-specific endocytosis, likely regulating the uptake of non-hyaluronated particles. Finally, confocal microscopy corroborated the findings from the uptake assays, additionally revealing that ND predominantly localized in the perinuclear region.

Subsequently, the potential of the bare and hyaluronated ND to increase ROS generation under irradiation was investigated. This assessment was done by evaluating the production of $^{\bullet}OH$ radicals formed in aqueous solution upon γ-photon irradiation, employing terephthalic acid (TPA) as a fluorogenic probe molecule. Thanks to the formation of the fluorescent 2-hydroxyterephthalic acid (HTPA) by reaction with $^{\bullet}OH$, these species were detected and quantified through fluorescence spectroscopy. To correlate radical production with biological effects, the combination of ND and γ-radiation was also preliminary tested on a radio-resistant human pancreatic cell line.

To measure $^{\bullet}OH$ production, due to the well-known scavenging action of HA towards radical species, preliminary tests were carried out to assess any potential influence of HA on the analyses. These showed that $^{\bullet}OH$ are not significantly reduced by low HA concentrations, as the one theoretically corresponding to the amount non-covalently bound to the surface of the functionalized ND, thus allowing to perform subsequent measurements. The data on ND samples indicate that hydrogenated particles produce a slight enhancement in $^{\bullet}OH$ generation, becoming more pronounced when they are decorated with HA. On one hand, this phenomenon was rationalized based on the emission of electrons expected from hydrogenated ND, which initiate secondary radiolysis by interaction with water molecules, thus leading to ROS increase. On the other hand, the difference between bare and hyaluronated ND was explained in terms of their different hydrodynamic behavior. As functionalized ND exhibit improved dispersibility, they should have a larger surface area exposed to the aqueous

phase, likely promoting the transfer of emitted electrons to water and causing more marked ROS enhancement.

Preliminary viability assays on pancreatic adenocarcinoma cells showed that ND particles combined with γ-photon irradiation cause a relevant decrease in cell viability. Notably, treatment with hyaluronated hydrogenated ND induces a significant reduction in viability, probably ascribable to increased ROS production. This was not observed for non-functionalized hydrogenated ND, probably due to a reduced effect on ROS enhancement. Nevertheless, the significant reductions in cell viability registered with other types of ND were difficult to rationalize. Overall, these results highlighted the need for further investigations focusing on additional viability assays, including testing on other cell types, as well as detailed biological studies to clarify the role of the combination of ND and ionizing radiation on cell functioning.

After addressing the aspects related to ND surface, the last part of the thesis work focused on ND core features, specifically the creation NV centers, to render ND suitable probes for free radical measurement *via* T_1-relaxometry. With the aim of identifying a procedure allowing to obtain highly fluorescent particles characterized by a high concentration of NV^- centers, ND were irradiated with 2 MeV protons at different ion fluences in the 1.0×10^{13} cm^{-2} - 1.2×10^{18} cm^{-2} range. The particles were then analyzed *via* photoluminescence spectroscopy (PL) to evaluate PL intensity and the formed NV^-/NV^0 ratio in the different conditions. PL characterization of proton beam-irradiated ND showed that PL increased at low fluences, due to the increase of NV centers concentration, and, after reaching a maximum, decreased as a result of defects-induced PL quenching phenomena. NV^-/NV^0 ratio was found to exhibit a similar trend, with the final decrease due to the lowering of nitrogen atoms acting as electron donors, favoring the formation of NV^0 over NV^-. The combination of the results allowed to identify the fluence of 1.0×10^{16} cm^{-2} as the value maximizing NV^-/NV^0 ratio and simultaneously enabling to obtain highly fluorescent ND. ND irradiated with protons at 1.0×10^{16} cm^{-2} were finally tested in preliminary T_1-relaxometry measurements to assess their performances in the detection of paramagnetic species. Measurements performed in the presence of Gd^{3+} ions revealed a decrease in T_1-relaxation time, thus evidencing the potential of the particles as probes for paramagnetic free radicals. Nevertheless, a notable dispersion among the individual T_1 values was noticed. This was attributed to the presence of ND with different sizes, showing different relaxation times. Such observations evidenced the necessity of future activities for further optimization of the particles, by sorting them by size, to perform reliable measurements. Moreover, also the impact of different concentrations of paramagnetic ions should be tested.

On the whole, the candidate investigations suggest that ND hold the potential to be used as a platform combining ROS enhancement and measurement, paving the way for further steps in this direction.

Appendix A

Figure 55 presents a table summarizing the details of the '*Ox*' and '*H_2-II*' thermal processes performed on the ^{l}ND (240 nm median diameter), ^{s}ND (55 nm median diameter), and µD (6 µm median diameter) described in section 3.1, as well as the ^{s}ND samples analyzed in sections 3.2 and 3.3.

Section	Samples	Thermal treatment	Processing details
3.1	^{l}ND (240 nm), ^{s}ND (55 nm), µD (6 µm)	*Ox*	air, 12 h, 475 °C
		H_2-II	H_2, 2 h, 800 °C
3.2 and 3.3	^{s}ND (55 nm)	*Ox*	air, 36 h, 500 °C
		H_2-II	H_2, 3 h, 850 °C

Figure 55-Details of the '*Ox*' and '*H_2-II*' thermal processes carried out on the samples presented in sections 3.1, 3.2, and 3.3.

Figure 56 provides the specifications for the preparation of the ion-irradiated ND examined in section 3.4. More specifically, the schemes in Figure 56A and Figure 56B refer respectively to the ^{l}ND (240 nm median diameter) described in sub-section 3.4.1 and the ^{m}ND (125 nm median diameter) outlined in sub-section 3.4.2. Notably, after irradiation with H^+ at 2 MeV, both samples underwent an annealing treatment in nitrogen flux atmosphere at 800 °C for 2 h ('*Ann*') to couple nitrogen impurities with the vacancies created by ion irradiation.

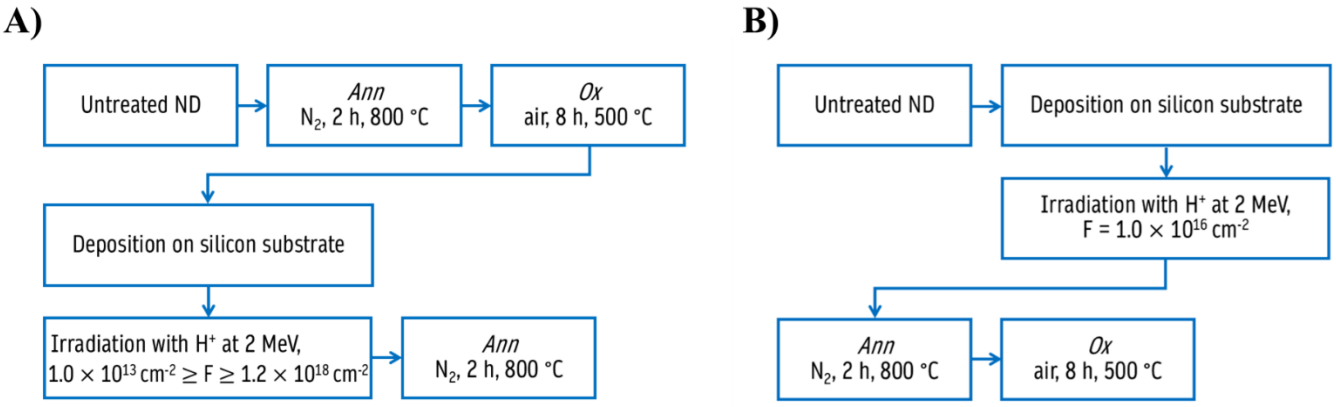

Figure 56-Details of the preparation of the ion-irradiated ND illustrated in section 3.4. A) Processing steps applied to the ^{l}ND (240 nm median diameter) of sub-section 3.4.1. B) Processing steps applied to the ^{m}ND (125 nm median diameter) of sub-section 3.4.2.

Appendix B

This appendix reports the results of additional analyses performed on the [l]ND (240 nm median diameter) illustrated in sub-section 3.1.1.

Figure 57 shows the Raman spectra of the samples labelled as ND '*Ann*', ND '*Ann* + *Ox*', ND '*Ann* + *Mild-Ox*', ND '*Ann* + *Ox* + *Ann*', ND '*Ann* + H_2-*I*'and ND '*Ann* + *Ox* + H_2-*II*'. It is possible to note that the only evident feature is the first-order Raman peak of diamond at 1332 cm^{-1}, while the graphite G-band at 1580 cm^{-1} is not detectable. Such observations allowed to rule out the influence of surface graphite on samples electrical properties, which have indeed a different origin (Grotthus mechanism in surface adsorbed water or water-triggered transfer-doping), as determined from samples DRIFT spectra (shown in Figure 32B and Figure 33B).

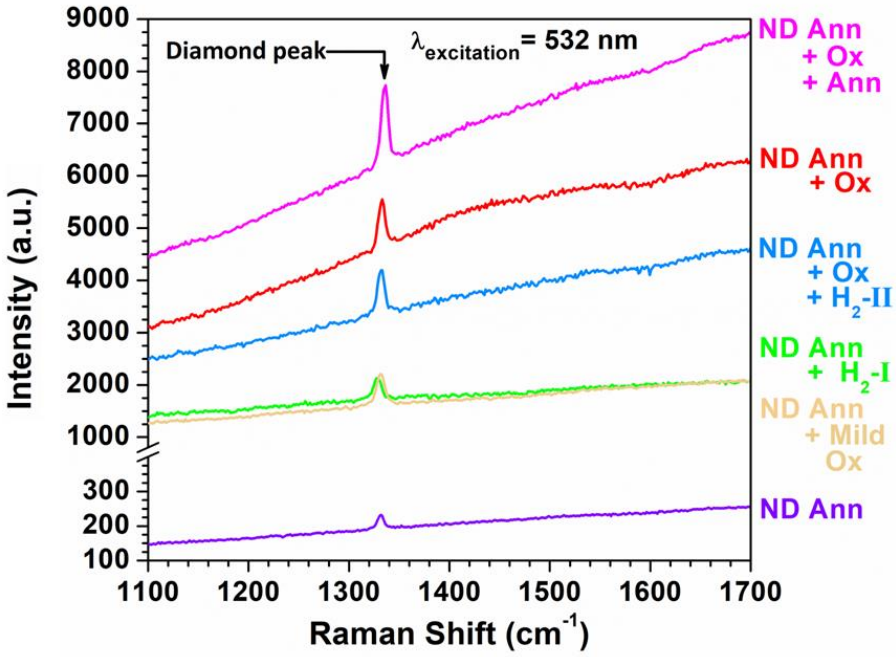

Figure 57-Raman spectra of the [l]ND (240 nm median diameter) samples indicated as ND '*Ann*', ND '*Ann* + *Ox*', ND '*Ann* + *Mild Ox*', ND '*Ann* + *Ox* + *Ann*', ND '*Ann* + H_2-*I*' and ND '*Ann* + *Ox* + H_2-*II*'. The position of the diamond peak is displayed.

Figure 58A shows the |Z| values of the ND '*HT-Ann*' registered after 15 min vacuum exposure. These impedances are equal to the ones measured at non-zero relative humidity, thus indicating that the conductivity of the ND '*HT-Ann*' is water-independent, as confirmed by DRIFT analysis. In the DRIFT spectra from the ND '*HT-Ann*', shown in Figure 58B, the presence of water, as well as that of any relevant surface moiety, is indeed not evident. The conductivity of the ND subjected to the '*HT-Ann*' processes is therefore attributable to the sp^2 phases detected by means of Raman spectroscopy (refer to Figure 34).

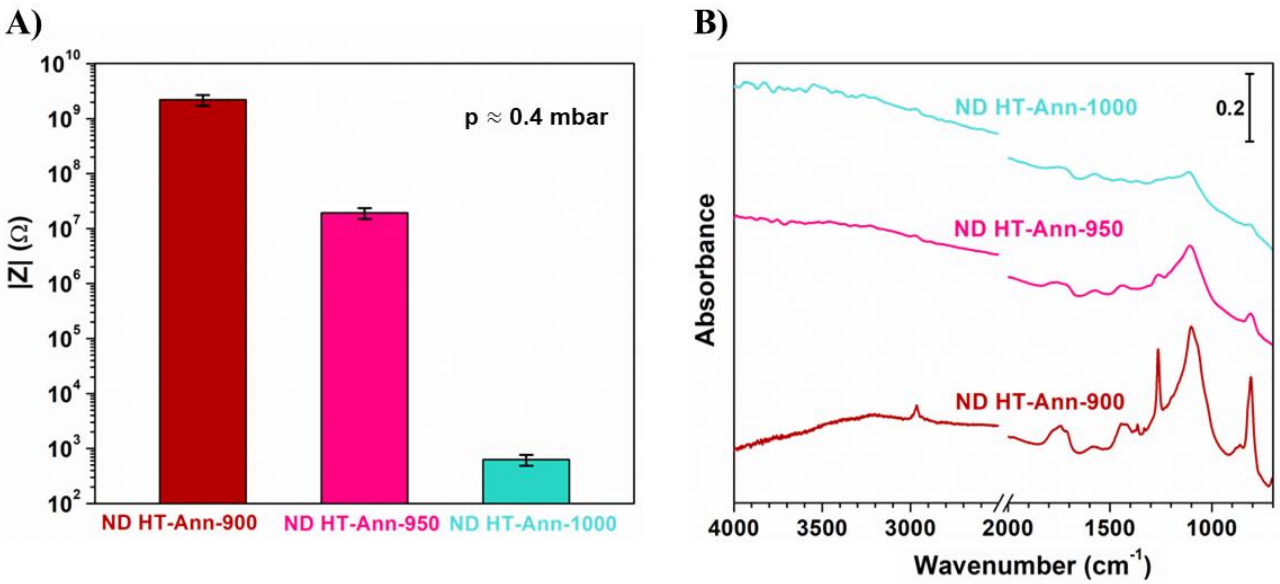

Figure 58-Electrical and spectroscopic characterization of the [1]ND (240 nm median diameter) samples labelled as ND '*HT-Ann*'. A) Values of the impedance of the ND '*HT-Ann*' measured in vacuum (p ≈ 0.4 mbar). B) DRIFT spectra of the ND '*HT-Ann*'.

Appendix C

Figure 59 display the DRIFT spectra of the ^{s}ND (55 nm median diameter) and µD (6 µm) described in sub-section 3.1.2. Besides the spectra of '*Ann* + *Ox*' samples and '*Ann*+ *Ox* + *H₂-II*' samples also those ones of the '*Ann*' samples are shown for sake of comparison.

From Figure 59A it is possible to notice that the spectra of the ^{s}ND exhibit several analogies with those of sub-section 3.1.1 collected from ^{l}ND (displayed in Figure 32B and Figure 33B). The spectrum from ^{s}ND '*Ann*' shows bands in the 2990 cm^{-1} - 2800 cm^{-1} range (labelled as "ν_{C-H}"), attributable to C-H surface bonds. At the same time, such spectrum does not display features neither between 3650 cm^{-1} and 3000 cm^{-1}, which is the region associated to O-H stretching (indicated as "ν_{O-H}"), nor in the spectral range related to C=O stretching (indicated as "$\nu_{C=O}$"). This reveals that both surface adsorbed water and oxygenated surface groups are absent [205–208]. On the other hand, the spectrum of ^{s}ND '*Ann* + *Ox*' is characterized by the disappearance of C-H stretching signals. Additionally, it shows the presence of a broad band in ν_{O-H}, a band at 1800 cm^{-1} in $\nu_{C=O}$, and features in the 1500 cm^{-1} - 1300 cm^{-1} range, which are associated with both oxygenated surface moieties and water adsorbed on the surface [206–208]. Notably, the signature of water on ^{s}ND is evident not only from the O-H stretching band in ν_{O-H}, but also from the signal at 1630 cm^{-1}, which is ascribed to the H-O-H bending mode [205]. The high surface hydrophilicity of ^{s}ND '*Ann* + *Ox*', resulting from oxygen-containing groups, is hence confirmed. Finally, the spectrum of ^{s}ND '*Ann* + *Ox* + *H₂-II*' features prominent C-H stretching bands, along with the suppression of water-related and oxygenated moieties-related bands, thus confirming the formation of hydrophobic surface hydrogen terminations.

Similar considerations to the ones discussed for the spectra from ^{s}ND and ^{l}ND can be applied to the one from µDs, presented in Figure 59B. Notably, a broad feature in the 2700 cm^{-1} - 1900 cm^{-1} spectral range and two bands at 1344 cm^{-1} and 1130 cm^{-1} are visible in all of them. While the former is linked to vibrations of the diamond lattice, the bands at 1344 cm^{-1} and 1130 cm^{-1} are attributed to nitrogen impurities [228,229]. These bands are typically observed in bulk diamond [228,229] and the fact that they could be detected also in µDs is due to their bigger size compared to ^{s}ND and ^{l}ND, resulting in a greater similarity of these particles with a large crystal. The spectra from µD '*Ann*' and µD '*Ann* + *Ox* + *H₂-II*' are featured by defined C-H stretching bands and irrelevant signals in ν_{O-H} and $\nu_{C=O}$. The spectrum from µD '*Ann* + *Ox*' instead shows extremely faint bands in ν_{C-H} and detectable signals ascribable to O-H and C=O stretching, as well as the band at 1630 cm^{-1}, due to water H-O-H bending. The effectiveness of '*Ox*' and '*H₂-II*' processes is hence again confirmed.

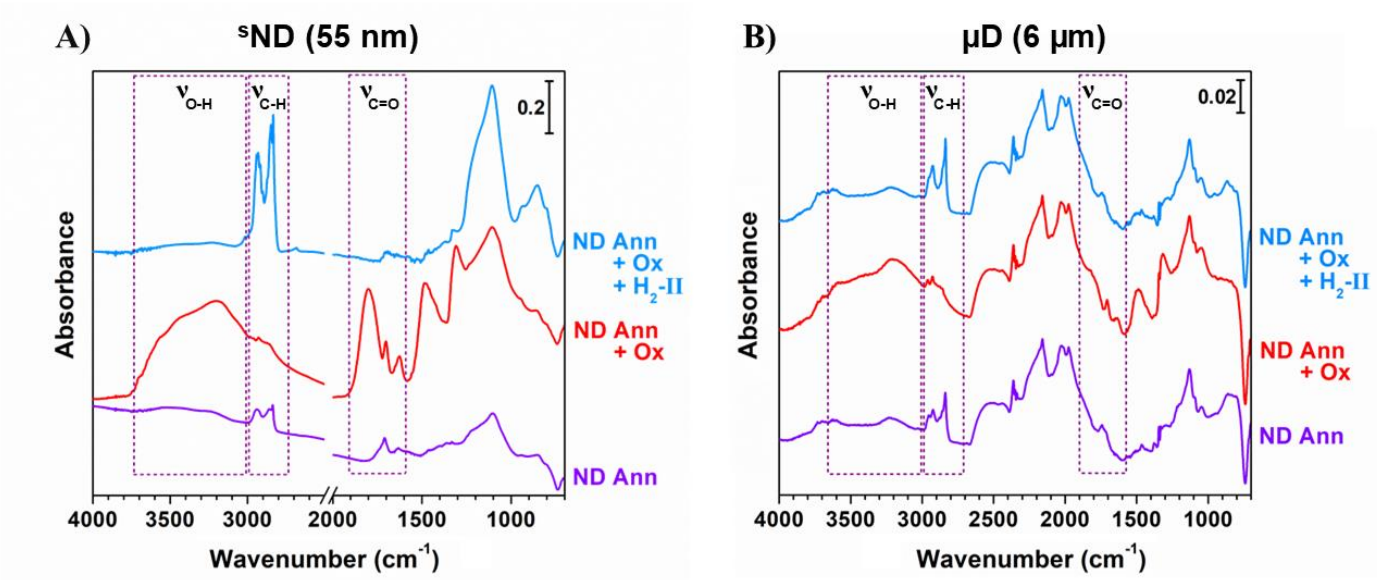

Figure 59-DRIFT spectra of the ˢND (55 nm median diameter) and µD (6 µm) described in section 3.1.2. Besides the spectra of the '*Ann + Ox*' samples and '*Ann + Ox + H_2-II*' samples, also the ones of the '*Ann*' samples are shown for comparison purpose. The regions of O-H stretching (ν_{O-H}), C-H stretching (ν_{C-H}) and C=O stretching ($\nu_{C=O}$) are marked with dashed contours rectangles. A) DRIFT spectra of the ˢND. B) DRIFT spectra of the µD.

Appendix D

This appendix presents the results of additional characterizations related to section 3.2, regarding the functionalization of thermally treated ^{s}ND (55 nm median diameter) with a HA/DMPE conjugate.

Figure 60 reports the DRIFT spectra of the ND_{Ox} functionalized by employing different HA/DMPE:ND weight ratios, namely 1:5, 1:10 and 1:15 (the samples are respectively indicated as HA-$ND_{Ox\_1:5}$, HA-$ND_{Ox\_1:10}$, and HA-$ND_{Ox\_1:15}$), along with that of the bare ND_{Ox} and of pure HA. As discussed in sub-section 3.2.2 in relation to ND DRIFT spectroscopy characterization, reducing the amount of conjugate relative to the particles results in a noticeable decrease in the intensity of the bands associated with HA in the hyaluronated samples. This is particularly evident when focusing on the signals in the 3700 cm^{-1} - 3000 cm^{-1} spectral range and in the 1750 cm^{-1} - 1500 cm^{-1} interval. Such observations confirm that the presence of new spectral features in the HA-decorated ND is due to the attachment of HA on the surface of the ND, allowing to further validate the conclusions discussed in sub-section 3.2.2 on the efficacy of the functionalization approach.

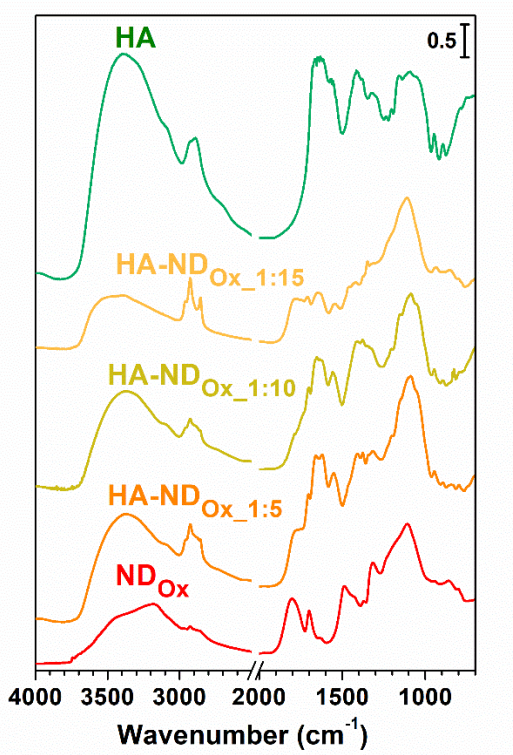

Figure 60-DRIFT spectra of ND_{Ox} (^{s}ND; 55 nm median diameter) functionalized by employing different HA/DMPE:ND weight ratios , *i.e.*, 1:5 (HA-$ND_{Ox\_1:5}$), 1:10 (HA-$ND_{Ox\_1:10}$) and 1:15 (HA-$ND_{Ox\_1:15}$). Also the spectra of bare ND_{Ox} and of pure HA are reported for comparison. The spectrum labeled as "HA-$ND_{Ox\_1:5}$" is the one indicated simply as "HA-ND_{Ox}" in the main text.

Figure 61 presents the results of cell viability assays conducted on human pancreatic adenocarcinoma cells Capan-1 (characterized by low CD44 receptor expression; $CD44^{low}$) and PANC-1 (characterized

by high CD44 receptor expression; CD44^{high}), as well as human breast cancer cells MCF-7 (CD44^{low}) and MDA-MB-231 (CD44^{high}). As highlighted in the discussion of the graphs in Figure 45 (in sub-section 3.2.3), the data show that viability reductions do not exceed 30% across all the tested time points, concentration conditions, and cell types, underscoring the biocompatibility of the particles in all the examined cases.

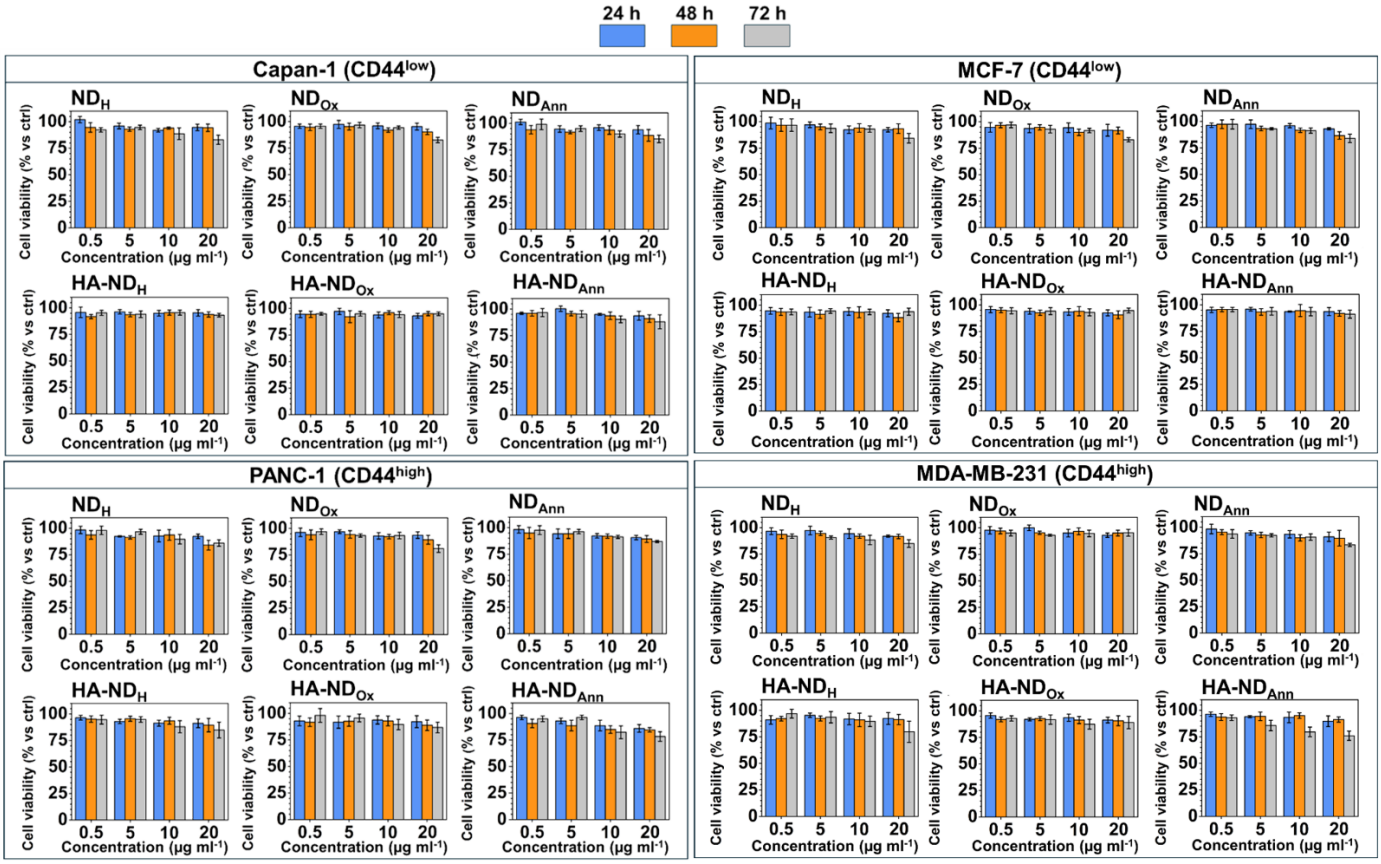

Figure 61-Viability values at 24 h, 48 h and 72 h measured for human pancreatic adenocarcinoma cells Capan-1 (CD44^{low}) and PANC-1 (CD44^{high}), and human breast cancer cells MCF-7 (CD44^{low}) and MDA-MB-231 (CD44^{high}) incubated with ND_{Ann}, ND_H, ND_{Ox}, HA-ND_{Ann}, HA-ND_H and HA-ND_{Ox} (^{s}ND; 55 nm median diameter) at 0.5 μg ml^{-1}, 5 μg ml^{-1}, 10 μg m^{-1}, and 20 μg ml^{-1}. The results were obtained *via* chemiluminescence-based assay performed in triplicate (n = 3 independent experiments).

Figure 62 presents the results of ND cellular uptake measurements conducted on human pancreatic adenocarcinoma cells Capan-1 (CD44^{low}) and PANC-1 (CD44^{high}), as well as human breast cancer cells MCF-7 (CD44^{low}) and MDA-MB-231 (CD44^{high}). As mentioned in connection with the data concerning Calu-3 (CD44^{low}) and A549 (CD44^{high}) lung cancer cells (in sub-section 3.2.3), particles uptake rises with increasing ND concentration and incubation time also in these cell models. For the bare ND, no significant differences in uptake are registered by varying CD44 expression from high to low, while a lower internalization is observed for ND_{Ox} compared to ND_{Ann} and $ND_{H\ in}$ PANC-1

(CD44^{high}) and MDA-MB-231 (CD44^{high}) cells, probably due to their negative surface charge hindering interactions with cells surface [216,217]. On the other hand, for the hyaluronated ND the uptake in CD44^{low} cells is similar though slightly increased with respect to that of their non-functionalized counterparts. Notably, a significant reduction in their uptake at 24 h can be observed when CD44-blocking antibody or excess HA are present. This decrease become more prominent when considering CD44^{high} cells, where also the difference in the uptake between HA-decorated ND and non-functionalized ones is enhanced. As commented in the main text, the results of uptake measurements allow to confirm that functionalization with HA increases the internalization of ND in CD44-rich cells, demonstrating that they can be effectively targeted by these particles.

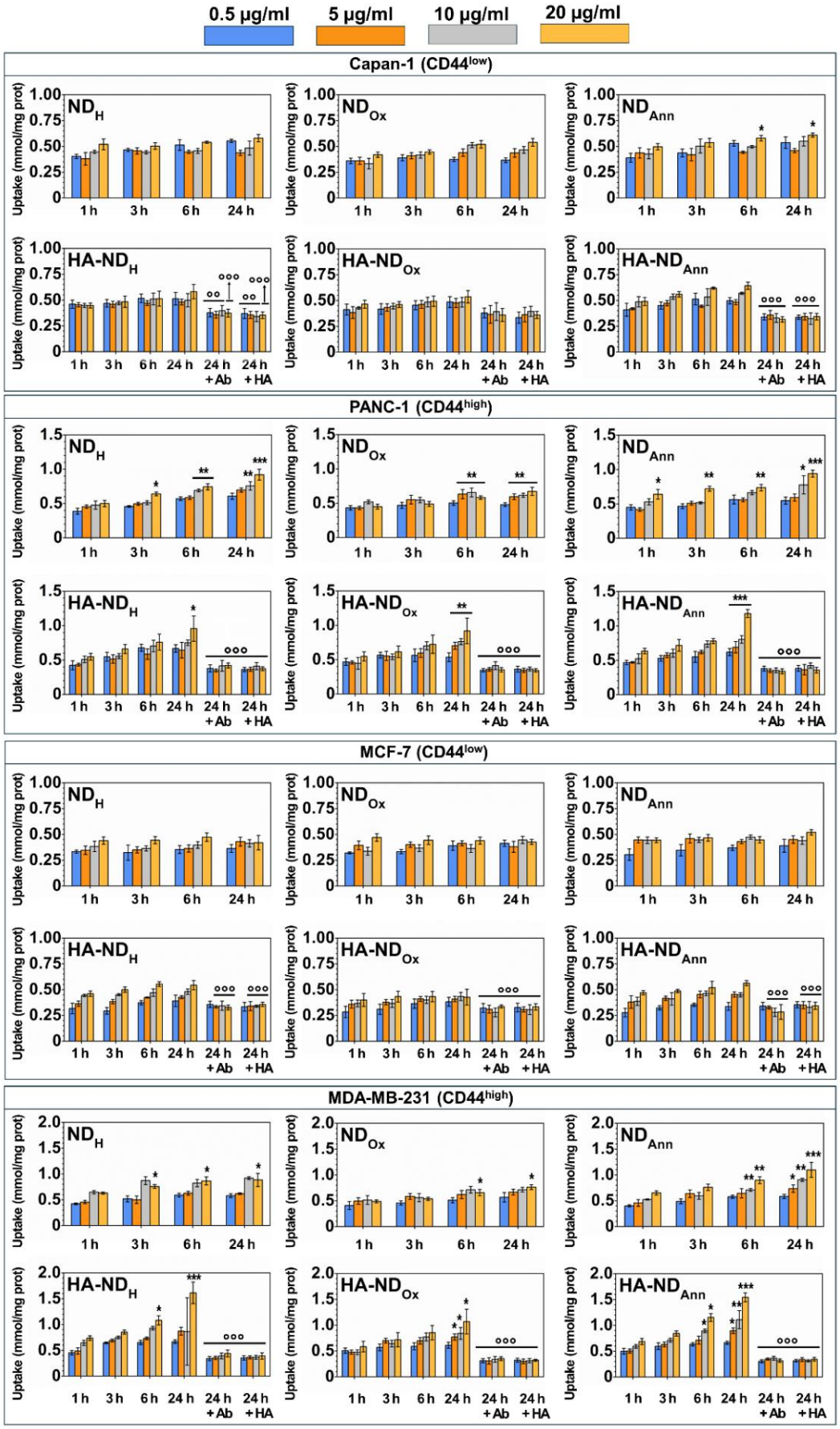

Figure 62-Uptake of ND_{Ann}, ND_H, ND_{Ox}, HA-ND_{Ann}, HA-ND_H and HA-ND_{Ox} (^{s}ND; 55 nm median diameter) at 0.5 µg ml^{-1}, 5 µg ml^{-1}, 10 µg ml^{-1}, and 20 µg ml^{-1}, after 1 h, 3 h, 6 h, and 24 in non-small human pancreatic adenocarcinoma

cancer cells Capan-1 ($CD44^{low}$) and PANC-1 ($CD44^{high}$), and human breast cancer cells MCF-7 ($CD44^{low}$) and MDA-MB-231 ($CD44^{high}$). The results were obtained by a fluorimetry-based assay performed in triplicate (n = 3 independent experiments). When indicated, an anti-CD44 neutralizing antibody (labelled as Ab and diluted 1:100) or 100 μM hyaluronic acid (HA) were co-incubated. Significance levels are indicated with asterisks (*) or circles (○). The asterisks refer to comparisons between cells treated with ND and control sample (ND-free cells): *$p < 0.05$; ***$p < 0.001$. The circles refer instead to comparisons between the cells treated with Ab/HA and the cells without Ab/HA: ○○$p < 0.01$; ○○○$p < 0.001$.

Publications

1. **S. Sturari**, V. Varzi, P. Aprà, A. Britel, N.-H. Amine, G. Andrini, E. Corte, G. Tomagra, L. Mino, P. Olivero, F. Picollo, A comprehensive study of the effect of thermally induced surface terminations on nanodiamonds electrical properties, Surfaces and Interfaces, 38, 2023, 102831, ISSN 2468-0230, https://doi.org/10.1016/j.surfin.2023.102831.

2. **S. Sturari**, V. Varzi, P. Aprà, G. Tomagra, V. Monti, V. Bincoletto, B. Zurletti, E. A. Durisi, S. Arpicco, C. Riganti, P. Olivero, F. Picollo, Functionalization of nanodiamonds with hyaluronic acid: a study for their potential applications in radiosensitization and selective tumor detection Proceedings of the workshop NANO23@uniVR European Journal of Histochemistry 2023 (Proceedings of the workshop NANO23@uniVR), vol.67, 2023, 4991, https://doi.org/10.4081/ejh.2023.3778

3. **S. Sturari**, I. Andreana, P. Aprà, V. Bincoletto, J. Kopecka, L. Mino, B. Zurletti, B. Stella, C. Riganti, S. Arpicco, F. Picollo, Designing Functionalized Nanodiamonds with Hyaluronic Acid-Phospholipid Conjugates for Enhanced Cancer Cell Targeting and Fluorescence Imaging Capabilities, Nanoscale, 2024,16, 11610-11622. https://doi.org/10.1039/D4NR00932K

4. P. Aprà, L. Mino, A. Battiato, P. Olivero, **S. Sturari**, M. C. Valsania, V. Varzi, F. Picollo, "Interaction of Nanodiamonds with Water: Impact of Surface Chemistry on Hydrophilicity, Aggregation and Electrical Properties", Nanomaterials, 11, 2740, 2021, https://www.mdpi.com/2079-4991/11/10/2740

5. V. Varzi, E. Fratini, M. Falconieri, D. Giovannini, A. Cemmi, J. Scifo, I. Di Sarcina , P. Aprà, **S. Sturari**, L. Mino, G. Tomagra, E. Infusino, V. Landoni, C. Marino, M. Mancuso, F. Picollo and S. Pazzaglia, Nanodiamond Effects on Cancer Cell Radiosensitivity: The Interplay between Their Chemical/Physical Characteristics and the Irradiation Energy, International Journal of Molecular Sciences, 24, 2023, 16622, https://doi.org/10.3390/ijms242316622

6. G. Tomagra, A. Re, V. Varzi, P. Aprà, A. Britel, C. Franchino, **S. Sturari**, N.-H. Amine, R. H. S. Westerink, V. Carabelli, F. Picollo, Enhancing the Study of Quantal Exocytotic Events: Combining Diamond Multi–Electrode Arrays with Amperometric Peak Analysis (APE) an Automated Analysis Code, Biosensors, 13, 2023, 1033, https://doi.org/10.3390/bios13121033

7. A. Britel, G. Tomagra, P. Aprà, V. Varzi, **S. Sturari**, N.-H. Amine, P. Olivero, F. Picollo, 3D printing in microfluidics: experimental optimization of droplet size and generation time

through flow focusing, phase, and geometry variation, RSC Advances, 2024, 14, 7770–7778. https://doi.org/10.1039/d4ra00752b

8. P. Aprà, N.-H. Amine, A. Britel, **S. Sturari**, V. Varzi, M. Ziino, L. Mino, P. Olivero, F. Picollo, Creation, Control, and Modeling of NV Centers in Nanodiamonds, Advanced Functional Materials, 2024, 2404831. https://doi.org/10.1002/adfm.202404831

9. G. Zanelli, G. Andrini, P. Aprà, A. Britel, M. Campostrini, D. Carlucci, E. Corte, I. Degiovanni, M. Genovese, L. La Torre, E. Moreva, E. Nieto Hernández, V. Rigato, **S. Sturari**, P. Traina, V. Varzi, P. Olivero, J. Forneris, F. Picollo, S. Ditalia Tchernij, Optical characterization of MeV He-implanted SiC upon laser annealing treatment, *LNL annual Report 2021*, 2022, 74-77 (2022)

References

[1] A.J.P.O. de Almeida, J.C.P.L. de Oliveira, L.V. da Silva Pontes, J.F. de Souza Júnior, T.A.F. Gonçalves, S.H. Dantas, M.S. de Almeida Feitosa, A.O. Silva, I.A. de Medeiros, ROS: Basic Concepts, Sources, Cellular Signaling, and its Implications in Aging Pathways, Oxid. Med. Cell. Longev. 2022 (2022) 1–23. https://doi.org/10.1155/2022/1225578.

[2] A. Rauf, A.A. Khalil, S. Awadallah, S.A. Khan, T. Abu-Izneid, M. Kamran, H.A. Hemeg, M.S. Mubarak, A. Khalid, P. Wilairatana, Reactive oxygen species in biological systems: Pathways, associated diseases, and potential inhibitors—A review, Food Sci. Nutr. 12 (2024) 675–693. https://doi.org/10.1002/fsn3.3784.

[3] D. Chapelot, K. Charlot, Physiology of energy homeostasis: Models, actors, challenges and the glucoadipostatic loop, Metabolism. 92 (2019) 11–25. https://doi.org/10.1016/j.metabol.2018.11.012.

[4] C.A. Juan, J.M. Pérez de la Lastra, F.J. Plou, E. Pérez-Lebeña, The Chemistry of Reactive Oxygen Species (ROS) Revisited: Outlining Their Role in Biological Macromolecules (DNA, Lipids and Proteins) and Induced Pathologies, Int. J. Mol. Sci. 22 (2021) 4642. https://doi.org/10.3390/ijms22094642.

[5] B. Castro, M. Citterico, S. Kimura, D.M. Stevens, M. Wrzaczek, G. Coaker, Stress-induced reactive oxygen species compartmentalization, perception and signalling, Nat. Plants. 7 (2021) 403–412. https://doi.org/10.1038/s41477-021-00887-0.

[6] H. Sies, V. V. Belousov, N.S. Chandel, M.J. Davies, D.P. Jones, G.E. Mann, M.P. Murphy, M. Yamamoto, C. Winterbourn, Defining roles of specific reactive oxygen species (ROS) in cell biology and physiology, Nat. Rev. Mol. Cell Biol. 23 (2022) 499–515. https://doi.org/10.1038/s41580-022-00456-z.

[7] B. Baselet, C. Rombouts, A.M. Benotmane, S. Baatout, A. Aerts, Cardiovascular diseases related to ionizing radiation: The risk of low-dose exposure (Review), Int. J. Mol. Med. 38 (2016) 1623–1641. https://doi.org/10.3892/ijmm.2016.2777.

[8] B. Perillo, M. Di Donato, A. Pezone, E. Di Zazzo, P. Giovannelli, G. Galasso, G. Castoria, A. Migliaccio, ROS in cancer therapy: the bright side of the moon, Exp. Mol. Med. 52 (2020) 192–203. https://doi.org/10.1038/s12276-020-0384-2.

[9] Q. Zhang, Q. Luo, Z. Liu, M. Sun, X. Dong, Nano-ROS-generating approaches to cancer dynamic therapy: Lessons from nanoparticles, Chem. Eng. J. 457 (2023) 141225. https://doi.org/10.1016/j.cej.2022.141225.

[10] V. Nogueira, N. Hay, Molecular Pathways: Reactive Oxygen Species Homeostasis in Cancer Cells and Implications for Cancer Therapy, Clin. Cancer Res. 19 (2013) 4309–4314. https://doi.org/10.1158/1078-0432.CCR-12-1424.

[11] Z. Zou, H. Chang, H. Li, S. Wang, Induction of reactive oxygen species: an emerging approach for cancer therapy, Apoptosis. 22 (2017) 1321–1335. https://doi.org/10.1007/s10495-017-1424-9.

[12] R. Baskar, K.A. Lee, R. Yeo, K.W. Yeoh, Cancer and radiation therapy: Current advances and future directions, Int. J. Med. Sci. 9 (2012) 193–199. https://doi.org/10.7150/ijms.3635.

[13] U. Amaldi, G. Kraft, Radiotherapy with beams of carbon ions, Reports Prog. Phys. 68 (2005) 1861–1882. https://doi.org/10.1088/0034-4885/68/8/R04.

[14] P.K. Agarwalla, T.J. Royce, M.J. Koch, J. Daartz, J.S. Loeffler, Application of Current Radiation Delivery Systems and Radiobiology, in: Princ. Neurol. Surg., Fourth Edi, Elsevier Inc., 2018: pp. 714-726.e2. https://doi.org/10.1016/B978-0-323-43140-8.00050-0.

[15] O. Desouky, N. Ding, G. Zhou, Targeted and non-targeted effects of ionizing radiation, J. Radiat. Res. Appl. Sci. 8 (2015) 247–254. https://doi.org/10.1016/j.jrras.2015.03.003.

[16] and A.W. M. Tubiana, J. Dutreix, Introduction to radiobiology, Taylor & Francis, 1990. https://doi.org/10.1080/09553009214551901.

[17] L. Shirley, Biomolecular Action of Ionizing Radiation, Taylor & Francis, 2007.

[18] J.E. Turner, Interaction of Ionizing Radiation with Matter, Health Phys. 86 (2004) 228–252. https://doi.org/10.1016/B978-0-444-53632-7.00920-5.

[19] Illustration of photoelectric effect and Compton effect, (n.d.). https://epos.myesr.org/posterimage/esr/ecr2018/143546/mediagallery/764967?deliveroriginal=1.

[20] Z. Kuncic, S. Lacombe, Nanoparticle radio-enhancement: Principles, progress and application to cancer treatment, Phys. Med. Biol. 63 (2018). https://doi.org/10.1088/1361-6560/aa99ce.

[21] The 2007 Recommendations of the Internal Commission on Radiological Protection, 103. (2007).

[22] S. Le Caër, Water radiolysis: Influence of oxide surfaces on H2 production under ionizing radiation, Water. 3

(2011) 235–253. https://doi.org/10.3390/w3010235.
[23] H. Wang, X. Mu, H. He, X.D. Zhang, Cancer Radiosensitizers, Trends Pharmacol. Sci. 39 (2018) 24–48. https://doi.org/10.1016/j.tips.2017.11.003.
[24] L. Gong, Y. Zhang, C. Liu, M. Zhang, S. Han, Application of Radiosensitizers in Cancer Radiotherapy, Int. J. Nanomedicine. Volume 16 (2021) 1083–1102. https://doi.org/10.2147/IJN.S290438.
[25] M.A. Kebede, T. Imae, Low-Dimensional Nanomaterials, in: K. Ariga, M. Aono (Eds.), Adv. Supramol. Nanoarchitectonics, William Andrew Publishing, 2019: pp. 3–16. https://doi.org/https://doi.org/10.1016/B978-0-12-813341-5.00001-2.
[26] J. Fang, H. Nakamura, H. Maeda, The EPR effect: Unique features of tumor blood vessels for drug delivery, factors involved, and limitations and augmentation of the effect, Adv. Drug Deliv. Rev. 63 (2011) 136–151. https://doi.org/10.1016/j.addr.2010.04.009.
[27] Z. Ferdous, A. Nemmar, Health Impact of Silver Nanoparticles: A Review of the Biodistribution and Toxicity Following Various Routes of Exposure, Int. J. Mol. Sci. 21 (2020) 2375. https://doi.org/10.3390/ijms21072375.
[28] M. Jeyaraj, S. Gurunathan, M. Qasim, M.-H. Kang, J.-H. Kim, A Comprehensive Review on the Synthesis, Characterization, and Biomedical Application of Platinum Nanoparticles, Nanomaterials. 9 (2019) 1719. https://doi.org/10.3390/nano9121719.
[29] J.F. Hainfeld, D.N. Slatkin, H.M. Smilowitz, The use of gold nanoparticles to enhance radiotherapy in mice, Phys. Med. Biol. 49 (2004) N309–N315. https://doi.org/10.1088/0031-9155/49/18/N03.
[30] X.D. Zhang, Z. Luo, J. Chen, S. Song, X. Yuan, X. Shen, H. Wang, Y. Sun, K. Gao, L. Zhang, S. Fan, D.T. Leong, M. Guo, J. Xie, Ultrasmall glutathione-protected gold nanoclusters as next generation radiotherapy sensitizers with high tumor uptake and high renal clearance, Sci. Rep. 5 (2015) 1–7. https://doi.org/10.1038/srep08669.
[31] Y.S. Lee, D.W. Kim, Y.H. Lee, J.H. Oh, S. Yoon, M.S. Choi, S.K. Lee, J.W. Kim, K. Lee, C.-W. Song, Silver nanoparticles induce apoptosis and G2/M arrest via PKCζ-dependent signaling in A549 lung cells, Arch. Toxicol. 85 (2011) 1529–1540. https://doi.org/10.1007/s00204-011-0714-1.
[32] C.J. Labrador-Rached, R.T. Browning, L.K. Braydich-Stolle, K.K. Comfort, Toxicological Implications of Platinum Nanoparticle Exposure: Stimulation of Intracellular Stress, Inflammatory Response, and Akt Signaling In Vitro, J. Toxicol. 2018 (2018) 1–8. https://doi.org/10.1155/2018/1367801.
[33] M. van der Zande, R.J. Vandebriel, E. Van Doren, E. Kramer, Z. Herrera Rivera, C.S. Serrano-Rojero, E.R. Gremmer, J. Mast, R.J.B. Peters, P.C.H. Hollman, P.J.M. Hendriksen, H.J.P. Marvin, A.A.C.M. Peijnenburg, H. Bouwmeester, Distribution, Elimination, and Toxicity of Silver Nanoparticles and Silver Ions in Rats after 28-Day Oral Exposure, ACS Nano. 6 (2012) 7427–7442. https://doi.org/10.1021/nn302649p.
[34] M. Stefan, V. Melnig, D. Pricop, A. Neagu, M. Mihasan, L. Tartau, L. Hritcu, Attenuated effects of chitosan-capped gold nanoparticles on LPS-induced toxicity in laboratory rats, Mater. Sci. Eng. C. 33 (2013) 550–556. https://doi.org/10.1016/j.msec.2012.09.031.
[35] V.N. Mochalin, O. Shenderova, D. Ho, Y. Gogotsi, The properties and applications of nanodiamonds, Nat. Nanotechnol. 7 (2012) 11–23. https://doi.org/10.1038/nnano.2011.209.
[36] R. Grall, H. Girard, L. Saad, T. Petit, C. Gesset, M. Combis-Schlumberger, V. Paget, J. Delic, J.C. Arnault, S. Chevillard, Impairing the radioresistance of cancer cells by hydrogenated nanodiamonds, Biomaterials. 61 (2015) 290–298. https://doi.org/10.1016/j.biomaterials.2015.05.034.
[37] M. Kurzyp, H.A. Girard, Y. Cheref, E. Brun, C. Sicard-Roselli, S. Saada, J.C. Arnault, Hydroxyl radical production induced by plasma hydrogenated nanodiamonds under X-ray irradiation, Chem. Commun. 53 (2017) 1237–1240. https://doi.org/10.1039/c6cc08895c.
[38] A. Mzyk, A. Sigaeva, R. Schirhagl, Relaxometry with Nitrogen Vacancy (NV) Centers in Diamond, Acc. Chem. Res. 55 (2022) 3572–3580. https://doi.org/10.1021/acs.accounts.2c00520.
[39] Y. Zhang, M. Dai, Z. Yuan, Methods for the detection of reactive oxygen species, Anal. Methods. 10 (2018) 4625–4638. https://doi.org/10.1039/C8AY01339J.
[40] N. Soh, Recent advances in fluorescent probes for the detection of reactive oxygen species, Anal. Bioanal. Chem. 386 (2006) 532–543. https://doi.org/10.1007/s00216-006-0366-9.
[41] K.K. Griendling, R.M. Touyz, J.L. Zweier, S. Dikalov, W. Chilian, Y.-R. Chen, D.G. Harrison, A. Bhatnagar, Measurement of Reactive Oxygen Species, Reactive Nitrogen Species, and Redox-Dependent Signaling in the Cardiovascular System, Circ. Res. 119 (2016) e39–e75. https://doi.org/10.1161/RES.0000000000000110.
[42] P.K. Javvaji, A. Dhali, J.R. Francis, A.P. Kolte, A. Mech, S.C. Roy, A. Mishra, R. Bhatta, An Efficient Nitroblue

Tetrazolium Staining and Bright-Field Microscopy Based Method for Detecting and Quantifying Intracellular Reactive Oxygen Species in Oocytes, Cumulus Cells and Embryos, Front. Cell Dev. Biol. 8 (2020) 1–12. https://doi.org/10.3389/fcell.2020.00764.

[43] C.P. Rubio, J.J. Cerón, Spectrophotometric assays for evaluation of Reactive Oxygen Species (ROS) in serum: general concepts and applications in dogs and humans, BMC Vet. Res. 17 (2021) 226. https://doi.org/10.1186/s12917-021-02924-8.

[44] A.S. Deshpande, W. Muraoka, S. Andreescu, Electrochemical sensors for oxidative stress monitoring, Curr. Opin. Electrochem. 29 (2021) 100809. https://doi.org/10.1016/j.coelec.2021.100809.

[45] M. Ganesana, J.S. Erlichman, S. Andreescu, Real-time monitoring of superoxide accumulation and antioxidant activity in a brain slice model using an electrochemical cytochrome c biosensor, Free Radic. Biol. Med. 53 (2012) 2240–2249. https://doi.org/10.1016/j.freeradbiomed.2012.10.540.

[46] M. Katerji, M. Filippova, P. Duerksen-Hughes, Approaches and Methods to Measure Oxidative Stress in Clinical Samples: Research Applications in the Cancer Field, Oxid. Med. Cell. Longev. 2019 (2019) 1–29. https://doi.org/10.1155/2019/1279250.

[47] M.M. Roessler, E. Salvadori, Principles and applications of EPR spectroscopy in the chemical sciences, Chem. Soc. Rev. 47 (2018) 2534–2553. https://doi.org/10.1039/C6CS00565A.

[48] S. Zhao, G. Zang, Y. Zhang, H. Liu, N. Wang, S. Cai, C. Durkan, G. Xie, G. Wang, Recent advances of electrochemical sensors for detecting and monitoring ROS/RNS, Biosens. Bioelectron. 179 (2021) 113052. https://doi.org/10.1016/j.bios.2021.113052.

[49] Y. Tian, A.C. Nusantara, T. Hamoh, A. Mzyk, X. Tian, F. Perona Martinez, R. Li, H.P. Permentier, R. Schirhagl, Functionalized Fluorescent Nanodiamonds for Simultaneous Drug Delivery and Quantum Sensing in HeLa Cells, ACS Appl. Mater. Interfaces. 14 (2022) 39265–39273. https://doi.org/10.1021/acsami.2c11688.

[50] H.T. Li, R. Schirhagl, J. Eliveld, C. Reyes-San-Martin, I. Pronk, A. Hoek, A.E.P. Cantineau, A. Mzyk, Measuring free radicals with relaxometry: Pioneering steps for measurements in human semen, Diam. Relat. Mater. 140 (2023) 110388. https://doi.org/10.1016/j.diamond.2023.110388.

[51] A. Sigaeva, H. Shirzad, F.P. Martinez, A.C. Nusantara, N. Mougios, M. Chipaux, R. Schirhagl, Diamond-Based Nanoscale Quantum Relaxometry for Sensing Free Radical Production in Cells, Small. 18 (2022). https://doi.org/10.1002/smll.202105750.

[52] F. Perona Martínez, A.C. Nusantara, M. Chipaux, S.K. Padamati, R. Schirhagl, Nanodiamond Relaxometry-Based Detection of Free-Radical Species When Produced in Chemical Reactions in Biologically Relevant Conditions, ACS Sensors. 5 (2020) 3862–3869. https://doi.org/10.1021/acssensors.0c01037.

[53] H.O. Pierson, Handbook of Carbon, Graphite, Diamonds and Fullerenes, Noyes Publications, 1993. https://doi.org/10.1016/B978-0-8155-1339-1.50008-6.

[54] S. Ferro, Synthesis of diamond, J. Mater. Chem. 12 (2002) 2843–2855. https://doi.org/10.1039/b204143j.

[55] J.M. Zazula, On Graphite Transformations at High Temperature and Pressure Induced by Absorption of the LHC Beam, LHC Proj. Note n.78. (1997).

[56] M. Manutchehr-Danai, ed., Mohs' scale of hardness, in: Dict. Gems Gemol., Springer Berlin Heidelberg, Berlin, Heidelberg, 2009: p. 578. https://doi.org/10.1007/978-3-540-72816-0_14590.

[57] D.R. L. Tang, C. Tsai, W.W. Gerbeich, L Kruckeber, Kania, Biocompatibility of chemical-vapour-deposited diamond, Biomaterials. 16 (1995) 483–488.

[58] A.M. Zaitsev, Optical Properties of Diamond, Springer, 2001. https://link.aps.org/doi/10.1103/PhysRevLett.1.131.

[59] O.S. Okwundu, E.U. Aniekwe, C.E. Nwanno, Unlimited potentials of carbon: different structures and uses (a Review), Metall. Mater. Eng. 24 (2018) 145–171. https://doi.org/10.30544/388.

[60] R. Md Nor, S. Abu Bakar, T.M. Thandavan, M. Rusop, Diamond: Synthesis, Characterisation and Applications, in: Adv. Struct. Mater., 2010: pp. 195–217. http://www.springer.com/series/8611.

[61] J. Ristein, Diamond surfaces: Familiar and amazing, Appl. Phys. A Mater. Sci. Process. 82 (2006) 377–384. https://doi.org/10.1007/s00339-005-3363-5.

[62] Y. Kato, T. Teraji, Key technologies for device fabrications and materials characterizations, in: S. Koizumi, H. Umezawa, J. Pernot, M. Suzuki (Eds.), Power Electron. Device Appl. Diam. Semicond., Woodhead Publishing, 2018: pp. 219–294. https://doi.org/https://doi.org/10.1016/B978-0-08-102183-5.00004-2.

[63] G. Alba, M. Pilar Villar, R. Alcántara, J. Navas, D. Araujo, Surface states of (100) O-terminated diamond: Towards other 1 × 1:O reconstruction models, Nanomaterials. 10 (2020) 1–15.

https://doi.org/10.3390/nano10061193.
[64] F. Maier, J. Ristein, L. Ley, Electron affinity of plasma-hydrogenated and chemically oxidized diamond (100) surfaces, Phys. Rev. B - Condens. Matter Mater. Phys. 64 (2001) 1–7. https://doi.org/10.1103/PhysRevB.64.165411.
[65] J. Ristein, The physics of hydrogen-terminated diamond surfaces, in: AIP Conf. Proc., 2005: pp. 377–380. https://doi.org/10.1063/1.1994145.
[66] V. Seshan, D. Ullien, A. Castellanos-Gomez, S. Sachdeva, D.H.K. Murthy, T.J. Savenije, H.A. Ahmad, T.S. Nunney, S.D. Janssens, K. Haenen, M. Nesládek, H.S.J. Van Der Zant, E.J.R. Sudhölter, L.C.P.M. De Smet, Hydrogen termination of CVD diamond films by high-temperature annealing at atmospheric pressure, J. Chem. Phys. 138 (2013). https://doi.org/10.1063/1.4810866.
[67] F. Maier, M. Riedel, B. Mantel, J. Ristein, L. Ley, Origin of Surface Conductivity in Diamond, Phys. Rev. Lett. 85 (2000) 3472–3475. https://link.aps.org/doi/10.1103/PhysRevLett.87.209705.
[68] L. Ostrovskaya, V. Perevertailo, V. Ralchenko, A. Dementjev, O. Loginova, Wettability and surface energy of oxidized and hydrogen plasma-treated diamond films, Diam. Relat. Mater. 11 (2002) 845–850. https://doi.org/10.1016/S0925-9635(01)00636-7.
[69] Y. Kaibara, K. Sugata, M. Tachiki, H. Umezawa, H. Kawarada, Control wettability of the hydrogen-terminated diamond surface and the oxidized diamond surface using an atomic force microscope, Diam. Relat. Mater. 12 (2003) 560–564. https://doi.org/10.1016/S0925-9635(02)00373-4.
[70] F. Jelezko, J. Wrachtrup, Single defect centres in diamond: A review, Phys. Status Solidi Appl. Mater. Sci. 203 (2006) 3207–3225. https://doi.org/10.1002/pssa.200671403.
[71] F.C. Waldermann, P. Olivero, J. Nunn, K. Surmacz, Z.Y. Wang, D. Jaksch, R.A. Taylor, I.A. Walmsley, M. Draganski, P. Reichart, A.D. Greentree, D.N. Jamieson, S. Prawer, Creating diamond color centers for quantum optical applications, Diam. Relat. Mater. 16 (2007) 1887–1895. https://doi.org/10.1016/j.diamond.2007.09.009.
[72] T. Iwasaki, Y. Miyamoto, T. Taniguchi, P. Siyushev, M.H. Metsch, F. Jelezko, M. Hatano, Tin-Vacancy Quantum Emitters in Diamond, Phys. Rev. Lett. 119 (2017) 253601. https://doi.org/10.1103/PhysRevLett.119.253601.
[73] E. Corte, G. Andrini, E. Nieto Hernández, V. Pugliese, Â. Costa, G. Magchiels, J. Moens, S.M. Tunhuma, R. Villarreal, L.M.C. Pereira, A. Vantomme, J.G. Correia, E. Bernardi, P. Traina, I. Pietro Degiovanni, E. Moreva, M. Genovese, S. Ditalia Tchernij, P. Olivero, U. Wahl, J. Forneris, Magnesium-Vacancy Optical Centers in Diamond, ACS Photonics. 10 (2023) 101–110. https://doi.org/10.1021/acsphotonics.2c01130.
[74] J.N. Becker, E. Neu, The silicon vacancy center in diamond, in: Semicond. Semimetals, 1st ed., Elsevier Inc., 2020: pp. 201–235. https://doi.org/10.1016/bs.semsem.2020.04.001.
[75] G. Thiering, A. Gali, Color centers in diamond for quantum applications, in: Semicond. Semimetals, 2020: pp. 1–36. https://doi.org/10.1016/bs.semsem.2020.03.001.
[76] C. Shi, H. Luo, Z. Xu, F. Fang, Nitrogen-Vacancy Color Centers in Diamond Fabricated by Ultrafast Laser Nanomachining, in: Simul. Exp. Mater. Ultra-Precision Mach., Springer Singapore, 2019: pp. 277–305. https://doi.org/10.1007/978-981-13-3335-4.
[77] M.W. Doherty, N.B. Manson, P. Delaney, F. Jelezko, J. Wrachtrup, L.C.L. Hollenberg, The nitrogen-vacancy colour centre in diamond, Phys. Rep. 528 (2013) 1–45. https://doi.org/10.1016/j.physrep.2013.02.001.
[78] L. Rondin, G. Dantelle, A. Slablab, F. Grosshans, F. Treussart, P. Bergonzo, S. Perruchas, T. Gacoin, M. Chaigneau, H.-C. Chang, V. Jacques, J.-F. Roch, Surface-induced charge state conversion of nitrogen-vacancy defects in nanodiamonds, Phys. Rev. B. 82 (2010) 115449. https://doi.org/10.1103/PhysRevB.82.115449.
[79] F. Treussart, I.I. Vlasov, Photoluminescence of color centers in nanodiamonds, in: J.-C. Arnault (Ed.), Nanodiamonds Adv. Mater. Anal. Prop. Appl., Elsevier, 2017: pp. 155–181. https://doi.org/https://doi.org/10.1016/B978-0-32-343029-6.00007-6.
[80] V. Petráková, A. Taylor, I. Kratochvílová, F. Fendrych, J. Vacík, J. Kučka, J. Štursa, P. Cígler, M. Ledvina, A. Fišerová, P. Kneppo, M. Nesládek, Luminescence of Nanodiamond Driven by Atomic Functionalization: Towards Novel Detection Principles, Adv. Funct. Mater. 22 (2012) 812–819. https://doi.org/10.1002/adfm.201101936.
[81] L. Rondin, J.-P. Tetienne, T. Hingant, J.-F. Roch, P. Maletinsky, V. Jacques, Magnetometry with nitrogen-vacancy defects in diamond, Reports Prog. Phys. 77 (2014) 056503. https://doi.org/10.1088/0034-4885/77/5/056503.
[82] G.-Q. Liu, X.-Y. Pan, Quantum information processing with nitrogen–vacancy centers in diamond, Chinese Phys. B. 27 (2018) 020304. https://doi.org/10.1088/1674-1056/27/2/020304.

[83] J. Harrison, M.. Sellars, N.. Manson, Optical spin polarisation of the N-V centre in diamond, J. Lumin. 107 (2004) 245–248. https://doi.org/10.1016/j.jlumin.2003.12.020.
[84] J.-P. Tetienne, T. Hingant, L. Rondin, A. Cavaillès, L. Mayer, G. Dantelle, T. Gacoin, J. Wrachtrup, J.-F. Roch, V. Jacques, Spin relaxometry of single nitrogen-vacancy defects in diamond nanocrystals for magnetic noise sensing, Phys. Rev. B. 87 (2013) 235436. https://doi.org/10.1103/PhysRevB.87.235436.
[85] E. Janitz, K. Herb, L.A. Völker, W.S. Huxter, C.L. Degen, J.M. Abendroth, Diamond surface engineering for molecular sensing with nitrogen—vacancy centers, J. Mater. Chem. C. 10 (2022) 13533–13569. https://doi.org/10.1039/D2TC01258H.
[86] Magnetometry with single NV centers in diamond, (n.d.). http://www.qolah.org/research/nv_v2/nv_v2.html.
[87] A. Datta, M. Kirca, Y. Fu, A.C. To, Surface structure and properties of functionalized nanodiamonds: a first-principles study, Nanotechnology. 22 (2011) 065706. https://doi.org/10.1088/0957-4484/22/6/065706.
[88] K. van der Laan, M. Hasani, T. Zheng, R. Schirhagl, Nanodiamonds for In Vivo Applications, Small. 14 (2018) 1–17. https://doi.org/10.1002/smll.201703838.
[89] E.A. Ekimov, O.S. Kudryavtsev, N.E. Mordvinova, O.I. Lebedev, I.I. Vlasov, High-Pressure Synthesis of Nanodiamonds from Adamantane: Myth or Reality?, ChemNanoMat. 4 (2018) 269–273. https://doi.org/10.1002/cnma.201700349.
[90] M. Alkahtani, J. Lang, B. Naydenov, F. Jelezko, P. Hemmer, Growth of High-Purity Low-Strain Fluorescent Nanodiamonds, ACS Photonics. 6 (2019) 1266–1271. https://doi.org/10.1021/acsphotonics.9b00224.
[91] M. Frenklach, W. Howard, D. Huang, J. Yuan, K.E. Spear, R. Koba, Induced nucleation of diamond powder, Appl. Phys. Lett. 59 (1991) 546–548. https://doi.org/10.1063/1.105434.
[92] T.L. Daulton, M.A. Kirk, R.S. Lewis, L.E. Rehn, Production of nanodiamonds by high-energy ion irradiation of graphite at room temperature, Nucl. Instruments Methods Phys. Res. Sect. B Beam Interact. with Mater. Atoms. 175–177 (2001) 12–20. https://doi.org/10.1016/S0168-583X(00)00603-0.
[93] G.-W. Yang, J.-B. Wang, Q.-X. Liu, Preparation of nano-crystalline diamonds using pulsed laser induced reactive quenching, J. Phys. Condens. Matter. 10 (1998) 7923–7927. https://doi.org/10.1088/0953-8984/10/35/024.
[94] J. Zheng, B. Lienhard, G. Doerk, M. Cotlet, E. Bersin, H.S. Kim, Y.-C. Byun, C.-Y. Nam, J. Kim, C.T. Black, D. Englund, Top-down fabrication of high-uniformity nanodiamonds by self-assembled block copolymer masks, Sci. Rep. 9 (2019) 6914. https://doi.org/10.1038/s41598-019-43304-5.
[95] V. V. Danilenko, On the history of the discovery of nanodiamond synthesis, Phys. Solid State. 46 (2004) 595–599. https://doi.org/10.1134/1.1711431.
[96] A.M. Panich, A.I. Shames, D. Mogilyansky, S.D. Goren, V.Y. Dolmatov, Detonation nanodiamonds fabricated from tetryl: Synthesis, NMR, EPR and XRD study, Diam. Relat. Mater. 108 (2020) 107918. https://doi.org/10.1016/j.diamond.2020.107918.
[97] J.-P. Boudou, P.A. Curmi, F. Jelezko, J. Wrachtrup, P. Aubert, M. Sennour, G. Balasubramanian, R. Reuter, A. Thorel, E. Gaffet, High yield fabrication of fluorescent nanodiamonds, Nanotechnology. 20 (2009) 235602. https://doi.org/10.1088/0957-4484/20/23/235602.
[98] G. Reina, L. Zhao, A. Bianco, N. Komatsu, Chemical Functionalization of Nanodiamonds: Opportunities and Challenges Ahead, Angew. Chemie Int. Ed. 58 (2019) 17918–17929. https://doi.org/10.1002/anie.201905997.
[99] J.-Y. Lee, D.-S. Lim, Tribological behavior of PTFE film with nanodiamond, Surf. Coatings Technol. 188–189 (2004) 534–538. https://doi.org/10.1016/j.surfcoat.2004.07.102.
[100] C.-C. Chou, S.-H. Lee, Tribological behavior of nanodiamond-dispersed lubricants on carbon steels and aluminum alloy, Wear. 269 (2010) 757–762. https://doi.org/10.1016/j.wear.2010.08.001.
[101] I. Neitzel, V. Mochalin, J.A. Bares, R.W. Carpick, A. Erdemir, Y. Gogotsi, Tribological properties of nanodiamond-epoxy composites, Tribol. Lett. 47 (2012) 195–202. https://doi.org/10.1007/s11249-012-9978-8.
[102] Y. Zhang, J.R. Choi, S.-J. Park, Thermal conductivity and thermo-physical properties of nanodiamond-attached exfoliated hexagonal boron nitride/epoxy nanocomposites for microelectronics, Compos. Part A Appl. Sci. Manuf. 101 (2017) 227–236. https://doi.org/10.1016/j.compositesa.2017.06.019.
[103] Y. Zhang, K.Y. Rhee, D. Hui, S.-J. Park, A critical review of nanodiamond based nanocomposites: Synthesis, properties and applications, Compos. Part B Eng. 143 (2018) 19–27. https://doi.org/10.1016/j.compositesb.2018.01.028.
[104] Z. Li, Y. Wang, M. Ma, H. Ma, W. Hu, X. Zhang, Z. Zhuge, S. Zhang, K. Luo, Y. Gao, L. Sun, A. V. Soldatov, Y. Wu, B. Liu, B. Li, P. Ying, Y. Zhang, B. Xu, J. He, D. Yu, Z. Liu, Z. Zhao, Y. Yue, Y. Tian, X. Li, Ultrastrong conductive in situ composite composed of nanodiamond incoherently embedded in disordered multilayer

graphene, Nat. Mater. 22 (2023) 42–49. https://doi.org/10.1038/s41563-022-01425-9.
[105] Y. Song, H. Li, L. Wang, D. Qiu, Y. Ma, K. Pei, G. Zou, K. Yu, Nanodiamonds: A critical component of anodes for high performance lithium-ion batteries, Chem. Commun. 52 (2016) 10497–10500. https://doi.org/10.1039/c6cc04490e.
[106] H. Wang, Y. Cui, Nanodiamonds for energy, Carbon Energy. 1 (2019) 13–18. https://doi.org/10.1002/cey2.9.
[107] D. Miliaieva, P. Matunova, J. Cermak, S. Stehlik, A. Cernescu, Z. Remes, P. Stenclova, M. Muller, B. Rezek, Nanodiamond surface chemistry controls assembly of polypyrrole and generation of photovoltage, Sci. Rep. 11 (2021) 590. https://doi.org/10.1038/s41598-020-80438-3.
[108] A. Seral-Ascaso, A. Luquin, M.J. Lázaro, G.F. de la Fuente, M. Laguna, E. Muñoz, Synthesis and application of gold-carbon hybrids as catalysts for the hydroamination of alkynes, Appl. Catal. A Gen. 456 (2013) 88–95. https://doi.org/10.1016/j.apcata.2013.02.008.
[109] P.A. Kalmykov, N.A. Magdalinova, M. V. Klyuev, Comparison of palladium catalysts based on nanodiamonds and activated carbon in hydrogenation reactions, Pet. Chem. 55 (2015) 63–67. https://doi.org/10.1134/S0965544115010065.
[110] J. Diao, Z. Feng, R. Huang, H. Liu, S.B.A. Hamid, D.S. Su, Selective and Stable Ethylbenzene Dehydrogenation to Styrene over Nanodiamonds under Oxygen-lean Conditions, ChemSusChem. 9 (2016) 662–666. https://doi.org/10.1002/cssc.201501516.
[111] M. Khan, A. Hayat, S.K. Baburao Mane, T. Li, N. Shaishta, D. Alei, T.K. Zhao, A. Ullah, A. Zada, A. Rehman, W.U. Khan, Functionalized nano diamond composites for photocatalytic hydrogen evolution and effective pollutant degradation, Int. J. Hydrogen Energy. 45 (2020) 29070–29081. https://doi.org/10.1016/j.ijhydene.2020.07.274.
[112] H. Zhang, X. Chen, Z. Yin, Quantum Information Processing and Precision Measurement Using a Levitated Nanodiamond, Adv. Quantum Technol. 4 (2021) 2000154. https://doi.org/10.1002/qute.202000154.
[113] M. Radulaski, J.L. Zhang, Y.K. Tzeng, K.G. Lagoudakis, H. Ishiwata, C. Dory, K.A. Fischer, Y.A. Kelaita, S. Sun, P.C. Maurer, K. Alassaad, G. Ferro, Z.X. Shen, N.A. Melosh, S. Chu, J. Vučković, Nanodiamond Integration with Photonic Devices, Laser Photonics Rev. 13 (2019) 1–14. https://doi.org/10.1002/lpor.201800316.
[114] L.-M. Zhou, K.-W. Xiao, J. Chen, N. Zhao, Optical levitation of nanodiamonds by doughnut beams in vacuum, Laser Photon. Rev. 11 (2017) 1600284. https://doi.org/10.1002/lpor.201600284.
[115] J.-X. Qin, X.-G. Yang, C.-F. Lv, Y.-Z. Li, K.-K. Liu, J.-H. Zang, X. Yang, L. Dong, C.-X. Shan, Nanodiamonds: Synthesis, properties, and applications in nanomedicine, Mater. Des. 210 (2021) 110091. https://doi.org/10.1016/j.matdes.2021.110091.
[116] N. Yang, Novel Aspects of Diamond, Springer International Publishing, Cham, 2019. https://doi.org/10.1007/978-3-030-12469-4.
[117] A. Krueger, D. Lang, Functionality is Key: Recent Progress in the Surface Modification of Nanodiamond, Adv. Funct. Mater. 22 (2012) 890–906. https://doi.org/10.1002/adfm.201102670.
[118] C. Li, X. Zhang, E.F. Oliveira, A.B. Puthirath, M.R. Neupane, J.D. Weil, A.G. Birdwell, T.G. Ivanov, S. Kong, T. Gray, H. Kannan, A. Biswas, R. Vajtai, D.S. Galvao, P.M. Ajayan, Systematic comparison of various oxidation treatments on diamond surface, Carbon N. Y. 182 (2021) 725–734. https://doi.org/10.1016/j.carbon.2021.06.050.
[119] F. Picollo, L. Mino, A. Battiato, S. Ditalia Tchernij, J. Forneris, K. Martina, M. Sacco, S. Tagliapietra, E. Vittone, P. Olivero, A. Barge, Synthesis and characterization of porphyrin functionalized nanodiamonds, Diam. Relat. Mater. 91 (2019) 22–28. https://doi.org/10.1016/j.diamond.2018.11.001.
[120] J.-R. Bertrand, C. Pioche-Durieu, J. Ayala, T. Petit, H.A. Girard, C.P. Malvy, E. Le Cam, F. Treussart, J.-C. Arnault, Plasma hydrogenated cationic detonation nanodiamonds efficiently deliver to human cells in culture functional siRNA targeting the Ewing sarcoma junction oncogene, Biomaterials. 45 (2015) 93–98. https://doi.org/10.1016/j.biomaterials.2014.12.007.
[121] D.P. Mitev, A.M. Alsharabasy, L. Morrison, S. Wittig, C. Diener, A. Pandit, Plasma & Microwaves as Greener Options for Nanodiamond Purification: Insight Into Cytocompatibility, Front. Bioeng. Biotechnol. 9 (2021) 1–18. https://doi.org/10.3389/fbioe.2021.637587.
[122] M. Khan, A. Hamid, L. Tiehu, A. Zada, F. Attique, N. Ahmad, A. Ullah, A. Hayat, I. Mahmood, A. Hussain, Y. Khan, I. Ahmad, A. Ali, T.K. Zhao, Surface optimization of detonation nanodiamonds for the enhanced mechanical properties of polymer/nanodiamond composites, Diam. Relat. Mater. 107 (2020) 107897. https://doi.org/10.1016/j.diamond.2020.107897.
[123] P. Aprà, L. Mino, A. Battiato, P. Olivero, S. Sturari, M.C. Valsania, V. Varzi, F. Picollo, Interaction of

Nanodiamonds with Water: Impact of Surface Chemistry on Hydrophilicity, Aggregation and Electrical Properties, Nanomaterials. 11 (2021) 2740. https://doi.org/10.3390/nano11102740.
[124] S. Sturari, V. Varzi, P. Aprà, A. Britel, N.-H. Amine, G. Andrini, E. Corte, G. Tomagra, L. Mino, P. Olivero, F. Picollo, A comprehensive study of the effect of thermally induced surface terminations on nanodiamonds electrical properties, Surfaces and Interfaces. 38 (2023) 102831. https://doi.org/10.1016/j.surfin.2023.102831.
[125] D.H. Jariwala, D. Patel, S. Wairkar, Surface functionalization of nanodiamonds for biomedical applications, Mater. Sci. Eng. C. 113 (2020) 110996. https://doi.org/10.1016/j.msec.2020.110996.
[126] Y.Y. Hui, C.-L. Cheng, H.-C. Chang, Nanodiamonds for optical bioimaging, J. Phys. D. Appl. Phys. 43 (2010) 374021. https://doi.org/10.1088/0022-3727/43/37/374021.
[127] N. Mohan, C.S. Chen, H.H. Hsieh, Y.C. Wu, H.C. Chang, In vivo imaging and toxicity assessments of fluorescent nanodiamonds in caenorhabditis elegans, Nano Lett. 10 (2010) 3692–3699. https://doi.org/10.1021/nl1021909.
[128] W.W.W. Hsiao, Y.Y. Hui, P.C. Tsai, H.C. Chang, Fluorescent Nanodiamond: A Versatile Tool for Long-Term Cell Tracking, Super-Resolution Imaging, and Nanoscale Temperature Sensing, Acc. Chem. Res. 49 (2016) 400–407. https://doi.org/10.1021/acs.accounts.5b00484.
[129] J.I. Chao, E. Perevedentseva, P.H. Chung, K.K. Liu, C.Y. Cheng, C.C. Chang, C.L. Cheng, Nanometer-sized diamond particle as a probe for biolabeling, Biophys. J. 93 (2007) 2199–2208. https://doi.org/10.1529/biophysj.107.108134.
[130] C.-C. Fu, H.-Y. Lee, K. Chen, T.-S. Lim, H.-Y. Wu, P.-K. Lin, P.-K. Wei, P.-H. Tsao, H.-C. Chang, W. Fann, Characterization and application of single fluorescent nanodiamonds as cellular biomarkers, Proc. Natl. Acad. Sci. 104 (2007) 727–732. https://doi.org/10.1073/pnas.0605409104.
[131] S.-J. Yu, M.-W. Kang, H.-C. Chang, K.-M. Chen, Y.-C. Yu, Bright Fluorescent Nanodiamonds: No Photobleaching and Low Cytotoxicity, J. Am. Chem. Soc. 127 (2005) 17604–17605. https://doi.org/10.1021/ja0567081.
[132] M.D. Torelli, A.G. Rickard, M. V. Backer, D.S. Filonov, N.A. Nunn, A. V. Kinev, J.M. Backer, G.M. Palmer, O.A. Shenderova, Targeting Fluorescent Nanodiamonds to Vascular Endothelial Growth Factor Receptors in Tumor, Bioconjug. Chem. 30 (2019) 604–613. https://doi.org/10.1021/acs.bioconjchem.8b00803.
[133] B. Zhang, Y. Li, C. Fang, C. Chang, C. Chen, Y. Chen, H. Chang, Receptor-Mediated Cellular Uptake of Folate-Conjugated Fluorescent Nanodiamonds: A Combined Ensemble and Single-Particle Study, Small. 5 (2009) 2716–2721. https://doi.org/10.1002/smll.200900725.
[134] M.-F. Weng, S.-Y. Chiang, N.-S. Wang, H. Niu, Fluorescent nanodiamonds for specifically targeted bioimaging: Application to the interaction of transferrin with transferrin receptor, Diam. Relat. Mater. 18 (2009) 587–591. https://doi.org/10.1016/j.diamond.2008.07.012.
[135] B.M. Chang, H.H. Lin, L.J. Su, W. Der Lin, R.J. Lin, Y.K. Tzeng, R.T. Lee, Y.C. Lee, A.L. Yu, H.C. Chang, Highly fluorescent nanodiamonds protein-functionalized for cell labeling and targeting, Adv. Funct. Mater. 23 (2013) 5737–5745. https://doi.org/10.1002/adfm.201301075.
[136] D. Terada, S. Sotoma, Y. Harada, R. Igarashi, M. Shirakawa, One-Pot Synthesis of Highly Dispersible Fluorescent Nanodiamonds for Bioconjugation, Bioconjug. Chem. 29 (2018) 2786–2792. https://doi.org/10.1021/acs.bioconjchem.8b00412.
[137] K. Kvakova, M. Ondra, J. Schimer, M. Petrik, Z. Novy, H. Raabova, M. Hajduch, P. Cigler, Visualization of Sentinel Lymph Nodes with Mannosylated Fluorescent Nanodiamonds, Adv. Funct. Mater. 32 (2022) 1–14. https://doi.org/10.1002/adfm.202109960.
[138] G. Mattheolabakis, L. Milane, A. Singh, M.M. Amiji, Hyaluronic acid targeting of CD44 for cancer therapy: from receptor biology to nanomedicine, J. Drug Target. 23 (2015) 605–618. https://doi.org/10.3109/1061186X.2015.1052072.
[139] F. Dosio, S. Arpicco, B. Stella, E. Fattal, Hyaluronic acid for anticancer drug and nucleic acid delivery, Adv. Drug Deliv. Rev. 97 (2016) 204–236. https://doi.org/10.1016/j.addr.2015.11.011.
[140] C. Chen, S. Zhao, A. Karnad, J.W. Freeman, The biology and role of CD44 in cancer progression: Therapeutic implications, J. Hematol. Oncol. 11 (2018) 1–23. https://doi.org/10.1186/s13045-018-0605-5.
[141] M. Hassn Mesrati, S.E. Syafruddin, M.A. Mohtar, A. Syahir, CD44: A Multifunctional Mediator of Cancer Progression, Biomolecules. 11 (2021) 1850. https://doi.org/10.3390/biom11121850.
[142] M. d'Amora, A. Camisasca, A. Boarino, S. Arpicco, S. Giordani, Supramolecular functionalization of carbon nano-onions with hyaluronic acid-phospholipid conjugates for selective targeting of cancer cells, Colloids Surfaces B Biointerfaces. 188 (2020) 110779. https://doi.org/10.1016/j.colsurfb.2020.110779.

[143] S. Arpicco, M. Bartkowski, A. Barge, D. Zonari, L. Serpe, P. Milla, F. Dosio, B. Stella, S. Giordani, Effects of the Molecular Weight of Hyaluronic Acid in a Carbon Nanotube Drug Delivery Conjugate, Front. Chem. 8 (2020) 1–12. https://doi.org/10.3389/fchem.2020.578008.

[144] T.H. Yun, G. Ahn, I. Choi, Y. Bae, K. Hwang, S. Kang, S. Choi, Fabrication of nanodiamonds modified with hyaluronic acid and chlorin e6 for selective photothermal and photodynamic tumor therapy, Polym. Adv. Technol. 31 (2020) 2990–2998. https://doi.org/10.1002/pat.5022.

[145] H.H. Han, H. Kang, S.-J. Kim, R. Pal, A.T.N. Kumar, H.S. Choi, S.K. Hahn, Fluorescent nanodiamond – hyaluronate conjugates for target-specific molecular imaging, RSC Adv. 11 (2021) 23073–23081. https://doi.org/10.1039/D1RA03936A.

[146] X. Cui, X. Deng, Z. Liang, J. Lu, L. Shao, X. Wang, F. Jia, Z. Pan, Q. Hu, X. Xiao, Y. Wu, W. Sheng, Multicomponent-assembled nanodiamond hybrids for targeted and imaging guided triple-negative breast cancer therapy: Via a ternary collaborative strategy, Biomater. Sci. 9 (2021) 3838–3850. https://doi.org/10.1039/d1bm00283j.

[147] X. Cui, Z. Liang, J. Lu, X. Wang, F. Jia, Q. Hu, X. Xiao, X. Deng, Y. Wu, W. Sheng, A multifunctional nanodiamond-based nanoplatform for the enhanced mild-temperature photothermal/chemo combination therapy of triple negative breast cancer: Via an autophagy regulation strategy, Nanoscale. 13 (2021) 13375–13389. https://doi.org/10.1039/d1nr03161a.

[148] M.G. Chernysheva, A. V. Sinolits, V.S. Votyakova, A.G. Popov, G.A. Badun, Preparation and properties of Miramistin–hyaluronic acid coatings on the nanodiamond surface, Mendeleev Commun. 32 (2022) 501–503. https://doi.org/10.1016/j.mencom.2022.07.023.

[149] S. Ramanathan, S.C.B. Gopinath, Z.H. Ismail, M.K. Md Arshad, P. Poopalan, Aptasensing nucleocapsid protein on nanodiamond assembled gold interdigitated electrodes for impedimetric SARS-CoV-2 infectious disease assessment, Biosens. Bioelectron. 197 (2022) 113735. https://doi.org/10.1016/j.bios.2021.113735.

[150] Y. Wu, T. Weil, Recent Developments of Nanodiamond Quantum Sensors for Biological Applications, Adv. Sci. 9 (2022) 2200059. https://doi.org/10.1002/advs.202200059.

[151] G. Petrini, E. Moreva, E. Bernardi, P. Traina, G. Tomagra, V. Carabelli, I. Pietro Degiovanni, M. Genovese, Is a Quantum Biosensing Revolution Approaching? Perspectives in NV-Assisted Current and Thermal Biosensing in Living Cells, Adv. Quantum Technol. 3 (2020) 2000066. https://doi.org/10.1002/qute.202000066.

[152] Y. Wu, M.N.A. Alam, P. Balasubramanian, A. Ermakova, S. Fischer, H. Barth, M. Wagner, M. Raabe, F. Jelezko, T. Weil, Nanodiamond Theranostic for Light-Controlled Intracellular Heating and Nanoscale Temperature Sensing, Nano Lett. 21 (2021) 3780–3788. https://doi.org/10.1021/acs.nanolett.1c00043.

[153] G. Petrini, G. Tomagra, E. Bernardi, E. Moreva, P. Traina, A. Marcantoni, F. Picollo, K. Kvaková, P. Cígler, I. Pietro Degiovanni, V. Carabelli, M. Genovese, Nanodiamond–Quantum Sensors Reveal Temperature Variation Associated to Hippocampal Neurons Firing, Adv. Sci. 9 (2022) 2202014. https://doi.org/10.1002/advs.202202014.

[154] L. Nie, A.C. Nusantara, V.G. Damle, M. V. Baranov, M. Chipaux, C. Reyes-San-Martin, T. Hamoh, C.P. Epperla, M. Guricova, P. Cigler, G. van den Bogaart, R. Schirhagl, Quantum Sensing of Free Radicals in Primary Human Dendritic Cells, Nano Lett. 22 (2022) 1818–1825. https://doi.org/10.1021/acs.nanolett.1c03021.

[155] R. Sharmin, T. Hamoh, A. Sigaeva, A. Mzyk, V.G. Damle, A. Morita, T. Vedelaar, R. Schirhagl, Fluorescent Nanodiamonds for Detecting Free-Radical Generation in Real Time during Shear Stress in Human Umbilical Vein Endothelial Cells, ACS Sensors. 6 (2021) 4349–4359. https://doi.org/10.1021/acssensors.1c01582.

[156] E. Mayerhoefer, A. Krueger, Surface Control of Nanodiamond: From Homogeneous Termination to Complex Functional Architectures for Biomedical Applications, Acc. Chem. Res. 55 (2022) 3594–3604. https://doi.org/10.1021/acs.accounts.2c00596.

[157] J. Chen, S.Z. Deng, J. Chen, Z.X. Yu, N.S. Xu, Graphitization of nanodiamond powder annealed in argon ambient, Appl. Phys. Lett. 74 (1999) 3651–3653. https://doi.org/10.1063/1.123211.

[158] L. Ginés, S. Mandal, Ashek-I-Ahmed, C.L. Cheng, M. Sow, O.A. Williams, Positive zeta potential of nanodiamonds, Nanoscale. 9 (2017) 12549–12555. https://doi.org/10.1039/c7nr03200e.

[159] X. Song, G. Wang, X. Liu, F. Feng, J. Wang, L. Lou, W. Zhu, Generation of nitrogen-vacancy color center in nanodiamonds by high temperature annealing, Appl. Phys. Lett. 102 (2013) 133109. https://doi.org/10.1063/1.4800219.

[160] S. Pezzagna, D. Rogalla, D. Wildanger, J. Meijer, A. Zaitsev, Creation and nature of optical centres in diamond for single-photon emission—overview and critical remarks, New J. Phys. 13 (2011) 035024.

https://doi.org/10.1088/1367-2630/13/3/035024.
[161] V.L. Kuznetsov, A.L. Chuvilin, Y. V Butenko, I.Y. Mal'kov, V.M. Titov, Onion-like carbon from ultra-disperse diamond, Chem. Phys. Lett. 222 (1994) 343–348. https://doi.org/10.1016/0009-2614(94)87072-1.
[162] S. Tomita, T. Sakurai, H. Ohta, M. Fujii, S. Hayashi, Structure and electronic properties of carbon onions, J. Chem. Phys. 114 (2001) 7477–7482. https://doi.org/10.1063/1.1360197.
[163] Z. Qiao, J. Li, N. Zhao, C. Shi, P. Nash, Graphitization and microstructure transformation of nanodiamond to onion-like carbon, Scr. Mater. 54 (2006) 225–229. https://doi.org/10.1016/j.scriptamat.2005.09.037.
[164] S. Osswald, G. Yushin, V. Mochalin, S.O. Kucheyev, Y. Gogotsi, Control of sp2/sp3 carbon ratio and surface chemistry of nanodiamond powders by selective oxidation in air, J. Am. Chem. Soc. 128 (2006) 11635–11642. https://doi.org/10.1021/ja063303n.
[165] N.S. Xu, J. Chen, S.Z. Deng, Effect of heat treatment on the properties of nano-diamond under oxygen and argon ambient, Diam. Relat. Mater. 11 (2002) 249–256. https://doi.org/10.1016/S0925-9635(01)00680-X.
[166] B.R. Smith, D. Gruber, T. Plakhotnik, The effects of surface oxidation on luminescence of nano diamonds, Diam. Relat. Mater. 19 (2010) 314–318. https://doi.org/10.1016/j.diamond.2009.12.009.
[167] X. Xu, Z. Yu, Y. Zhu, B. Wang, Influence of surface modification adopting thermal treatments on dispersion of detonation nanodiamond, J. Solid State Chem. 178 (2005) 688–693. https://doi.org/10.1016/j.jssc.2004.12.025.
[168] P. Aprà, N.H. Amine, A. Britel, S. Sturari, V. Varzi, M. Ziino, L. Mino, P. Olivero, F. Picollo, Creation, Control, and Modeling of NV Centers in Nanodiamonds, Adv. Funct. Mater. 2404831 (2024). https://doi.org/10.1002/adfm.202404831.
[169] T. Kondo, I. Neitzel, V.N. Mochalin, J. Urai, M. Yuasa, Y. Gogotsi, Electrical conductivity of thermally hydrogenated nanodiamond powders, J. Appl. Phys. 113 (2013) 214307. https://doi.org/10.1063/1.4809549.
[170] O.A. Williams, J. Hees, C. Dieker, W. Jäger, L. Kirste, C.E. Nebel, Size-dependent reactivity of diamond nanoparticles, ACS Nano. 4 (2010) 4824–4830. https://doi.org/10.1021/nn100748k.
[171] S. Stehlik, T. Glatzel, V. Pichot, R. Pawlak, E. Meyer, D. Spitzer, B. Rezek, Water interaction with hydrogenated and oxidized detonation nanodiamonds - Microscopic and spectroscopic analyses, Diam. Relat. Mater. 63 (2016) 97–102. https://doi.org/10.1016/j.diamond.2015.08.016.
[172] V. Varzi, E. Fratini, M. Falconieri, D. Giovannini, A. Cemmi, J. Scifo, I. Di Sarcina, P. Aprà, S. Sturari, L. Mino, G. Tomagra, E. Infusino, V. Landoni, C. Marino, M. Mancuso, F. Picollo, S. Pazzaglia, Nanodiamond Effects on Cancer Cell Radiosensitivity: The Interplay between Their Chemical/Physical Characteristics and the Irradiation Energy, Int. J. Mol. Sci. 24 (2023) 16622. https://doi.org/10.3390/ijms242316622.
[173] V.L. Kuznetsov, Y.V. Butenko, A.L. Chuvilin, A.I. Romanenko, A.V. Okotrub, Electrical resistivity of graphitized ultra-disperse diamond and onion-like carbon, Chem. Phys. Lett. 336 (2001) 397–404. https://doi.org/10.1016/S0009-2614(01)00135-X.
[174] M. Bevilacqua, S. Patel, A. Chaudhary, H. Ye, R.B. Jackman, Electrical properties of aggregated detonation nanodiamonds, Appl. Phys. Lett. 93 (2008) 132115. https://doi.org/10.1063/1.2996026.
[175] A. Chaudhary, J.O. Welch, R.B. Jackman, Electrical properties of monodispersed detonation nanodiamonds, Appl. Phys. Lett. 96 (2010) 242903. https://doi.org/10.1063/1.3446966.
[176] J. Čermák, H. Kozak, Š. Stehlík, V. Švrček, V. Pichot, D. Spitzer, A. Kromka, B. Rezek, Microscopic Electrical Conductivity of Nanodiamonds after Thermal and Plasma Treatments, MRS Adv. 1 (2016) 1105–1111. https://doi.org/10.1557/adv.2016.112.
[177] J.O. Welch, P. Li, A. Chaudhary, R. Edgington, R.B. Jackman, The influence of surface functionalisation on the electrical properties and thermal stability of nanodiamonds, J. Appl. Phys. 116 (2014) 133705. https://doi.org/10.1063/1.4897218.
[178] E.-Z. Piña-Salazar, K. Sagisaka, Y. Hattori, T. Sakai, R. Futamura, E. Ōsawa, K. Kaneko, Electrical conductivity changes of water-adsorbed nanodiamonds with thermal treatment, Chem. Phys. Lett. 737 (2019) 100018. https://doi.org/10.1016/j.cpletx.2019.100018.
[179] S.A. Denisov, G.A. Sokolina, G.P. Bogatyreva, T.Y. Grankina, O.K. Krasil'nikova, E. V. Plotnikova, B. V. Spitsyn, Adsorption and electrical properties of nanodiamond powders in the presence of water vapor, Prot. Met. Phys. Chem. Surfaces. 49 (2013) 286–291. https://doi.org/10.1134/S2070205113030088.
[180] E. Brun, H.A. Girard, J.-C. Arnault, M. Mermoux, C. Sicard-Roselli, Hydrogen plasma treated nanodiamonds lead to an overproduction of hydroxyl radicals and solvated electrons in solution under ionizing radiation, Carbon N. Y. 162 (2020) 510–518. https://doi.org/10.1016/j.carbon.2020.02.063.
[181] R. Li, T. Vedelaar, A. Mzyk, A. Morita, S.K. Padamati, R. Schirhagl, Following Polymer Degradation with

Nanodiamond Magnetometry, ACS Sensors. 7 (2022) 123–130. https://doi.org/10.1021/acssensors.1c01782.
[182] A. Morita, T. Hamoh, F.P. Perona Martinez, M. Chipaux, A. Sigaeva, C. Mignon, K.J. van der Laan, A. Hochstetter, R. Schirhagl, The fate of lipid-coated and uncoated fluorescent nanodiamonds during cell division in yeast, Nanomaterials. 10 (2020) 1–17. https://doi.org/10.3390/nano10030516.
[183] N. Norouzi, A.C. Nusantara, Y. Ong, T. Hamoh, L. Nie, A. Morita, Y. Zhang, A. Mzyk, R. Schirhagl, Relaxometry for detecting free radical generation during Bacteria's response to antibiotics, Carbon N. Y. 199 (2022) 444–452. https://doi.org/10.1016/j.carbon.2022.08.025.
[184] K. Wu, L. Nie, A.C. Nusantara, W. Woudstra, T. Vedelaar, A. Sigaeva, R. Schirhagl, Diamond Relaxometry as a Tool to Investigate the Free Radical Dialogue between Macrophages and Bacteria, ACS Nano. 17 (2023) 1100–1111. https://doi.org/10.1021/acsnano.2c08190.
[185] T.A. Vedelaar, T.H. Hamoh, F.P.P. Martinez, M. Chipaux, R. Schirhagl, Optimizing Data Processing for Nanodiamond Based Relaxometry, Adv. Quantum Technol. 2300109 (2023) 1–9. https://doi.org/10.1002/qute.202300109.
[186] S.A. Bogdanov, A.M. Gorbachev, D.B. Radishev, A.L. Vikharev, M.A. Lobaev, S.A. Gusev, D.A. Tatarsky, S. V. Bolshedvorskii, A. V. Akimov, V. V. Chernov, Creation of Localized NV Center Ensembles in CVD Diamond by Electron Beam Irradiation, Tech. Phys. Lett. 45 (2019) 281–284. https://doi.org/10.1134/S1063785019030222.
[187] S. Kollarics, F. Simon, A. Bojtor, K. Koltai, G. Klujber, M. Szieberth, B.G. Márkus, D. Beke, K. Kamarás, A. Gali, D. Amirari, R. Berry, S. Boucher, D. Gavryushkin, G. Jeschke, J.P. Cleveland, S. Takahashi, P. Szirmai, L. Forró, E. Emmanouilidou, R. Singh, K. Holczer, Ultrahigh nitrogen-vacancy center concentration in diamond, Carbon N. Y. 188 (2022) 393–400. https://doi.org/10.1016/j.carbon.2021.12.032.
[188] P. Aprà, A. Battiato, S.D. Tchernij, J. Forneris, Proton Beam Induced Fluorescence in 5 nm Detonation Nanodiamond, Lab. Naz. Di Legnaro Annu. Rep. 2017. (2018) 5–6.
[189] S. Sturari, I. Andreana, P. Aprà, V. Bincoletto, J. Kopecka, L. Mino, B. Zurletti, B. Stella, C. Riganti, S. Arpicco, F. Picollo, Designing functionalized nanodiamonds with hyaluronic acid–phospholipid conjugates for enhanced cancer cell targeting and fluorescence imaging capabilities, Nanoscale. 16 (2024) 11610–11622. https://doi.org/10.1039/D4NR00932K.
[190] O.A. Alduchov, R.E. Eskridge, Improved Magnus Form Approximation of Saturation Vapor Pressure, J. Appl. Meteorol. 35 (1996) 601–609. https://doi.org/10.1175/1520-0450(1996)035<0601:IMFAOS>2.0.CO;2.
[191] D. Titus, E. James Jebaseelan Samuel, S.M. Roopan, Nanoparticle characterization techniques, in: Green Synth. Charact. Appl. Nanoparticles, Elsevier, 2019: pp. 303–319. https://doi.org/10.1016/B978-0-08-102579-6.00012-5.
[192] D. Wolverson, Raman Spectroscopy, in: An Introd. to Laser Spectrosc., Springer US, Boston, MA, 1995: pp. 91–114. https://doi.org/10.1007/978-1-4613-0337-4_6.
[193] K.D. Vernon-Parry, Scanning electron microscopy: an introduction, III-Vs Rev. 13 (2000) 40–44. https://doi.org/10.1016/S0961-1290(00)80006-X.
[194] R. Pecora, Dynamic Light Scattering Measurement of Nanometer Particles in Liquids, J. Nanoparticle Res. 2 (2000) 123–131. https://doi.org/10.1023/A:1010067107182.
[195] H.-A. Kim, J.-K. Seo, T. Kim, B.-T. Lee, Nanometrology and its perspectives in environmental research, Environ. Health Toxicol. 29 (2014). https://doi.org/10.5620/eht.e2014016.
[196] Dynamic Light Scattering : An Introduction in 30 Minutes, (n.d.). https://warwick.ac.uk/fac/cross_fac/sciencecity/programmes/internal/themes/am2/booking/particlesize/intro_to_dls.pdf.
[197] Zeta potential: An Introduction in 30 minutes, (n.d.). https://www.materials-talks.com/wp-content/uploads/2017/09/mrk654-01_an_introduction_to_zeta_potential_v3.pdf.
[198] Measuring zeta potential – laser doppler electrophoresis, (n.d.). http://www.pct.hu/wsp_images/zetalde.pdf.
[199] Measuring zeta potential using phase analysis light scattering (PALS), (n.d.). http://www.pct.hu/wsp_images/zetapals.pdf.
[200] W. Freinbichler, L. Bianchi, M.A. Colivicchi, C. Ballini, K.F. Tipton, W. Linert, L. Della Corte, The detection of hydroxyl radicals in vivo, J. Inorg. Biochem. 102 (2008) 1329–1333. https://doi.org/10.1016/j.jinorgbio.2007.12.017.
[201] S.E. Page, W.A. Arnold, K. McNeill, Terephthalate as a probe for photochemically generated hydroxyl radical, J. Environ. Monit. 12 (2010) 1658. https://doi.org/10.1039/c0em00160k.

[202] E.B. Yan, J.K. Unthank, M. Castillo-Melendez, S.L. Miller, S.J. Langford, D.W. Walker, Novel method for in vivo hydroxyl radical measurement by microdialysis in fetal sheep brain in utero, J. Appl. Physiol. 98 (2005) 2304–2310. https://doi.org/10.1152/japplphysiol.00617.2004.
[203] I. Šnyrychová, É. Hideg, The first application of terephthalate fluorescence for highly selective detection of hydroxyl radicals in thylakoid membranes, Funct. Plant Biol. 34 (2007) 1105. https://doi.org/10.1071/FP07150.
[204] E.A. Donley, T.P. Heavner, F. Levi, M.O. Tataw, S.R. Jefferts, Double-pass acousto-optic modulator system, Rev. Sci. Instrum. 76 (2005) 3–8. https://doi.org/10.1063/1.1930095.
[205] L. Mino, C. Negri, R. Santalucia, G. Cerrato, G. Spoto, G. Martra, Morphology, Surface Structure and Water Adsorption Properties of TiO2 Nanoparticles: A Comparison of Different Commercial Samples, Molecules. 25 (2020) 4605. https://doi.org/10.3390/molecules25204605.
[206] T. Petit, L. Puskar, FTIR spectroscopy of nanodiamonds: Methods and interpretation, Diam. Relat. Mater. 89 (2018) 52–66. https://doi.org/10.1016/j.diamond.2018.08.005.
[207] M. Acik, G. Lee, C. Mattevi, A. Pirkle, R.M. Wallace, M. Chhowalla, K. Cho, Y. Chabal, The Role of Oxygen during Thermal Reduction of Graphene Oxide Studied by Infrared Absorption Spectroscopy, J. Phys. Chem. C. 115 (2011) 19761–19781. https://doi.org/10.1021/jp2052618.
[208] L. Mino, C. Negri, A. Zecchina, G. Spoto, Photodegradation of Organic Pollutants on TiO 2 P25 Surfaces Investigated by Transmission FTIR Spectroscopy Under In Situ UV-Vis Irradiation, Zeitschrift Für Phys. Chemie. 230 (2016) 1441–1451. https://doi.org/10.1515/zpch-2015-0733.
[209] S. Ji, T. Jiang, K. Xu, S. Li, FTIR study of the adsorption of water on ultradispersed diamond powder surface, Appl. Surf. Sci. 133 (1998) 231–238. https://doi.org/10.1016/S0169-4332(98)00209-8.
[210] S. Stehlik, T. Petit, H.A. Girard, J.-C. Arnault, A. Kromka, B. Rezek, Nanoparticles Assume Electrical Potential According to Substrate, Size, and Surface Termination, Langmuir. 29 (2013) 1634–1641. https://doi.org/10.1021/la304472w.
[211] L. Mino, Á. Morales-García, S.T. Bromley, F. Illas, Understanding the nature and location of hydroxyl groups on hydrated titania nanoparticles, Nanoscale. 13 (2021) 6577–6585. https://doi.org/10.1039/D1NR00610J.
[212] R. Gilli, M. Kacuráková, M. Mathlouthi, L. Navarini, S. Paoletti, FTIR studies of sodium hyaluronate and its oligomers in the amorphous solid phase and in aqueous solution, Carbohydr. Res. 263 (1994) 315–326. https://doi.org/10.1016/0008-6215(94)00147-2.
[213] K. Haxaire, Y. Maréchal, M. Milas, M. Rinaudo, Hydration of polysaccharide hyaluronan observed by IR spectrometry. I. Preliminary experiments and band assignments, Biopolymers. 72 (2003) 10–20. https://doi.org/10.1002/bip.10245.
[214] M.E. Cano, D. Lesur, V. Bincoletto, E. Gazzano, B. Stella, C. Riganti, S. Arpicco, J. Kovensky, Synthesis of defined oligohyaluronates-decorated liposomes and interaction with lung cancer cells, Carbohydr. Polym. 248 (2020) 116798. https://doi.org/10.1016/j.carbpol.2020.116798.
[215] S.P.M. Crouch, R. Kozlowski, K.J. Slater, J. Fletcher, The use of ATP bioluminescence as a measure of cell proliferation and cytotoxicity, J. Immunol. Methods. 160 (1993) 81–88. https://doi.org/10.1016/0022-1759(93)90011-U.
[216] A. Verma, F. Stellacci, Effect of Surface Properties on Nanoparticle–Cell Interactions, Small. 6 (2010) 12–21. https://doi.org/10.1002/smll.200901158.
[217] T.-G. Iversen, T. Skotland, K. Sandvig, Endocytosis and intracellular transport of nanoparticles: Present knowledge and need for future studies, Nano Today. 6 (2011) 176–185. https://doi.org/10.1016/j.nantod.2011.02.003.
[218] A. Sigaeva, V. Merz, R. Sharmin, R. Schirhagl, A. Krueger, Intracellular behavior of nanodiamonds functionalized with a zwitterionic shielding moiety, J. Mater. Chem. C. 11 (2023) 6642–6650. https://doi.org/10.1039/D3TC00590A.
[219] P. Dewangan, A. Mourya, P.K. Singh, M. Chaudhary, R. Sharma, N. Bajwa, A. Baldi, K.K. Singh, S.B. Singh, J. Madan, K.P. Namdeo, Drug delivery: The conceptual perspectives and therapeutic applications, in: Polym. Conjug., Elsevier, 2023: pp. 1–38. https://doi.org/10.1016/B978-0-323-91663-9.00010-2.
[220] T.M. Tamer, C. Of, T. Applications, Polymeric Nanocomposites: Structure, Manufacture, And Properties, in: Eng. Polym. Chem. Complexity, Vol. II, Apple Academic Press, 2014: pp. 21–52. https://doi.org/10.1201/b16876-7.
[221] A. Lierova, J. Kasparova, A. Filipova, J. Cizkova, L. Pekarova, L. Korecka, N. Mannova, Z. Bilkova, Z. Sinkorova, Hyaluronic Acid: Known for Almost a Century, but Still in Vogue, Pharmaceutics. 14 (2022) 838.

https://doi.org/10.3390/pharmaceutics14040838.
[222] M. Dovedytis, Z.J. Liu, S. Bartlett, Hyaluronic acid and its biomedical applications: A review, Eng. Regen. 1 (2020) 102–113. https://doi.org/10.1016/j.engreg.2020.10.001.
[223] Y. Tokita, H. Sakashita, A. Okamoto, K. Kubota, Kinetic study of a radical scavenging effect of hyaluronic acid, Polym. Int. 38 (1995) 161–164. https://doi.org/10.1002/pi.1995.210380208.
[224] R. Moseley, M. Leaver, M. Walker, R.J. Waddington, D. Parsons, W.Y.J. Chen, G. Embery, Comparison of the antioxidant properties of HYAFF®-11p75, AQUACEL® and hyaluronan towards reactive oxygen species in vitro, Biomaterials. 23 (2002) 2255–2264. https://doi.org/10.1016/S0142-9612(01)00360-X.
[225] C. Ke, L. Sun, D. Qiao, D. Wang, X. Zeng, Antioxidant acitivity of low molecular weight hyaluronic acid, Food Chem. Toxicol. 49 (2011) 2670–2675. https://doi.org/10.1016/j.fct.2011.07.020.
[226] S.T. Alsid, J.F. Barry, L.M. Pham, J.M. Schloss, M.F. O'Keeffe, P. Cappellaro, D.A. Braje, Photoluminescence Decomposition Analysis: A Technique to Characterize NV Creation in Diamond, Phys. Rev. Appl. 12 (2019) 044003. https://doi.org/10.1103/PhysRevApplied.12.044003.
[227] C. Laube, T. Oeckinghaus, J. Lehnert, J. Griebel, W. Knolle, A. Denisenko, A. Kahnt, J. Meijer, J. Wrachtrup, B. Abel, Controlling the fluorescence properties of nitrogen vacancy centers in nanodiamonds, Nanoscale. 11 (2019) 1770–1783. https://doi.org/10.1039/C8NR07828A.
[228] C. Fang, Y. Zhang, Z. Zhang, C. Shan, W. Shen, X. Jia, Preparation of "natural" diamonds by HPHT annealing of synthetic diamonds, CrystEngComm. 20 (2018) 505–511. https://doi.org/10.1039/C7CE02013A.
[229] D. Gatto Monticone, F. Quercioli, R. Mercatelli, S. Soria, S. Borini, T. Poli, M. Vannoni, E. Vittone, P. Olivero, Systematic study of defect-related quenching of NV luminescence in diamond with time-correlated single-photon counting spectroscopy, Phys. Rev. B. 88 (2013) 155201. https://doi.org/10.1103/PhysRevB.88.155201.

Acknowledgments/Ringraziamenti

It feels surreal to write these acknowledgements, marking the end of a journey that has been both tough and challenging, but ultimately rewarding. To truly do justice to the past few years, this section would need to capture everything that has happened, but that would require another 140 pages. So, I will keep it brief, hoping to convey the essence of my gratitude to all those who have accompanied me on this path.

In primis, ringrazio sinceramente tutti i membri del gruppo di Fisica dello Stato Solido, in particolare il gruppo *Diamantisti*. Desidero ringraziare profondamente il mio supervisor, il Prof. Federico Picollo, per aver seguito la mia attività con infinita attenzione, disponibilità e pazienza (un'*ultima cosa* dopo l'altra!) sin dai tempi della mia tesi magistrale, guidandomi nel mio percorso di crescita scientifica e ispirandomi anche sul piano personale, con il suo spirito ottimista e positivo, che mi ha insegnato a non considerare mai nulla perduto.

Un sincero ringraziamento va anche tutti gli altri componenti ed ex-componenti del gruppo *Diamond for Bio*, che sono stati non soltanto compagni di lavoro quotidiano, ma anche amici preziosi in questi anni. Un grazie speciale va al Dott. Pietro Aprà per avermi costantemente aiutato, supportato (ricoprendo anche il ruolo di co-relatore della mia tesi magistrale, nonché di *corresponding author* del mio primo articolo) e, in più, per essere un amico fidato e sincero, con cui ho condiviso moltissimi momenti, sia in laboratorio che fuori. Il suo incoraggiamento e il suo sostegno mi hanno sempre spronata, sia nella ricerca che nella vita, risollevandomi e strappandomi una risata anche nei momenti più difficili. Ringrazio di cuore anche la Dott.ssa Veronica Varzi, vera amica e fonte di sostegno scientifico (soprattutto nelle famigerate misure con il TPA!) e morale; anche con lei ho passato molto tempo durante questi ultimi anni e spero che ci saranno occasioni di vederci spesso anche in futuro, anche se ora percorriamo cammini lavorativi diversi. Un sentito grazie va anche alla Dott.ssa Giulia Tomagra, a cui sono grata per tutto l'aiuto e la disponibilità in moltissime occasioni, nonché per l'amicizia dimostrata, pur avendo avuto meno opportunità di trascorrere del tempo insieme in contesti extra-accademici. Le auguro il meglio per il bellissimo capitolo che sta per iniziare. I would also like to express my gratitude to Dr. Nour-Hanne Amine, who started this PhD journey with me. We attended courses and schools together, supporting each other along the way, both in research and in life. Many of the best moments in these last years were shared with her and Pietro, both in and outside the lab. A special thanks also goes to Dr. Adam Britel for his helpfulness and technical support on multiple occasions. I am especially grateful for his assistance in 3D printing the cell that played a crucial role in my first paper.

Un ringraziamento speciale al Prof. Lorenzo Mino per il suo aiuto fondamentale nelle misure di spettroscopia DRIFT e i suoi preziosi consigli, nonché per l'assistenza nel lavoro sull'rGO, che, pur non essendo stato incluso in questa tesi, ha rappresentato una tappa importante del mio percorso di dottorato. La sua disponibilità costante è stata essenziale, soprattutto nelle attività più delicate di questi anni.

Desidero inoltre ringraziare per la collaborazione fondamentale nella funzionalizzazione dei nanodiamanti la Prof.ssa Silvia Arpicco e il suo gruppo di ricerca, in particolare la Prof.ssa Barbara Stella, le Dott.sse Valeria Bincoletto e Ilaria Andreana, e la Dott.ssa Beatrice Zurletti, che nel tempo è diventata anche un'amica. Ringrazio anche la Prof.ssa Chiara Riganti, la Dott.ssa Joanna Kopecka e il Dott. Stefano Boetti per la collaborazione negli aspetti biologici del lavoro di ricerca e per il tempo dedicato allo svolgimento dei test *in vitro*.

Dank u wel to Prof. Romana Schirhagl for hosting me in her laboratories at the Universitair Medisch Centrum Groningen, and to her research group. In particular, I would like to thank Dr. Felipe Perona Martínez, Dr. Hui-Ting Li, Dr. Adéla Melcrová, and Dr. Elkin Escobar-Chaves, who closely followed me during my internship, introducing me to the technique of T_1-relaxometry and providing valuable advice (not only in research, but also for life in Groningen). I am truly grateful for the opportunity I had to work there, expanding my knowledge and improving my ability to adapt to new challenges.

I also want to acknowledge Prof. Silvia Giordani and Prof. Bohuslav Rezek for reviewing and evaluating my thesis work.

A big thank also goes to the friends who emerged during my time at university but have not been explicitly mentioned yet, namely Akhil Kuriakose and Sachin Singh. We shared many conversations about the challenges of our academic journey, as well as many laughs and enjoyable moments together, including with Pietro and Nour-Hanne, which truly brightened these years.

Infine, ma non certo per importanza, desidero ringraziare tutta la mia famiglia per tutti gli incoraggiamenti, il supporto e l'affetto costante. Grazie infinite mamma e papà per essermi sempre accanto, aiutarmi costantemente, sopportarmi pazientemente quando sono intrattabile (spesso e volentieri) e aver sempre fiducia in me, soprattutto quando io la perdo. Perdonatemi per tutti i momenti di nervosismo e frustrazione...sappiate che vi considero i pilastri della mia vita e che, senza di voi, non avrei potuto arrivare fin qui.